

UNCLASSIFIED

AD NUMBER

AD884106

LIMITATION CHANGES

TO:

Approved for public release; distribution is unlimited.

FROM:

Distribution authorized to U.S. Gov't. agencies and their contractors; Critical Technology; MAY 1971. Other requests shall be referred to Air Force Avionics Lab., Attn: AVWE, Wright-Patterson AFB, OH 45433. This document contains export-controlled technical data.

AUTHORITY

AFWAL ltr dtd 8 Jun 1982

THIS PAGE IS UNCLASSIFIED

AD

884/06

AUTHORITY:

AFWAL
174 8 Jun 82





AD884106

AD No. _____
DDC FILE COPY

THE RESPONSE OF TERRESTRIAL SURFACES
AT MICROWAVE FREQUENCIES

(2440-7)

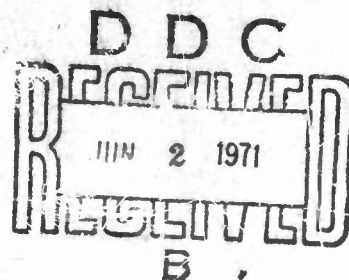
W.H. Peake and T.L. Oliver

The Ohio State University
ElectroScience Laboratory

Department of Electrical Engineering
Columbus, Ohio 43212

Technical Report AFAL-TR-70-301

May 1971



This document is subject to special export controls and each transmittal to foreign governments or foreign nationals may be made only with prior approval of AFAL(AVWE), Wright-Patterson Air Force Base, Ohio 45433.

Air Force Avionics Laboratory
Air Force Systems Command
Wright-Patterson Air Force Base, Ohio 45433

278

UNCLASSIFIED

Security Classification

DOCUMENT CONTROL DATA - R&D		
(Security classification of title, body of abstract and indexing annotation must be entered when the overall report is classified)		
1. ORIGINATING ACTIVITY (Corporate author) ElectroScience Laboratory Department of Electrical Engineering, The Ohio State University, Columbus, Ohio		2a. REPORT SECURITY CLASSIFICATION UNCLASSIFIED 2b. GROUP
3. REPORT TITLE THE RESPONSE OF TERRESTRIAL SURFACES AT MICROWAVE FREQUENCIES		
4. DESCRIPTIVE NOTES (Type of report and inclusive dates)		
5. AUTHOR(S) (Last name, first name, initial) W.H. Peake and T.L. Oliver		
6. REPORT DATE May 1971	7a. TOTAL NO. OF PAGES 255	7b. NO. OF REFS 105
8a. CONTRACT OR GRANT NO. F33615-67-C-1663 ✓ b. PROJECT NO. 4 144 c. TASK d. BPSN: 7-63781014	9a. ORIGINATOR'S REPORT NUMBER(S) ElectroScience Laboratory 2440-7 9b. OTHER REPORT NO(S) (Any other numbers that may be assigned this report) AFAL-TR-70-301	
10. AVAILABILITY/LIMITATION NOTICES This document is subject to special export controls and each transmittal to foreign governments or foreign nationals may be made only with prior approval of AFAL(AVWE), Wright-Patterson Air Force Base, Ohio 45433.		
11. SUPPLEMENTARY NOTES	12. SPONSORING MILITARY ACTIVITY Air Force Avionics Laboratory Wright-Patterson Air Force Base, Ohio	
13. ABSTRACT This report reviews the basic properties and terrestrial surface responses of microwave sensors, both active (radar) and passive (microwave radiometer). Appropriate surface responses (bistatic coefficient, emissivity etc.) are defined and used to provide general formulas for the system response (receiver power, antenna temperature, doppler spectrum) in terms of system geometry and configuration. The dielectric properties of terrestrial surfaces are reviewed, and data on the complex dielectric constant of rocks, soils and vegetation are tabulated. Theoretical models for surface response are provided for a variety of surface classes, including the surface of uniform layers, the surface with large scale undulation, the slightly rough surface, the surface of individual scatterers (Lommel-Seeliger surface) and the empirical models (Lambert surfaces). Finally, the report includes a large number of typical surface responses at microwave frequencies. Measured bistatic scattering coefficients, radar return, and surface brightness temperature for many terrestrial surface classes are presented and interpreted in terms of the influence of such parameters as surface roughness, dielectric constant, polarization, frequency, angle of incidence etc. on the response.		

DD FORM 1473
1 JAN 64

UNCLASSIFIED

Security Classification

UNCLASSIFIED

Security Classification

14. KEY WORDS	LINK A		LINK B		LINK C	
	ROLE	WT	ROLE	WT	ROLE	WT
Radar return Bistatic scattering Microwave radiometer Brightness temperature Terrain Sea surface Complex dielectric constant Microwave sensor						

INSTRUCTIONS

1. **ORIGINATING ACTIVITY:** Enter the name and address of the contractor, subcontractor, grantee, Department of Defense activity or other organization (*corporate author*) issuing the report.

2a. **REPORT SECURITY CLASSIFICATION:** Enter the overall security classification of the report. Indicate whether "Restricted Data" is included. Marking is to be in accordance with appropriate security regulations.

2b. **GROUP:** Automatic downgrading is specified in DoD Directive 5200.10 and Armed Forces Industrial Manual. Enter the group number. Also, when applicable, show that optional markings have been used for Group 3 and Group 4 as authorized.

3. **REPORT TITLE:** Enter the complete report title in all capital letters. Titles in all cases should be unclassified. If a meaningful title cannot be selected without classification, show title classification in all capitals in parenthesis immediately following the title.

4. **DESCRIPTIVE NOTES:** If appropriate, enter the type of report, e.g., interim, progress, summary, annual, or final. Give the inclusive dates when a specific reporting period is covered.

5. **AUTHOR(S):** Enter the name(s) of author(s) as shown on or in the report. Enter last name, first name, middle initial. If military, show rank and branch of service. The name of the principal author is an absolute minimum requirement.

6. **REPORT DATE:** Enter the date of the report as day, month, year, or month, year. If more than one date appears on the report, use date of publication.

7a. **TOTAL NUMBER OF PAGES:** The total page count should follow normal pagination procedures, i.e., enter the number of pages containing information.

7b. **NUMBER OF REFERENCES:** Enter the total number of references cited in the report.

8a. **CONTRACT OR GRANT NUMBER:** If appropriate, enter the applicable number of the contract or grant under which the report was written.

8b, 8c, & 8d. **PROJECT NUMBER:** Enter the appropriate military department identification, such as project number, subproject number, system numbers, task number, etc.

9a. **ORIGINATOR'S REPORT NUMBER(S):** Enter the official report number by which the document will be identified and controlled by the originating activity. This number must be unique to this report.

9b. **OTHER REPORT NUMBER(S):** If the report has been assigned any other report numbers (*either by the originator or by the sponsor*), also enter this number(s).

10. **AVAILABILITY/LIMITATION NOTICES:** Enter any limitations on further dissemination of the report, other than those imposed by security classification, using standard statements such as:

- (1) "Qualified requesters may obtain copies of this report from DDC."
- (2) "Foreign announcement and dissemination of this report by DDC is not authorized."
- (3) "U. S. Government agencies may obtain copies of this report directly from DDC. Other qualified DDC users shall request through _____."
- (4) "U. S. military agencies may obtain copies of this report directly from DDC. Other qualified users shall request through _____."
- (5) "All distribution of this report is controlled. Qualified DDC users shall request through _____."

If the report has been furnished to the Office of Technical Services, Department of Commerce, for sale to the public, indicate this fact and enter the price, if known.

11. **SUPPLEMENTARY NOTES:** Use for additions! explanatory notes.

12. **SPONSORING MILITARY ACTIVITY:** Enter the name of the departmental project office or laboratory sponsoring (*paying for*) the research and development. Include address.

13. **ABSTRACT:** Enter an abstract giving a brief and factual summary of the document indicative of the report, even though it may also appear elsewhere in the body of the technical report. If additional space is required, a continuation sheet shall be attached.

It is highly desirable that the abstract of classified reports be unclassified. Each paragraph of the abstract shall end with an indication of the military security classification of the information in the paragraph, represented as (TS), (S), (C), or (U).

There is no limitation on the length of the abstract. However, the suggested length is from 150 to 225 words.

14. **KEY WORDS:** Key words are technically meaningful terms or short phrases that characterize a report and may be used as index entries for cataloging the report. Key words must be selected so that no security classification is required. Identifiers, such as equipment model designation, trade name, military project code name, geographic location, may be used as key words but will be followed by an indication of technical context. The assignment of links, rules, and weights is optional.

UNCLASSIFIED

Security Classification

THE RESPONSE OF TERRESTRIAL SURFACES
AT MICROWAVE FREQUENCIES

(2440-7)

May 1971

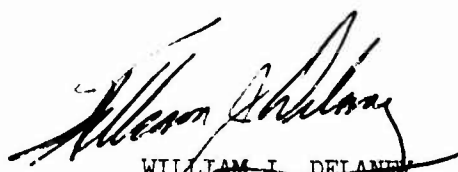
This document is subject to special export controls and each transmittal to foreign governments or foreign nationals may be made only with prior approval of AFAL(AVWE), Wright-Patterson Air Force Base, Ohio 45433.

FOREWORD

This report, OSURF Report Number 2440-7, was prepared by The Ohio State University ElectroScience Laboratory, Department of Electrical Engineering at Columbus, Ohio. Research was conducted under Contract F33615-67-C-1663 of the Air Force Avionics Laboratory at Wright-Patterson Air Force Base, Ohio. Mr. Gale Urban, AVNT, was the AFAL Program Monitor for this research conducted under Project Number 4144 (Task 14).

This report was submitted August 24, 1970.

This report has been reviewed and is approved for publication.



WILLIAM J. DELANEY
Lt Colonel, USAF
Chief, Navigation &
Guidance Division

ABSTRACT

This report reviews the basic properties and terrestrial surface responses of microwave sensors, both active (radar) and passive (microwave radiometer). Appropriate surface responses (bistatic coefficient, emissivity etc.) are defined and used to provide general formulas for the system response (receiver power, antenna temperature, doppler spectrum) in terms of system geometry and configuration. The dielectric properties of terrestrial surfaces are reviewed, and data on the complex dielectric constant of rocks, soils and vegetation are tabulated. Theoretical models for surface response are provided for a variety of surface classes, including the surface of uniform layers, the surface with large scale undulation, the slightly rough surface, the surface of individual scatterers (Lommel-Seeliger surface) and the empirical models (Lambert surfaces). Finally, the report includes a large number of typical surface responses at microwave frequencies. Measured bistatic scattering coefficients, radar return, and surface brightness temperature for many terrestrial surface classes are presented and interpreted in terms of the influence of such parameters as surface roughness, dielectric constant, polarization, frequency, angle of incidence etc. on the response.

LIST OF ILLUSTRATIONS

Figure		Page
1.	Geometry of the scattering problem.	25
2.	Bistatic scattering geometry.	26
3.	Range ring.	27
4.	Beam and pulse limited geometries.	28
5.	Isodop contours and doppler spectrum.	29
6.	Geometry of a radiometer system.	30
7.	The doppler spectrum.	31
8.	The centroid concept for small targets.	32
9.	Relative complex dielectric constant of water. (Typical)	45
10.	Dielectric constant of soils vs moisture content.	46
11.	Relative dielectric constant of vegetation at 8.5 GHz.	47
12.	Loss tangent of fir wood as a function of frequency.	48
13.	Dielectric constant of fir wood as a function of frequency.	49
14.	(a) "Slightly rough" surface $h \ll \lambda$. Scattered beam- width determined by transmitter beamwidth; - predomin- antly coherent.	84
	(b) Undulating "rough" surface $h \gg \lambda$, slopes $\ll 1$. Scattered beamwidth \approx r.m.s. surface slope; specular (not coherent).	84
	(c) The Lambert type of "rough" surface with large re- entrant cavities.	84
	(d) The Lommel-Seeliger type of "rough" surface with many independent scatterers.	84
15.	Geometry of the scattering problem.	85

LIST OF ILLUSTRATIONS (Contd.)

Figure		Page
16.	Geometry of layered surface.	86
17.	The small scale component has Gaussian surface height correlation coefficient with $\rho(r) = \exp(-r^2/\ell^2)$ (ℓ is small scale correlation length, h is the mean square height of the small scale process. Solid curve $k\ell=1$, $kh=0.2$; dotted curve $k\ell=1$, $kh=0.1$. The complex dielectric constant $55(1-j.55)$ corresponds roughly to sea water at λ -band.	87
18.	Backscattering from cylindrical vegetation model.	88
19.	Lommel-Seeliger cross section vs. frequency.	89
20.	Optical depth vs. frequency.	90
21.	Photo of loam with stubble and rough sand.	119
22.	Bistatic scattering cross sections, in the plane of incidence, for smooth sand and loam	120
23.	Bistatic patterns for smooth sand, dry grass, and rough sand.	121
24.	Bistatic scattering behavior, in the azimuth cone, for smooth sand, loam, and soybean foliage.	122
25.	Experimental and theoretical reflection coefficients; solid curves are theoretical values for smooth surfaces - Reference 1.	123
26.	Reflection coefficients measured by Sherwood and Ginzton for a tidal flat with some organic material; solid curves are theoretical for $\epsilon_r = 10$ - Reference 9.	124
27.	Effects of polarization on the azimuthal bistatic scattering pattern for smooth sand.	125
28.	Effects of polarization on the azimuthal bistatic scattering pattern for soybean foilage.	125
29.	Effects of polarization on the bistatic cross section, in the plane of incidence, for smooth sand.	126
30.	Effects of polarization on the bistatic cross section, in the plane of incidence, for dry grass.	126

LIST OF ILLUSTRATIONS (Contd.)

Figure		Page
31.	Radar backscattering cross sections for three smooth surfaces (limestone, asphalt, and concrete) at X-band.	127
32.	Radar backscattering cross sections for three rubble type surfaces (sand, pea gravel, and crushed stone) at X-band. (C.P. - Circular Polarization)	127
33.	Radar backscattering cross section for large blocks of pumice at Mono Crater, California.	128
34.	Pumice blocks at Mono Crater. The photograph shows the large angular blocks of pumice that underlie the rugged topography near the summit of one of the Mono Craters. Note the large size of the vesicles. The scale is in inches.	129
35.	Radar backscatter for green soybeans at X-band.	130
36.	Radar backscatter for green oats at X-band - Reference 6.	130
37.	Measured and computed difference between vertical and horizontal backscatter for "smooth" limestone at X-band.	131
38.	Measured and computed difference between vertical and horizontal backscatter for "smooth" asphalt at X-band.	131
39.	Angular dependence of the radar backscatter for slightly rough gravel; average diameter of rounded gravel \approx 1 cm. - Reference 4.	132
40.	Radar return vs. normalized roughness for crushed stone, gravel, and sand surfaces at X-, K_U -, and K_A -bands - Reference 4.	133
41.	Seasonal changes of grass at X-band - Reference 3.	134
42.	Seasonal changes of grass at K_U -band - Reference 3.	135
43.	Seasonal changes of grass at K_A -band - Reference 3.	136

LIST OF ILLUSTRATIONS (Contd.)

Figure		Page
44.	Effects of rain on a smooth asphalt road at K_a -band - Reference 3.	137
45.	Effects of rain on two-inch grass at K_a -band - Reference 3.	137
46.	Frequency dependence of radar backscattering for a smooth asphalt surface.	138
47.	Frequency dependence of radar backscattering for a smooth sand surface - Reference 4.	139
48.	Frequency dependence of radar backscattering for a slightly rough gravel surface; average diameter of rounded gravel ≈ 1 cm - Reference 4.	140
49.	Frequency dependence of radar backscattering for a rough crushed stone surface; average diameter of stone ≈ 3 to 5 cm - Reference 4.	141
50.	Frequency dependence of radar backscattering for a rough grey pumice surface.	142
51.	Frequency dependence of radar backscattering for a vegetated surface (oats).	143
52.	Polarization dependence of the radar backscattering for a "smooth" limestone surface at X-band - Reference 5.	144
53.	Polarization dependence of the radar backscattering for a smooth sand surface at X-band - Reference 4.	145
54.	Polarization dependence of the radar backscattering for a slightly rough gravel surface at X-band - Reference 4.	145
55.	Polarization dependence of the radar backscattering for a rough stone surface at X-band - Reference 4.	146
56.	Polarization dependence of the radar backscattering for a vegetated surface (oats) at X-band - Reference 6.	147
57.	Brightness temperature of smooth asphalt at 10 GHz.	148

LIST OF ILLUSTRATIONS (Contd.)

Figure		Page
58.	Brightness temperature of smooth asphalt at 35 GHz.	149
59.	Brightness temperatures for different size fractions of limestone at 13.5 GHz, - Reference 11.	150
60.	Brightness temperature for dense, broken, grey pumice at 10 GHz.	151
61.	Brightness temperature for light weight, dark pumice at 10 GHz.	151
62.	Brightness temperature for large blocks of obsidian at 10 GHz.	152
63.	Photographs of volcanic materials at Mono Craters, California - Reference 7.	153
64.	Brightness temperature of alfalfa at 10 GHz.	154
65.	Brightness temperature of green wheat, in head, at 10 GHz.	154
66.	Brightness temperature of green oats, in head, at 10 GHz.	155
67.	Computed and measured brightness temperatures for coal (near Cadiz, Ohio), limestone (near Marblehead, Ohio), and asphalt surfaces at 10 GHz, vertical polarization (Data normalized to 300°K at the Brewster Angle).	156
68.	Brightness temperatures of playa sediments, with variable moisture, at 13.4 GHz - Reference 11.	157
69.	Brightness temperature of three pumices (Mono Crater, California) at X-band.	158
70.	Brightness temperatures for irrigated and non-irrigated soybeans at X-band.	159
71.	Brightness temperature of smooth asphalt at 10 GHz and 35 GHz.	160
72.	Brightness temperature of lapilli (volcanic ash) at 10 GHz and 35 GHz (Mono Crater, California).	161

LIST OF ILLUSTRATIONS (Contd.)

Figure		Page
73.	Close-up of lapilli surface. Note the concentration of coarse pumice lapilli in botches and bands, and the sparse ground vegetation and scattered pine needles. Scale is in inches.	162
74.	Brightness temperature of "rough" dark pumice at 10 GHz and 35 GHz (Mono Crater, California).	163
75.	Bistatic scattering cross section, in the plane of incidence, for smooth sand at X-band.	164
76.	Bistatic scattering cross section, in the azimuth cone, for smooth sand at X-band.	166
77.	Bistatic scattering cross section, in the plane of incidence, for smooth loam at X-band.	168
78.	Bistatic scattering cross section, in the azimuth cone, for smooth loam at X-band.	170
79.	Bistatic scattering cross section, in the plane of incidence, for rough sand at X-band.	172
80.	Bistatic scattering cross section, in the plane of incidence, for stubble at X-band. ($\phi = 0$ or 180° except where marked).	174
81.	Bistatic scattering cross section, in the plane of incidence, for dry grass at X-band.	178
82.	Bistatic scattering cross section, in the plane of incidence, for soybean foliage at X-band.	180
83.	Bistatic scattering cross section, in the azimuth cone, for soybean foliage at X-band.	181
84.	Bistatic scattering cross section of the sea (sea state 3) at C-band, vertical polarization - Reference 13.	182
85.	Bistatic scattering cross section of the sea (sea state 1) at C-band, vertical polarization - Reference 13. (Depression Angle = Grazing Angle = $90^\circ - \theta_i$).	183

LIST OF ILLUSTRATIONS (Contd.)

Figure		Page
86.	Bistatic scattering cross section of the sea (sea state 2) at C-band, vertical polarization - Reference 13.	184
87.	Bistatic scattering cross section of the sea (sea state 3) at C-band, vertically-polarized transmitter and horizontally-polarized receiver - Reference 13.	185
88.	Bistatic scattering cross section of the sea (sea state 1) at C-band, vertically-polarized transmitter and horizontally-polarized receiver - Reference 13.	186
89.	Bistatic scattering cross section of the sea (sea state 2) at C-band, vertically-polarized transmitter and horizontally-polarized receiver - Reference 13.	187
90.	Radar backscattering cross sections for several slightly rough surfaces - Reference 3.	188
91.	Radar backscattering cross section for normal desert at X-band.	189
92.	Radar backscattering cross section for Pisgah Lava Flow at X-band and K_u -band.	189
93.	Radar backscattering cross section for Bristol (Dry Salt) Lake at X-band - Reference 16.	190
94.	Radar backscattering cross section for Lavic Dry Lake playa at X-band and k_u -band.	190
95.	Lavic Lake Playa. The surface of the playa is almost perfectly flat except for small scale roughness generated by contraction (dessication) cracks. These cracks break the playa surface into polygons of three distinct sizes: A - measured in terms of 10's of feet; B - measured in terms of a few feet; and C - measured in terms of a few inches. In the intermediate distance is the radar truck being used to make calibration measurements and in the far distance to the left are the black basalt lava flows from Sunshine Crater. The view is to the northwest.	191

LIST OF ILLUSTRATIONS (Contd.)

Figure		Page
96.	Radar backscattering cross sections for the lunar and planetary surfaces.	192
97.	Frequency dependence of the radar backscattering cross section for the Moon - Reference 21.	192
98.	Polarization dependence of the radar backscattering cross section for the Moon at 23 cm - Reference 22.	193
99.	Polarization dependence of the radar backscattering cross section for the Moon at 68 cm - Reference 22.	193
100.	Radar cross section of the lunar surface vs. angle of incidence for Surveyor V (13.3 GHz).	194
101.	Radar cross section of the lunar surface vs. angle of incidence for Surveyor VI (13.3 GHz).	194
102.	Radar cross section for the lunar surface vs. angle of incidence for Surveyor VII (13.3 GHz).	194
103.	Radar backscattering cross section for wooded terrain at X-band.	195
104.	Radar backscattering cross section for Arizona farmland at X-band - Reference 16.	196
105.	Radar backscattering cross section for 24"-36" green soybeans at S-, X-, and K_a -bands. Shaded area is envelope of measured curves.	197
106.	Radar backscattering cross section for 10"-36" oats at S-, X-, and K_a -bands.	198
107.	Radar backscattering cross section for wheat at 297 MHz, 5.87 GHz, and 9.375 GHz - Reference 25.	199
108.	Radar backscattering cross section for cities at 220 MHz and 428 MHz.	200
109.	Radar backscattering cross section for cities at X-band.	200
110.	Radar backscattering cross section for the sea at 428 MHz, vertical polarization - Reference 27.	201

LIST OF ILLUSTRATIONS (Contd.)

Figure		Page
111.	Radar backscattering cross section for the sea at 428 MHz, horizontal polarization - Reference 27.	201
112.	Radar backscattering cross section for the sea at 1.228 GHz, vertical polarization - Reference 27.	202
113.	Radar backscattering cross section for the sea at 1.228 GHz, horizontal polarization - Reference 27.	202
114.	Radar backscattering cross section for the sea at 4.455 GHz, vertical polarization - Reference 27.	203
115.	Radar backscattering cross section for the sea at 4.455 GHz, horizontal polarization - Reference 27.	203
116.	Radar backscattering cross section for the sea at 8.91 GHz, vertical polarization - Reference 27.	204
117.	Radar backscattering cross section for the sea at 8.91 GHz, horizontal polarization - Reference 27.	204
118.	Radar backscattering cross section for the sea with oil slicks at 8.91 GHz, vertical polarization - Reference 27.	205
119.	Radar backscattering cross section for the sea with oil slicks at 8.91 GHz, horizontal polarization - Reference 27.	205
120.	Radar backscattering cross section for the sea at 13.3 GHz.	206
121.	Radar backscattering cross section for the sea at 8.8 GHz, (average of vertical and horizontal polarization) - Reference 29.	206
122.	Radar backscattering cross section for the sea at 9.4 GHz, vertical polarization - Reference 24.	207
123.	Radar backscattering cross section for the sea at 24 GHz, vertical polarization - Reference 24.	207

LIST OF ILLUSTRATIONS (Contd.)

Figure		Page
124.	Radar backscattering cross section for the sea at 35 GHz, vertical polarization - Reference 24.	208
125.	Radar backscattering cross section for the sea at 9.6 GHz, vertical polarization - Reference 30.	208
126.	Radar backscattering cross section for the sea at 24 GHz, vertical polarization - Reference 30.	209
127.	Radar backscattering cross section for the sea at 35 GHz, vertical polarization - Reference 30.	209
128.	Radar backscattering cross section for the sea at 48.7 GHz, vertical polarization - Reference 30.	210
129.	Effects of polarization on the radar backscattering for the sea at 24 GHz - Reference 30.	210
130.	Near-grazing radar backscatter for trees (X-band and S-band) and cotton seedlings (X-band).	211
131.	Near-grazing radar backscatter for cultivated terrain at 10 GHz - Reference 32. Parameter is per cent of returns exceeding given ordinate.	212
132.	Near-grazing radar backscatter for wooded terrain at 10 GHz - Reference 32. Parameter is per cent of returns exceeding given ordinate.	212
133.	Seasonal variation in the radar backscatter distribution for cultivated terrain, at 10 GHz, for a 1.25° depression angle - Reference 32.	213
134.	Seasonal variation in the radar backscatter distribution for cultivated terrain, at 10 GHz, for a 2.5° depression angle - Reference 32.	214
135.	Seasonal variation in the radar backscatter distribution for cultivated terrain, at 10 GHz, for a 5° depression angle - Reference 32.	215

LIST OF ILLUSTRATIONS (Contd.)

Figure		Page
136.	Seasonal variation in the radar backscatter distribution for wooded terrain, at 10 GHz, for a 0.7° depression angle - Reference 32.	216
137.	Distribution of average values of σ_0 for different types of terrain, at X-band, horizontal polarization, for a 1° depression angle - Reference 33.	217
138.	Distribution of average values of σ_0 for different types of terrain, at X-band, horizontal polarization, for a 5° depression angle - Reference 33.	218
139.	Distribution of average values of σ_0 for different types of terrain, at X-band, horizontal polarization, for a 30° depression angle - Reference 33.	219
140.	Brightness temperature for asphalt at 10 GHz and 35 GHz.	220
141.	Brightness temperature for glacially polished limestone at 10 GHz.	221
142.	Brightness temperature for Pittsburg #8 Coal at 10 GHz.	222
143.	Deviation envelope and mean value curve for the radiometric temperature of Palo Alto Marine mud at 13.5 GHz - Reference 34.	223
144.	Deviation envelope and mean value curve for the radiometer temperature of Palo Alto Marine mud at 37 GHz - Reference 34.	224
145.	Deviation envelope and mean value curve for the radiometric temperature of LaJolla Beach sand at 13.5 GHz - Reference 34.	225
146.	Deviation envelope and mean value curve for the radiometric temperature of LaJolla Beach sand at 37 GHz - Reference 34.	226
147.	Brightness temperature for lapilli (volcanic ash) at 10 GHz and 35 GHz.	227

LIST OF ILLUSTRATIONS (Contd.)

Figure		Page
148.	Brightness temperature for disced, bare soil (2"-3" ridges) at 10 GHz.	228
149.	Radiometric temperature for silt loam soil (Davis, California) at 13.4 GHz and 37 GHz - Reference 35.	229
150.	Radiometric temperature for sandy loam soil with 10% vegetation cover (Rocky Mtn. Arsenal) at 13.4 GHz and 37 GHz - Reference 35.	229
151.	Brightness temperature for dense, broken grey pumice at 10 GHz and 35 GHz.	230
152.	Brightness temperature for light weight, dark pumice (block) at 10 GHz and 35 GHz.	230
153.	Brightness temperature for large blocks of obsidian at 10 GHz.	231
154.	Radiometric measurements of playa sediments, lava flow, and lava flow beneath playa sediments at 13.5 GHz - Reference 34.	232
155.	Radiometric measurements of playa sediments, lava flow, and lava flow beneath playa sediments at 37 GHz - Reference 34.	233
156.	Brightness temperature of green oats, in head, at 10 GHz.	234
157.	Brightness temperature of ripe oats at 10 GHz.	234
158.	Brightness temperature of green wheat at 10 GHz.	235
159.	Brightness temperature of green sorghum, in tassel, at 10 GHz.	235
160.	Brightness temperature of green alfalfa at 10 GHz.	236
161.	Brightness temperature of irrigated, green soybeans at 10 GHz.	236
162.	Brightness temperature of irrigated, green soybeans at 10 GHz.	237

LIST OF ILLUSTRATIONS (Contd.)

Figure		Page
163.	Brightness temperature of irrigated soybeans at 10 GHz.	237
164.	Brightness temperature of irrigated, ripe soybeans at 10 GHz.	238
165.	Deviation envelope and mean value curve for the radiometric temperature of Palo Alto marsh foliage at 13.4 GHz - Reference 34.	239
166.	Deviation envelope and mean value curve for the radiometric temperature of Palo Alto marsh foliage at 37 GHz - Reference 34.	240
167.	Radiometric temperature for dense marsh vegetation (Seal Beach Tidal Marsh) at 13.4 and 94 GHz - Reference 35.	241
168.	Radiometric temperature for pasture gras (Thousand Oaks) at 13.4 GHz and 94 GHz - Reference 35.	241
169.	Radiometric temperature for flower stocks (Oxnard) at 13.4, 37, and 94 GHz - Reference 35.	241
170.	Radiometric temperature for celery crops (Oxnard) at 13.4, 37, and 94 GHz - Reference 35.	242
171a.	Brightness temperature of the Salton Sea at 1.55 cm - Reference 36.	243
171b.	Brightness temperature of the ocean at low and medium wind speeds for 1.41, 8.31 and 19.34 GHz. Reference 39.	244
172.	Deviation envelope and mean value curve for the radiometric temperature of sea water (Palo Alto) at 13.5 GHz - Reference 34.	245
173.	Deviation envelope and mean value curve for the radiometric temperature of sea water (Palo Alto) at 37 GHz - Reference 34.	246

LIST OF ILLUSTRATIONS (Contd.)

Figure		Page
174.	Comparison of mean radiometric temperatures at 13.5 GHz - Reference 34.	247
175.	Comparison of mean radiometric temperatures at 37 GHz - Reference 34.	248
176.	Comparison of measured radiometric temperatures at 35 GHz, horizontal polarization - Reference 38.	249

TABLE OF CONTENTS

Chapter		Page
I	INTRODUCTION	1
II	THE BASIC SENSOR RESPONSE	3
	A. <u>The Radar Response</u>	3
	B. <u>Temporal Fluctuations. The Doppler Spectrum</u>	9
	C. <u>The Microwave Radiometer</u>	12
	D. <u>Large Extended Targets - Bias Errors</u>	16
	E. <u>Small Extended Targets. The Centroid Concept.</u>	19
	F. <u>System Limitations Due to Fluctuations in Antenna Pointing</u>	23
	REFERENCES	33
III	THE CONSTITUTIVE PARAMETERS	35
	A. <u>Introduction</u>	35
	B. <u>The Dielectric Constant of Water and Ice</u>	38
	C. <u>Rocks and Powders</u>	39
	D. <u>Soils</u>	1
	E. <u>Vegetation</u>	41
	REFERENCES	50
IV	THEORETICAL MODELS FOR SCATTERING AND EMISSION	52
	A. <u>Introduction</u>	52
	B. <u>The Flat Surface</u>	54
	C. <u>The Slightly Rough Surface</u>	65
	D. <u>The Rough Continuous Surface - Physical Optics Models</u>	71
	E. <u>The Composite Surface</u>	74
	F. <u>The Lambert Model</u>	78
	G. <u>Scattering by Individual Elements (Lommel-Seeliger Scattering)</u>	79
	REFERENCES	91

TABLE OF CONTENTS (Contd.)

Chapter		Page
V	EXPERIMENTAL DATA	93
	A. Introduction	93
	D. <u>Bistatic Scattering Data</u>	95
	C. <u>Backscattering Data</u>	98
	D. <u>Brightness Temperature Data</u>	103
	E. <u>Special Surface Categories</u>	107
	F. <u>Backscattering Data</u>	108
	G. <u>Brightness Temperature Data</u>	115
	REFERENCES	251

THE RESPONSE OF TERRESTRIAL SURFACES AT MICROWAVE FREQUENCIES

I. INTRODUCTION

The purpose of this report is to summarize the electromagnetic response of terrestrial surfaces at microwave frequencies. Although a large number of data on both the scattering properties (radar return) and the thermal emission (radiometric or brightness temperature) of such surfaces has been collected during the last decade, there has not been available a comprehensive review which could serve the newer applications of remote sensing at microwave frequencies.

A significant fraction of this data is, of course, available in the several "data banks" that are now in operation, and these banks have been valuable in providing rather complete records of surface response, and in compelling a more uniform format for data reporting. They have not, however, addressed themselves to the problem of providing a critical understanding of the data they contain. While this report cannot aspire to duplicate the completeness of the data banks, it is our hope to provide an appropriate theoretical and conceptual framework for understanding the significance of the microwave data collections.

This kind of understanding is now particularly important because of the widespread interest in exploiting microwave sensors, for a variety of purposes, by investigators in other (i.e., non-engineering) disciplines, such as geology, agronomy, etc. Many of these newer users of the data are unfamiliar with the nature of the relationships between the surface parameters (roughness, dielectric constant, etc.) and the microwave response. Even such specialists as radar or radiometer system designers may also benefit from a more systematic discussion of the role of the various factors which control the instrument response.

In the succeeding sections, we shall discuss first the basic properties of microwave sensors, particularly the manner in which the geometry and other system parameters affect the system output. Then the various kinds of surface models are reviewed and the relation between the predictions of the model, the properties of the surface, and the measured response are compared. Finally a representative selection of data, for both active and passive sensors, is used to discuss in a more empirical way the range of surface response to be expected from terrestrial surfaces. The principal emphasis in the report is on the average properties of the response, although some discussion of the statistical properties is also given.

II. THE BASIC SENSOR RESPONSE

Before discussing the nature of the interaction between sensor and surface, it is desirable to review a number of system concepts in order to introduce appropriate definitions of the parameters used to describe the surface. Because a number of textbooks on radar systems,[1,2,3,4] and radar[5] and radio astronomy[6] are now available, no extensive discussion of system operation will be given here. We have, however, attempted to mention some of the limitations of the conventional treatment, and to provide operationally useful definitions from which (e.g., by computer simulation if need be) the system performance may be estimated under any conditions. A large number of convenient approximate formulas for various specialized geometries are given in References 1-6.

A. The Radar Response

The most useful descriptor of the active microwave response of a terrestrial surface is the average bistatic scattering cross-section per unit area, $\sigma_{is}^0(\theta_i, \theta_s, \phi_s)$ for angle of incidence θ_i (with respect to the mean surface normal); scattering angles θ_s, ϕ_s ; incident polarization state specified by first subscript (i) and polarization component of scattered radiation specified by second subscript (s) (see Fig. 1). This parameter is defined as follows. Consider a plane wave of intensity I_0 watts/meter² incident with unit propagation vector \vec{n}_i in the xz plane and polarization state \vec{p}_i . That is, the incident electric field is $E_0 \vec{p}_i \exp[-jk\vec{n}_i \cdot \vec{r} + j\omega t]$ where $f = \omega/2\pi$ is the frequency; $\lambda = 2\pi/k$ is the wave length; $I_0 = |E_0|^2/Z_0$ and Z_0 is the impedance of free space. Let that component of the field scattered by an element of area dA (dA is the projection of the actual surface onto the xy plane) which has polarization state \vec{p}_s (where $\vec{p}_s \cdot \vec{p}_s^* = \vec{p}_i \cdot \vec{p}_i^* = 1$) have an intensity dI_s at distance r_s in the scattering direction. Then the bistatic cross-section per unit area is by definition

$$(1) \quad \sigma_{is}^0(\theta_i, \theta_s, \phi_s) \equiv 4\pi r_s^2 \langle dI_s \rangle / I_0 dA$$

where the symbol $\langle \rangle$ indicates that the measurement is repeated many times with different members of an ensemble of similar surfaces, and the average scattered intensity taken. It is a consequence of the reciprocity theorem that

$$(2) \quad \sigma_{is}^0(\theta_i \phi_i, \theta_s \phi_s) = \sigma_{si}^0(\theta_s \phi_s, \theta_i \phi_i)$$

where the incident plane wave can now have any azimuth direction ϕ_i .

Since the scattering cross section is defined in terms of statistical average power densities, there are certain limitations on its applicability. For the definition to be consistent, it is necessary that the receiver be in the far field of the scattering pattern of the element dA in order that dI_s be proportional to $1/r_s^2$. This implies that $r_s > 2\ell^2/\lambda$ where ℓ is a coherence length for the surface structure. Secondly, the surface element must be sufficiently large and irregular that the (ensemble) average scattered power is proportional to dA . A smooth sea surface near normal incidence, for example, fails to satisfy these conditions; the scattering contains a coherent part (i.e., a part which remains identical in amplitude and phase when one member of an ensemble is substituted for another), and great difficulty is encountered in trying to interpret the results of experiments over such a surface in terms of the parameter σ_0 . Finally, it must be remembered that in many system applications, it is important to know the statistical properties of the return (i.e., the first probability distribution of σ_0 , the correlation between returns measured at two different adjacent frequencies, etc.). For most surfaces it turns out that many simple statistical properties can be inferred from a knowledge of σ_0 alone. However, determination of the statistics for some surfaces, particularly for higher order statistical properties, requires a detailed scattering model, or actual measurements.

To determine the average power collected by a real radar system viewing a surface target, (see Fig. 2) consider a radar antenna at T in the xz plane, a distance r_i from the origin O, which radiates power $P_0(t)$ with a one way power pattern $f_i(\psi_i, \xi_i)$. For convenience the origin of coordinates is chosen to lie on the axis TO of the antenna pattern. The angle ψ_i is between TO and the line from the antenna to the surface element dA. The angle ξ_i is an azimuthal pattern coordinate, conveniently taken as the angle -Y-O-dA projected onto a plane perpendicular to TO. The receiving antenna is at R, specified by r_s, θ_s, ϕ_s with pattern $f_r(\psi_r, \xi_r)$. (Because of these choices of angle, which are appropriate for high gain antennas aimed at the origin, the magnitude of the pattern $f_r(0, \xi_r)$ does not necessarily attain its maximum value along the direction RO.) The ensemble average power $\bar{P}_r(t)$ collected by the receiver at time t is then

$$(3) \quad \bar{P}_r(r) = \frac{A_{\text{emr}} G_t}{(4\pi)^2} \iint P_0(t - (r_i + r_s)/c) \{f_i(\psi_i, \xi_i) f_r(\psi_r, \xi_r) \cdot \sigma_{is}^0(\theta_i', \theta_s', \phi_s') \frac{dA}{r_i^2 r_s^2}$$

where the integral is taken over the entire xy plane, and

A_{emr} = maximum collecting aperture of receiving antenna

G_t = maximum gain of transmitting antenna

$\theta_i', \theta_s', \phi_s'$ = local incidence and scattering angles at dA.

c = velocity of propagation

The polarization specifications in this equation must be handled with care. The equation represents the actual received power due to an actual transmitting antenna. The patterns $f_r(\psi_r)$ and $f_i(\psi_i)$ do not in general represent pattern measurements made with a fixed polarization test antenna such as a dipole. They represent the total power density (whatever its specific polarization state may be) transmitted in a

given direction. By the same token the subscripts on σ_{is} cannot represent arbitrary polarization states but must correspond to the actual polarization states of the two antenna patterns. The more general case of arbitrary transmitting and receiving antenna polarization requires an extensive formal development to handle correctly, since the complex scattering amplitudes for the surface must be introduced. Simplification of the resulting equation depends on making plausible assumptions about the correlation between the various terms of the scattering matrix. For the purposes of this report, it is sufficient to point out that the situation remains simple if the more conventional choice is made of specifying two orthogonal polarization states (e.g., horizontal, \vec{p}_i^h, \vec{p}_s^h in the xy plane perpendicular to \vec{n}_i, \vec{n}_s respectively; and vertical $\vec{p}_i^v = \vec{n}_i \times \vec{p}_i^h$ and $\vec{p}_s^v = \vec{n}_s \times \vec{p}_s^h$).

Thus if horizontal polarization is transmitted, then the term $\{f_i f_r \sigma_{is}\}$ in Eq. (3) must be replaced by

$$(4) \quad \{f_i f_r \sigma_{is}\} \rightarrow f_i^h(\psi_i, \xi_i) f_r^h(\psi_r, \xi_r) \sigma_{hh} + f_i^h f_r^v \sigma_{hv}$$

where, for example, (see Fig. 2) $f_i^v(\psi_i, \xi_i)$ is the power pattern of the transmitting antenna as measured with a "vertical" dipole oriented along \vec{p}_i^v . The pattern factors are normalized so that the maximum value of $f_i^v(\psi_i) + f_i^h(\psi_i)$ is equal to unity and it is assumed that the four components of the scattering matrix σ_{ij} are uncorrelated. In most cases, well designed high gain antennas have almost constant polarization over the main beam and first few side lobes, so that only one term in the sum of Eq. (4) will be important.

It is often convenient, for high gain antennas, to have estimates of the value of the integral of Eq. (3). If the antenna patterns can be approximated, at least over the main beam region, by $f_i(\psi_i) = \exp[-A(1-\cos\psi_i)]$ and $f_r(\psi_r) = \exp[-B(1-\cos\psi_r)]$, one can show that for a cw system,

$$(5) \quad \bar{P}_r \simeq \frac{P_o A_{emr} G_t}{8\pi C} \sigma_o(\theta_i, \theta_s, \phi_s)$$

$$C = [A^2 r_s^4 \cos^2 \theta_i + B^2 r_i^4 \cos^2 \theta_s + A B r_i^2 r_s^2 (\cos^2 \theta_i + \cos^2 \theta_s + \sin^2 \theta_i \sin^2 \theta_s \cos^2 \phi_s)]$$

or for back scattering, $r_i = r_s$,

$$(6) \quad \bar{P}_r \simeq \frac{P_o A_{emr} G_t}{(4\pi r_i)^2} \left(\frac{\pi \sigma_o}{A \cos \theta_i} \right)$$

Equations (5) and (6) represent the received power levels for the cw case. When pulse radars are used, it is of interest to know the time variation (i.e., pulse shape) of the ensemble average received pulse. This can most readily be computed by converting dA in Eq. (3) to an infinitesimal area contributing to the return at a specified time, that is (see Fig. 3) a range ring of radius ρ and width $d\rho$. One can now utilize the relationship between "receiver time" t' (defined so that t' is zero when the leading edge of the pulse reflected from the subradar point reaches the receiver) and the angle ψ between the z axis and the line of sight to the range ring. If the radar is at altitude h , then Eq. (3) becomes

$$(7) \quad \bar{P}_r(t') = \frac{G_t A_{emr}}{(4\pi h)^2} \int_0^{2\pi} \int_0^{t'} P_o \left(t' - \frac{2r}{c} \right) r^2(\psi, \phi) \sigma_o(\psi, \phi) \cos^3 \psi \left(\frac{cdT}{2h} \right) d\phi$$

where the dummy variable of integration is T , and ψ and r are functions of T , viz

$$(8) \quad \cos \psi(T) = (1 + cT/2h)^{-1}$$

$$r(T) = h/\cos \psi(T).$$

When a constant amplitude pulse of power level P_0 and pulse length τ seconds is used, and both the antenna patterns and σ_0 are independent of ψ , Eq. (7) becomes

$$(9) \quad \bar{P}_r(t') = \frac{P_0 G_t A_{em}}{8\pi h^2} \int_{(t'-\tau)U(t'-\tau)}^{t'} p^2(\psi) \sigma_0(\psi) \cos^3 \psi \left(\frac{cdT}{2h} \right)$$

where $U(x)$ is the unit step function and ψ is again a function of T . In this form, the time response of the pulse may be used to illustrate the difference between the so-called "beam-limited" and the "pulse-length-limited" geometries. If $t' < \tau$ (see Fig. 4a) then the lower limit of the integral of Eq. (8) is zero, and the area of ground contributing to the return power at receive time t' is a circle. The build up of energy in the receiver is independent of pulse length but may be limited by the antenna pattern if the antenna beamwidth is smaller than the angle subtended by the illuminated circle. This situation is referred to as a "beamwidth-limited" geometry.

On the other hand, when $t' > \tau$, the effective illuminated area and thus the magnitude of the received power is an expanding annulus whose width is controlled by τ ; this is the "pulse-length limited" geometry. It is clear from Eq. (8) that at receiver time t' the area actually contributing to receiver power is that subtended by the cones $\psi(t')$ and $\psi(t'-\tau)$ (see Fig. 4b). Thus the "effective" area is $A_{eff} = \pi(h \sec \psi(t'))^2 - \pi(h \sec \psi(t'-\tau))^2$ and this is approximately, for $t' \gg \tau$, equal to $A_{eff} = 2\pi h \tan \psi(t') [(c\tau/2)/\sin \psi(t')]$. This will be recognized as the annulus whose outer radius is fixed by the leading edge of the pulse, and whose width is the projection of a pulse of length $c\tau/2$ onto the xy plane. Thus it is often said that the "effective" pulse length is $\tau/2$.

B. Temporal Fluctuations. The Doppler Spectrum

The instantaneous power $P_r(t)$ returned from a natural surface is not the constant value indicated by the ensemble average $\bar{P}_r(t)$ of Eqs. (3) or (7), but varies in time, or from pulse to pulse (unless both the surface and the transmitter are immobile, that is, unless both the transmitter position and the surface are "frozen"). The statistical properties of $P_r(t)$ depend on the nature of the transmitted signal, the velocity of the sensor platform relative to the mean surface, and the local motion of the surface itself (e.g., the movement of leaves and branches, or wave motion over the ocean). The actual computation of statistics of the return signal cannot be carried out without a detailed model of the surface scattering mechanism. However certain statistics, such as the power spectral density of the scattered signal due to transmitter motion (in the case where the surface is frozen) can be calculated from geometrical considerations alone.

Consider, for example, a transmitter moving with velocity \vec{v} with respect to a fixed motionless surface (see Fig. 5), and emitting a signal of frequency $f_0(t)$. Then the frequency of the signal returned to the receiver at time t from the area dA in direction \vec{n}_i is

$$(10) \quad f(t) = f_0(t - 2r/c) (1 + 2 \vec{v} \cdot \vec{n}_i / c)$$

where r is the range to the actual surface point at dA . This equation is correct to first order in v/c . The second order terms (of order $(v/c)^2$) must be computed according to the special theory of relativity; expressions of the type $(1 + \vec{v} \cdot \vec{n}_i) / (1 - \vec{v} \cdot \vec{n}_i) f_0/c$ are based on a false analogy with acoustical doppler shifts and give incorrect second order terms.

The lines on the surface for which $f(t)$ is constant are called isodops and in the case that $f_0(t)$ (the transmitter frequency) is constant (excluding f.m. doppler and short pulse systems, for example) they are found as the intersection of the cone $\vec{v} \cdot \vec{n}_i = \text{constant}$ with the surface. Note that the doppler shift in no way depends on the slope of the surface at dA , but only on the direction of \vec{v} and the line of sight \vec{n}_i .

For a plane surface the isodops are conic sections, namely the intersection of the xy plane with the cone obtained by rotating \vec{n}_i around \vec{v} , i.e., the cone $\vec{n}_i \cdot \vec{v} = \text{constant}$. These isodop curves are ellipses if the cone does not intersect the horizon, and hyperbolas if any part of the cone does rise above the horizon.

The average doppler spectrum, i.e., the average power per unit positive frequency interval may be found by integrating over the area between two isodop lines. Thus if the isodops chosen correspond to frequencies f_1 and f_2 , with interval $\Delta f = |f_2 - f_1|$, then the spectrum $S(f)$ is, for the backscattering cw case

$$(11) \quad S(f) = \frac{dP}{\Delta f} = \frac{A_{\text{emr}} G_t P_o(f_o)}{(4\pi)^2 \Delta f} \int_{\text{Isodop strip between frequencies } f_1 \text{ and } f_2} f^2(\psi_i, \epsilon_i) \sigma_o(\theta_i) \frac{dA}{r^4}$$

In general, this integral is impossible to evaluate, although numerical integration for certain special cases are available.

Even for high gain antennas the peak of the doppler spectrum does not correspond to the doppler shift from the ground point illuminated by the axis of the main beam. This effect is largest over

surfaces such as the ocean, for which $\sigma(\theta)$ varies rapidly with θ , and is responsible for the land-sea bias effect in doppler navigation systems.

The power spectral density of the return signal, as given by Eq. (11), combined with the assumption that the return is a Gaussian random noise signal, provides sufficient statistical detail for most radar design purposes. The bandwidth of the signal is approximately equal to the difference between the highest and lowest doppler shifts occurring in the area illuminated by the beam. However, certain special purpose systems (e.g., those depending on frequency agility to detect ship targets in the ocean) may require a more detailed knowledge of the fluctuation of the return signal.

If the surface is also in motion, the doppler spectrum is broadened in a manner that must be computed from the kinematic behavior of the surface scattering elements. The bandwidth of this "natural line width" effect is approximately equal to the doppler shift associated with the rms velocity of the random motion of the surface. Let the surface element at x, y have a "natural" doppler broadening spectrum $S_n(f-f_0)$ (see Fig. 5b) with

$$\int_0^{\infty} S_n(f) df = 1$$

when the surface is illuminated with a plane wave of frequency f_0 coming from the transmitter position at T with the transmitter motionless ($\vec{v} = 0$). Then the total, broadened spectrum $S_t(f)$ when the transmitter is also moving with velocity \vec{v} becomes, for a cw signal,

$$(13) \quad S_t(f) = \frac{A_{\text{emr}} G_t P_o(f_0)}{(4\pi)^2} \int_{\text{xy plane}} f^2(\psi_i, \epsilon_i) \sigma_o(\theta_i') S_n(f_0 - f + 2\vec{v} \cdot \vec{n}_i f_0 / c) \frac{dA}{r^4} .$$

This expression gives the doppler spectrum when both transmitter and parts of the surface are in motion. In the most general case, $S_n(f)$ may also depend on position, incidence angle, etc., along with $\sigma_0(\theta_i)$. When the surface is motionless, $S_n(f-f_0)$ is a delta function $\delta(f-f_0)$ and Eq. (13) reduces to Eq. (12), since the integrand is zero except over the isodop specified by $\vec{v} \cdot \vec{n}_i$.

For the bistatic case, the doppler spectrum at the receiver can be computed from the above formulas by replacing the doppler shift $f_0(2\vec{v} \cdot \vec{n}_i/c)$ by $f_0(\vec{v} \cdot \vec{n}_i - \vec{v} \cdot \vec{n}_s)/c$ where \vec{n}_s is the unit vector from dA to the receiver. The isodops then become the loci $\vec{v}_i \cdot (\vec{n}_i - \vec{n}_s) = \text{constant}$. When the transmitted signal is not a cw signal but a short pulse, the return pulse will have a spectrum given by the convolution of the pulse spectrum with the doppler spectrum given above.

C. The Microwave Radiometer

The microwave radiometer (see Fig. 6) estimates the brightness temperature of the thermal radiation incident upon it radiated by the ground surface and the surrounding atmosphere. If the radiometer antenna is illuminated by radiation of brightness temperature $T_B^k(\psi_i, \epsilon_i)$ (where, as in Fig. 6, ψ_i and ϵ_i are polar and azimuth angles for the antenna power pattern $f_k(\psi, \epsilon)$ and T_B^k represents the brightness temperature of the radiation in state k incident on the antenna) then the corresponding antenna temperature is

$$(14) \quad T_a^j(\theta_0) = \frac{\sum_{k=1}^2 \int f_k(\psi, \epsilon) T_B^k(\psi, \epsilon) d\Omega}{\sum_{k=1}^2 \int f_k(\psi, \epsilon) d\Omega}$$

where θ_0 is the angle between the antenna axis and the surface normal, the superscript j identifies the nominal polarization of the receiving antenna, and the subscripts k indicate any two orthogonal polarization

states, one of which is customarily taken as identical to state j of the antenna. In well designed antennas, only the design polarization is significant over the main beam, but the orthogonal polarized terms may contribute a non-negligible fraction of the total received power (e.g., 2%) in the side lobes and back lobes.

The antenna temperature $T_a(\theta_c)$ is the sensor output, i.e., the quantity measured by the microwave radiometer system. However, the quantity desired is usually $T_b^j(\psi=0) = T_b^j(\theta_0)$, that is, the brightness temperature of the radiation incident along the main beam direction of the antenna. Thus Eq. (14) must be regarded as an integral equation relating the desired brightness temperature and the measured antenna temperature. Except in radio-astronomical measurements, the inversion process is not usually carried out. It can be performed in a number of ways including: (i) the "bootstrap" method in which $T_a(\theta, \phi)$ is measured over 4π steradians. A trial brightness $T_b'(\theta, \phi)$ is assumed equal to the measured antenna temperature ($T_b' \equiv T_a(\theta, \phi)$) and this is inserted into Eq. (14) to obtain a desired value of $T_a'(\theta, \phi)$, (the value the antenna temperature would have if the brightness were $T_b'(\theta, \phi)$). A new trial brightness temperature $T_b^{(2)}(\theta)$ is estimated from $T_b^{(2)}(\theta) = 2T_a(\theta) - T_a'(\theta)$ and the process is repeated until successive trials converge; (ii) the Fourier transform method in which the integral in Eq. (14) is recognized as the convolution of the pattern function and the brightness distribution. By converting ψ, ξ to "rectangular" co-ordinates $x'y'$ (e.g., the coordinates of the point where the line of sight specified by ψ, ξ intersects a plane perpendicular to the axis RO of the main beams) and assuming pattern multiplication holds, Eq. (14) may be put in the form of a two dimensional convolution. In that case the Fourier transform of $T_b(x'y')$ is the ratio of the transforms of $T_a(x'y')$ and $f(x'y')$. Only rather smooth, well behaved antenna patterns are suited to this technique; (iii) a side lobe correction procedure in which estimates are made of the beam efficiency, and the power entering the antenna via the side lobes and back lobes.

This is the simplest method and gives reasonably accurate estimates of T_b if the beam efficiency is high.

The brightness temperature $T_b(\theta_0)$ incident upon the antenna is closely related to the bistatic scattering coefficients $\sigma_{jk}^0(\theta_0, \theta_s, \phi_s)$. Consider, see Fig. 6, an antenna viewing a surface at an angle θ_0 from nadir. The brightness temperature along the direction OR is the sum of two contributions; the first is the emission from the ground, equal to a brightness temperature $e_j(\theta_0)T_g$ where $e_j(\theta_0)$ is the emissivity (for radiation in polarization state j) of the ground, and T_g is the physical or "thermometer" temperature of the ground. This is assumed to be uniform to a distance of several skin depths below the surface. The second contribution is the sky noise (which is due primarily to atmospheric absorption at microwave frequencies) reflected by the ground towards the antenna. If the sky noise has a brightness temperature distribution $T_s(\theta_s, \phi_s)$ then the total brightness temperature of the incident radiation coming from direction θ_0 in the j polarization state is [15,16]

$$\begin{aligned}
 (15) \quad T_b^j(\theta_0) = & \underbrace{a(r)}_{\substack{\text{path} \\ \text{attenuation}}} \left\{ \underbrace{\epsilon_j(\theta_0)T_g}_{\substack{\text{ground emission}}} + \underbrace{\iint [\sigma_{jj}^0(\theta_0, \theta_s, \phi_s) + \sigma_{jk}^0(\theta_0, \theta_s, \phi_s)]}_{\substack{\text{reflected sky radiation}}} \right. \\
 & \left. T_s(\theta_s, \phi_s) \frac{d\Omega_s}{4\pi \cos\theta_0} \right\} \\
 & + \underbrace{\int_0^r T_m(\rho) e(\rho) [a(r)/a(\rho)] d\rho}_{\substack{\text{atmospheric path} \\ \text{emission}}}
 \end{aligned}$$

where

$$\epsilon_j(\theta_0) = 1 - \iint [\sigma_{jj}^0(\theta_0, \theta_s, \phi_s) + \sigma_{jk}^0(\theta_0, \theta_s, \phi_s)] \frac{d\Omega_s}{4\pi \cos \theta_0}$$

= emissivity = 1 - albedo

$$a(\rho) = \exp\left[-\int_0^\rho \alpha(\rho') d\rho'\right]$$

= attenuation of the atmosphere in nepers from the surface to a point a distance ρ from the surface along the line of sight. (i.e., $\rho = Z \sec \theta_0$)

(16) $\alpha(\rho)$ = power attenuation coefficient in nepers/meter of the atmosphere at a distance ρ from the surface along the line of sight.

$$a(r)/a(\rho) = \exp\left[-\int_\rho^r \alpha(\rho') d\rho'\right]$$

$T_m(\rho)$ = physical (thermometer) temperature of the attenuating medium.

$e(\rho)$ = emission coefficient (per meter) of the atmosphere

This equation includes a factor $a(r)$ to account for the path loss between ground and antenna, and a term

$$\int_0^r T_m(\rho) \cdots d\rho$$

to account for the emission corresponding to this warm absorbing path. The actual surface brightness consists of two terms, $\epsilon_j T_g$ giving the ground emission, and

$$\int \sum \sigma_{jk} \cdot T_s \cdot d\Omega_s$$

giving the sky radiation reflected towards the receiver.

If losses (i.e., attenuation) due to scattering by the intervening medium between surface and sensor is negligible compared to losses due to absorption, then one may assume $e(\rho) = \alpha(\rho)$. Otherwise $e(\rho)$ is equal to that part of the total attenuation due to absorption. The above equation assumes that the sky radiation $T_s(\theta_s, \phi_s)$ incident on the ground is unpolarized, and that the atmospheric attenuation and absorption coefficients α and e are the same for either of two orthogonal polarization states.

It is often tempting to write the terrain dependent part of Eq. (15) in the form

$$\epsilon_j(\theta_0) T_g + \tilde{\rho}_j \tilde{T}_s \text{ with } \tilde{\rho}_j = 1 - e_j(\theta_0)$$

where $\tilde{\rho}$ and \tilde{T}_s represent some appropriate average values for the surface reflectivity and illumination. This is possible for a perfectly flat surface, but it is clear that for the general surface, no independent definitions of \tilde{T}_s and $\tilde{\rho}$ can be made consistent with the choice $\tilde{\rho} + \epsilon = 1$.

D. Large Extended Targets - Bias Errors

There are a number of configurations in which a relatively high gain (narrow pencil beam) antenna is used to estimate the properties of an extended surface. Because the system response is a convolution of the antenna pattern with the target response (see, e.g., Eq. (3) for the back-scattering response, Eq. (11) for the doppler response, Eq. (14) for the brightness temperature response) a number of "bias"

errors can occur when the target properties change rapidly with look angle. It is often convenient to make first order corrections for these effects, in order to avoid the need for inverting the convolution integral.

We summarize here these first order corrections when the antenna pattern is assumed to be of the form

$$f(\psi) = e^{-A(1-\cos\psi)}$$

since this approximates a Gaussian beam when A is large. The half power beam width θ_B (between 3 dB points) of such a pattern is

$$\theta_B = 2 (2 \ln 2/A)^{1/2}$$

radians, and the directivity D is approximately $D \simeq 2A$ ($A \gg 1$). In this case if the beam axis makes an angle θ_0 with respect to the mean surface normal, we find the radar response (c.w.) to be

$$P_r(\theta_0) = \frac{P_o G A_{emr}}{(4\pi r)^2} \left[\frac{\pi \sigma^0(\theta_0)}{A \cos \theta_0} \right] \left(1 + \frac{S_i}{D} \right)$$

where

$$S_i = 2 \sec^2 \theta_0 \left[7 \sin^2 \theta_0 - 2 - (\cot \theta_0 / 4) \frac{\sigma'_0(\theta_0)}{\sigma_0(\theta_0)} (7 \sin^2 \theta_0 - 1) + \frac{\sigma''_0(\theta_0)}{\sigma_0(\theta_0)} (\cos^2 \theta_0 / 4) \right]$$

$$\sigma'_0(\theta_0) = \left. \frac{\delta \sigma}{\delta \theta} \right|_{\theta=\theta_0} \text{ etc.}$$

Thus, the correction due to the biasing effect of the surface and the geometry of the experiment is of order $1/D$, and does not go to zero even for an isotropic surface ($\sigma' = \sigma'' = 0$); the fixed error is due predominantly to the $1/r^4$ weighting of the scattering contribution from dA .

For a radiometer antenna viewing a surface for which the total brightness temperature incident on the antenna is $T_b(\theta_0)$, the antenna temperature is given by

$$(17) \quad T_a(\theta_0) = T_b(\theta_0) + \Delta T/D$$

$$\Delta T = T_B''(\theta_0) - T_B'(\theta_0) (9 \sin^2 \theta - 1) \sec \theta_0 \operatorname{cosec} \theta_0.$$

This assumes that the beam efficiency of the antenna is 100%. That is, it does not take account of energy entering the antenna via side and back lobes. If the actual antenna has a beam efficiency of 100F%, (i.e., if the actual antenna pattern can be written in the form

$$f(\psi) = \exp(-A(1-\cos\psi)) + f_s(\psi)$$

where $f_s(\psi)$ is the side lobe contribution, and $\int f_s d\Omega / \int f d\Omega = (1-F)$, then the bias error correction is just F times as large as that given in Eq. (17). For the radiometer measurement a "grey body" surface ($T_b'(\theta) = T_b''(\theta) = 0$) gives no bias effect, since (see Eq. (14)) $T_b(\theta)$ is weighted only by $d\Omega$.

The most significant of the bias errors occurs in estimating the doppler spectrum of a radar signal. Because of the difficulty in computing the spectrum by straightforward integrations over the isodop contours, it is simpler, in this case, to estimate the bias effect by

computing the moments of the doppler spectrum $S(f)$. We define the n^{th} moment of the spectrum with respect to the transmitter frequency f_0 by

$$\overline{\Delta^n f} = \int_0^\infty S(f) (f - f_0)^n df / \int_0^\infty S(f) df$$

If now Δf_0 is the doppler shift associated with the line of sight along the axis TO of the beam (i.e., $\Delta f_0 = 2f_0 v/c \sin\theta_0 \cos(\eta)$ where \vec{v} is taken, as in Fig. 7, in the xy plane with $\vec{v} \cdot \vec{i}_y = v \cos(\eta)$), then relations can be found between Δf_0 (the "nominal" doppler along the main beam axis line of sight) and the moments. The first two moments give the relations

$$\begin{aligned} \Delta f_0 &= \overline{\Delta^1 f} - 2(v/c) f_0 \bar{\delta} \\ (18) \quad (\Delta f_0)^2 &= 2 \left(\overline{\Delta^1 f} \right)^2 - \left(\overline{\Delta^2 f} \right) + (2vf_0/c)^2 \bar{\delta}^2 - \frac{4vf_0}{c} \bar{\delta} \left(\overline{\Delta^1 f} \right) \end{aligned}$$

where

$$\bar{\delta} = (1/D) \left\{ 2 \frac{\sigma'_0(\theta_0)}{\sigma_0(\theta_0)} \cos\theta_0 - 12 \sin\theta_0 \right\} \cos\eta$$

$$\bar{\delta}^2 = (1/D) (\cos^2\theta_0 \cos^2\eta + \sin^2\eta)$$

Thus, by measuring the first moment of the doppler spectrum $\overline{\Delta^1 f}$, and using the first of Eq. (18), the nominal doppler Δf_0 may be estimated.

E. Small Extended Targets. The Centroid Concept.

In certain situations, (as for example in determining the position of an island in the ocean) one may wish to estimate the sensor response

as the beam passes over a small extended target. (That is, the "target" is small in the sense that it subtends an angle comparable to or smaller than a beamwidth). If $\sigma_0(\theta)$ and $T_b(\theta)$ are known for all elements dA of the target area, (and this implies that both σ_0 and T_b may be rapidly varying functions of x,y , the position coordinates of dA), then the sensor response may be computed for each point of the antenna trajectory as it passes over the target area. It is often more convenient to estimate sensor response in terms of parameters which can be computed independently for the target and for the experimental geometry. This is possible by introducing the centroid concept. If we consider only the c- ω radar and microwave radiometer systems, the contribution of a target area (see Fig. 8) to the total received power dP_r or to the antenna temperature, dT_a , can be written

$$dT_a(\theta_0) = \Omega_B^{-1} \int_A f(x,y) T_b[x,y, \theta'(x,y)] \frac{\cos \theta'}{r^2} dx dy$$

$$(19) \quad \Omega_B \equiv \int f(\psi) d\Omega = \text{antenna beamwidth}$$

$$dP_r(\theta_0) = \frac{P_o G_t A_{em}}{(4\pi)^2} \int_A \sigma_0 [x,y, \theta'(x,y)] f^2(x,y) \frac{dx dy}{r^4}$$

$$\theta'(x,y) = \text{local angle of incidence at } x,y,$$

where the integration is over the target area A , and the antenna pattern $f(\psi, \xi)$ is written as a function of x and y . Now these equations are of the form

$$dR(\theta_0) = C \int_A S(x,y) g(xy) dx dy$$

where $dR(\theta_0)$ = sensor response at look angle θ_0

$$S(x,y) = \left\{ \begin{array}{l} \sigma_0(x,y,\theta'(x,y)) \\ T_b(x,y,\theta'(xy)) \end{array} \right\} \quad \text{the surface property}$$

$$g(xy) = \left\{ \begin{array}{l} f(xy) \cos \theta' / r^2 \\ f^2(x,y) / r^4 \end{array} \right\} \quad \text{geometry and beam.}$$

$C = \text{constant}$

If a suitable point x_c, y_c (the centroid) is chosen, then the function $g(xy)$ can be expanded about the centroid

$$g(x,y) = g(x_c, y_c) + \frac{\partial g}{\partial x_c} (x-x_c) + \frac{\partial g}{\partial y_c} (y-y_c) + \frac{1}{2!} \frac{\partial^2 g}{\partial x_c^2} (x-x_c)^2 + \dots$$

The target parameter s can be expanded about the reference angle θ_0 ,

$$s(x,y,\theta') = s(x,y,\theta_0) + \left(\frac{\partial s}{\partial \theta'} \right)_{\theta_0} (\theta' - \theta_0) + \dots$$

Substituting these expansions into Eq. (19), and forcing the first order terms in $(x-x_c)$, $(y-y_c)$ to be zero, the centroid parameter can be defined, viz;

$$\begin{aligned} x_c &= \int x s(x,y,\theta_0) dA / \int s(x,y,\theta_0) dA \\ y_c &= \int y s dA / \int s dA \end{aligned} \quad (20)$$

where all integrals are over the area of the target. Then

$$dP_r = g(x_c, y_c) \left[\int s(x,y,\theta_0) da \right] + \text{second order terms}$$

and the sensor response is written as the product of a target term independent of transmitter pattern and geometry, and a geometrical term $g(x_c, y_c)$ dependent only on the experimental geometry. Thus for the radiometer,

$$(21) \quad dT_a(\theta_0) = \left(\frac{\cos \theta_c}{r_c^2 \Omega_B} f(x_c, y_c) \right) [\int T_b(\theta_0) dA] + \text{second order}$$

where r_c, θ_c are the range and angle of incidence for the centroid point, and the centroid is defined by

$$\begin{Bmatrix} x_c \\ y_c \end{Bmatrix} = \int \begin{Bmatrix} x \\ y \end{Bmatrix} T(x, y, \theta_0) dx dy / \int T(x, y) dx dy .$$

Similarly, the radar response is

$$(22) \quad dP_r(\theta_0) = \frac{P_o G_t A_{em}}{(4\pi)^2} \frac{f^2(x_c, y_c)}{r_c^4} \int \sigma_0(x, y, \theta_0) dA + \text{second order}$$

where the radar centroid is determined by

$$\begin{Bmatrix} x_c \\ y_c \end{Bmatrix} = \int \begin{Bmatrix} x \\ y \end{Bmatrix} \sigma_0(x, y, \theta_0) dA / \int \sigma_0(x, y) dA .$$

The magnitude of the second order terms can only be found by comparing the exact integration (Eq. (19)) with Eqs. (21) and (22). The corresponding pointing errors, (i.e., the errors incurred by assuming the defined centroid lies on the axis of the main beam when the measured system response dR is a maximum) are quite small, and do not impose a serious

limitation on the centroid concept under most circumstances. Nevertheless it is usually desirable to check system performance by numerical integration in systems requiring high pointing accuracy, particularly if the target has a very irregular distribution of surface properties $\sigma^0(xy)$ or $T_b(x,y)$.

F. System Limitations Due to Fluctuations in Antenna Pointing

It is not always appreciated that in many operational microwave radiometer systems, the limiting factor in system performance may be determined not by the inherent precision of the instrument, but by "noise" introduced by fluctuations in look angle, or by the fluctuation due to surface inhomogeneities or to atmospheric path loss variations. Suppose, for example, that a small target contributes brightness temperature $T_t(\theta)$ to the antenna temperature, and the antenna undergoes r.m.s. fluctuations of $(d\theta)^2$ in look angle due to vehicle oscillation or the antenna steering control system. Then the total fluctuations in antenna output are approximately

$$\Delta T_a \simeq \left[(\Delta T_0)^2 + \left[\frac{T_t(\theta)}{\partial \theta} \right]^2 (d\theta)^2 \right]^{1/2}$$

where ΔT_0 is the inherent sensitivity of the radiometer.

$$\Delta T_0 = K T_{\text{eff}} / (B\tau)^{1/2}$$

K = constant of order unity

B = RF bandwidth of radiometer

τ = radiometer time constant

T_{eff} = effective receiver noise temperature.

It may often happen that the second term is of the same order or larger than the first and the supposed precision of measurement ΔT_0 cannot be achieved in practice. Similar effects occur when a moving antenna views a fluctuating background brightness, or when the attenuation of the atmosphere fluctuates. For example if the surface has a brightness temperature T_b and the atmosphere has physical temperature T_{atm} and attenuation α ($0 < \alpha < 1$) between surface and antenna, then the antenna temperature is approximately

$$T_a = (1-\alpha) T_b + \alpha T_{atm}.$$

Thus, fluctuations in T_a due to fluctuation in α are approximately

$$(\Delta T_a)^2 \approx (\Delta \alpha)^2 (T_b - T_{atm})^2.$$

Since $(T_b - T_{atm})$ may be of the order of 100°K over reflective surfaces, fluctuations in α of the order of 0.04 dB may introduce fluctuations of order 1°K in T_a . Very small amounts of condensed water, as in clouds, can produce attenuations of this order at the higher microwave frequencies.[14]

Finally, systematic errors can occur in target-seeking split-lobe or double beam systems, in which the background temperature differs for the two beams (e.g., the temperature due to the sea background for an island seeking system). This shift in null temperature is of order $[\partial T_B(\theta)/\partial \theta] \Delta \theta$ where $\Delta \theta$ is the angular separation of the two beams. Again, the error incurred by assuming the target is located in the null direction may be larger than the nominal pointing accuracy of the system over a homogeneous background.

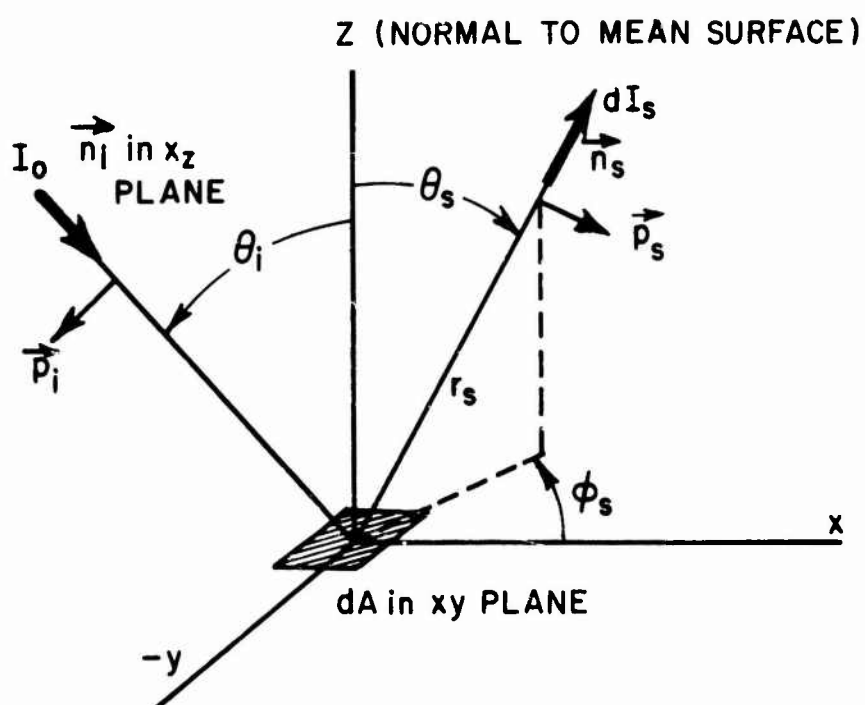


Fig. 1. Geometry of the scattering problem.

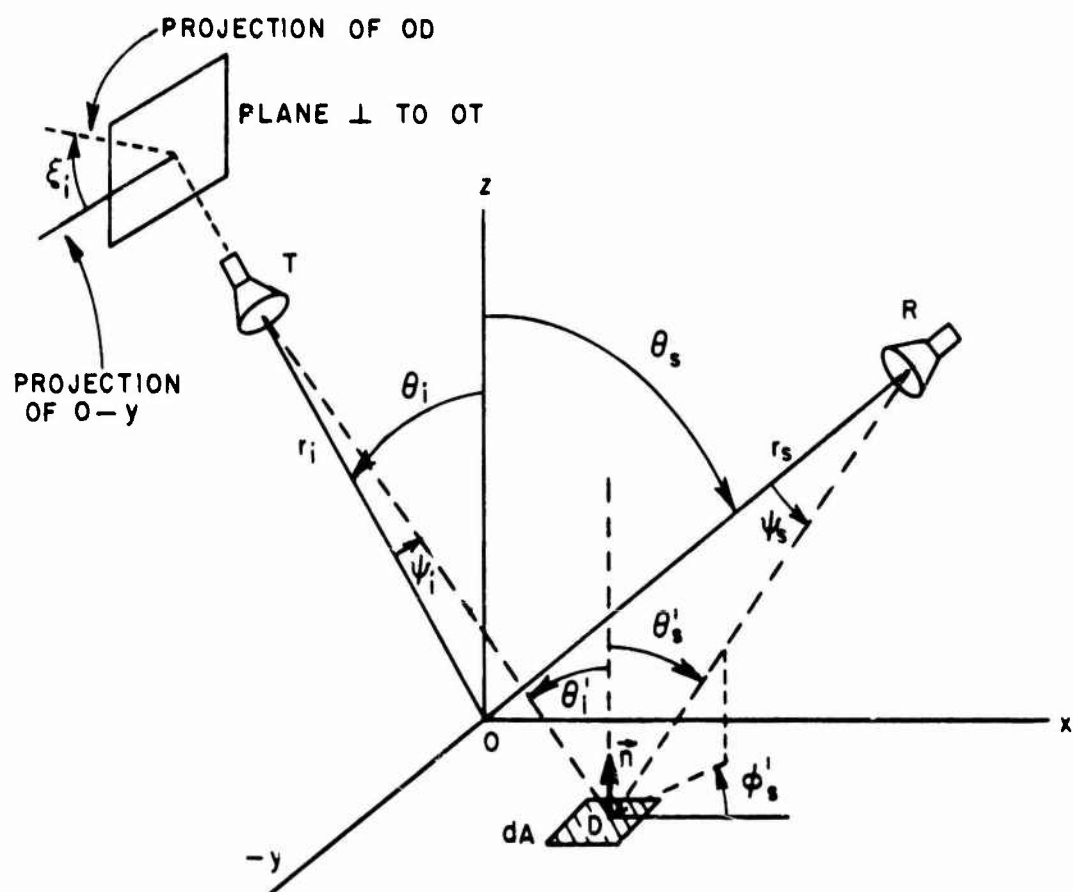


Fig. 2. Bistatic scattering geometry.

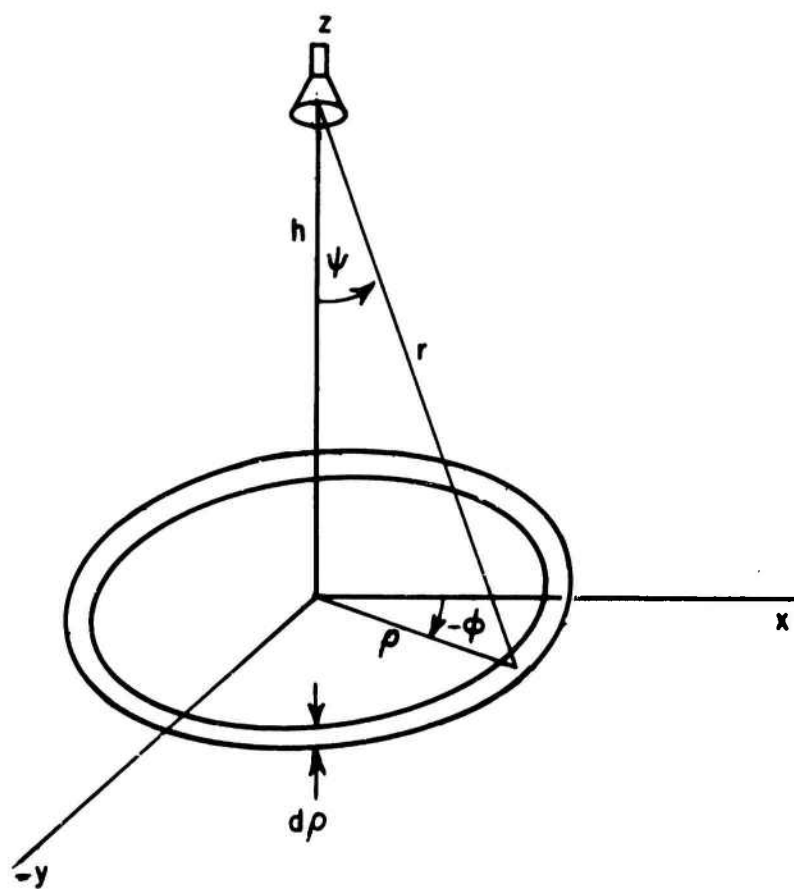
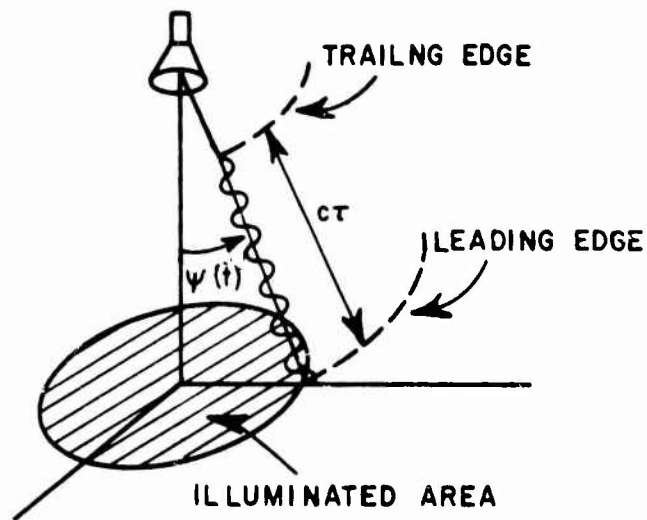
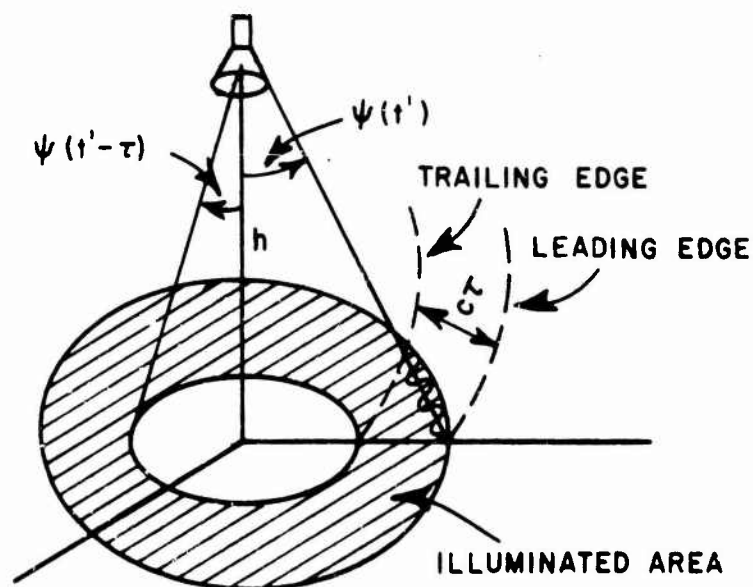


Fig. 3. Range ring.



(a) $t' < \tau$ BEAM LIMITED



(b) $t' > \tau$ PULSE LIMITED

Fig. 4. Beam and pulse limited geometries.

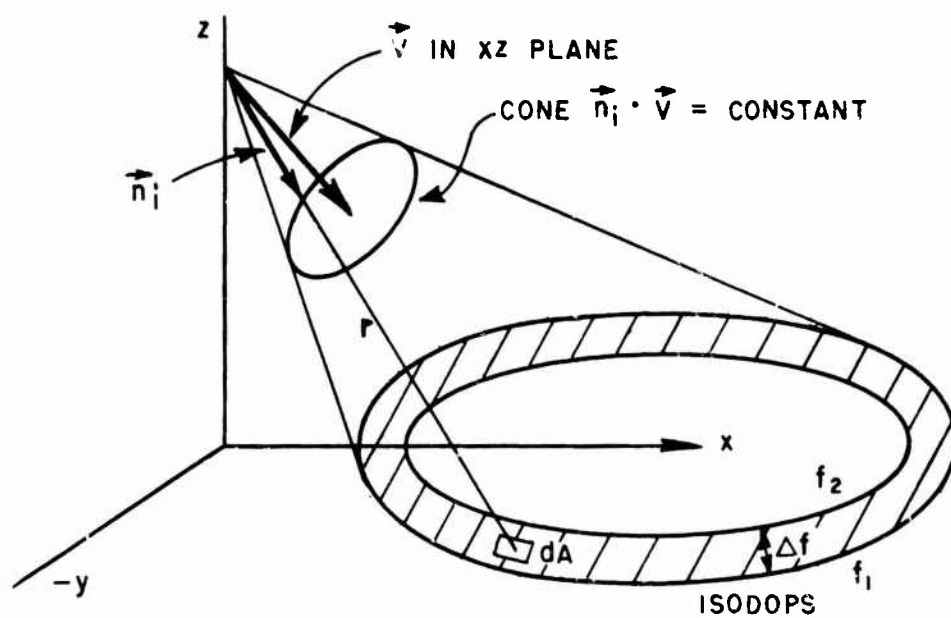


Fig. 5. Isodop contours and doppler spectrum.

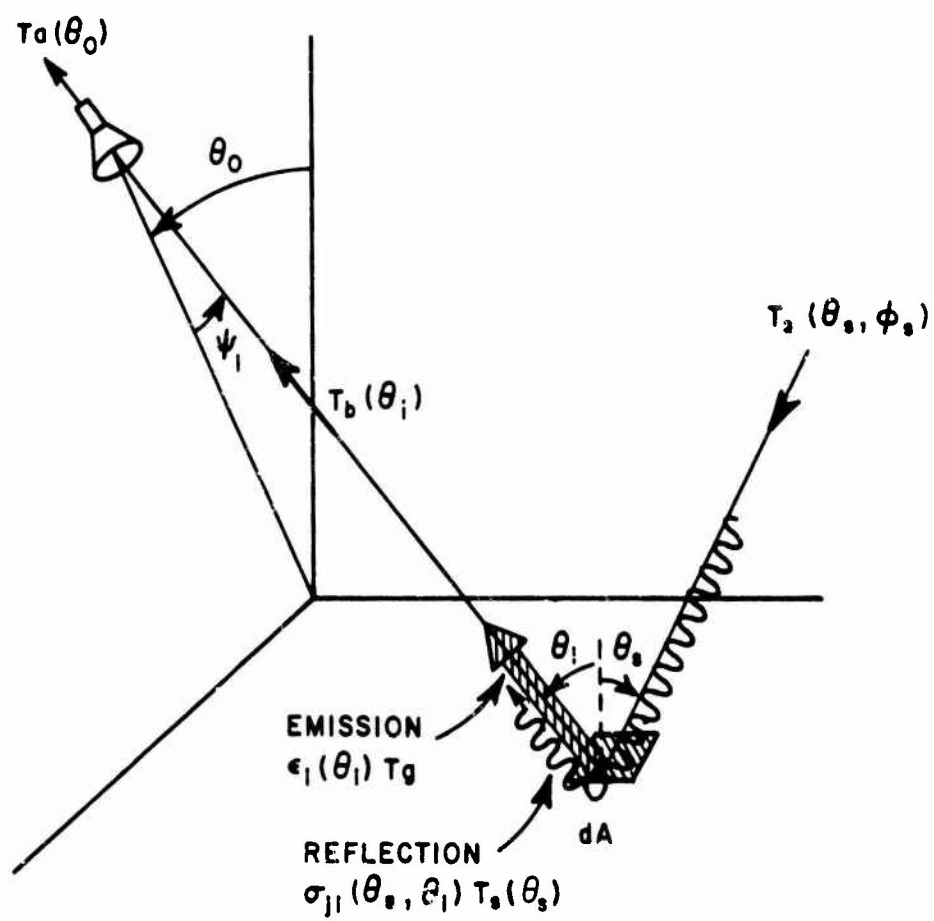


Fig. 6. Geometry of a radiometer system.

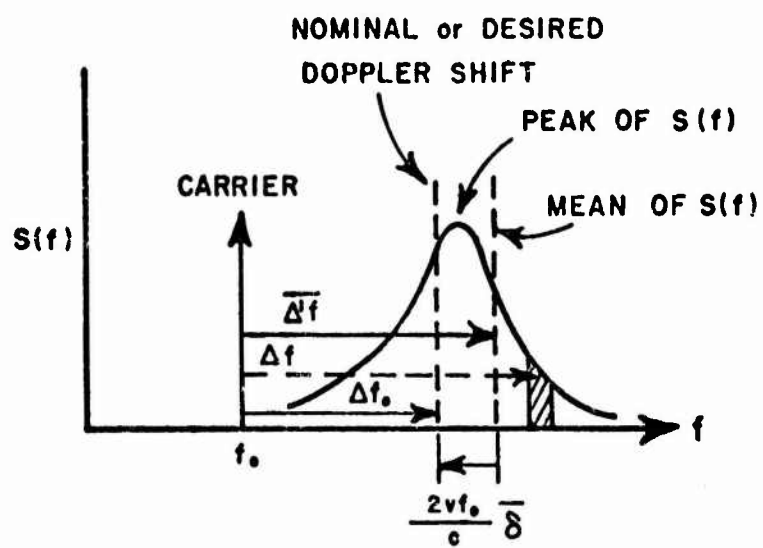


Fig. 7. The doppler spectrum.

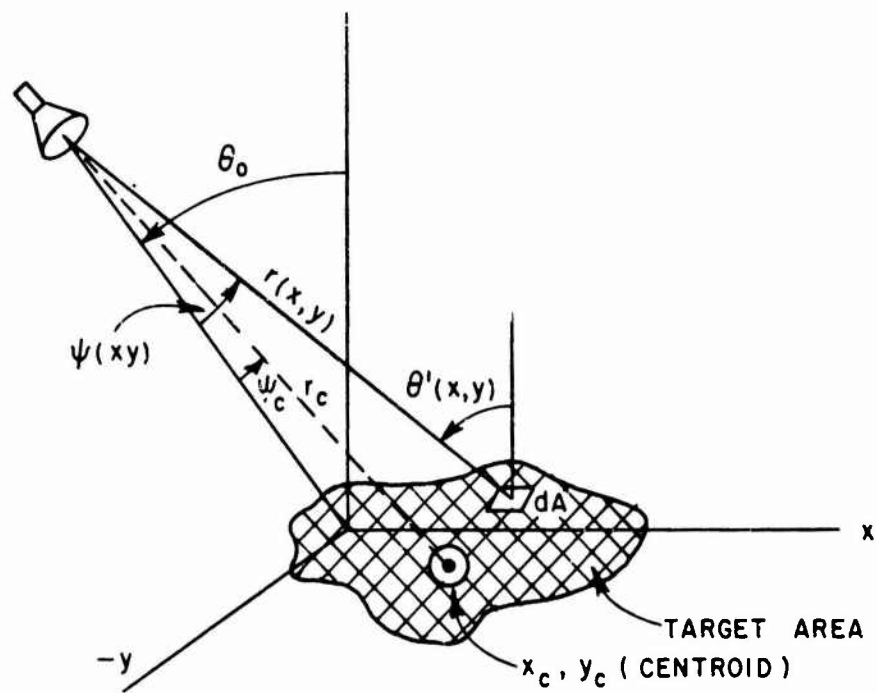


Fig. 8. The centroid concept for small targets.

REFERENCES

1. Skolnik, M.I., Introduction to Radar Systems, McGraw-Hill, New York, 1962.
2. Barton, D.K., Radar Systems Analysis, Prentice Hall, Englewood Cliffs, N. J., 1964.
3. Nathanson, F.E., Radar Design Principles, McGraw-Hill, New York, 1969.
4. Berkowitz, R.S., Ed. Modern Radar - Analysis Evaluation and System Design, John Wiley & Sons, New York, 1965.
5. Evans, J.V. and Hagfors, T., Radar Astronomy, McGraw-Hill, New York, 1968.
6. Kraus, J.D., Radio Astronomy, McGraw-Hill, New York, 1969.
7. Ruck, G.T., Barrick, D.E., Stuart, W.D. and Krichbaum, C.K., Radar Cross-Section Handbook, Plenum Press, New York, 1970, See Sections 2.1.3. and 2.1.4. for discussion of polarization effects.
8. Hagfors, T., "A Study of the Depolarization of Lunar Radar Echoes," Radio Science, Vol. 2, 445, 1967.
9. Moore, R.K. and Williams, C.S., "Radar Terrain Return at Near Vertical Incidence," Proc. IRE 45, 228, 1957.
10. Farrel, J.L. and Taylor, R.L., "Doppler Radar Clutter," IEEE Trans. ANE-11, pp. 162-172, 1964.

11. Friedlander, A.L. and Greenstein, L.J., "A Generalized Computation Procedure for Airborne Pulse Doppler Radars," IEEE Trans., AES-6, pp. 51-61, 1970.
12. Barrick, D.E., "Radar Clutter in an Air Defense System," Report RSIC-798, Redstone Arsenal, Alabama, January 1968.
13. Peake, W.H., "Estimates of Bias Errors in Narrow Beam Microwave Systems," Report 2440-3, 23 December 1968, ElectroScience Laboratory, Department of Electrical Engineering, The Ohio State University Research Foundation; prepared under Contract F 33615-67-C-1663 for Air Force Avionics Laboratory, Wright-Patterson Air Force Base, Ohio.
14. Kriess, W.T., "The Influence of Clouds on Microwave Brightness Temperatures," Proc. IEEE 57, p. 440, 1969.
15. Peake, W.H., "Interaction of Electromagnetic Waves With Some Natural Surfaces," IRE Trans. AP-7, p. S324, December 1959.
16. Peake, W.H. and Chen, S.N.C., "Apparent Temperatures of Smooth and Rough Terrain," IRE Trans. AP-9, p. 567, 1961.

III. THE CONSTITUTIVE PARAMETERS

A. Introduction

The scattering from natural surfaces is controlled by both the structure, or roughness of the surface, and the electrical properties, that is the complex electric permittivity and magnetic permeability. The magnetic properties play a rather small role at microwave frequencies since, except for a few minerals, the permeability may be taken as unity.

To define the various parameters used to describe the electrical properties of matter, it is convenient to start with Maxwell's equation for a source free region

$$\nabla \times \vec{H} = \frac{\partial \vec{D}}{\partial t} + \vec{J}_c$$

where H is the magnetic field, D the electric displacement and J_c the total conduction current. In order to solve for the fields within a body, it is necessary to provide a connection between D , J and the electric field E . This is done by introducing the constitutive parameters, ϵ_0 (the permittivity of vacuum, $\epsilon_0 \simeq 8.85 \times 10^{-12}$ farad-meter⁻¹) ϵ_r (the real relative dielectric constant of the medium) and σ (the real conductivity of the medium in mhos-meter⁻¹). When the fields vary as $e^{j\omega t}$, then Maxwell's equation becomes

$$(1) \quad \nabla \times \vec{H} = [j\omega\epsilon_0\epsilon_r + \sigma] \vec{E} = j\omega\epsilon_0\epsilon_c \vec{E}.$$

The complex proportionality factor ϵ_c may be written in a number of ways.

$$\epsilon_c = (\epsilon_r + \sigma/j\omega\epsilon_0) \quad (\text{the complex dielectric constant})$$

$$(2) \quad \epsilon_c = \epsilon_r - j\epsilon_{im} \quad (\text{the real and imaginary parts of } \epsilon_c)$$

$$\epsilon_c = \epsilon_r(1 - j \tan \delta) \quad (\tan \delta \text{ is the "loss tangent"})$$

where $\tan \delta = \sigma/\omega\epsilon_0\epsilon_r = \epsilon_{im}/\epsilon_r$ etc. On the other hand, in the theory of metals it is customary to emphasize the complex conductivity σ_c by the definitions

$$(3) \quad \nabla \times \vec{H} = [\sigma + j(\omega\epsilon_0\epsilon_r)] \vec{E} = \sigma_c \vec{E} = (\sigma + j\sigma_{im}) \vec{E}$$

$$\sigma_{im} = \omega\epsilon_0\epsilon_r \quad (\text{the imaginary part of the conductivity})$$

$$\sigma_c = j\omega\epsilon_0\epsilon_c$$

In fact, at any frequency one can measure only the complex number ϵ_c or σ_c . How one assigns significance to the real and imaginary parts depends on how detailed a model is used to describe the interaction of radiation and matter at the molecular level. For example, the relaxation model for sea water provides different mechanisms for the losses associated with the polar molecules and with the ion transport. Thus for such models one often writes

$$\epsilon_c = \epsilon_r - j\epsilon'' - j(\sigma_{dc}/\omega\epsilon_0)$$

where now ϵ_{im} is the sum of two terms $\epsilon_{im} = \epsilon'' + \sigma_{dc}/\omega\epsilon_0$. Here σ_{dc} is the d.c. conductivity of the substance. At any other frequency only the total loss ϵ_{im} can be measured, and the difference between the measured loss and the term $\sigma_{dc}/\omega\epsilon_0$ is ascribed to the polar relaxation mechanism. Naturally for sea water the terms ϵ'' and $\sigma_{dc}/\omega\epsilon_0$ have quite different dependences on temperature, frequency etc. so that

in this case the separation is quite plausible. Nevertheless, the interaction at any frequency depends only on the single complex number $\epsilon_c(\omega)$.

In the time domain, a corresponding connection obtains between E and D , and it is not hard to show, by considering Eq. (3) as the Fourier transform of the time dependent equations that

$$\vec{D}(t) = \epsilon_\infty \vec{E}(t) + \int_0^\infty h(\tau) \vec{E}(t-\tau) d\tau$$

$$(4) \quad h(\tau) = \frac{1}{2\pi} \int_{-\infty}^\infty [\epsilon_c(\omega) - \epsilon_\infty] e^{+j\omega\tau} d\omega$$

$$\epsilon_\infty = \lim_{\omega \rightarrow \infty} \epsilon_c(\omega)$$

that is, D is the convolution of E with the "impulse response" of the dielectric where the latter is the Fourier transform of $(\epsilon_c(\omega) - \epsilon_\infty)$. (The infinite frequency part ϵ_∞ is subtracted off to avoid the appearance of δ functions in Eq. (4)). Because a dielectric may be regarded as a causal linear system, ($h(t) = 0$ for $t < 0$), $\epsilon_r(\omega)$ and $\epsilon_{im}(\omega)$ constitute a pair of Hilbert transforms, a connection sometimes referred to as the causality condition, the Kramers-Kronig relation, or the dispersion relation, viz

$$[\epsilon_r(\omega) - \epsilon_\infty] = \frac{1}{\pi} \int_{-\infty}^\infty \frac{\epsilon_{im}(\omega') d\omega'}{\omega - \omega'}$$

$$(5) \quad \epsilon_{im}(\omega) = -\frac{1}{\pi} \int_{-\infty}^\infty \frac{(\epsilon_r(\omega') - \epsilon_\infty)}{\omega - \omega'} d\omega'$$

These relations are often helpful in determining the behaviour of ϵ_r or ϵ_{im} over short frequency intervals.

There is a second group of parameters, originating in optics, which are also used to describe the electrical properties of matter. If one considers a plane wave propagating in the x direction in a medium with parameters $\epsilon_0 \epsilon_c$, μ_0 then the spatial dependence of the fields may be written as $\exp[-\gamma x + j\omega t]$ where γ is a complex number referred to as the complex propagation constant. The real and imaginary parts are

$$\begin{aligned}\gamma &= \alpha' + j\beta = j\omega\sqrt{\mu_0\epsilon_0\epsilon_c} = (2\pi/\lambda_0) j\sqrt{\epsilon_c} = j(2\pi/\lambda_0) n_c \\ \alpha' &= \text{attenuation constant (nepers/meter)} \\ \beta &= \text{wave number (radians/meter)} \\ \lambda_0 &= \text{vacuum wavelength} = (\omega\sqrt{\mu_0\epsilon_0})^{-1} (2\pi) \\ n_c &= \sqrt{\epsilon_c} \text{ complex index of refraction.}\end{aligned}$$

The wavelength in the medium is $\lambda = 2\pi/\beta$; the skin depth δ or penetration depth in the medium is $\delta = 1/\alpha'$ meters. Note that the power attenuation coefficient used in Eq. (16) of Chapter I is $\alpha(\rho) = 2\alpha'$.

B. The Dielectric Constant of Water and Ice

Because of the overwhelming influence of water in modifying the dielectric constant of many terrestrial surfaces at microwave frequencies, it is desirable to have simple estimates for ϵ_c . These may be obtained from the formula[1]

$$\epsilon_c = \epsilon_\infty + \frac{\epsilon_d - \epsilon_\infty}{(1 + jf/f_0)} - j \frac{\sigma}{\omega\epsilon_0}$$

which is applicable to both water and ice. Here

σ = ionic conductivity. This is of order 4 mhos/meter for sea water, and is proportional to the salinity. σ is negligible for distilled water.

$$\epsilon_{\infty} = 5.5 \text{ for water and } 3.2 \text{ for ice}$$

$$\epsilon_d = 87.7 - 0.4(T-273) \text{ for water } (T_{in} \text{ } ^\circ\text{K})$$

$$\epsilon_d = 90 + T/550 \text{ for ice } (T_{in} \text{ } ^\circ\text{C})$$

$$f_o = 9.1 \text{ GHz for water at } 273 \text{ } ^\circ\text{K}$$

$$f_o = 12.6 \text{ GHz for water at } 283 \text{ } ^\circ\text{K}$$

$$f_o = 17.2 \text{ GHz for water at } 293 \text{ } ^\circ\text{K}$$

$$f_o = 21.6 \text{ GHz for water at } 303 \text{ } ^\circ\text{K}$$

$$f_o = 10 \text{ KHz for ice at } 273 \text{ } ^\circ\text{K}$$

$$f_o = 3 \text{ KHz for ice at } 263 \text{ } ^\circ\text{K}$$

$$f_o = 1 \text{ KHz for ice at } 253 \text{ } ^\circ\text{K}.$$

The dissipative properties of ice are not well represented by this formula at microwave frequencies, particularly for sea ice, the properties of which can vary widely depending on the conditions under which it was formed. For this reason, measured values[2] of loss tangent should be used for ice at microwave frequencies. The general features of the electrical properties of water (and ice) are shown in Fig. 9, in which ϵ_r is plotted against ϵ_{im} , with frequency as the parameter.

C. Rocks and Powders

Rocks and minerals in the solid form have dielectric constants in the range of $\epsilon_r = 2$ to 10 at microwave frequencies, and show a tendency for the dielectric constant to be proportional to density and almost independent of frequency. The loss tangent for such materials, however, can range over several orders of magnitude, and may vary widely with frequency, particularly if the material contains water inclusions. Penetration depths lie in the range of 0.5 to 10 meters for frequencies between 0.5 GHz to 35 GHz,[5] for dry materials. Tables I and II

summarize a number of measurements reported in References 1, 4 and 5. Reference 5 also includes calculated penetration depths for the samples listed in Table II.

When rocks are ground into powder, the properties of the powder can be obtained, approximately from the powder density and the bulk dielectric constants of the solid material. A convenient general mixing formula has the form of

$$\frac{\epsilon_m - \epsilon_i}{\epsilon_m + u} = V \frac{\epsilon_b - \epsilon_i}{\epsilon_b + u}$$

where

- ϵ_m is the complex dielectric constant of the mixture
- ϵ_i is the complex dielectric constant of one component (typically air, $\epsilon_i = 1$ for powders)
- ϵ_b is the bulk complex dielectric constant of the other component.
- V is the volume fraction of the total volume occupied by component ϵ_b .
- u is a form number, $0 < u < \infty$.

The form number has a particular value for mixtures of a particular type, depending principally on the shape of the particles. A value $u = 2$ has been found to give reasonable results for powders of low density[5] ($\approx 1 \text{ gm/cm}^3$) whereas $u = 2\epsilon_b$ appears to give better agreement for higher density "mixtures" such as sand. It may be of interest to note that the dielectric constant of powdered rocks[5] seems to depend almost entirely on the powder density; some 20 of the samples from Table II exhibit an ϵ_r in the range 1.9 to 2.1 when powdered to a uniform density of 1 gm/cm^3 .

D. Soils

The dielectric constant of soils at microwave frequencies depends predominantly on their moisture content. Fig. 10 shows measurements of ϵ_r vs moisture content for two common soils.[3] The imaginary part ϵ_{im} is also shown for the 0.3 GHz case. It is clear from these figures, and other similar data,[2,6] that both the real and the imaginary parts of the dielectric constant for typical soils are much higher than would be expected as the basis of laboratory measurements on dry samples, and at any given frequency are approximately proportional to water content, and independent of soil type. One consequence of this fact is clearly illustrated in Fig. 68 (Chapter V) which shows the systematic changes in brightness temperature of a soil surface as moisture content is varied.

At frequencies below 100 mc the electrical properties of rocks and soils[8] are exceedingly complex, and no attempt should be made to extrapolate the results given here to lower frequencies.

E. Vegetation

The dielectric constant of vegetation is also controlled, at microwave frequencies, by the water content. For example, Fig. 11 shows the real and imaginary parts of the dielectric constant of typical leaf material at 8.5 GHz. At frequencies near X-Band the results can be roughly represented by a formula of the type

$$\epsilon_{\text{vegetation}} \simeq (F/2)\text{Re}(\epsilon_w) - j(F/3)\text{Im}(\epsilon_w)$$

where F is the fraction of water by weight in the vegetation and ϵ_w is the complex dielectric constant of water. At lower frequencies (say 1 GHz and below) the ionic conductivity of the dissolved salts in the leaf must also be taken into account in estimating the dielectric constant.[9]

A similar situation obtains for the woody parts of vegetation. For example, [10] oak and wych elm wood at 70 - 75% moisture content have $\epsilon_r \approx 45$ at 0.1 GHz; Figs. 12 and 13 show the complex dielectric constant and loss tangent of fir wood for a number of moisture contents.

TABLE I
(Data from Refs. 2 and 4)

Freq. in GHz	ϵ_r	$\tan \delta$	Density	Material
35	2.3	0.08		Red Granite
35	2.4	0.06		White Granite Crushed
35	1.7	0.012		White Pumice Crushed
35	1.6	0.02		Black Pumice Crushed
1.0	35	0.175	3.01	Chondritic Meteorite
14	4.6	0.006	1.81	Halite
14	3.8	0.012	1.56	Halite
14	3.3	0.009	1.42	Halite
10	4	0.1		Limonite (Coarse)
10	4	0.01		Limonite (Fine)
8.5	3.3	0.0055	1.11	Magnesite Hard Packed
8.5	2.45	0.002	1.22	Quartz Powder
0.1	10	0.02		Basalt (Hawaii) Oven Dry
0.1	10	0.08		Basalt (Hawaii) 0.36% Water
0.1	7 to 9	0.1		Granite (Quincy)
0.1	8.4	0.006 to .018	2.65	Limestone (Lucerne Valley)
0.1	5.5	0.001		Rhyolite
10	4.8	0.005	2.45	Basalt (Vesicular)
10	4.4	0.013	2.63	Biotite Granite
10	5.1	0.081	2.35	Obsidian
10	4.8	0.009	2.74	Olivine Basalt
10	5.4	0.086	2.68	Serpentine
10	5.0	0.027	1.62	Volcanic Ash
10	4.7	0.017	2.27	Altered Tuff
10	5.5	0.016	2.03	Tuff
10	4.7	0.01	2.3	Horn Blende
10	3.0	0.012	0.78	Mono Pumice
14	2.9	0.011	1.63	Desert Sand
14	8.2 to 8.6	0.004 to .02	2.65	Limestone (Lucerne Valley)
14	4.7 to 6	0.01 to 0.1	2.35	Asphalt
14	4.5 to 5.2	0.02 to .06	2.1	Concrete
10	2.7	0.008	1.9	Pumice (Mono)
10	1.7	0.016	0.45	Pumice (Mono)

TABLE II
(Data from Ref. 5)*

Rock	Source	450 MHz		35 GHz	
		ϵ'	$\tan \delta$	ϵ'	$\tan \delta$
andesite, hornblende	Mt. Shasta, Calif.	5.1	0.004	5.0	0.014
anorthosite	Essex County, N. Y.	6.8	0.008	6	0.016
basalt	Lintz, Rhenish-Prussia, Germany	8.9	0.018	9.2	0.09
basalt, hornblende	Chaffee County, Colo.	6.7	0.013	6.5	0.04
basalt, olivine	Jefferson County, Colo.	8.1	0.017	8.0	0.09
basalt, tholeiitic	Columbia River, Ore.	9.6	0.09	8.0	0.112
basalt, vesicular	Chaffee County, Colo.	7	0.017	5.3	0.04
gabbro, bytownite	Duluth, Minn.	7	0.02	7	0.018
granite, alkali	Quincy, Mass.	5.2	0.034	5.3	0.023
granite, biotite	Westerly, R. I.	6	0.02	5.7	0.05
granite, biotite	Llano, Texas	5.4	0.007	5.5	0.015
granite, hornblende	Rockport, Mass.	6	0.010	5.2	0.01
obsidian	Lake County, Ore.	6.8	0.13	5.6	0.05
obsidian	Newberry Caldera, Ore.	5.5	0.0134	5.4	0.0381
peridotite, mica	Tompkins County, N. Y.	6.0	0.034	5.3	0.034
peridotite, olivine (dunite)	Jackson County, N. C.	6.2	0.01	6.1	0.02
phonolite	Beacon Hill, Colo.	6.5	0.03	6.3	0.029
pumice	Millard County, Utah	2.5	0.007	2.4	0.02
ryholite	Castle Rock, Colo.	3.38	0.015	3.41	0.007
serpentine	Cardiff, Md.	6.4	0.011	6.4	0.04
serpentine	Rogue River, Ore.	7	0.019	6.4	0.06
syenite, augite (larvikite)	Larvik, Norway	8	0.05	6.7	0.2
trachyte	Mineral Hill, Colo.	5	0.026	5.43	0.025
tuff, grey	near Cripple Creek, Colo.	6.1	0.06	5.4	0.07
tuff, semi-welded	Bend Quarry, Ore.	2.6	0.011	2.6	0.03
volcanic ash shale	near Florissant, Colo.	2.7	0.03	2.6	0.015

* All samples vacuum dried.

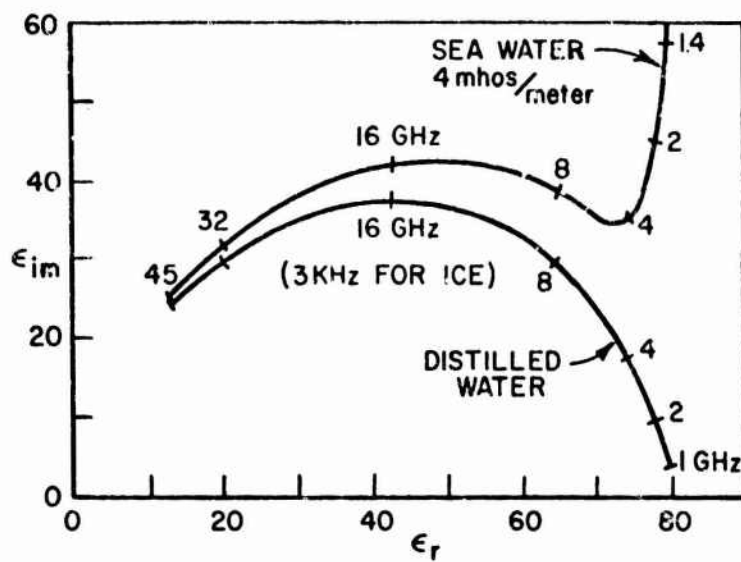


Fig. 9. Relative complex dielectric constant of water. (typical)

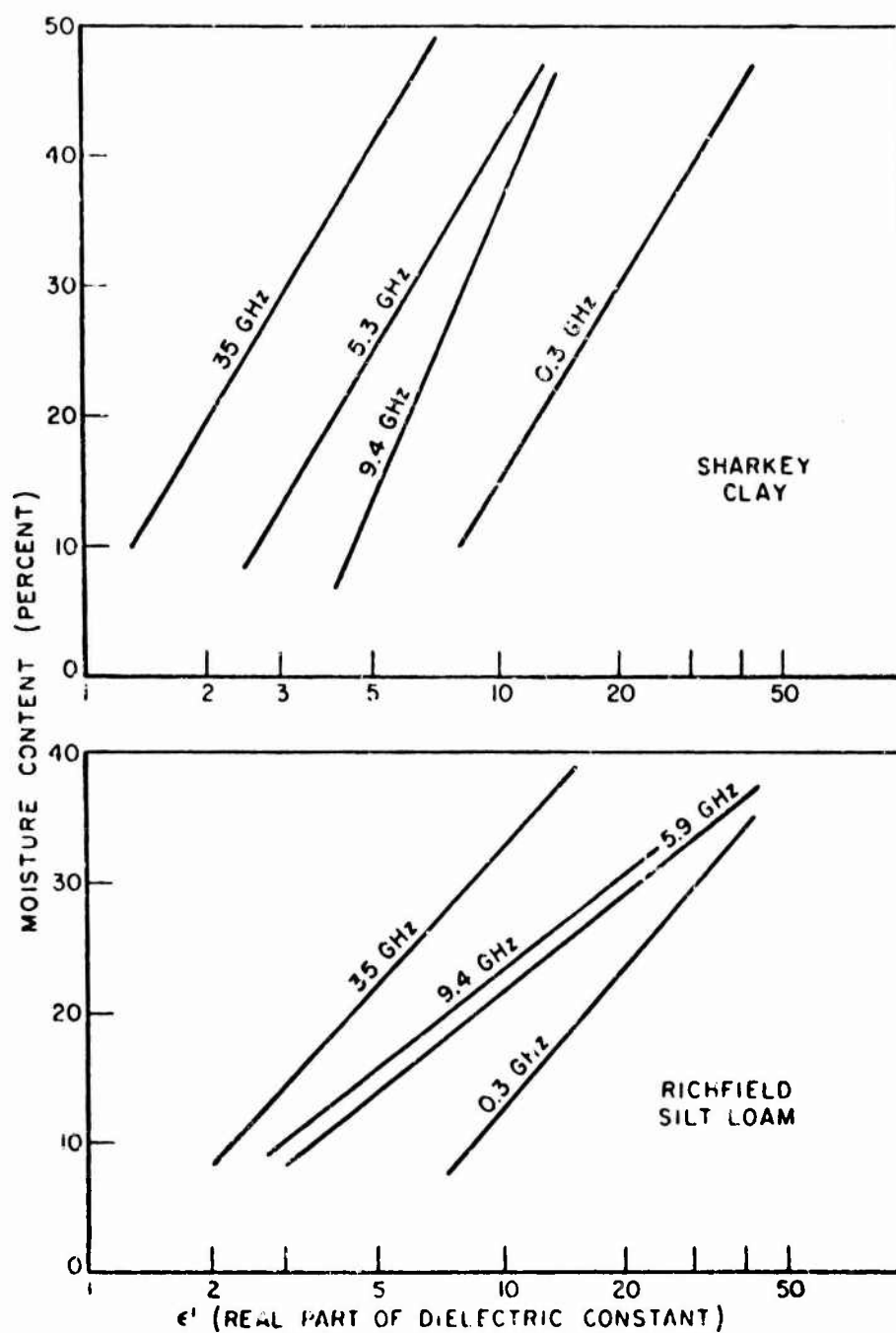


Fig. 10. Dielectric content of soils vs. moisture content. (Ref. 3)

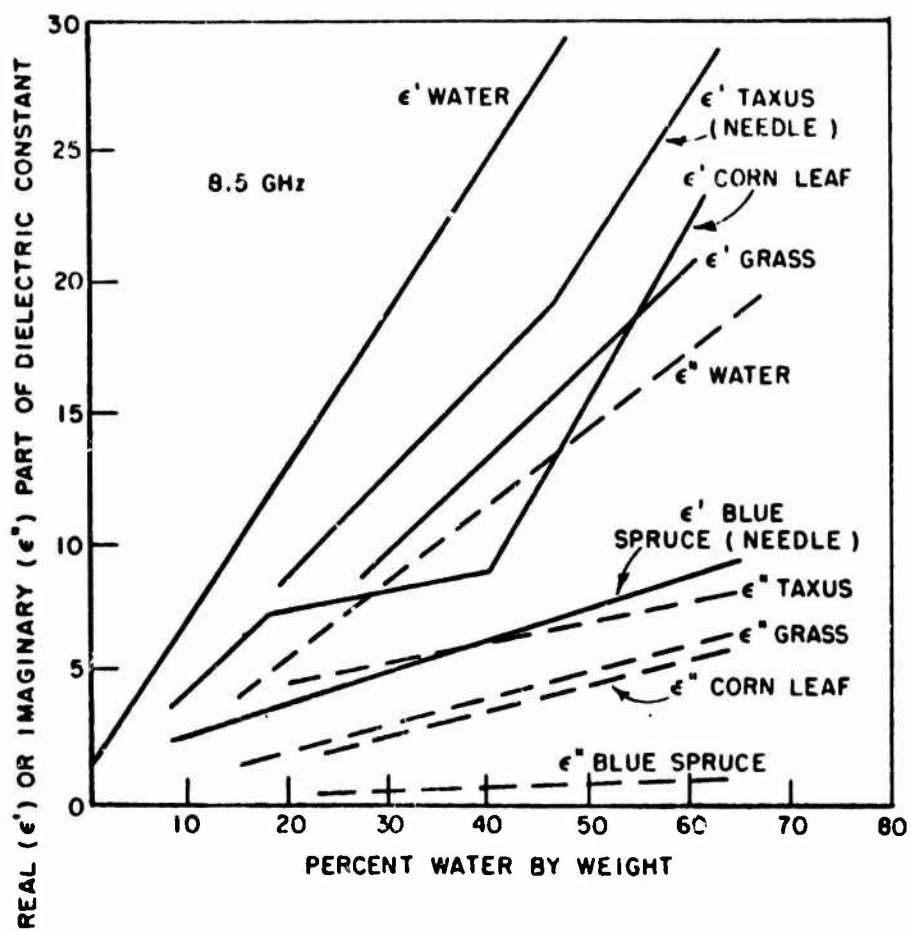


Fig. 11. Relative dielectric constant of vegetation at 8.5 GHz. (Ref. 7)

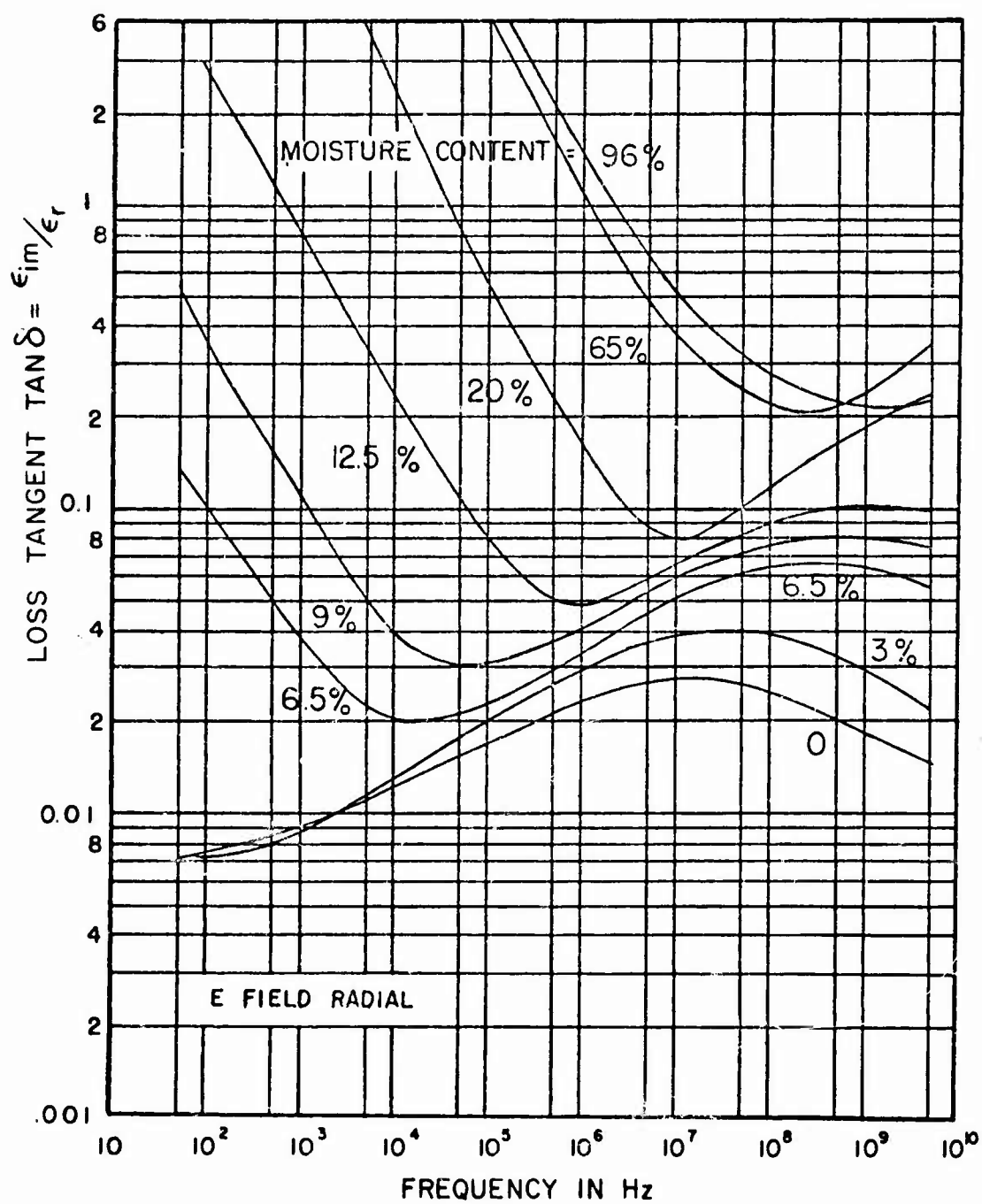


Fig. 12. Loss tangent of fir wood as a function of frequency.
(Ref. 10)

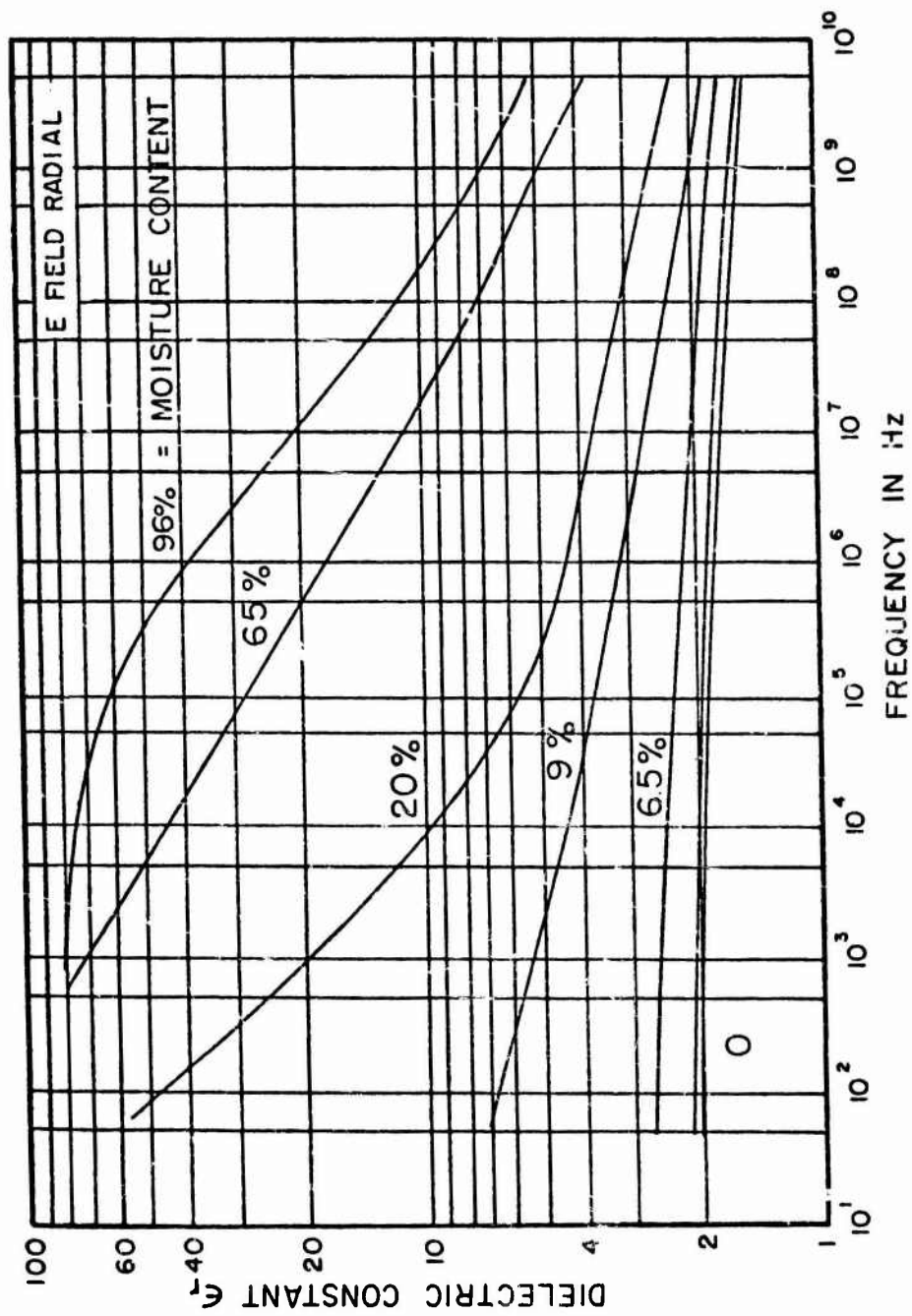


Fig. 13. Dielectric constant of fir wood as a function of frequency.
(Ref. 10)

REFERENCES

1. Hasted, J.B., "The Dielectric Properties of Water" in Advances in Dielectrics, Vol. 3, Wiley, 1961.
2. Iglesias, J. and Westphal, W.B., "Supplementary Dielectric Constant and Loss Measurements," Tech. Report No. 203, Laboratory for Insulation Research, Massachusetts Institute of Technology, January 1967.
3. Lundien, J.R., "Terrain Analysis by Electromagnetic Means," Report 2, (Radar Responses to Laboratory Prepared Soil Samples), Tech. Report No. 3-693, U. S. Army Engineers, Waterways Experiment Station, September 1966.
4. Shaw, J.D. and Barlow, C.A., "Radar Analysis of the Moon-Surface Properties," AFCRL Report 64-74.

M. Brunschwig et. al., "Estimation of the Physical Constants of the Lunar Surface," Report 3544-1-F, Radiation Laboratory, University of Michigan, November 1960.
5. Campbell, M.J. and Ulrichs, J., "Electrical Properties of Rocks and Their Significance for Lunar Radar Observations," Jour. Geo. Research, 74, pp. 5867-5881, 1969.
6. Johnson, C.N. et.al., "Microwave Radiometer Studies in Relation to Mine Detection," Army Engineer Research and Dev. Lab., Ft. Belvoir, RAERDL 1875, November 1966.
7. Carlson, N.L., "Dielectric Constant of Vegetation at 8.5 GHz," Report 1903-5, 31 March 1967, ElectroScience Laboratory, Department of Electrical Engineering, The Ohio State University; prepared under Contract NSR-36-008-027 for National Aeronautics and Space Administration.

8. DeLoor, G.P., The Dielectric Properties of Soils. (Preprint)
9. Du, L.J. and Peake, W.H., "Rayleigh Scattering from Leaves," Proc. IEEE, 57, pp. 1227-1229, 1969.
10. Pounds, D.J. and LaGrone, A.H., "Considering Forest Vegetation as an Imperfect Dielectric Slab," AFCRL Report 63-483, Electrical Engineering Research Laboratory Report 6-53, University of Texas, May 1963.
11. Parkhomenko, E.I., The Electrical Properties of Rocks, Plenum Press, 1967

IV. THEORETICAL MODELS FOR SCATTERING AND EMISSION

A. Introduction

In this section, a number of models for the scattering and emissive properties of natural surfaces are reviewed. Such models provide an insight into the mechanisms which control the scattering from a variety of surface types. Thus, the models can be used to identify the parameters which are likely to affect the microwave behavior of the surface in a significant way. As in section 1, emphasis will be placed on theoretical descriptions which are suitable for computer modelling of the sensor response. Thus, general formulas, or chains of relatively simple formulas, will be given rather than a large number of special forms derived by algebraic manipulation. Wherever possible, theoretical predictions will be compared with measured responses, in order to illustrate the extent to which the models may be useful.

An excellent survey of the theoretical foundations of rough surface scattering is given in the recent review by Barrick, et. al., [1] which supplements the older survey by Beckman and Spizzichino. [2] Many "special case" formulas may be found in these two references.

Before discussing scattering laws in detail, it may be desirable to review briefly some general ideas about the classification of rough surfaces, and the nature of the scattering from the several classes.

In the first place, a surface may be perfectly flat, in which case an incident plane wave is reflected specularly as a plane wave, with a reduced, polarization dependent amplitude given by the well known Fresnel reflection coefficient. If such a plane surface has superimposed on it some small irregularities with their rms deviation from the plane (rms height = h) much less than a wavelength, then the principal scattering is still a coherent, specularly reflected plane wave, but the power density is reduced by a factor

$$|R|^2 \exp[-2(kh \cos \theta_i)^2]$$

where $|R|^2$ is the appropriate Fresnel coefficient and the factor

$$\exp[-2(kh \cos \theta_i)^2]$$

represents the effect of roughness in diminishing the forward scattered energy. The remaining power, (of order of magnitude $|R|^2 2(kh \cos \theta_i)^2$) is scattered incoherently into all directions, i.e., may be considered a diffusely scattered contribution. (See Fig. 14a). There are two points to be made. The first is a distinction, not always observed, between "specular" and "coherent". The specular power leaves the mean surface in the same direction, approximately, as the specularly reflected power from a flat surface. It may or may not be phase coherent with the incident wave. The coherent part of the specular power is phase coherent with the incident wave, that is, if the surface is removed and replaced by another member of an ensemble of such surfaces, the coherently reflected power will have the same amplitude and phase at any point as it did before. The incoherent power will not, in general. The slightly rough surfaces are usually treated by perturbation methods.

The second point to be made is that the factor

$$e^{-2(kh \cos \theta_i)^2}$$

illustrates, in more quantitative form, Rayleigh's criterion for distinguishing between a smooth and a rough surface. We normally say a surface behaves as a smooth (or slightly rough surface), and thus retains an appreciable fraction of coherent power in the scattered beam, if

$$\exp(-2(kh \cos \theta_i)^2) \approx 1, \text{ or } kh \cos \theta_i < 1/4.$$

This transitional behaviour is illustrated in Fig. 40.

The number $1/4$ is quite arbitrary; various authors have chosen different numerical criteria depending on their particular application. It will be observed that near grazing, $\cos \theta \ll 1$, a surface acts more nearly like a smooth surface than that at normal incidence. If, on the other hand ($kh \cos \theta > \sqrt{2}$), one may call the surface rough. Then two limiting situations occur. In the first the surface may be gently undulating, i.e., with radius of curvature much less than λ . In this case (see Fig. 14b) each part of the surface (say over local areas of one or two Fresnel zones) is locally smooth, and, from the point of view of geometrical optics, reflects the incident radiation as if it were a tilted flat surface. The total scattered field is then the sum of the reflections from these locally flat areas, and it seems reasonable (and is correct) to estimate that the scattered power forms a specular beam with a beamwidth approximately equal to the rms slope of the surface. Furthermore, since the scattered field is the sum of many local contributions, it will not be phase coherent with the incident beam. The total power in the specular beam is, again, approximately $|R|^2$ times the power in the incident beam. Surfaces of this type are usually, in practice, treated by physical optics methods.

Finally a surface may have many areas of large slope, vertical or re-entrant walls, etc., as in a layer of crushed rock, or may be made up of many independent scatterers, such as the leaves of vegetation. In this case there is seldom observed any forward lobe in the scattering pattern. The scattering is more or less isotropic, and is referred to as diffuse scattering. This class of surface is most often treated in terms of empirical scattering laws, such as Lambert's law and its generalizations, and the Lommel-Seeliger scattering type laws. (See Figs. 14c and 14d.)

B. The Flat Surface

The simplest "surface" is the perfectly flat surface, i.e., a half-space with complex constitutive parameters ϵ_c and μ_c . The scattering

properties of such a surface depend solely on ϵ_c , μ_c and the illumination pattern of the antenna. Simple as it may appear, even the primitive case of dipole illumination (often referred to as the "Sommerfeld Problem") presents formidable difficulties, and has generated a vast literature. Little of this is relevant to microwave scattering, but there are some important applications to back scattering from the ocean surface at HF and lower frequencies.[3]

For high gain antennas, and geometry not too near grazing, one may consider the flat surface to produce a reflected beam identical to the beam from an antenna at the image position but diminished in amplitude by the appropriate Fresnel coefficient. The reflected field is coherent with the incident field, since replacing a flat surface by another identical one does not change the boundary. (Near grazing, the total field is the sum of the direct and reflected fields; this produces a lobe structure in the fields generated, for example, by ground based radars. Such effects are not considered here.[2]) Although the reflected field intensity falls off as $1/r_s^2$, it is not proportional to the illuminated area, and thus, one cannot define σ_0 for the flat surface. Instead, it is customary to describe the scattered field in terms of an effective reflection coefficient.

While the flat surface does not possess any scattering properties of interest, its radiometric properties constitute one of the standard geometries, and provide an insight into the behaviour of many terrestrial surfaces. The flat surface also affords an opportunity to discuss a number of details concerning polarization states and the geometry of specular reflection. Consider a flat surface with unit normal \vec{n} , specified by the polar angles θ , ϕ , illuminated by a beam along \vec{n}_i (see Fig. 15). Then the direction of the reflected ray is along the unit vector \vec{n}_s , the so called "specular" direction. The relations between these three vectors are given by

$$(1) \quad \vec{n}_s = \vec{n}_i + 2 \cos \alpha \vec{n}$$

$$\vec{n} = (\vec{n}_s - \vec{n}_i) / (2 \cos \alpha)$$

where α is the local angle of incidence

$$(2) \quad \cos \alpha = \vec{n} \cdot \vec{n}_i = \vec{n} \cdot \vec{n}_s$$

$$\cos 2\alpha = \vec{n}_i \cdot \vec{n}_s$$

These relations allow the specular scattering direction \vec{n}_s to be found given \vec{n} , \vec{n}_i etc. If explicit values of θ_s , ϕ_s etc. are required it is only necessary to write out the unit vectors in polar form,

$$\vec{n}_i = -\vec{i}_z \cos \theta_i + \vec{i}_x \sin \theta_i$$

$$(3) \quad \vec{n}_s = i_z \cos \theta_s + i_y \sin \theta_s \sin \phi_s + i_x \sin \theta_s \cos \phi_s$$

$$\vec{n} = i_z \cos \theta + i_y \sin \theta \sin \phi + i_x \sin \theta \cos \phi$$

Thus, one may easily find

$$(4) \quad \cos \theta_s = (\vec{n}_i + 2 \cos \alpha \vec{n}) \cdot i_z$$

$$\sin \phi_s = (\vec{n}_i + 2 \cos \alpha \vec{n}) \cdot i_y / \sin \theta_s$$

etc, with similar formulas for $\cos \theta$, $\sin \phi$ if the term $(\vec{n}_i + 2 \cos \alpha \vec{n})$ is replaced by $(\vec{n}_s - \vec{n}_i) / 2 \cos \alpha$.

Many special forms of these relations may be found in References 1 and 4. Here we note only that when \vec{n} is specified and $\cos \theta_s = 1$ (so that $\sin \theta_s$ is zero) then ϕ_s is indeterminate; it is desirable to set $\phi_s = \pi$ in this case. Similarly when \vec{n}_s is specified and $\cos \theta = 1$ then ϕ is indeterminate; in this case it is desirable to choose $\phi = 0$.

There is one other feature of plane surface reflection of interest in connection with the randomly tilted surface. If the normal \vec{n} is allowed to lie in a small solid angle $d\Omega$, then the reflected ray will lie in a small solid angle $d\Omega_S$. The connection between the two solid angles, i.e., the Jacobian of the transformation between θ, ϕ and θ_S, ϕ_S , is

$$(5) \quad d\Omega_S = 4 \cos \alpha \, d\Omega.$$

To calculate the field strength of the reflected ray, one must know the polarization state of the incident ray with respect to the plane of incidence (i.e., the plane of \vec{n}, \vec{n}_S , and \vec{n}_i). However, the polarization state is often specified in terms of "horizontal" and "vertical" unit vectors (see Fig. 15). These are defined such that $\vec{h}_i = -\vec{i}_y$ and $\vec{v}_i = \vec{n}_i \times \vec{n}$. The "vertical" and "horizontal" unit vectors for the reflected ray are given by $\vec{h}_S = \vec{n}_S \times \vec{i}_z / \sin \theta_S$ (with $\vec{h}_S = -\vec{i}_y$ if $\theta_S = 0$) and $\vec{v}_S = \vec{n}_S \times \vec{n}$. Now any arbitrary incident polarization may be written in the form

$$(6) \quad \vec{p}_i = a_1 \vec{h}_i + a_2 \vec{v}_i$$

where a_1 and a_2 are complex numbers such that $\vec{p}_i \cdot \vec{p}_i^* = 1$. (For example, for linear polarization with the electric field making an angle δ with the "horizontal," $a_1 = \cos \delta$, $a_2 = \sin \delta$; for circular polarization, $a_1 = 1/\sqrt{2}$, $a_2 = \mp j/\sqrt{2}$. The state of polarization \vec{p}_k orthogonal to \vec{p}_i is found from $\vec{p}_i \cdot \vec{p}_k^* = 0$). To calculate the reflected wave, however, the incident polarization \vec{p}_i must be resolved along unit vectors perpendicular ($\vec{s}_i = \vec{n}_i \times \vec{n} / \sin \alpha$ with $\vec{s}_i = -\vec{i}_y$ when $\alpha = 0$) and parallel ($\vec{t}_i = \vec{s}_i \times \vec{n}_i$) to the plane of incidence. If now the incident electric field has the form

$$(7) \quad \vec{E}_{inc} = E_0 \vec{p}_i e^{-jk(\vec{n}_i \cdot \vec{r}) + j\omega t}$$

then the reflected wave will have the form

$$(8) \quad \vec{E}_{\text{refl}} = E_0 \vec{p}_{\text{sp}} e^{-jk(\vec{n}_s \cdot \vec{r}) + j\omega t}$$

where the polarization vector \vec{p}_{sp} of the specular reflected wave is

$$(9) \quad \vec{p}_{\text{sp}} = \{(\vec{p}_i \cdot \vec{s}_i) R_{\perp}(\alpha)\} \vec{s}_s + \{(\vec{p}_i \cdot \vec{t}_i) R_{\parallel}(\alpha)\} \vec{t}_s.$$

Note that \vec{p}_{sp} is not a unit vector, but contains the reflection coefficients; here \vec{s}_s and $\vec{t}_s = \vec{s}_s \times \vec{n}_s$ are the "perpendicular" and "parallel" unit vectors for the plane of incidence defined by the specular direction. The Fresnel coefficients $R_{\perp}(\alpha)$ and $R_{\parallel}(\alpha)$ for perpendicular and parallel polarizations are

$$(10) \quad R_{\perp}(\alpha) = \frac{(\mu_c \cos \alpha - \sqrt{\mu_c \epsilon_c - \sin^2 \alpha})}{(\mu_c \cos \alpha + \sqrt{\mu_c \epsilon_c - \sin^2 \alpha})}$$

$$R_{\parallel}(\alpha) = \frac{\epsilon_c \cos \alpha - \sqrt{\mu_c \epsilon_c - \sin^2 \alpha}}{\epsilon_c \cos \alpha + \sqrt{\mu_c \epsilon_c - \sin^2 \alpha}}$$

The angles η_i, η_s between the "vertical" and "parallel" states for the incident and reflected fields respectively are conveniently found from $\sin \eta_i = \vec{t}_i \cdot \vec{h}_i$ and $\sin \eta_s = \vec{t}_s \cdot \vec{h}_s$.

If the amount of power in a particular polarization state is desired, one may describe the state by $\vec{p}_s = b_1 \vec{h}_s + b_2 \vec{v}_s$ where b_1 and b_2

are two complex numbers (analogous to a_1 and a_2 for the incident polarization state), with $\vec{p}_s \cdot \vec{p}_s^* = 1$; to find the strength of the component \vec{p}_s of the specular reflected field when the incident field is polarized in state \vec{p}_i , one must take the dot product $\vec{p}_{sp} \cdot \vec{p}_s^*$. Thus, one may regard

$$(11) \quad R_{is}(\alpha) = \vec{p}_{sp} \cdot \vec{p}_s^*$$

as the general Fresnel coefficient for reflection from state p_i into state p_s . For example the strength of the vertically polarized component, when the incident field is vertically polarized, is

$$(12a) \quad E_{VV} = \sin \eta_i \sin \eta_s R_L(\alpha) + \cos \eta_i \cos \eta_s R_H(\alpha).$$

Similarly, one can show the left circular polarized (left cp) component of the reflected wave when right cp is incident is given by

$$(12b) \quad E_{RL} = E_0 e^{j(\eta_i + \eta_s)} (R_L(\alpha) - R_H(\alpha))/2.$$

The relations above permit one to compute the amplitude and phase of any component of the reflected field due to any arbitrary incident polarization, if the surface normal is specified. Many convenient special cases are given in References 1 and 4, but for computer evaluation of, say, polarization or angle of incidence effects, a direct sequential computation based on the above chains of formulas and definitions, will often prove more convenient than the use of a single complicated formula.

The emissive properties of a flat surface are as simple as the reflective properties, as long as the incident sky illumination is unpolarized. In this case let the sky radiation incident on the surface from direction $-\vec{n}_s$ (see Fig. 15) have brightness temperature

$T_{sky}(\theta_s, \phi_s)$, where \vec{n}_s is the specular direction appropriate to the surface normal \vec{n} and the viewing direction \vec{n}_i . Then the brightness temperature of the radiation traveling along $-\vec{n}_i$ is

$$(13a) \quad T_s^B(\theta_i) = T_{sky}(\theta_s, \phi_s) |R_{\perp}(\alpha)|^2 + T_g (1 - |R_{\perp}(\alpha)|^2)$$

for the component perpendicular to the local plane of incidence, and

$$(13b) \quad T_t^B(\theta_i) = T_{sky}(\theta_s, \phi_s) |R_{\parallel}(\alpha)|^2 + T_g (1 - |R_{\parallel}(\alpha)|^2)$$

for the component parallel to the plane of incidence, where the direction θ_s, ϕ_s refers to the specular direction defined by \vec{n}_i and \vec{n} . In general, one wishes to know the brightness temperature $T_B(\theta_i)$ that would be received by an ideal antenna of arbitrary polarization state \vec{p}_i (i.e., the antenna as a transmitter would produce an electric field of the form of Eq. (7)). This is found from

$$(14) \quad T_B(\theta_i) = |\vec{e}_i \cdot \vec{p}_i|^2 T_t^B(\theta_i) + |\vec{s}_i \cdot \vec{p}_i|^2 T_s^B(\theta_i).$$

This relatively simple representation of the brightness temperature "received" by an antenna with polarization state \vec{p}_i is only possible because of the assumption that the incident sky radiation is unpolarized (and this is a good assumption at microwave frequencies where the sky radiation is due solely to atmospheric absorption). In the case of partially polarized sky radiation the more general techniques of radio astronomy, [11] utilizing either a Stokes parameter or a coherency matrix description must be used.

The discussion just given for the brightness temperature of a flat surface assumes that the Kinetic temperature T_g of the ground is

uniform down to a distance of several skin depths. If the Kinetic temperature is not uniform, but is given by $T(z)$ ($z < 0$) as a function of depth below the surface, and if the power attenuation coefficient $a(z)$ (i.e., $a(z) = -2 \operatorname{Im} [\omega^2 \mu_0 \epsilon_0 \epsilon_c]^{1/2}$) is also a function of depth, then the Kinetic temperature T_g above must be replaced by

$$(15) \quad T_{\text{eff}} = \int_{-\infty}^0 T_g(z) a(z) e^{-\int_z^0 a(\xi) d\xi / \cos \theta_r} dz / \cos \theta_r$$

where θ_r is the angle of refraction, i.e., the angle such that $\sin \theta_r = \sin \theta_i / \operatorname{Re}(\epsilon_c^{1/2})$.

The next order of complexity in the flat surface is the surface composed of uniform layers (see Fig. 16). Here the cw scattering properties are the same as for a half space, i.e., the beam is reflected coherently as if emanating from the image point; the reflection coefficient must be computed for the layered structure (see below). The brightness temperature, however, particularly when the layers are taken to be at different, (but uniform) temperature must be computed by summing the contributions from each layer. This can most easily be accomplished by the use of a reciprocity principal. This asserts that if a plane wave is incident on the surface from direction θ_i and if a fraction f of the total incident power is absorbed in a certain layer at a Kinetic or "thermometer" temperature T , then the contribution of that layer to the total brightness temperature of the radiation leaving the surface in the direction θ_i is fT . To implement this computation, and to determine the required reflection coefficients, an iterative procedure introduced by Richmond[5] has been found convenient. Consider the location of the N layers to be specified by their upper surfaces, $z_0 = 0$ (the bottom "layer" extending to $z = -\infty$), $z_1, z_2 \dots z_N$. Each layer has thickness d_n and uniform Kinetic temperature T_n , with the boundary between the surface and the atmosphere being at

$$z_N = \sum_{n=1}^N d_n.$$

Consider now a plane wave incident from the direction θ_i , i.e., along $+\vec{n}_i$. It will have a reflection coefficient $R(\theta_i)$ and will set up a combination of downward and upward waves in each layer. Considering first the "horizontal" or "perpendicular" or "TE" polarization the incident wave would be given by

$$(16) \quad \vec{E}_{inc} = A_H \vec{i}_x \exp(jky \sin \theta_i + jkz \cos \theta_i)$$

where A_H is an incident electric field strength. In each layer the appropriate fields may then be written (e.g., for the layer whose upper surface is z_n)

$$(17) \quad \begin{aligned} E_n^x &= (A_n e^{\gamma_n z} + B_n e^{-\gamma_n z}) e^{jky \sin \theta_i} \\ H_n^y &= (-\gamma_n / jk Z_0 \mu_n) (A_n e^{\gamma_n z} - B_n e^{-\gamma_n z}) e^{jky \sin \theta_i} \end{aligned}$$

where $Z_0 = (\mu_0 / \epsilon_0)^{1/2}$; ϵ_n , μ_n are the relative electric and magnetic permittivities of the n th layer, and the complex propagation constant is given by

$$(18) \quad \gamma_n = jk (\mu_n \epsilon_n - \sin^2 \theta_i)^{1/2}.$$

By enforcing the boundary conditions, one finds[5] that the coefficients for the $n+1^{st}$ layer can be found from those of the layer below it,

$$(19) \quad \begin{aligned} A_{n+1} &= P_n A_n + Q_n B_n \\ B_{n+1} &= R_n A_n + S_n B_n \end{aligned}$$

where

$$(20) \quad \begin{aligned} P_n &= (\frac{1}{2})(1 + \rho_n) \exp((\gamma_n - \gamma_{n+1})z_n) \\ Q_n &= (\frac{1}{2})(1 - \rho_n) \exp((- \gamma_n - \gamma_{n+1})z) \\ R_n &= (\frac{1}{2})(1 - \rho_n) \exp((\gamma_n + \gamma_{n+1})z) \\ S_n &= (\frac{1}{2})(1 + \rho_n) \exp((- \gamma_n + \gamma_{n+1})z) \\ \rho_n &= (\mu_{n+1} \gamma_n) / (\mu_n \gamma_{n+1}). \end{aligned}$$

An iterative solution for the relative field strength is easily found by setting $A_0 = 1$, $B_0 = 0$ (no upward wave in the lower halfspace $z < 0$; if the bottom most layer is a perfect conductor, however, one should put $B_0 = -1$). Since the incident electric field strength is A_{N+1} and the reflected field strength is B_{N+1} , the power reflection coefficient is

$$(21) \quad |R(\theta_i)|^2 = |B_{N+1}/A_{N+1}|^2.$$

The next problem is the determination of f_n , the fraction of the incident power density dissipated or absorbed in the n th layer. This is seen to be, for $0 < n < N$,

$$(22) \quad f_n = (P_n - P_{n-1})/P_{inc}$$

where

$$P_n = \text{Re} \left[-E_n^x H_n^{y*} \right]_{z=z_n}$$

$$P_{\text{inc}} = A_{N+1} \cdot A_{N+1}^* / Z_0$$

and one must define P_{-1} to be $P_{-1} = 0$. If now the sky brightness is given by $T_{\text{sky}}(\theta_i)$ then the total brightness temperature of the surface is given by

$$(23) \quad T_b(\theta_i) = T_s(\theta_i) |R(\theta_i)|^2 + \sum_0^N f_n T_n.$$

Since all the energy not reflected is absorbed, we must also have

$$\sum_0^N f_n = 1 - |R|^2.$$

This produces the standard result when all layers are at the same temperature. For the case of "parallel", "vertical" or "TM" polarization, the results are identical except that now the fields are found from an assumed incident magnetic field

$$(24) \quad \vec{H}_{\text{inc}} = A_v \vec{T}_x \exp(jky \sin \theta_i + jkz \cos \theta_i)$$

with the layer fields given by

$$(25) \quad \begin{aligned} H_n^x &= (A_n e^{\gamma_n z} + B_n e^{-\gamma_n z}) e^{jky \sin \theta_i} \\ E_n^y &= + (\gamma_n Z_0 / jk\epsilon_n) (A_n e^{\gamma_n z} - B_n e^{-\gamma_n z}) e^{jky \sin \theta_i} \end{aligned}$$

with

$$\rho_n = (\epsilon_{n+1} \gamma_n) / (\epsilon_n \gamma_{n+1})$$

$$(26) \quad P_{inc} = A_{N+1} A_{N+1}^* Z_0$$

$$P_n = \text{Re} [E_n^y H_n^{x*}]$$

The expressions for $R(\theta_i)$, $T_b(\theta_i)$ etc. are identical to the TE case. Attempts to find closed form expressions for the brightness lead to formulas of great complexity, even for the simple case of two layers. However, by computing the fields layer by layer upward from the infinite half space representing the deepest layer, it is a relatively simple matter to find the actual brightness temperature for any given distribution of layers. One interesting case which has received some attention in the literature[12] is the brightness temperature of a layer of ice forming over a water surface. Here oscillations in brightness of over 100°K were observed due to the oscillations in reflection coefficient of the layered structure.

C. The Slightly Rough Surface

The slightly rough surface is one for which the surface height $z(x,y)$ above the mean surface satisfies the condition $z(x,y)/\lambda \ll 1$; $\partial z/\partial x \ll 1$; $\partial z/\partial y \ll 1$. That is, the surface height is every where significantly less than a wavelength and the surface slopes are not too large. If these conditions are satisfied, the scattering can be found by a perturbation method described by S.O. Rice.[13] The first order bistatic coefficients for such a surface have been worked out in detail by Barrick;[1] the second order coefficients have been obtained by Valenzuela[6] for the backscattering case.

The general feature of the scattering from such a surface is that there is a specular (and also coherent) reflection process identical to that occurring from a perfectly flat surface (see Fig. 14a) but

diminished in amplitude by a factor of order $\exp(-2(kh \cos \theta_i)^2)$ where h is the rms surface roughness, and thus provides one criterion for judging whether the surface may be considered "slightly rough".

The bistatic coefficients are given by[1]

$$(27) \quad \sigma_{ij}^0(\theta_i, \theta_s, \phi_s) = k^4 h^2 \cos^2 \theta_i \cos^2 \theta_s |\alpha_{ij}|^2 I \\ = \pi^2 k^4 \cos^2 \theta_i \cos^2 \theta_s |\alpha_{ij}|^2 W$$

where

$$k = 2\pi/\lambda$$

$$h^2 = \text{mean square surface roughness} = \langle \zeta^2 \rangle$$

$$I = 2\pi \int_0^\infty r(r) J_0(rk \sqrt{\xi_x^2 + \xi_y^2}) dr$$

$$I = (\pi^2/h^2) W(k \sqrt{\xi_x^2 + \xi_y^2})$$

$$\xi_x = \sin \theta_i - \sin \theta_s \cos \phi_s \quad (2 \sin \theta_i \text{ for backscatter})$$

$$\xi_y = \sin \theta_s \sin \phi_s \quad (0 \text{ for backscatter})$$

Here $\rho(r)$ is the correlation function for the surface height

$$(28) \quad \rho(r) = \langle \zeta(x,y) \zeta(x',y') \rangle / h^2 \\ r = \sqrt{(x-x')^2 + (y-y')^2}$$

and W , the Hankel transform of ρ , is the roughness spectral density. The matrix elements α_{ij} which connect the polarization states of the incident and scattered waves are given in the general case in Reference 1. For the simpler case $\mu_c = 1$ (i.e., a non magnetic surface) they are

$$\begin{aligned}
\alpha_{hh} &= \frac{(\epsilon_c - 1) \cos \phi_s}{(\cos \theta_i + \sqrt{\epsilon_c - \sin^2 \theta_i}) (\cos \theta_s + \sqrt{\epsilon_c - \sin^2 \theta_s})} \\
\alpha_{vh} &= \frac{-\sin \phi_s (\epsilon_c - 1) \sqrt{\epsilon_c - \sin^2 \theta_s}}{(\cos \theta_i + \sqrt{\epsilon_c - \sin^2 \theta_i}) (\epsilon_c \cos \theta_s + \sqrt{\epsilon_c - \sin^2 \theta_s})} \\
(29) \quad \alpha_{hv} &= \frac{\sin \phi_s (\epsilon_c - 1) \sqrt{\epsilon_c - \sin^2 \theta_i}}{(\epsilon_c \cos \theta_i + \sqrt{\epsilon_c - \sin^2 \theta_i}) (\cos \theta_s + \sqrt{\epsilon_c - \sin^2 \theta_s})} \\
\alpha_{vv} &= \frac{(\epsilon_c - 1) [(\epsilon_c \sin \theta_i \sin \theta_s - \cos \phi_s \sqrt{\epsilon_c - \sin^2 \theta_i} \sqrt{\epsilon_c - \sin^2 \theta_s})]}{(\epsilon_c \cos \theta_i + \sqrt{\epsilon_c - \sin^2 \theta_i}) (\epsilon_c \cos \theta_s + \sqrt{\epsilon_c - \sin^2 \theta_s})}
\end{aligned}$$

A very large number of special cases of these formulas, including those for perfect conductors ($\epsilon_c \rightarrow \infty$), for circular and tilted linear polarizations, for particular types of correlation functions etc. are given in Reference 1, together with many numerical examples. Here we mention only two of these special cases. First, for circular polarization states L (left circular) and R (right circular) the matrix elements become

$$\begin{aligned}
\alpha_{LL} &= \frac{1}{2} [(\alpha_{hh} - \alpha_{vv}) \pm j (\alpha_{hv} + \alpha_{vh})] \\
RR \\
(30) \quad \alpha_{LR} &= \frac{1}{2} [(\alpha_{hh} + \alpha_{vv}) \mp j (\alpha_{hv} - \alpha_{vh})]
\end{aligned}$$

For linear polarization states $\vec{p}_i = \vec{h}_i \sin \beta_i - \vec{v}_i \cos \beta_i$ and $\vec{p}_s = \vec{h}_s \sin \beta_s - \vec{v}_s \cos \beta_s$ we have for the "direct" polarized return $\beta_s = \beta_i$

$$(31a) \quad \alpha_{\beta_i \beta_i} = \alpha_{vv} \cos^2 \beta_i + \alpha_{hh} \sin^2 \beta_i$$

and for the "cross"-polarized return $\beta_s = \beta_i + \pi/2$

$$(31b) \quad \alpha_{\beta_i \beta_i + \pi/2} = -(\alpha_{vv} - \alpha_{hh}) \sin \beta_i \cos \beta_i.$$

The scattering in any direction for the slightly rough surface is proportional to the power spectral density of the surface height appropriate to the wave numbers k_{ξ_x} , k_{ξ_y} . These correspond to the Bragg condition for scattering from a periodic lattice and for this reason, particularly in the literature on sea return, such scattering is referred to as Bragg scatter.

There have been two useful applications of the slightly rough surface. The first[7] is to surfaces such as asphalt or concrete runways or roadways, which clearly satisfy the conditions of the theory at microwave frequencies. Here if the surface is known to be slightly rough, then one may estimate the roughness h^2 from the backscattering coefficient; the dielectric constant ϵ_c can be estimated from the difference between the backscattering coefficients for vertical and horizontal polarization (see Figs. 37 and 38 of Chapter V). The second application is to the sea surface,[3,8,9] where the capillary waves at the lower microwave frequencies,[9] and the entire surface at H.F. and lower frequencies satisfy the conditions of the model.

The radiometric properties of the slightly rough surface are essentially the same as those of a flat surface, due to the predominant effect of the coherent reflection process. If the corrections due to

the small scale roughness is required one must compute the brightness in two parts. The first is the "specular" contribution identical to that for a flat surface as given by Eq. (13), but with the Fresnel coefficients $|R|^2$ multiplied by an additional factor F to account for the loss of energy due to the diffuse scatter. This factor is of order $\exp(-2(kh \cos \theta_i)^2)$ but must be computed by subtracting the total power diffusely scattered into the upper hemisphere, i.e., the factor is, for vertical polarization

$$(32) \quad F_v = 1 - (4\pi \cos \theta_i)^{-1} \int_{\text{hemisphere}} [\sigma_{vv}(\theta_i, \theta_s, \phi_s) + \sigma_{vh}(\theta_i, \theta_s, \phi_s)] d\Omega_s$$

with a corresponding expression (interchange v and h) for horizontal polarization. To this must be added the "diffuse" contribution,

$$(33) \quad \Delta T_d^v(\theta_i) = (1 - F_v) T_g + (4\pi \cos \theta_i)^{-1} \int (\sigma_{vv} + \sigma_{vh}) T_{sky}(\theta_s, \phi_s) d\Omega_s$$

in accordance with Eq. (14) of Chapter II. Thus, for example, a flat surface with normal \vec{n} in the z -direction will have a brightness

$$\gamma_v^B(\theta_i) = T_{sky}(\theta_{sp}) F_r |R_v|^2 + T_g (1 - F_v |R_v|^2) + \Delta T_d^v(\theta_i)$$

where

$$R_v = R_{||}(\theta_i).$$

The spectrum of the power scattered by a slightly rough surface has been derived by Barrick[14] and Valenzuela.[15] For the back-scattering case, the spectrum for the "natural line width", due to motion of the

surface, may be expressed[14] in terms of a radar cross-section per unit area per unit bandwidth, $\sigma_0(f)$ such that the standard cross-section is given by

$$\sigma_0 = \int_{-\infty}^{\infty} \sigma_0(f) df.$$

Here

$$(34) \quad \sigma_0(f) = 4\pi k^4 \cos^4 \theta_i \left| \alpha_{ij} \right|^2 W_T(-2k \sin \theta_i, 0, 2\pi(f - f_0))$$

where f_0 is the transmitter frequency and the joint spatial, frequency spectrum W_T is given by

$$(35) \quad W_T(p, q, \omega) = (h^2/\pi^2) \int_{-\infty}^{\infty} \int_{-\infty}^{\infty} \int_{-\infty}^{\infty} R_1(\Delta x, \Delta y, \Delta t) e^{-jp\Delta x - jq\Delta y - j\omega\Delta t} d(\Delta x) d(\Delta y) d(\Delta t)$$

where

$$(36) \quad h^2 R_1(\Delta x, \Delta y, \Delta t) = \langle \zeta(x, y, t) \zeta(x+\Delta x, y+\Delta y, t+\Delta t) \rangle$$

and $\zeta(x, y, t)$ is the surface height as a function of x, y and t . The exact form of the correlation function R_1 depends on the dynamic processes controlling the structure of the surface. If one assumes, for example, a gaussian height and time correlation,

$$R_1 = \exp(-\Delta x^2/\ell^2 - \Delta y^2/\ell^2 - \Delta t^2/T^2)$$

where ℓ and T are the correlation length and correlation time respectively, then $\sigma_0(t)$ becomes[14]

$$(37) \quad \sigma_0(f) = \sigma_0(\theta_i) T \sqrt{\pi} e^{-\pi^2 T^2 f^2}$$

where $\sigma_0(\theta_i)$ is the conventional back scattering coefficient. The reason for referring to the spectrum due to surface motion as the natural line width is now apparent. The bandwidth (in this case) does not depend on the transmitter frequency, but only on the correlation time T . For example, for the capillary scattering of microwaves by the ocean, where $T \sim 1/5$ sec, the bandwidth is of order 2.5 Hz. For the HF range where the scatter is due to the entire structure of the ocean surface T is considerably longer (of the order of several seconds) and the bandwidth correspondingly narrower, viz a few tenths of a Hertz.

D. The Rough Continuous Surface - Physical Optics Models

When the surface is of the gently undulating type, of continuous structure with radius of curvature everywhere several times larger than an electromagnetic wavelength, the scattering may be computed by physical optics methods. With the possible exception of the sand dunes in certain barren desert areas, no known natural surface satisfies the conditions of this model at microwave frequencies, although the surface of the sea might be considered an appropriate one at optical frequencies. Nevertheless an enormous amount of theoretical work has been devoted to this model. A recent review is given in Reference [15]. Although the formulation of such theories has taken many different forms, it can be shown[15] that, at least insofar as the average scattered power is concerned, the scattering mechanism is equivalent to geometrical reflection from the specular points of the surface (see Fig. 14b). Thus the cross-section σ_0 can be found by determining the average number and radii of curvature of the specular points from the statistical properties of the surface, or even more directly from the statistical distribution of surface slopes, since at each specular point the slope must be

appropriate for specular reflection into the specified scattering direction. The bistatic cross-section is found to be

$$(38) \quad \sigma_{ij}^0(\theta_i, \theta_s, \phi_s) = \pi \sec \theta_i \left| R_{is}(\alpha) \right|^2 p(\theta, \phi) \\ = \pi \sec^4 \theta_i \left| R_{is}(\alpha) \right|^2 p(\zeta_x, \zeta_y)$$

where

$$p(\theta, \phi) \sin \theta \, d\theta \, d\phi = \text{probability that surface normal } \vec{n} \text{ lies} \\ \text{in } d\Omega = \sin \theta \, d\theta \, d\phi \\ \zeta(x, y) = \text{surface height} \\ p(\zeta_x, \zeta_y) \, d\zeta_x \, d\zeta_y = \text{joint probability that surface slopes } \zeta_x, \\ \zeta_y \text{ lie in } d\zeta_x \, d\zeta_y \\ \vec{n} = (\vec{i}_z - \vec{i}_x \zeta_x - \vec{i}_y \zeta_y) / (1 + \zeta_x^2 + \zeta_y^2)^{1/2} \\ R_{is}(\alpha) = \text{Fresnel coefficient for states } i, s. \\ \alpha = \text{local angle of incidence defined by } \theta_i, \theta_s.$$

In evaluating the probabilities above, the angles θ, ϕ for the surface normal, or ζ_x, ζ_y for the surface slopes are to be chosen such that \vec{n} corresponds to a direction which reflects specularly into the desired scattering direction θ_s, ϕ_s . The appropriate relations between \vec{n} and \vec{n}_s and the local angle of incidence α , are given in Eqs. (1)-(4). Similarly the appropriate Fresnel coefficient for scattering from a state \vec{p}_i into a polarization state \vec{p}_s is given by Eq. (11).

From the scattering cross-section of the physical optics surface, one can estimate the dielectric constant and the distribution of surface slopes. It is customary to assume particular forms for $p(\theta, \phi)$ or $p(\zeta_x, \zeta_y)$; a large number of special cases (gaussian, exponential,

etc.) are given in References 1 and 15. For example, for backscattering, where $\alpha = 0$, $\zeta_x = \tan \theta_i$, $\zeta_y = 0$, the direct polarized return is

$$(39) \quad \sigma_{ii}^0 = \sigma_{hh}^0 = \sigma_{vv}^0 = \sigma_{RL}^0 = [3 \sec^4 \theta_i / S^2] |R_{\perp}(0)|^2 \exp(-\sqrt{6} \tan \theta_i / S)$$

for the exponential, and

$$(40) \quad \sigma_{ii}^0 = [\sec^4 \theta_i / S^2] |R_{\perp}(0)|^2 \exp[-\tan^2 \theta_i / S^2]$$

for the gaussian slope distribution models. Here S^2 is the mean square surface slope. These two cases are plotted in Fig. 17.

The radiometric properties of the physical optics model have been worked out in detail by Stogryn,[16] who has given a number of examples of application of the model to the sea surface.[17] Since the bistatic coefficients are known, for any given slope probability distribution, it is only necessary to substitute the expression Eq. (38) into the general result (Eq. (15) of Chapter II.). Thus, if the effects of the atmosphere between the surface and ground are ignored, one has

$$(41) \quad T_b^j(\theta_i) = \epsilon_j(\theta_i) T_g + \int [|R_{jj}(\alpha)|^2 + R_{jk}(\alpha)^2] \pi \sec \theta_i p(\theta, \phi) d\Omega_s / (4\pi \cos \theta_i)$$

$$\epsilon_j(\theta_i) = 1 - \int [|R_{jj}(\alpha)|^2 + R_{jk}(\alpha)^2] \pi \sec \theta_i p(\theta, \phi) d\Omega_s / (4\pi \cos \theta_i)$$

where for each point $d\Omega_s$ in the integration, α , θ and ϕ must be found from Eqs. (1)-(4); here state j is the desired or receiver polarization, and k is the orthogonal polarization state, with R_{jj} , R_{jk} from Eq. (11). The evaluation of these formulas is straight forward but computationally tedious. Examples are given in Reference 17. The results, especially for vertical polarization, are very similar to the brightness temperatures for a flat surface. The model appears to predict the brightness temperatures of the ocean at microwave frequencies fairly well as long as no significant part of the ocean surface is foam covered. (See Fig. 171b.)

The spectrum of the signal scattered by the physical optics surface, $\sigma_0(f)$, depends on the motion of the specular points as the surface changes shape, and is given by [14] for backscattering,

$$(42) \quad \sigma_0(f) = \pi \sec^4 \theta_i |R(0)|^2 \left[\frac{\sec \theta_i}{4\pi} \lambda \right] p \left(\tan \theta_i, 0, \frac{(f - f_0) c}{2 \cos \theta_i f_0} \right)$$

where here $p(\zeta_x, \zeta_y, \zeta_t)$ is the joint probability density function for the surface slopes ζ_x, ζ_y and the surface vertical velocity ζ_t ($\zeta_t = \partial \zeta / \partial t$); that is $p(\zeta_x, \zeta_y, \zeta_t) d\zeta_x d\zeta_y d\zeta_t$ is the joint probability that the slopes lie in $d\zeta_x d\zeta_y$, and the vertical velocity ζ_t of the surface lies in $d\zeta_t$.

E. The Composite Surface

The very restricted conditions under which one may use the slightly rough surface and the physical optics models have led to the development [15,18] of the composite model, in which the total surface height $\zeta(x,y)$ is considered to be the sum of two independent random processes $u(x,y)$ and $s(x,y)$, i.e.,

$$\zeta(x,y) = u(x,y) + s(x,y).$$

Here $u(x,y)$, called the large scale component, satisfies the conditions for the physical optics model (radius of curvature $\gg \lambda$). Superimposed on this large scale structure is a small scale structure $s(x,y)$ which, relative to the local surface specified by $u(x,y)$, satisfies the conditions of the slightly rough surface model, i.e., slopes $\partial s/\partial x$, $\partial s/\partial y$ and normalized height s/λ all $\ll 1$. In the case of the sea at microwave frequencies, the "sea" and "swell" components of the wave spectrum would constitute the large scale process, and the capillary waves or ripples would constitute the small scale process. A satisfactory solution for the scattering from such a surface is quite difficult, but to a first approximation, it is usually [1] assumed that the total cross section for the composite model is the sum of two parts,

$$(43) \quad \sigma^0(\theta_i, \theta_s, \phi_s) = \sigma_{sp}^0(\theta_i, \theta_s, \phi_s) + \langle \sigma_d^0(\theta_i, \theta_s, \phi_s) \rangle$$

where

σ_{sp}^0 = scattering cross section for $u(x,y)$ process alone, computed from Eq. (38)

$\langle \sigma_d^0 \rangle$ = scattering cross-section for $s(x,y)$ process computed from Eq. (27) in a co-ordinate system referred to local normal of $u(x,y)$ process, and then averaged over the distribution of normals specified by the large scale process.

The process of averaging over the slope distribution must be carried out numerically. For this purpose, one chooses an incident angle θ_i and a normal \vec{n} . The incident wave must now be resolved into parallel and perpendicular components in the local surface co-ordinate system defined by the local normal, and the vector perpendicular to

the local plane of incidence, (i.e., the unit vectors \vec{n} , \vec{s}_i , \vec{t}_i in Fig. 15). Now the local angle of incidence α and the local polarization state (determined by the angle η_i in Fig. 15 for linear incident polarization states) may be found from Eqs. (1-4) and (6). The local scattering angles θ'_S , ϕ'_S are then found from $\cos\theta'_S = \vec{n}_S \cdot \vec{n}$, and $\tan\phi'_S = -\vec{n}_S \cdot \vec{s}_i / (\vec{n}_S \cdot \vec{t}_i)$. These angles θ'_S , ϕ'_S can now be substituted into Eqs. (27) and (29) to compute the contribution of the slightly rough component to scattering from \vec{n}_i into \vec{n}_S direction, when the slightly rough surface is tilted at an angle specified by the given \vec{n} . The average over the slope distribution is then carried out according to

$$(44) \quad \langle \sigma_{ij}(\theta_i, \theta_S, \phi_S) \rangle = \int \sigma_0(\theta_i, \theta'_S, \phi'_S) p(\vec{n}) d\Omega$$

where

$p(\vec{n})d\Omega$ = probability that the normal \vec{n} of the $u(xy)$ process lies in solid angle $d\Omega$.

If the mean square slope S^2 of the $u(xy)$ process is not too large, the diffuse contribution for the direct polarized components $\langle \sigma_{vv}^0 \rangle$, $\langle \sigma_{hh}^0 \rangle$ are nearly the same as the unaveraged values, except for horizontal polarization near grazing incidence, where the unaveraged cross-section decreases much more rapidly than the averaged $\langle \sigma_{hh} \rangle$.

The principal difference for the composite model is the existence of a cross-polarized term $\langle \sigma_{hv} \rangle$ in the backscattering direction, as a consequence of the fact that the incident polarization is no longer perpendicular to the local plane of incidence. Thus, for backscattering, for example

$$(45) \quad \langle \sigma_{hv}^0(\theta_i) \rangle \simeq 4\pi k^4 \langle |\alpha_{vv}(\alpha) - \alpha_{hh}(\alpha)|^2 \sin^2 \eta_i \cos^2 \eta_i \rangle W(-2k \sin \theta_i, 0).$$

Although the average is difficult to evaluate, one can illustrate the order of magnitude of the cross-polarized term by assuming the large scale process has a gaussian slope distribution with mean square slope S^2 . In this case

$$(46) \quad \langle \sigma_{hv}(\theta_i) \rangle \simeq 2\pi S^2 k^4 \cos^4 \theta_i \operatorname{cosec}^2 \theta_i |\alpha_{vv}(\theta_i) - \alpha_{hh}(\theta_i)|^2 W(-2k \sin \theta_i, 0).$$

The only significant application of the composite model has been to scattering of microwaves by the ocean.[8,9] In this case certain properties of the ocean surface height spectrum permit an explanation of a number of features of the back-scattering behavior, in particular, (i) the weak dependence on wavelength (because the wave number dependence of the surface height spectrum $W(k) \sim k^{-4}$ approximately "cancels" the k^4 dependence in Eq. (29)); (ii) the weak dependence on wind velocity at angles away from normal (because the ocean surface spectrum $W(k)$ tends to become saturated at moderate wind velocities for those larger wave numbers which control the microwave scattering); (iii) the difference between the horizontal and vertical direct polarized returns (because α_{hh} and α_{vv} differ in the off normal direction); (iv) the upwind/downwind/crosswind ratios (due to the asymmetric distribution of the slopes of the large scale component); (v) the power spectral density of the return signal. Other features, such as the return from near grazing angles, and certain features of the cross-polarized return, are, however, not well explained by the composite model.

F. The Lambert Model

Because of the relative simplicity of the model surfaces described in the preceding section, they have attracted the attention of theoreticians to an extent that is quite out of proportion to their possible application to terrestrial surfaces. Few natural surfaces can be conceptualized as continuous Gaussian random processes, and most must be treated by quite different kinds of models. One useful group of models are those based on empirical scattering laws, of which the best known is the "Lambert" law, with bistatic cross-section given by

$$(47) \sigma_{ij}(\theta_i, \theta_s, \phi_s) = r \cos\theta_i \cos\theta_s$$

$$\sigma_{ij}(\theta_i) = r \cos^2\theta_i \text{ (backscatter)}$$

where r is a constant. For the Lambert surface, the scattered energy is considered to be completely depolarized by the scattering process. For a completely reflecting Lambert surface, (i.e., a surface with albedo of unity) the constant r has a value of $r = 2$, since the total scattered power must be summed over both polarizations. For terrain surfaces the parameter r can be estimated from the back-scattering cross-section.

The type of surface likely to exhibit Lambert behavior at microwave frequencies is one which is highly re-entrant with large openings and many reflecting planes, for example a surface composed of large blocks of pumice (see Fig. 34). Because most of the surface structure is large in terms of wavelength, the typical Lambert surface should have scattering behavior almost independent of wavelength. The emissive properties of the Lambert surface are independent of viewing angle, i.e., the surface acts like a grey body. Backscattering and brightness temperature for a typical Lambert surface is shown in Figs. 50 and 61.

There are a number of other empirical scattering laws which have been proposed, several of the more useful of which are illustrated in Table I. This table also gives the albedo and emissivity for each law. Other examples of empirical scattering laws, mainly of theoretical interest, are given in Ref. 1.

G. Scattering by Individual Elements
(Lommel-Seeliger Scattering)

The second characteristic type of diffusely scattering surface is that composed of a number of individual scatterers disposed in either a surface or a volume distribution. The theoretical approach to this type of scattering is via the scattering functions for the individual particles, which are then used to compute the total scattering from the distribution of particles. Various levels of complexity in the resulting formulas then depend on the extent to which multiple scattering effects are considered and the probability distribution assumed for the particle orientations. Two rather detailed models of this type have been proposed to represent the scattering from vegetated surfaces at microwave frequencies. The first is appropriate to scattering from such linear vegetation as wheat, oats, sudan grass etc, where the individual elements may be approximated by a surface distribution of thin cylinders, which can be assumed to be much less than a wavelength in diameter. In this case the bistatic scattering cross section is given by formulas of the type[1,7]

$$(48) \quad \sigma_{ij}(\theta_i, \theta_s, \phi_s) = \frac{f_{ij} (AN)(AK^2) |\epsilon_c - 1|^2}{28\pi[3(\alpha/K)^2 + 3(\cos\theta_i + \cos\theta_s)^2 + (\sin^2\theta_i + \sin^2\theta_s - 2\sin\theta_i \sin\theta_s \cos\phi_s)]}$$

where ϵ_c = relative complex dielectric constant of the cylinder material
 A = cross-sectional area of each cylinder
 N = number of cylinders per unit surface area
 $K = 2\pi/\lambda$.
 α from Eq. 50

The polarization functions f_{ij} are factors of order unity which depend on the scattering and incidence angles, and the parameter

$$t = 2/(1 + \operatorname{Re}(\epsilon_c)).$$

For material of large dielectric constant, t is small, and the polarization factors are approximately

$$\begin{aligned} f_{hh} &= (3 - 2 \sin^2 \phi_s) \\ f_{vh} &= 1 + 2 \sin^2 \theta_i + 2 \cos^2 \theta_i \sin^2 \phi_s \\ (49) \quad f_{hv} &= 1 + 2 \sin^2 \theta_s + 2 \cos^2 \theta_s \sin^2 \phi_s \\ f_{vv} &= 3 - 2 \cos^2 \theta_i \cos^2 \theta_s \sin^2 \phi_s \\ &\quad + 12(\sin \theta_i \sin \theta_s - \cos \theta_i \cos \theta_s \cos \phi_s) (\sin \theta_i \sin \theta_s). \end{aligned}$$

The parameters α_h (for horizontal incident polarization) and α_v (for vertical incident polarization) are the attenuation factors for the incident field as it propagates through the cylinders, and are given by

$$\begin{aligned} (50) \quad \alpha_h &= (3K/16) AN (\operatorname{Im} \epsilon_c) \sec \theta_i (1 + 3t^2) \\ \alpha_v &= (3K/16) AN (\operatorname{Im} \epsilon_c) \sec \theta_i [1 + 3t^2 + \sin^2 \theta_i (1 - t^2)]. \end{aligned}$$

Thus $1/\alpha_v$, $1/\alpha_h$ give estimates of the depth of penetration (optical depth) of microwave radiation into such vegetated surfaces. Because these formulas contain a number of parameters, (A , N , ϵ_c etc.) which are rather difficult to estimate for actual vegetated surfaces, one cannot consider them to give quantitative agreement with measured results. They can, however, be useful in estimating penetration depths, and surveying the effects of changes in such parameters as vegetation moisture content, biomass density etc., on the radar return. Figure 18 shows typical behavior of the backscattering cross-sections for this model, which may be compared with, for example, Figs. 36, 43 and 107. A number of calculations based on these formulas, together with higher order terms in the expressions for f_{ij} , are given in references 1 and 7.

The second type of vegetated surface for which fairly detailed scattering models have been worked out is that for which the leaves can be modelled by a volume distribution of their circular discs. Such commercial crops as soybeans, cotton etc., as well as many deciduous trees and shrubs can be modelled in this way. Reference 20 gives a detailed derivation of the bistatic scattering cross-sections for these volume distributions of individual scatterers, viz

$$(51) \quad \sigma_{ij}^0(\theta_i, \theta_s, \phi_s) = \frac{\bar{\sigma}_s^{ij}(\theta_i, \theta_s, \phi_s)}{\bar{\sigma}_{sc}^i(\theta_i) + \bar{\sigma}_a^i(\theta_i)} \cdot \frac{\cos\theta_i \cos\theta_s}{\cos\theta_i + \cos\theta_s}$$

where

$\bar{\sigma}_s^{ij}$ is the scattering cross-section of an individual particle, (i.e., leaf) averaged over the probability distribution of the spatial orientation of the particle.

σ_{sc}^i is the total scattering cross section of the particle for incident angle θ_i and incident polarization state specified by index (i), averaged over all spatial orientations.

σ_a^i is the absorption cross section of the particle for incident angle θ_i and incident polarization state specified by the index (i), averaged over all spatial orientations.

Thus a detailed study of the scattering process of the individual particle, and a knowledge of the probability distribution of the spatial orientations of the particles, permits one to estimate the parameter Γ (see Table I) used in the empirical form of the Lommel-Seeliger Law. Detailed formulas based on low frequency and high frequency approximations to scattering by thin discs are given in Ref. 20, which also contain a number of calculations for the backscattering cross-sections for the model. Figure 19 shows typical calculations for backscattering for this model, which can be compared with, for example, Figs. 35 and 105. Again, because of the many parameters in the model, one should not expect quantitative agreement. However, using reasonable values for leaf thickness, area and dielectric constant, such models predict qualitatively the dependency of the scattering cross-sections and attenuation lengths on frequency, moisture constant etc. Figure 20 shows estimates of the attenuation length (optical depth) of vegetated layers, based on this model. The models are less successful in predicting the depolarized scattering, presumably because multiple scattering effects, which tend to increase the cross-polarized power, are neglected.

TABLE I

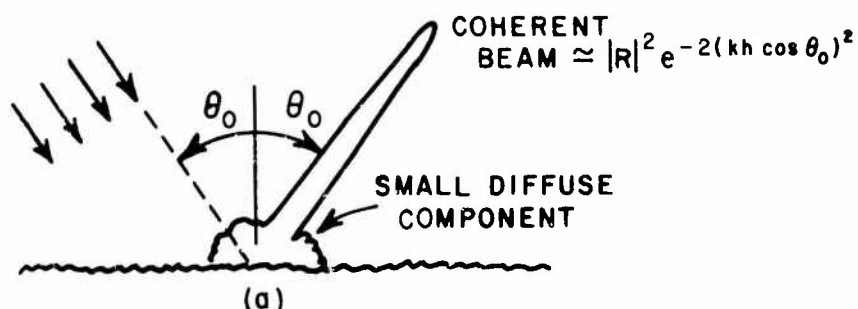
The Scattering Cross-Section $\sigma_{ij}^0(\theta_i, \theta_s, \phi_s)$ for Various Empirical Laws

Name	Bistatic Law	Backscattering Cross-Section	Albedo = 1-Emissivity*
Lambert	$\Gamma \cos \theta_i \cos \theta_s$	$\Gamma \cos^2 \theta_i$	$\frac{1}{2}$
Generalized Lambert	$\Gamma (\cos \theta_i \cos \theta_s)^n$	$\Gamma \cos^{2n} \theta_i$	$\frac{\Gamma \cos^{n-1} \theta_i}{(n+1)}$
Lommel-Seeliger (many layers of isotropic scatterers)	$\Gamma \frac{2(\cos \theta_i \cos \theta_s)}{\cos \theta_i + \cos \theta_s}$	$\Gamma \cos \theta_i$	$2\Gamma[1 - \cos \theta_i \log_e (1 + \sec \theta_i)]$
Lommel-Seeliger with multiple scatter	_____	$\Gamma \cos \theta_i [1 - \cos \theta_i \log_e (1 + \sec \theta_i)]$	_____
"Grass" (Empirical Law)	$\Gamma \frac{\cos \theta_i + \cos \theta_s}{2}$	$\Gamma \cos \theta_i$	$\frac{\Gamma}{2} \left(1 + \frac{\sec \theta_i}{2} \right)$
Single layer of isotropic scatterers (Euler)	$\Gamma_1 = NA_K$	Γ_1	$\Gamma_1 \sec \theta_i$

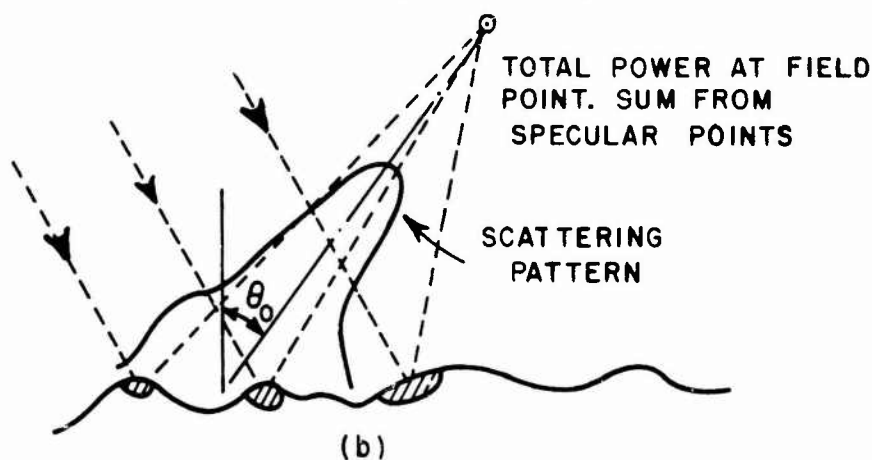
Γ, Γ_1 arbitrary constants

Angles θ_i, θ_s with respect to surface normal (not grazing angles)

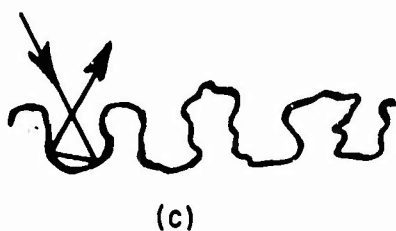
*Emissivity $e_i(\theta_i) = 1 - \int (\sigma_{ii} + \sigma_{is}) d\Omega_s (4\pi \cos \theta_i)^{-1}$ (Eqs. 2-16)



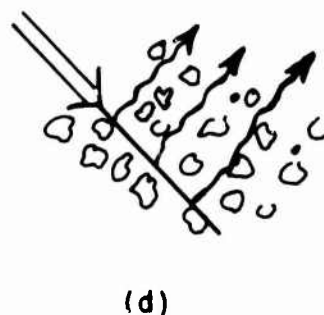
"Slightly rough" surface $h \ll \lambda$. Scattered beamwidth determined by transmitter beamwidth; - predominantly coherent.



Undulating "rough" surface $h \gg \lambda$, slopes $\ll 1$. Scattered beamwidth \approx r.m.s. surface slope; specular (not coherent).



The Lambert type of "rough" surface with large reentrant cavities.



The Lommel-Seeliger type of "rough" surface with many independent scatterers.

Fig. 14

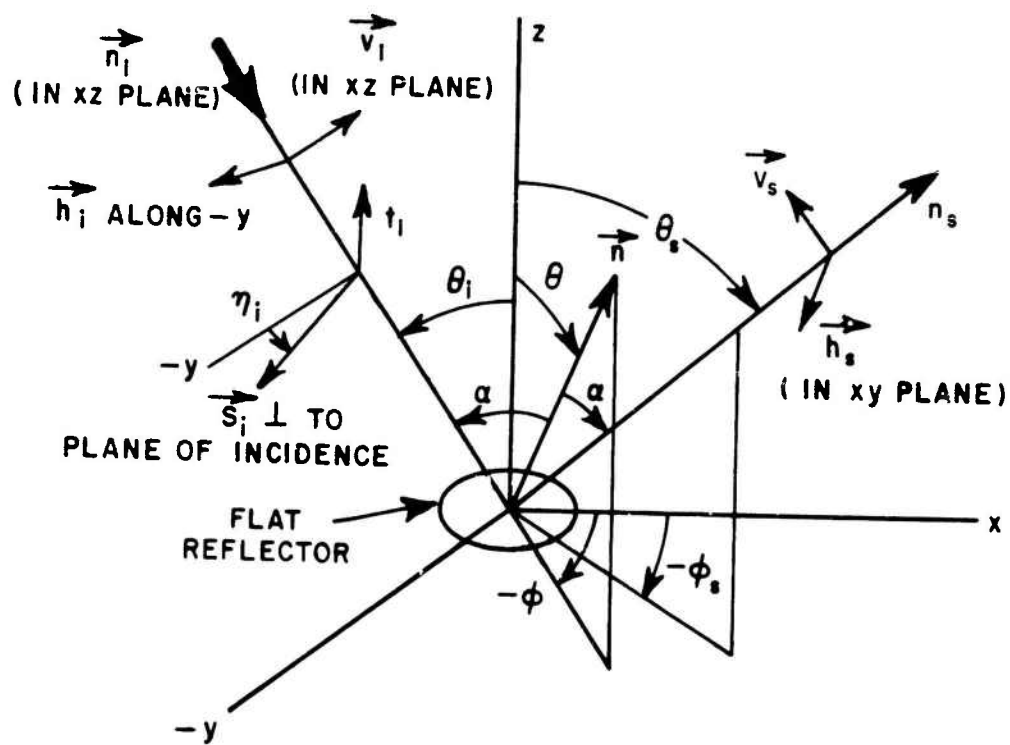


Fig. 15. Geometry of the scattering problem.

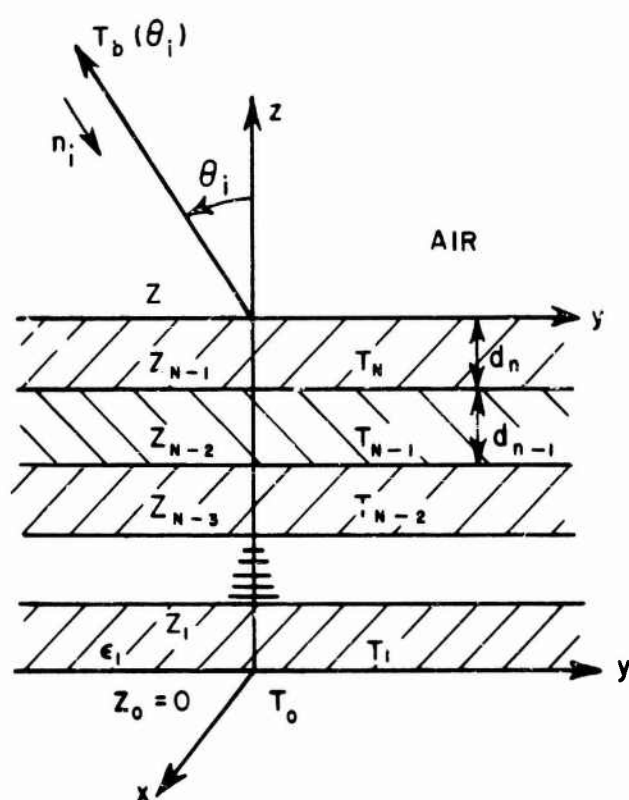
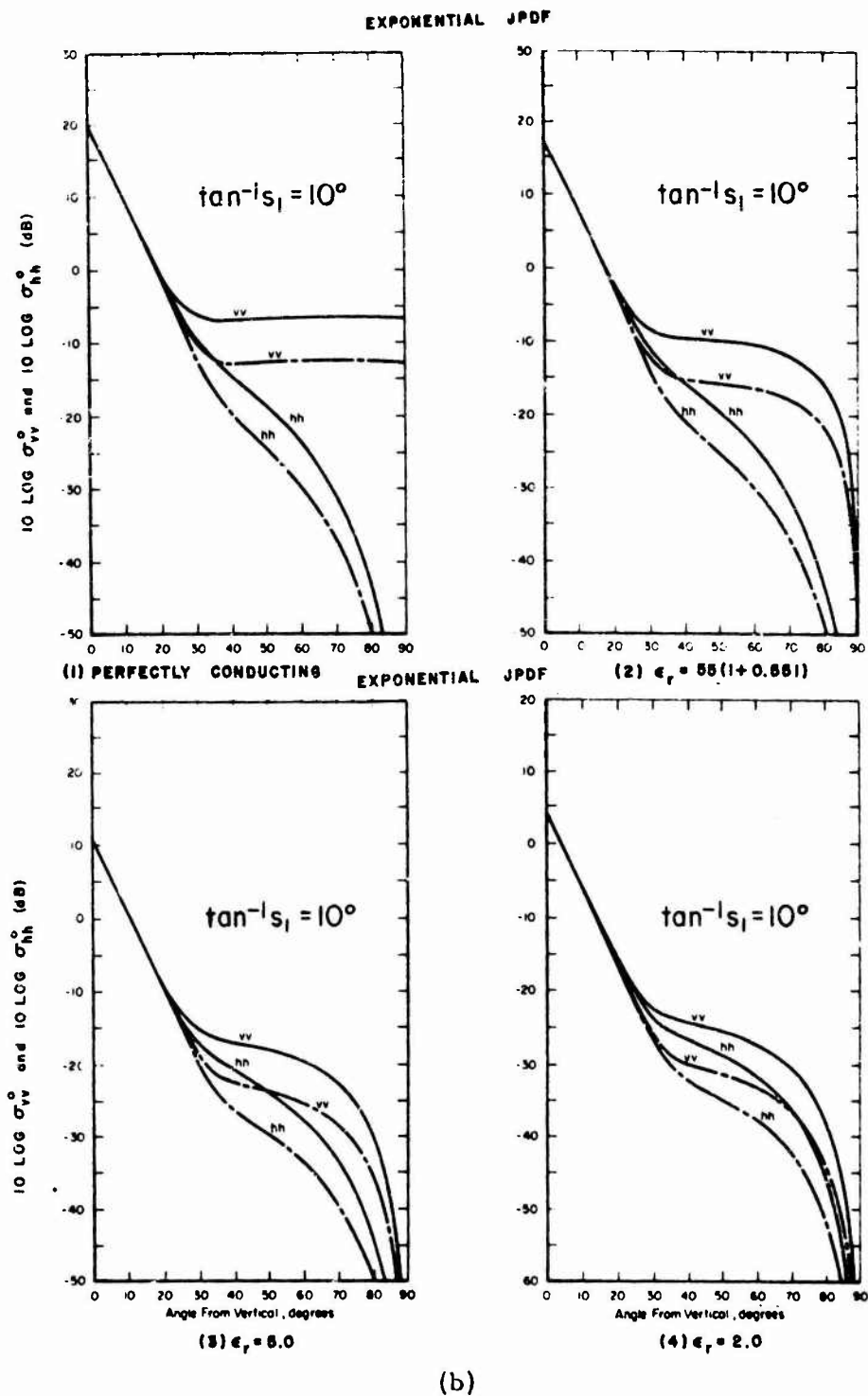
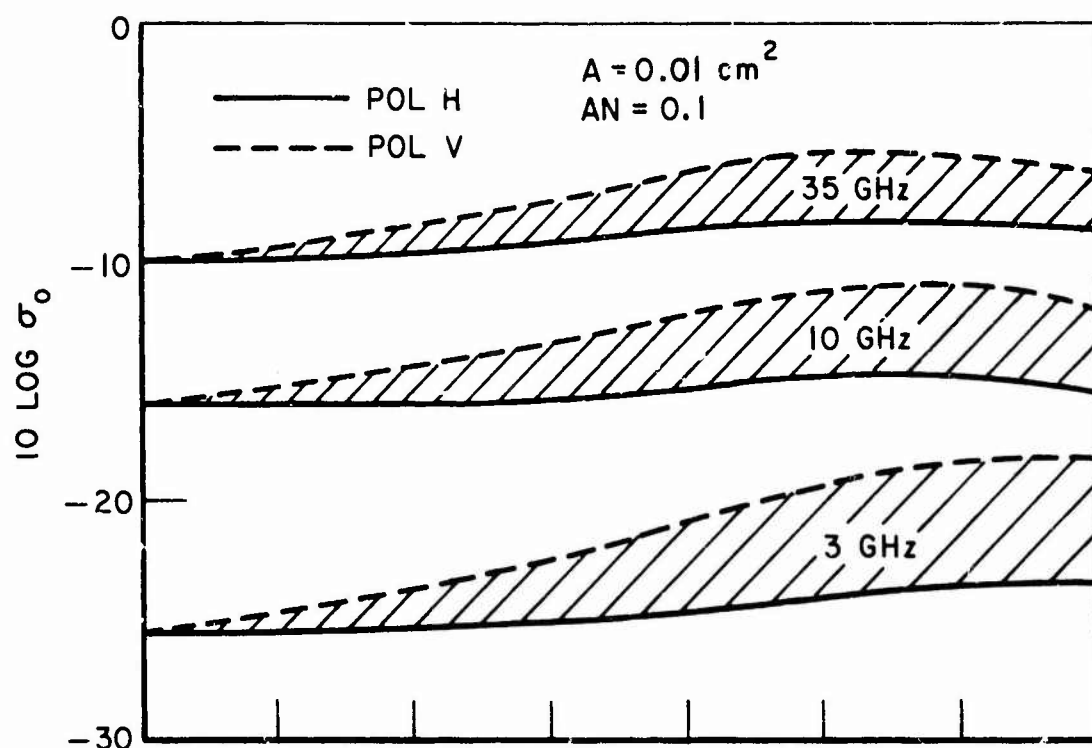


Fig. 16. Geometry of layered surface.

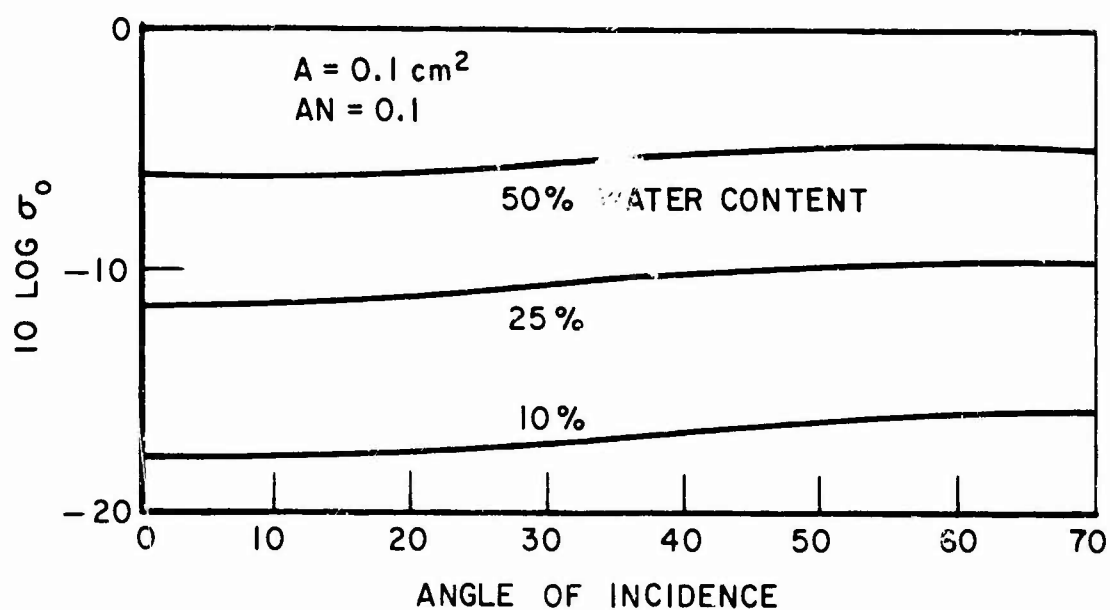


The small scale component has gaussian surface height correlation coefficient with $\rho(r) = \exp(-r^2/\ell^2)$ (ℓ is small scale correlation length, h is the mean square height of the small scale process. Solid curve $k_2=1$, $k_h=0.2$; dotted curve $k_2=1$, $k_h=0.1$. The complex dielectric constant $55(1-j.55)$ corresponds roughly to sea water at X-band. The large scale component has rms slope = s_1 .

Fig. 17. Backscattering cross-section for composite model.



a) σ_0 vs. θ_i for 50% water content at 3 frequencies.



b) σ_0 vs. θ_i at 10 GHz, horizontal polarization.

Fig. 18. Backscattering cross-section for cylinder vegetation model.

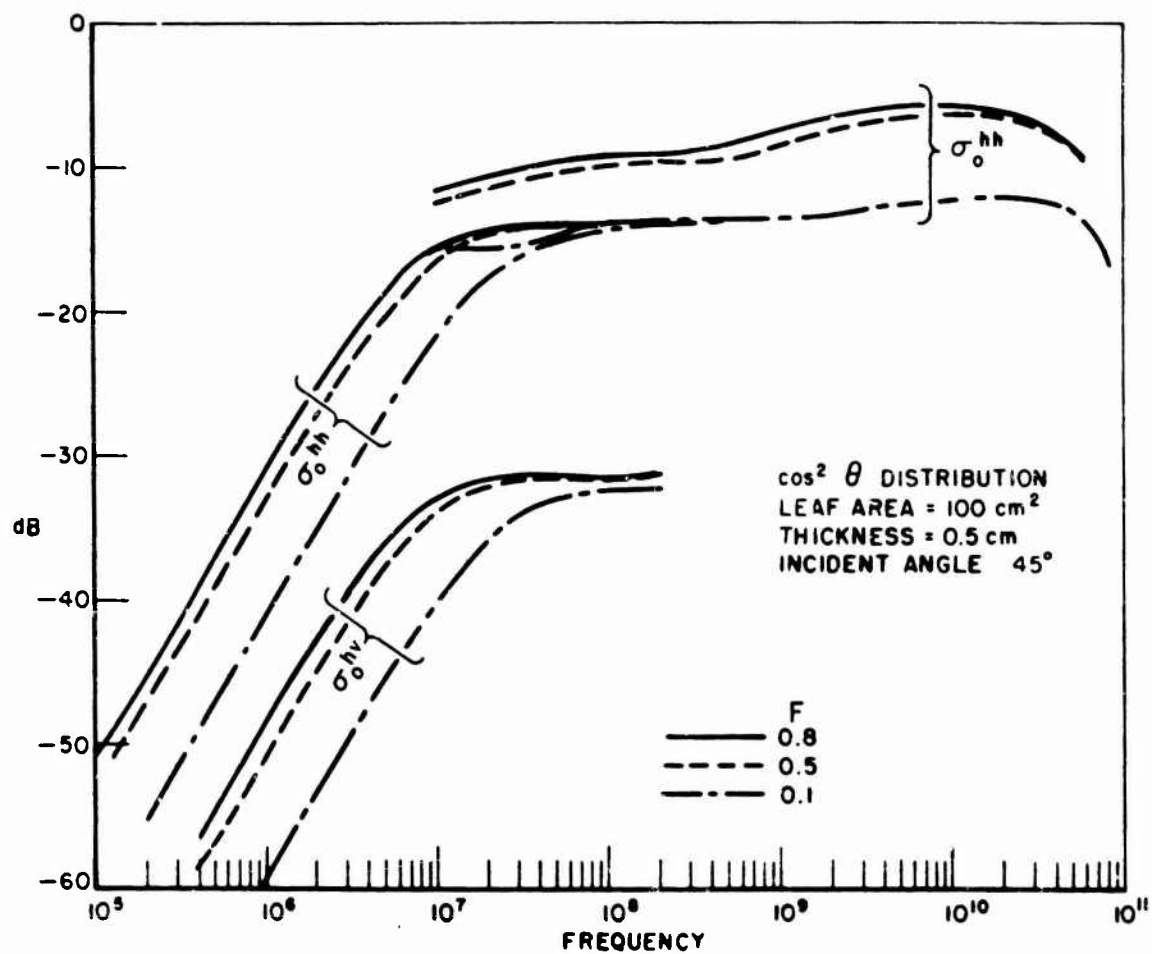


Fig. 19. Lommel-Seeliger cross section vs. frequency.
 (100F is percent water content.)

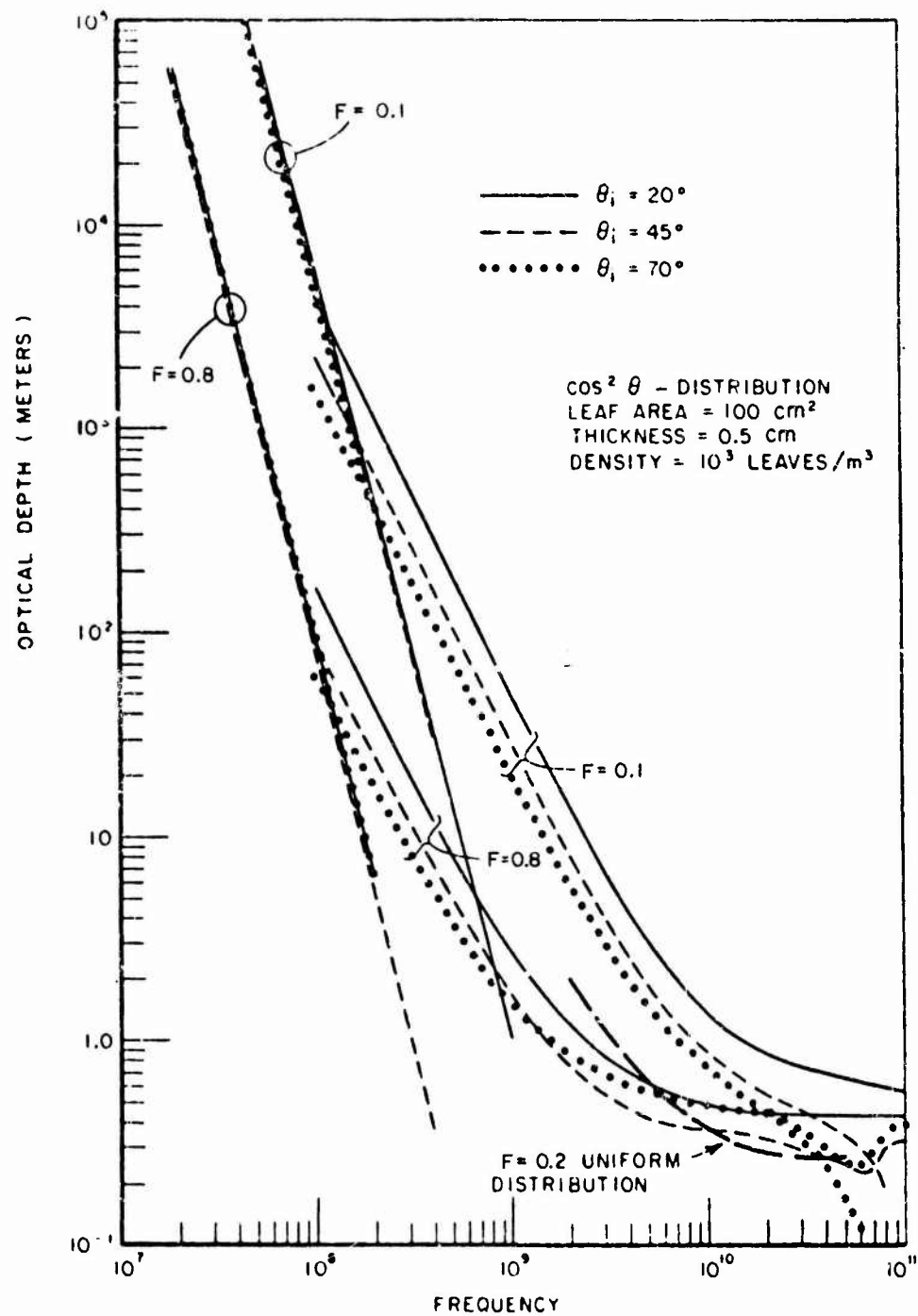


Fig. 20. Optical depth vs. frequency.

REFERENCES

1. Ruck, G.T., Barrick, D.E., Stuart, W.D. and Krichbaum, C.K., Radar Cross-Section Handbook, New York, Plenum, 1970.
2. Beckman, P. and Spizzichino, A., The Scattering of Electromagnetic Waves from Rough Surfaces, New York, McMillan, 1963.
3. Barrick, D.E., "The Interaction of HF-VHF Radio Waves With the Sea Surface and its Implications," AGARD Meeting, June 23, 1970, Paris, France.
4. Mitzner, K., "Change in Polarization on Reflection from a Tilted Plane," Radio Science, 1, pp. 27-29, 1966.
5. Richmond, J.H., "Efficient Recursive Solutions for Plane and Cylindrical Multilayers," Report 1968-1, 10 August 1965, Electro-Science Laboratory, Department of Electrical Engineering, Ohio State University Research Foundation; prepared under Contract N0w 65-0329-d for Bureau of Naval Weapons, Washington, D.C.
6. Valenzuela, G., "Depolarization of EM Waves by a Slightly Rough Surface," IEEE Trans., AP-15, p. 552, 1967.
7. Cosgrif, R.L., Peake, W.H. and Taylor, R.C., "Terrain Scattering Properties for Sensor System Design," Ohio State University Eng. Expt. Sta. Bull. No. 181, 1960.
8. Wright, J.W., "Backscattering from Capillary Waves with Application to Sea Clutter," IEEE Trans. AP-14, p. 749, 1966.
9. Guinard, N.W. and Daley, J.C., "An Experimental Study of a Sea Clutter Model," Proc. IEEE, 58, p. 543, 1970.

10. Clapp, R.E., "An experimental and Theoretical Study of Radar Ground Return," Rad. Lab., MIT Report No. 1024, 1946.
11. Ko, H.C., "On the Reception of Quasi Monochromatic, Partially Polarized Radio Waves," Proc. IRE 50, p. 1950, 1962.
12. Pascalar and Sakomoto, Third Symposium on Remote Sensing, University of Michigan, 1964.
13. Rice, S.O., "Reflection of E.M. Waves by Slightly Rough Surfaces," in Theory of Electromagnetic Waves, Interscience, 1963.
14. Barrick, D.E., "Radar Clutter in an Air Defense System," Part 1., Report RSIC-798, Redstone Scientific Information Center, Alabama, 1968.
15. Barrick, D.E. and Peake, W.H., "Scattering from Surfaces with Different Roughness Scales; Analysis and Interpretation," Report 1388-26, 15 September 1967, ElectroScience Laboratory, Department of Electrical Engineering, Ohio State University Research Foundation; prepared under Grant No. NSG-213-61 for National Aeronautics and Space Administration.
16. Stogryn, A., "Electromagnetic Scattering from Rough, Finitely Conducting Surfaces," Radio Science 2, p. 415, 1967.
17. Stogryn, A., "The Apparent Temperature of The Sea at Microwave Frequencies," IEEE Trans., AP-15, p. 278, 1967.
18. Valenzuela, R., "Scattering of EM Waves from a Tilted, Slightly Rough Surface," Radio Science, 3, p. 1058, 1968.
19. Barrick, D.E., "Theory of Ground Wave Propagation Across a Rough Sea at Dekameter Wavelengths," Battelle Memorial Institute, January 1970.

V. EXPERIMENTAL DATA

A. Introduction

In this section, a large number of data,* both radar and radiometric, are presented in a manner chosen to illustrate the relations between the sensor responses (σ_0 , γ , and T_b), and those parameters of the surface and the sensor which control them.

Among the parameters which can affect the magnitude of the sensor response are:

1. Surface roughness
2. Complex dielectric constant
3. Frequency
4. Polarization
5. Angle of incidence

For the most part, we have chosen to illustrate the effects of surface roughness, dielectric constant, frequency, and polarization, on the sensor responses by presenting the data as a function of angle of incidence (from normal). Some of the large angle data, however, are plotted as a function of the grazing angle. Because of the interrelations between the parameters above (e.g., polarization and dielectric constant effects for smooth surfaces) there is a certain amount of redundancy in the data presented.

The data are, of course, by no means complete, but it is believed they represent most of the categories of surface for which data are available. While a large part of the terrain data represent only the measurement of a single investigator, there are a number of surfaces (particularly the sea and the planets) which have been studied independently by several investigators. In general it may be assumed that

*Most of the backscattering data in this section display the parameter $\gamma = \sigma_0 \sec\theta_i$ rather than σ_0 .

the calibration procedures of any one investigator will be consistent from run to run, but that there may be systematic differences between the absolute levels measured with different experimental configurations. The most evident case where measurements of ostensibly the same surface give significantly different absolute levels occurs for the sea surface.

In this case, however, because the state of the surface can change rapidly, and is often specified indirectly (by using the wind velocity rather than the surface roughness as the descriptor) the observed discrepancies may be due to the fact that different surfaces were measured, rather than to systematic calibration errors. A further note of caution should be inserted about cross-polarized return. There is a tendency, especially over smooth surfaces near normal incidence, for the measured depolarized return to equal the polarization isolation of the antenna used in the experiment. In these cases, the measured return must be considered only as an upper limit to the actual depolarized power.

The data to be presented are organized in the following manner. First, the general characteristics of scattering from terrain surfaces are illustrated via the bistatic scattering pattern. Although complete hemispherical patterns have not been measured at microwave frequencies, certain cuts of the bistatic cross section (per unit surface area) $\sigma_0(\theta_i, \theta_r, \phi)$, have been measured[1] at 10 GHz for a number of well-defined surfaces, including smooth and rough sand, and smoothed loam, dry grass, and soybeans. The measurements cover a wide range of incidence, scattering, and azimuth angles, for vertical, horizontal, and crossed linear polarizations. Selected curves[1,2] are presented in Section B.

Ground-based measurements of the normalized radar backscattering cross section (per unit "projected" area), $\gamma(\theta_i)$, for a number of geological and vegetation-covered surfaces, have been made by this facility[3,4,5,6] in recent years, at 1.8 GHz, 10 GHz, 15 GHz, and 35 GHz.

A number of these results are presented in Section C to illustrate the relation between the backscattering cross section and the parameters of the surface and the sensor. It should be noted that the absolute levels of our earlier data[3] are consistently lower than our more recent data[5,6] for similar surfaces. This difference may be due to a static error in the earlier calibration technique.

Measurements of the brightness temperature, $T_b(\theta_i)$, of a number of terrestrial surfaces of geological and agricultural interest have been obtained,[7,8] over the past several years, with the Ohio State University truck-mounted radar-radiometer facility, at 10 GHz and 35 GHz. Curves, drawn from these data together with a number of measurements due to other investigators, are presented in Section D to illustrate the dependence of the radiometric temperature upon the surface roughness, dielectric constant, frequency, and polarization.

In Section E, representative measurements of radar bistatic and backscattering cross sections and radiometer brightness temperatures, are provided for several special surface categories including geological surfaces, vegetated surfaces, developed land areas (cities), and sea surfaces. The data compiled in these curves were gathered from many sources and should provide a convenient survey of microwave radar responses.

B. Bistatic Scattering Data

In this section, a number of data curves are presented, in Figs. 22-30, to illustrate the general features of the bistatic pattern of typical surfaces, and to show the relation of surface roughness, dielectric constant, and antenna polarization to the bistatic scattering patterns. Other bistatic data are given in Figs. 75-89. A complete description of the experimental processes, and a number of additional data curves are given in Reference 1. In order to separate

more clearly the several sets of data in each figure, the measured points have been arbitrarily connected by lines, but it should not be assumed that measurements at intermediate points would lie on the indicated curves. Photographs are shown in Fig. 21, of the actual measured surfaces which include: sand which had been smoothed with a board so that surface inequalities were less than $1/4$ wavelength ("smooth sand"); sand which had been moulded into hillocks with a roughness scale of several wavelengths ("rough sand"); loam which had been raked smooth so that it exhibited irregularities of about $1/4$ wavelength ("loam"); dry grass several inches long and partly matted down; loam with a stubble covering; and full grown soybean plants.

1. Effects of surface roughness

Figure 22, which exhibits the bistatic pattern in the plane of incidence ($\phi = 0$) for fixed values of incidence angle illustrate the characteristic behavior of a smooth surface, i.e., one for which the roughness is less than $1/4$ wavelength. A pronounced forward lobe, in approximately the specular direction is visible in each case with the smoother surface (smooth sand) having the larger return. Fig. 23 illustrates the characteristic difference between smooth and rough surfaces; for the latter the forward lobe is much less prominent and the scattering more nearly isotropic. Some trace of the forward lobe is still visible for the "dry grass" surface, showing penetration through the grass and reflection from the earth beneath. Deep surfaces of many independent scatterers, which should give an essentially isotropic scattering pattern, are illustrated by the soybean measurements of Figs. 24 and 28. A second type of rough surface (the "rough sand" surface composed of a distribution of large hemispheres) also exhibits a nearly isotropic scattering pattern as can be seen in Figs. 79(a) and 79(b). Here the scattering is nearly isotropic for the same reason that the scattering from a sphere is isotropic, although multiple scattering effects are clearly of some importance for this surface.

Scattering behavior in the azimuth cone is illustrated in Fig. 24, (with $\theta_i = \theta_r$ fixed; ϕ measured from forward direction). Again a pronounced forward lobe is evident for the smooth surfaces. It is interesting that in most cases the minimum scattering occurs when $\phi \approx 90^\circ$, with relatively larger returns in the backscattering direction.

2. Effects of complex dielectric constant

The best method to illustrate the effects of dielectric constant on the bistatic return is to examine the cross-sections for smooth surfaces (for example, see Fig. 22). For those situations where the scattering exhibits a distinct lobe in the specular direction, it is possible to calculate an equivalent "Fresnel" reflection coefficient from the measured cross section by the expression[1]

$$|R_{V,H}| = \sqrt{\frac{\sigma_0 I}{\pi}},$$

where σ_0 is the value measured at the specular angle ($\theta_r = \theta_i$, $\phi = 0$), because this is analogous to the case of a perfectly smooth surface. (Here $I \approx \pi/(B \cos \theta_i)$, where $e^{-B\psi^2/2}$ is an approximation to the one-way power pattern of identical transmitting and receiving antennas).

The reflection coefficients for smooth sand and loam at the two antenna polarizations were calculated in this manner and plotted in Fig. 25. The solid curves are calculated values of $|R|$ assuming perfectly smooth, lossless surfaces with relative dielectric constants 2 and 3, and the points clustered around these curves are the experimentally measured values. The contrast between the vertically polarized and horizontally polarized returns clearly illustrates that the Brewster effect is present, and suggests that the dry sand and dry loam surfaces have an effective dielectric constant of about 3.

Figure 26 shows results of reflection coefficient measurements made by Sherwood and Ginzton,[9] indicating that for the purpose of revealing the Brewster angle of a surface, (and therefore, the relative dielectric constant), a number of closely spaced measurements about the estimated Brewster angle is required for satisfactory results.

3. Effects of polarization

Effects of polarization are illustrated by Figs. 27-28 (azimuthal) and 29-30 (plane of incidence). (See also Fig. 22). As might be expected from the behavior of the Fresnel coefficients, the horizontal component is significantly larger than the vertical component for smooth surfaces in the specular direction, particularly near the Brewster angle. However, at angles near $\phi = 90^\circ$ the situation is reversed, with vertical predominating. For vegetated surfaces (e.g., Fig. 30) there is little difference between the two polarizations. Of some interest are the cross polarized returns, which for smooth surfaces, are small (relative to direct polarization) in the forward lobe, as would be expected, but are comparable to the direct returns at angles near $\phi = 90^\circ$ (Fig. 29). For vegetated surfaces, the cross-polarized return tends to follow the direct return (Fig. 30) but at a somewhat lower power level (see also Fig. 92). (Note in Fig. 30, the last few data points were made as snow began to fall.)

C. Backscattering Data

Curves are presented here to illustrate the dependence of the radar backscattering cross section, γ , upon such parameters as surface roughness, dielectric constant, frequency, and polarization. These data have been drawn from measurements by several investigators[3,4,5,6] at this facility. A complete description of the Ohio State University truck-mounted radar-radiometer facility and its operation, is given in Reference 10.

1. Effects of surface roughness

Figure 31 illustrates the characteristic behavior of the radar backscattering cross section, γ , for "smooth" surfaces; i.e., the return decreases monotonically as the angle of incidence increases and the magnitude of the horizontally polarized return is less than that of the vertically polarized as predicted by the perturbation model. For such slightly rough surfaces, the magnitude of the return provides an estimate of the rms roughness, and the difference between the vertical and horizontal return provides an estimate of the dielectric constant. The glacially polished limestone surface is level, with small scale roughness < 1 mm.

One form of transition from a "smooth" to a "rough" surface is exhibited by the radar backscattering cross sections of rubble type surfaces, at X-band, shown in Fig. 32. Here the surfaces were similar in character, i.e., sand, pea gravel, and crushed limestone (with a diameter of 3-5 cm for the individual rocks), but differed in roughness, with the sand satisfying the Rayleigh criteria for a "smooth" surface at 3 cm wavelength, while the crushed stone was "rough". Again the backscattering increases with roughness, as does the depolarized return relative to the direct, until the Rayleigh criterion is exceeded. For the crushed stone, the significant multiple scattering produces a cross-polarized return almost equal to the direct. Figure 33 illustrates the limiting form for this kind of roughness, that is, the discontinuously rough surface having large re-entrant cavities. Such surfaces exhibit a backscattering cross section almost independent of frequency, and behave more or less like a Lambert Law surface ($\gamma(\theta_i) \propto \cos \theta_i$). A photograph of the actual pumice surface, at Mono Crater, is shown in Fig. 34. The range of diameters of the individual boulders is 30 to 100 cm.

The other type of discontinuously rough surface (the Lommel-Seeliger type of scattering model; $\gamma = \text{constant}$) is illustrated by vegetation-covered terrain. Figures 35 and 36 exhibit the backscattering

cross sections at X-band, for vertical polarization, for two distinct types of vegetation: those in which the leaf structure is similar to a flat disc (soybeans), and those in which the leaves are essentially thin cylinders (oats). For vegetated surfaces, the magnitude of γ is seen to be almost independent of angle of incidence, as one would expect from the model. It is also not strongly dependent on crop type, although wheat tends generally to have a lower γ , and sugar beet a significantly higher γ than the crops illustrated here.

2. Effects of complex dielectric constant

The effect of the dielectric constant, for two slightly rough surfaces (the limestone and asphalt surfaces of Fig. 31), is illustrated in Figs. 37 and 38, showing the difference between the vertical and horizontal backscatter. The solid curves are computed values (using Eqs. 27,29 of Chapter IV) of the difference between γ_{VV} and γ_{HH} , independent of the surface roughness parameter. Thus, by measuring the backscattering for vertical and horizontal polarizations, as a function of angle of incidence, it is possible to estimate the dielectric constant for a slightly rough surface.

For surfaces of the rubble type with irregularities comparable to the Rayleigh criteria, the effect of roughness and dielectric constant on the radar backscatter is clarified if the data at a number of angles and wavelengths is plotted in terms of a normalized roughness parameter, $\xi = (D \cos \theta_i)/\lambda$, where D is the diameter of the individual particles. For example, if the return from gravel at 3 wavelengths in Fig. 39, and that of similar measurements on crushed rock ($D \approx 3-5$ cm) and sand are plotted versus the normalized roughness parameter, ξ , the result is Fig. 40. It is seen for $\xi < 1/4$, the return falls off roughly as $1/\lambda^2$, whereas for $\xi > 1/4$ the return is a constant, more or less independent of roughness (corresponding to "optical" scattering). The general level of the curve would move up or down for materials of different dielectric constant. Thus, by measuring

the backscattering from a surface of this type at a number of angles and wavelengths, it should be possible to estimate the roughness by locating the break-point ($\xi \pm 0.3$) and to estimate the dielectric constant by measuring the optical level.

The dependence of the backscattering cross section upon the dielectric constant is further illustrated by data[3] on seasonal changes of grass at three frequencies in Figs. 41-43. At X-band (Fig. 43) the variation in the magnitude of γ , which may be as large as 8 dB (regardless of the variation in height of the vegetation), is presumably due to changes in water content, with the resulting change in the effective dielectric constant of the grass blades. Other vegetated surfaces, however, (e.g., soybeans Fig. 35, oats Fig. 36, grass at K_u and K_a band Figs. 41 and 43) show little change in γ over most of the growing season.

Figures 44 and 45 illustrate the effects of rain on smooth (asphalt road) and rough (grass) surfaces, at K_a -band. Water on a relatively smooth surface tends to lower the return since the surface appears to be smoother, and this effect overrides the tendency of the water to increase the effective dielectric constant. On vegetation, however, the return may increase because the water drops on the leaves have effectively increased both the leaf thickness and its effective dielectric constant.

3. Effects of frequency

Figure 46 exhibits the frequency dependence of radar backscattering for a typical smooth (i.e., "slightly rough") asphalt surface. As the frequency decreases, the magnitude of γ should decrease at least as rapidly as f^2 . The particular surface shown has a rms roughness of approximately 0.3 mm and a relative dielectric constant of $\epsilon_r = 4.3 + j0.1$.

Figures 47-49 illustrate the frequency dependence of the radar backscattering for three rubble-type surfaces (sand, gravel, and crushed stone). The gravel surface (Fig. 48) shows the kind of increase in γ with frequency expected for a slightly rough surface. However, it is interesting to note that for the case of crushed stone surface the largest return was obtained at X-band, i.e., at the lowest frequency. It is possible that either resonance scattering, or a significant decrease in dielectric constant with frequency, could cause this behavior.

The characteristic behavior of the frequency dependence of γ for the two types of discontinuously rough surfaces, large blocks (pumice) and vegetation (oats), is shown in Figs. 50 and 51. As previously noted, the large blocks of pumice exhibit a radar return almost independent of angle and frequency (i.e., "optical" behavior). For the oats surface, however, a significant difference in the magnitude of γ exists between the 1.8 GHz and 10 GHz return. This frequency behavior would be expected on the basis of theoretical models, since at 1.8 GHz the vegetation layer may be less than one optical depth thick, and the scattering from an individual cylinder decreases rapidly as wavelength increases.

4. Effects of polarization

Figure 52 illustrates the polarization dependence of the radar backscattering cross section, γ , for a "smooth" surface (glacially polished limestone located near Marblehead, Ohio); i.e., the horizontally-polarized backscatter (γ_{HH}) is less than that of the vertically polarized (γ_{VV}), and the cross-polarized components (γ_{VH} and γ_{HV}) are at least 10 dB less than the direct-polarized components.

The polarization dependence (for both linear and circular polarization) of the radar backscattering, at X-band, for the three rubble-like-surfaces described previously, is shown in Figs. 53-55.

It can be seen that the vertically polarized return is larger than the horizontal for the quasi-smooth sand surface, and the cross polarized return is at least 10 to 15 dB down. However, as before, the depolarized component increases as the surface becomes rough in terms of wavelength.

Figures 33 and 56 illustrate the polarization behavior of the radar backscatter for discontinuously rough surfaces (pumice and green oats), i.e., γ almost independent of polarization for the direct returns, and cross-polarized returns (for the oats surface in particular) which are only slightly lower than the direct returns. This is in contrast with the relatively small cross-polarized returns for a slightly rough surface (e.g., Fig. 52), but is characteristic of surfaces in which multiple scattering plays a significant role.

D. Brightness Temperature Data

Measured microwave brightness temperatures are presented in this section to show their dependence on the parameters of the surface and the sensor. The measurements are primarily those obtained by this facility,[7,8] although a number of other data,[11] are included. In the case of the data of References 7 and 8, the integral equation relating brightness temperature and antenna temperature has been inverted by a bootstrap method, so that the data plotted are estimates of brightness temperature. In most other cases, raw antenna temperature is plotted.

1. Effects of surface roughness

The measured brightness temperatures for smooth asphalt, at 10 and 35 GHz, are shown in Figs. 57 and 58, respectively. The effect of the near zero reflection coefficient (and thus, emissivity very near unity) at the Brewster angle for vertical polarization, is prominent

for both frequencies. A fairly good estimate of the dielectric constant of the surface may be obtained from the characteristic shape of the curves.

Figure 59[11] illustrates the transition from "smooth" to "rough" for very homogeneous, rubble-type surfaces, composed of different size fractions of limestone, at 13.5 GHz. The gravel surface exhibits the characteristic of a slightly rough surface. The cobble surface shows some of the characteristics of a "smooth" surface but the Brewster angle effect is decreased. The cobbles included size fractions passing a 10 cm by 15 cm screen. The boulder surface (diameters of several feet) is characteristically rough; i.e., the brightness temperature is approximately independent of angle of incidence, i.e., approximately Lambertian.

Figures 60-62 present a set of X-band measurements[7] made at Mono Craters, California on a sequence of lavas of essentially the same chemical composition and structural roughness but different physical properties, ranging from light pumice to obsidian (see photographs in Fig. 63). The brightness temperatures again exhibit the characteristic behavior for a Lambert law surface, i.e., almost independent of angle of incidence. Here the denser obsidian has a higher dielectric constant, a higher reflection coefficient, and thus, a lower brightness temperature. Since the radar return for the surfaces also show the characteristic of a Lambert surface (e.g., see Fig. 33), the brightness temperature can be related directly to the radar return, and estimated from it.

Measurements of X-band brightness temperatures of cultivated farmland, in particular plots of alfalfa, wheat, and oats, are shown in Figs. 64-66. The vegetated surfaces behave as rough, diffusely scattering surfaces, as evidenced by the lack of angular dependence for the brightness temperatures.

2. Effects of complex dielectric constant

Figure 67 illustrates the effect of the dielectric constant on measured X-band brightness temperatures (vertical polarization) for asphalt, glacially polished limestone, and a smooth coal bed exposed by strip mining operations. The three curves represent brightness temperatures computed from the Fresnel reflection coefficients, using values of dielectric constant appropriate to the actual surfaces. It is clear that not only is there good agreement between measured and computed temperatures, but that such measurements offer a means for remotely determining the value of dielectric constant for exposed, smooth surfaces.

The dependence of the brightness temperature of soil on the soil moisture content (and hence on dielectric constant) is exhibited by 13.4 GHz data,[11] in Fig. 68, which were obtained on Harper Lake, a playa deposit in the Mojave Desert, California. It is noted from these data that, as the moisture content increases, the observed temperatures decrease, and the difference between the vertical and horizontal temperatures increase. This is in agreement with the fact that the effective dielectric constant, and thus the reflection coefficient of the surface increases with the moisture content.

Figure 69 illustrates the effect of dielectric constant on the measured X-band brightness temperatures for three pumice surfaces (see also Figs. 60-62). As noted previously,[12] the differences in temperature for these surfaces, are directly related to differences in dielectric constant, and indirectly to differences in density.[12]

The brightness temperatures, at X-band, for irrigated and non-irrigated soybeans, are shown in Fig. 70. For these surfaces, at least part of the difference in brightness temperature must be ascribed to a difference in moisture content of the two categories of vegetation.

3. Effects of frequency

The frequency dependence of T_b for a "smooth" surface, asphalt at X-band and K_a -band, is shown in Fig. 71. The Brewster angle effect is quite prominent at both frequencies, indicating a surface roughness less than the Rayleigh criteria. This is in agreement with the known rms roughness ≈ 0.3 m.m. The surface is cooler at the lower frequency as one would expect from the larger dielectric constant at X-band.

The transition from smooth to rough is illustrated in Fig. 72, which shows the brightness temperatures for a slightly rough lapilli surface (photograph in Fig. 73), at 10 GHz and 35 GHz. The brightness temperature at 10 GHz is similar to that of a smooth surface (for instance, Fig. 57). At 35 GHz, however, the return shows a character intermediate between a "smooth" surface and a "rough" surface (c.f., Fig. 61).

In Fig. 74, brightness temperatures are shown for a rough surface (dark pumice), at 10 GHz and 35 GHz. In contrast to the lapilli surface (Fig. 72), the brightness temperatures of the pumice surface are approximately independent of angle of incidence at both frequencies, as expected for a Lambert surface; furthermore, if the brightness temperatures are scaled according to the actual surface temperatures, the corresponding emissivities are practically identical, i.e., independent of frequency.

4. Effects of polarization

The dependence of the microwave brightness temperature on the antenna polarization can be noted from data in the previous sections. An excellent example of the polarization behavior of a "smooth" surface (asphalt) was shown in Fig. 57, i.e., a prominent Brewster angle effect for the vertical component and a continuous decrease with nadir angle for the horizontal component.

For rough, diffusely scattering surfaces, however, the microwave brightness temperatures are almost independent of polarization. This lack of polarization dependence is clearly evidenced by the two typical rough surfaces: dark pumice (Fig. 61) and oats (Fig. 66).

E. Special Surface Categories

1. Bistatic scattering data

In this section, X-band measurements[1] of σ_0 are presented for the following land surfaces: bare soil (smooth and rough sand, and loam), and vegetation (stubble, dry grass, and soybeans). A description and photographs (Fig. 21) of the actual surfaces measured, were presented in Section B. The measurements cover a wide range of incidence, scattering, and azimuth angles, for vertical, horizontal, and crossed linear polarization.

C-band measurements, by Pidgeon,[13] of σ_0 for the sea are also included. These measurements cover transmitter depression angles between 0.2° and 3° below the horizontal, and receiver depression angles between 10° and 90° , for vertical and crossed linear polarizations.

a) Bare soil surfaces.

The bistatic scattering patterns for smooth sand are shown in Figs. 75 (plane of incidence) and 76 (azimuth). Similar measurements for smoothed loam are shown in Figs. 77 and 78. These measurements again illustrate the pronounced, polarization dependent forward lobe for smooth surfaces.

Figure 79 shows the bistatic pattern in the plane of incidence for rough sand. For this surface the scattering is more nearly isotropic, corresponding to the behavior expected from a distribution of hemispheres on a plane.

b) Vegetated surfaces

The scattering behavior in the plane of incidence for three vegetated surfaces (stubble, dry grass, and soybeans) is shown in Figs. 80-82. For the soybean surface, the azimuth scattering is shown in Fig. 83, for $\theta_i = \theta_r = 60^\circ$ and 80° . For the vegetated surfaces, there is little difference between the two direct-polarized returns, and the scattering pattern tends to be nearly isotropic.

c) Sea surface (Data from Ref. 13)

Figures 84-86 show bistatic cross sections of the sea at C-band for vertically-polarized transmitter and receiver, for three values of sea state. The receiving antenna is located in the plane of incidence. Figures 87-89 present the bistatic cross sections for a vertically-polarized transmitter and a horizontally-polarized receiver. The results indicate values of σ_0 at sea state 3 are approximately 10 dB larger than corresponding values for sea state 1. The cross-polarized return is 10 to 15 dB less than the polarized return for transmitter depression angles less than 1° , but only 5 to 8 dB less at depression angles near 3° .

F. Backscattering Data

Measurements of γ (or σ_0) are presented in this section, for the following surface categories: geological, vegetated, developed land areas (cities), and sea. A limited number of near-grazing angle measurements are included separately.

1. Geological surfaces

The backscattering cross sections for several slightly rough surfaces, including smooth concrete, concrete, smooth asphalt, rough asphalt, and gravel, are shown in Fig. 90, at K_a -, K_u -, and X-band.

It is evident that the dependence upon angle decreases and the absolute level increases as the roughness increases in terms of wavelength. The mean square roughnesses were determined for four of the actual surfaces:

"smooth concrete"	$\overline{Z^2} = 2.3 \times 10^{-4} \text{ cm}^2$
"concrete"	$\overline{Z^2} = 2.6 \times 10^{-4} \text{ cm}^2$
"smooth asphalt"	$\overline{Z^2} = 1.6 \times 10^{-3} \text{ cm}^2$
"rough asphalt"	$\overline{Z^2} = 2.7 \times 10^{-3} \text{ cm}^2$

Figures 91-94 present measurements of the backscattering cross section for a number of terrestrial surfaces of geological interest. In particular, airborne data for "normal" desert surfaces, at X-band and horizontal polarization, are presented in Fig. 91. These data were obtained by the Naval Research Laboratory[14,15] and by the Goodyear Aircraft Corporation.[16] Measurements of σ_0 for the "Arizona Desert" surface, at 428 MHz, 1.228 GHz, 4.455 GHz, and 8.91 GHz, for horizontal, vertical, and crossed linear polarizations, may be found in Reference 15.

In Fig. 92, airborne measurements of γ , for a "Pisgah Lava Flow" surface, are compared with ground-based data[5] for a similar surface. It is noted that agreement between airborne and ground-based measurements is quite good.

Figures 93 and 94 exhibit the backscattering cross sections for Bristol Dry Lake (Amboy, California) and Lavi Dry Lake (Pisgah Crater in the Mojave Desert, California), respectively. A photograph of the Lavi Dry Lake playa (shown in Fig. 95) shows the surface to be almost perfectly flat, having a hard, dry crust.

Backscattering cross sections, $\gamma(\theta_i)$, for the Moon,[18] Venus[19] and Earth,[17,20] are shown in Fig. 96. The Moon ($\lambda = 3.8 \text{ cm}$, 23 cm, 68 cm) and Venus ($\lambda = 12.5 \text{ cm}$) radar transmissions were circularly

polarized. The vertically-polarized, 30 cm data from the surface of New Mexico (White Sands Missile Range) were obtained by a rocket radar which was designed to transmit vertical polarization, and receive both the vertical and cross-polarized components. The horizontally-polarized, 2.3 cm results were obtained by the Ryan 13.3 GHz Scatterometer.

Figures 97-102 present a portion of the radar backscattering cross section (σ_0 or γ) data for the lunar surface. The wavelength dependence of the circularly polarized backscatter is exhibited in Fig. 97, for wavelengths ranging from 8.6 mm to 6 m. These values of σ_0 are obtained by normalizing the relative power measurements to a total cross section of 0.065 times the geometrical lunar cross section.[21]

The polarization dependence of the lunar backscatter,[22] at 23 cm and 68 cm, is shown in Figs. 98 and 99, respectively. Measurements of the circularly-depolarized components indicate that the depolarization is increasing with decreasing wavelength. It should be noted that the "linear depolarized" measurements at 23 cm (see Fig. 98), include the return from a complete range ring of constant delay, and hence represent a statistical mixture of "vertical" and "horizontal" components relative to the local plane of incidence co-ordinates. As mentioned previously, near normal incidence, the separation between direct and crossed polarized return tends to equal the polarization separation of the antenna used in the experiment. Thus the rise in the depolarized return near normal incidence is more likely to be an artifact of the experiment rather than a property of the surface.

The radar cross section of the lunar surface, at 13.3 GHz,[23] for Surveyors V, VI, and VII, is shown in Figs. 100, 101, and 102, respectively. These data ($\lambda = 2.3$ cm) are in good agreement with the Earth-based 3.6 cm results[21] (solid curve).

2. Vegetated surfaces

Backscattering cross sections for a number of vegetated surfaces, are presented in Figs. 103-104. A large quantity of additional data may be found in References 3 and 6. In Fig. 103, airborne X-band radar measurements of γ for wooded terrain, obtained by NRL[14] and Goodyear,[16] are compared. These data are in fairly good agreement. It is noted that the radar return at X-band is approximately independent of tree type and height.

Figure 104 exhibits the backscattering cross sections, at X-band, for some typical Arizona farmland. The irrigated farmland area included the following crops: onions (less than one foot high), alfalfa and wheat (2 feet), and maize (2 to 3 feet).

The backscattering cross sections (at S-, X-, and K_a -bands) for soybeans and oats are shown in Figs. 105 and 106, respectively. These surfaces are representative of the two typical structures for agricultural crops: leafy (soybeans) and cylindrical (oats). The curves presented are the upper and lower limits of the measured data for the number of indicated dates. Only the vertically-polarized direct component has been plotted since the return is essentially independent of polarization.

Figure 107 presents the backscattering cross section for a wheat surface[25] at 297 MHz, 5.87 GHz, and 9.375 GHz for horizontal polarization. A point of interest is that oats and wheat have a rather similar structure, yet the X-band radar return from the wheat (Fig. 107) is nearly an order of magnitude less than from oats (Fig. 106). A similar result was noted by Peake,[12] from measurements at this facility.

3. Developed land areas (cities)

Figures 108 and 109 provide airborne measurements of the back-scattering cross section, γ , for cities. Measurements by NRL[15] at 428 MHz and Westinghouse[26] at 220 MHz, are shown in Fig. 108, for vertical polarization. In Fig. 109, X-band values of γ for cities, including Chicago, Phoenix, and New Jersey residential, are plotted from measurements by NRL.[14,15]

4. Sea surfaces

The radar backscattering cross section for the sea, $\sigma_0(\theta_i)$ (where θ_i is measured from normal), is presented in Figs. 110-129, for frequencies ranging from 428 MHz to 48.7 GHz. The order of presentation is such that the most recent data are shown first.

Figures 110-117 present the newer NRL data[27] which show little dependence of σ_0 on wind velocity at angles between 20° and 70° . In particular, the difference in return for "smooth" and "rough" sea conditions is less than 10 dB at all frequencies. X-band backscatter measurements[27] on sea surfaces with oil-slicks are shown in Figs. 118 and 119, together with data for four roughest sea conditions in July 1965. These results indicate very little scattering at angles more than 20° or 30° off normal incidence for sea surfaces with oil-slicks, in agreement with the concept that the "diffuse" part of sea surface scattering (i.e., the backscattering between 20° and 70°) is due to Bragg scatter by the capillary waves. These are suppressed by the oil slick.

The radar data[28,29,30] which show a more pronounced dependence of σ_0 on wind velocity are shown in Figs. 120-129. At the present time, the discrepancy between these results remains unresolved. It seems likely, however, that a part of the difference is due to different experimental geometries, and to the fact that some measurements were

taken over fully developed seas in the open ocean, whereas, others were taken under conditions of limited fetch (e.g., Fig. 121). In any case it is clear that there is a significant difference between sea return at very low wind velocities (say less than 5 knots) and that at the higher wind velocities.

5. Near-grazing angle data

Figure 130 presents small grazing angle measurements for trees[31] (X- and S-band) and cotton seedlings[16] (X-band). The most significant aspect of the data is the increase in γ as the grazing angle decreases from 1 to 3 degrees. This tendency of the backscattering near grazing to increase as grazing incidence is approached has been observed for many years, but has received no general explanation. Ground based X-band measurements of $\sigma_0(\theta_i)$, by Linell,[32] for cultivated and wooded terrain, are shown in Figs. 131 and 132, with the percentile value as the parameter indicated on the curves. No difference in the results between horizontal and vertical polarizations, was observed for either terrain. The curves for the cultivated terrain (Fig. 131) exhibit a characteristic upturn in γ for angles of less than 1.5 degrees.

The variation of σ_0 with season is shown for cultivated terrain in Figs. 133-135 and for a forested area in Fig. 116. In these figures, the grazing angle is fixed and σ_0 is plotted against the percentage value. The point of interest is that a strong variation of σ_0 with season exists for the cultivated terrain, but not for the forested area. It was noted that the forest consisted primarily of pines and firs, which remain green throughout the year.

Measured distributions of average values of σ_0 for different types of terrain, at grazing angles of 1°, 5°, and 30°, are shown in Figs. 137-139. These measurements were obtained by Ericson,[33] of the Research Institute of National Defense, Stockholm, Sweden, using an airborne X-band radar with a horizontally-polarized antenna. Table I provides a description of the different types of terrain.

TABLE I Types of terrain. (Ref. 33)

Code	Designation	The Map Shows	
		predominantly	remainder
0	cultivated land 1.	fields, farms, gardens bushes, single trees, etc.	groves, woods up to 25%
1	cultivated land 2.	as above	as above but up to 50%
2	Swamps	swamps, sparsely covered with trees and/or houses	wood up to 25%
3	Open wood	a) open wood b) wood	fields, pastures, farms, up to swamps, open wood etc 50%
4	Rocks	moss-covered or naked rocks or mountains, possibly covered with bushes and single trees	wood up to 25%
5	Wood	dense wood	as in 3b) above, but up to 25%
6	Archipelago terrain	sparsely covered smaller islands and holmes, naked rocks	(water)
7	Villa districts	dispersed smaller houses surrounded by gardens	
8	Small houses districts	concentrated lower buildings up to 3 floors (suburbans, provincial towns)	
9	High houses districts	Very concentrated higher buildings from 4 floor and up (to about 12 floors) (The center of Stockholm)	

Wood: every kind of tree included in the designation.

G. Brightness Temperature Data

Measurements of the microwave brightness temperature, which are presented in this section, are taken mostly from investigations by The Ohio State University[7,8] and Space-General Corporation.[34,35] The Ohio State data have been corrected by a boot-strap inversion of the integral equation; other data are in raw form. Data are given for a number of surfaces in the following categories: geological, vegetated, and sea. Finally, a comparison is made of the radiometric temperatures for a variety of natural surfaces.

1. Geological surfaces

Figures 140-142 are measured brightness temperatures for asphalt, glacially polished limestone (Marblehead, Ohio), and a smooth coal bed exposed by strip mining operations (Cadiz, Ohio). These surfaces exhibit the characteristic of a specular surface (see Section D).

Radiometric deviation envelopes and mean value curves[34] of barren mud (Palo Alto, California), without vegetation, are presented in Figs. 143 and 144. (The mean value curve is the simple average of all the data recorded at a particular angle). These curves also exhibit the characteristic shape for "smooth" surfaces.

Figures 145 and 146 are the deviation envelopes and mean value curves[34] of the radiometric temperature for La Jolla Beach sand at 13.5 GHz and 37 GHz, respectively. The sand shows a definite polarization dependence at both 13.5 GHz and 37 GHz. Examination of the general shape of the mean sand curves shows that the sand does not appear as a specular surface or a totally diffuse surface, but has some of the characteristics of each.

The brightness temperatures of lapilli (Mono Crater, California) and bare soil (Ohio State University Farms) are shown in Figs. 147 and

148, respectively. As was the case for the La Jolla Beach sand, these surfaces also show a character intermediate between a smooth surface and a diffuse surface.

The radiometric temperatures[35] for two other soil surfaces, silt loam and sandy loam, are presented in Figs. 149 and 130. These data show only the horizontally-polarized component of the brightness.

Figures 151-153 exhibit measurements[7] made at Mono Craters, California, on a sequence of lavas of essentially the same chemical composition but different physical properties, ranging from a very light pumice to obsidian. The brightness temperatures are almost independent of angle of incidence, which is characteristic of a Lambert Law surface, but depend on the density (i.e., the effective dielectric constant) of the material.

Figures 154 and 155 are radiometric measurements[34] collected near Pisgah Craters, California, at 13.5 GHz and 37 GHz, for horizontal and vertical polarizations. The response of a series of thick playa sediments, a thick lava flow, and a 1.5 foot layer of playa sediments covering the lava flow, are shown in each figure. In all cases, the radiometric temperature of the sediments is seen to be substantially different than that for the exposed lava.

2. Vegetated surfaces

Figures 156-164 provide measurements, by the Ohio State University, of X-band brightness temperatures for a number of native agricultural crops including oats, wheat, sorghum, and soybeans. The point of interest is that the oats, wheat, sorghum, and alfalfa surfaces have brightness temperatures ranging from 260°K to 290°K, while the soybean brightness temperatures are somewhat cooler, ranging from 240°K to 270°K. The lower brightness temperatures for the soybean

surface may partially result from irrigation, which decreases the soil temperature (for example, compare soil temperatures for alfalfa in Fig. 160 and soybeans in Fig. 161.

The deviation envelopes and mean values curves[34] for the brightness temperature of marsh foliage (salicornia) at 13.5 GHz and 37 GHz are presented in Figs. 165 and 166. The curves at both frequencies have the characteristics of a completely diffuse surface, i.e., a brightness temperature almost independent of angle of incidence and polarization.

Figures 167-170 are measurements, by Space-General Corporation,[35] of the radiometric temperatures for marsh vegetation, pasture grass, flowers, and celery crops. It is interesting to note that the brightness temperatures at 94 GHz for the grass, flower, and celery surfaces, are lower than at the longer wavelengths.

3. Sea surface

Figure 171(a) shows measured brightness temperatures, by Nordberg,[36] of a "smooth" and "rough" portion of the Salton Sea. The "smooth" data agrees quite well with the theoretical curve calculated by Stogryn[37] for a smooth sea. The "rough" data, however, are significantly higher than what would be predicted for a rough sea; it is presumed that the higher brightness temperature is due to the higher emissivity of foam patches over the rough sea. Figure 171(b) shows tower based measurements by Hollinger[39] at 1.4, 8.4 and 19.3 GHz, under conditions where the wind velocity and sea state could be carefully monitored. These measurements exhibit the behavior predicted by Stogryn, and confirm the concept that the brightness temperature is controlled by the slope distribution as long as foam is absent.

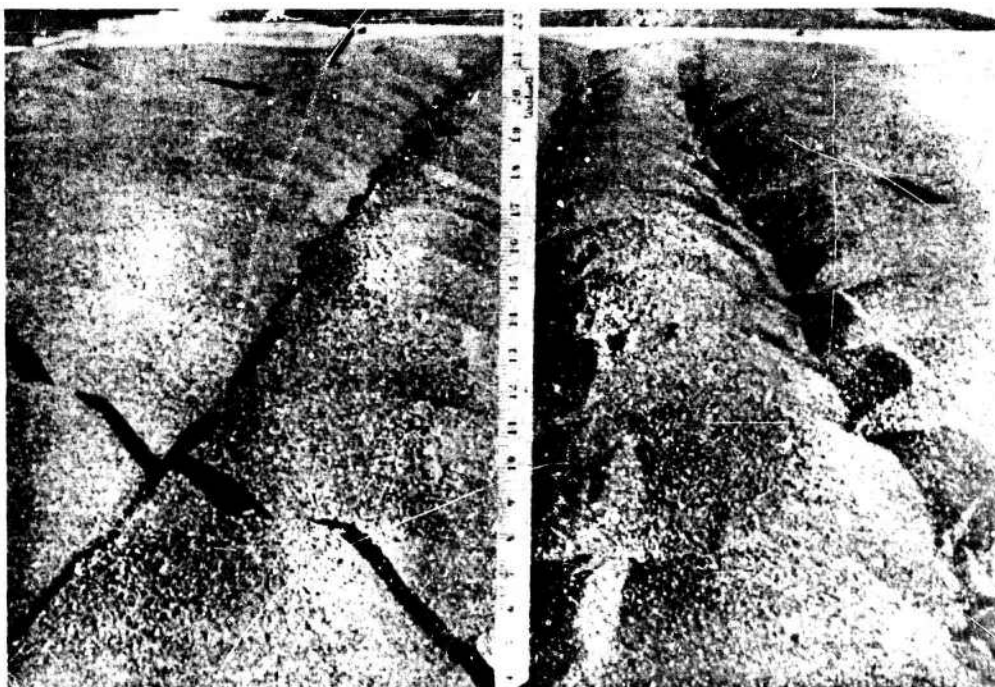
Figures 172 and 173 are data[34] for Palo Alto Sea water at 13.5 GHz and 37 GHz, respectively. Comparisons between 13.5 GHz and 37 GHz show the 37 GHz temperatures are from 30°K to 70°K hotter than those from 13.5 GHz.

4. Comparison of measured data

Figures 174-176 present some general comparisons of measured radiometric temperatures of a variety of surfaces at 13.5 GHz, 37 GHz, and 35 GHz, for horizontal and vertical polarizations. The data[34] in Figs. 174 and 175, are composites of the mean value curves presented in the previous section. These curves illustrate the effects of surface roughness and moisture content (mud and inundated mud). The 35 GHz data in Fig. 176 are older data[36] which are seen to agree favorably with the more recent data of Figs. 174-175.



Loam with stubble



NOT REPRODUCIBLE

Rough sand

Fig. 21

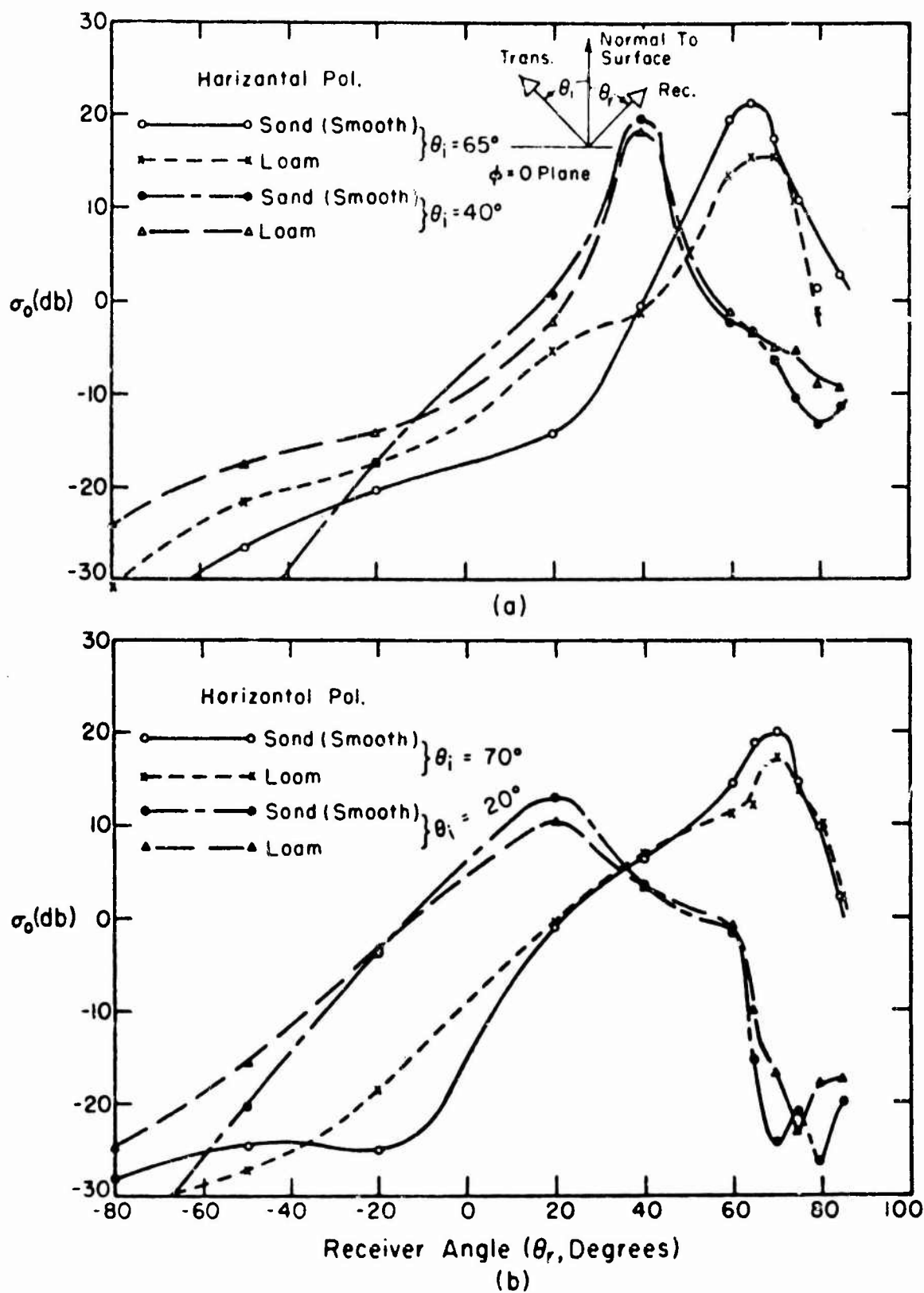
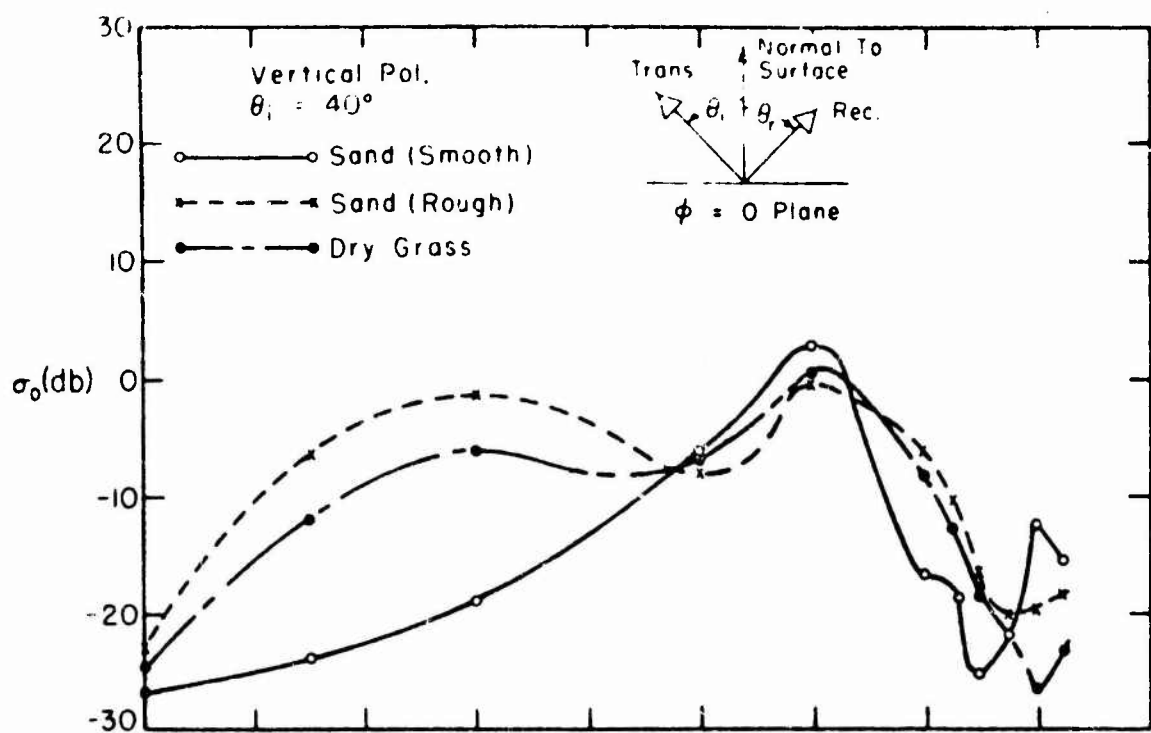
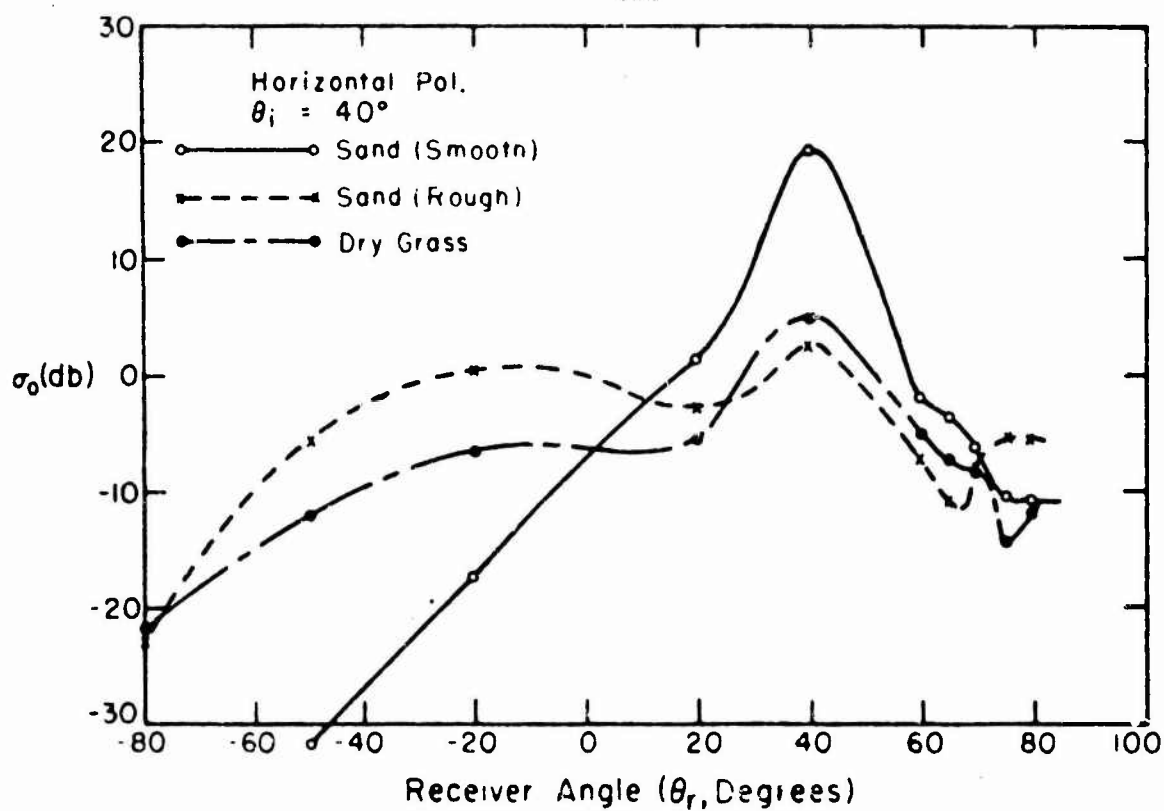


Fig. 22. Bistatic scattering cross sections, in the plane of incidence, for smooth sand and loam.

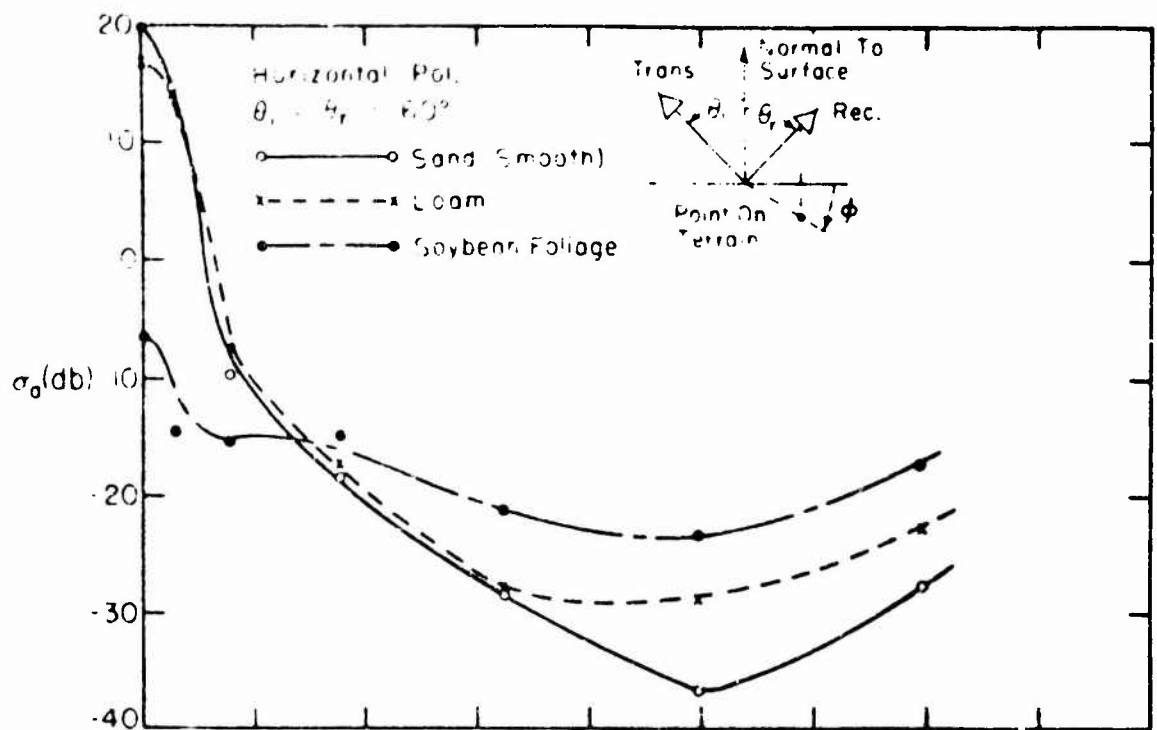


(a)

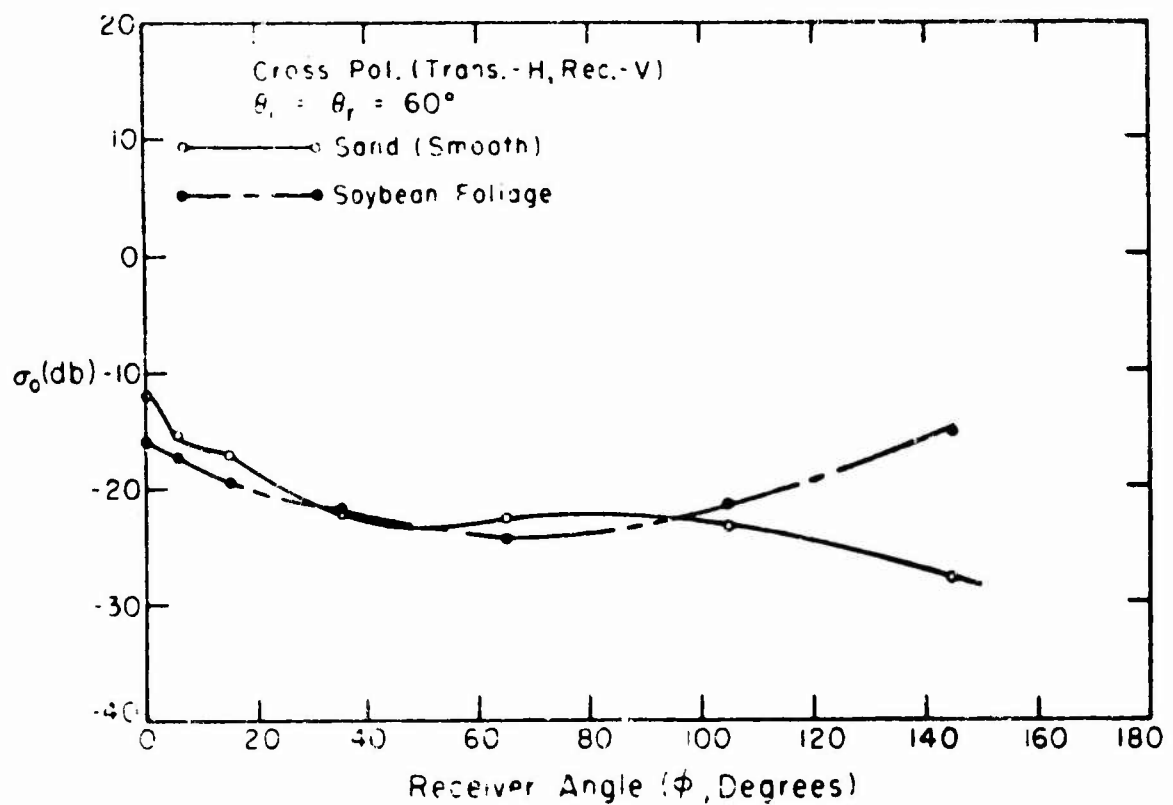


(b)

Fig. 23. Bistatic patterns for smooth sand, dry grass, and rough sand.



(a)



(b)

Fig. 24. Bistatic scattering behavior, in the azimuth cone, for smooth sand, loam, and soybean foliage.

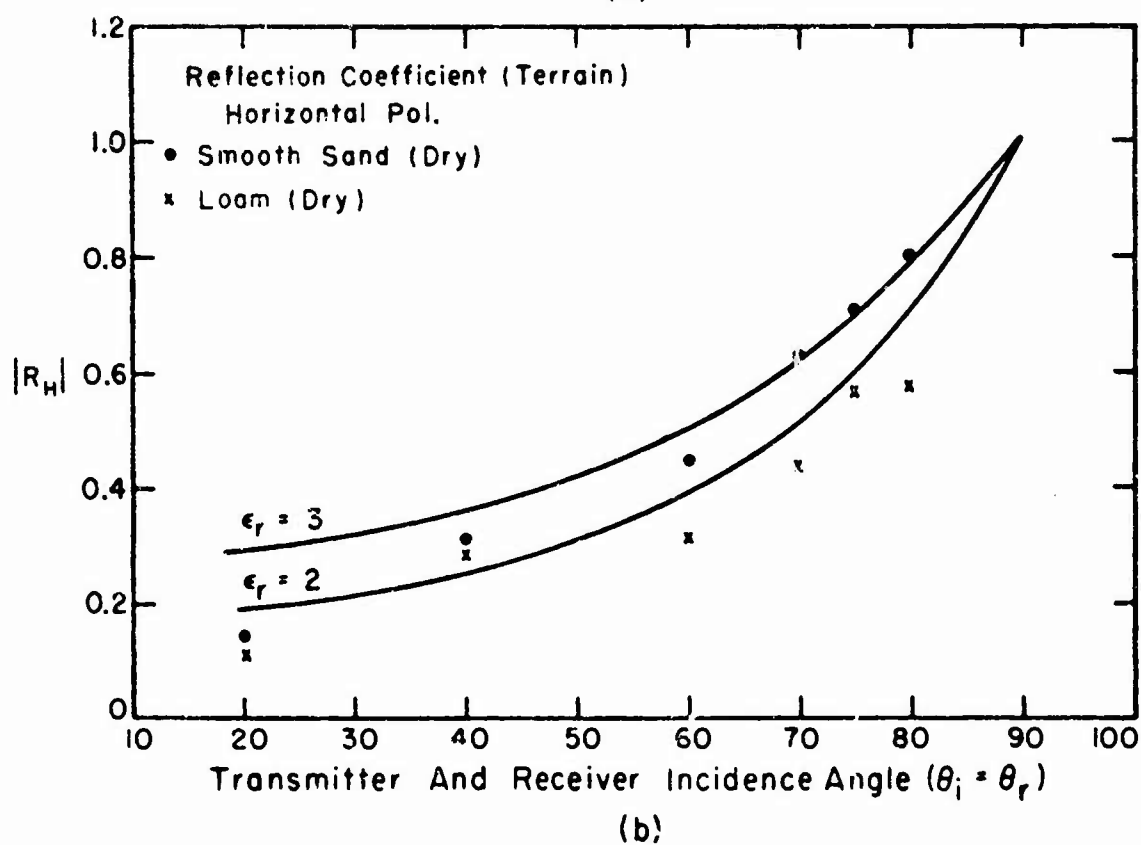
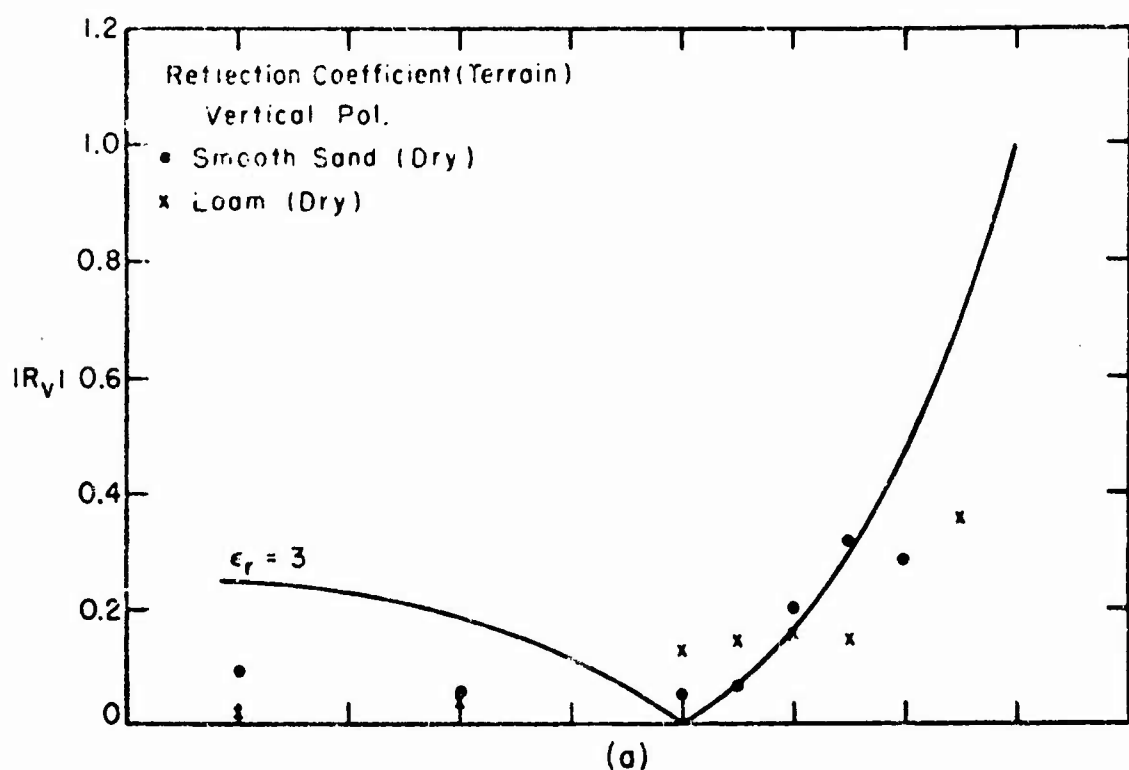


Fig. 25. Experimental and theoretical reflection coefficients; solid curves are theoretical values for smooth surfaces - Reference 1.

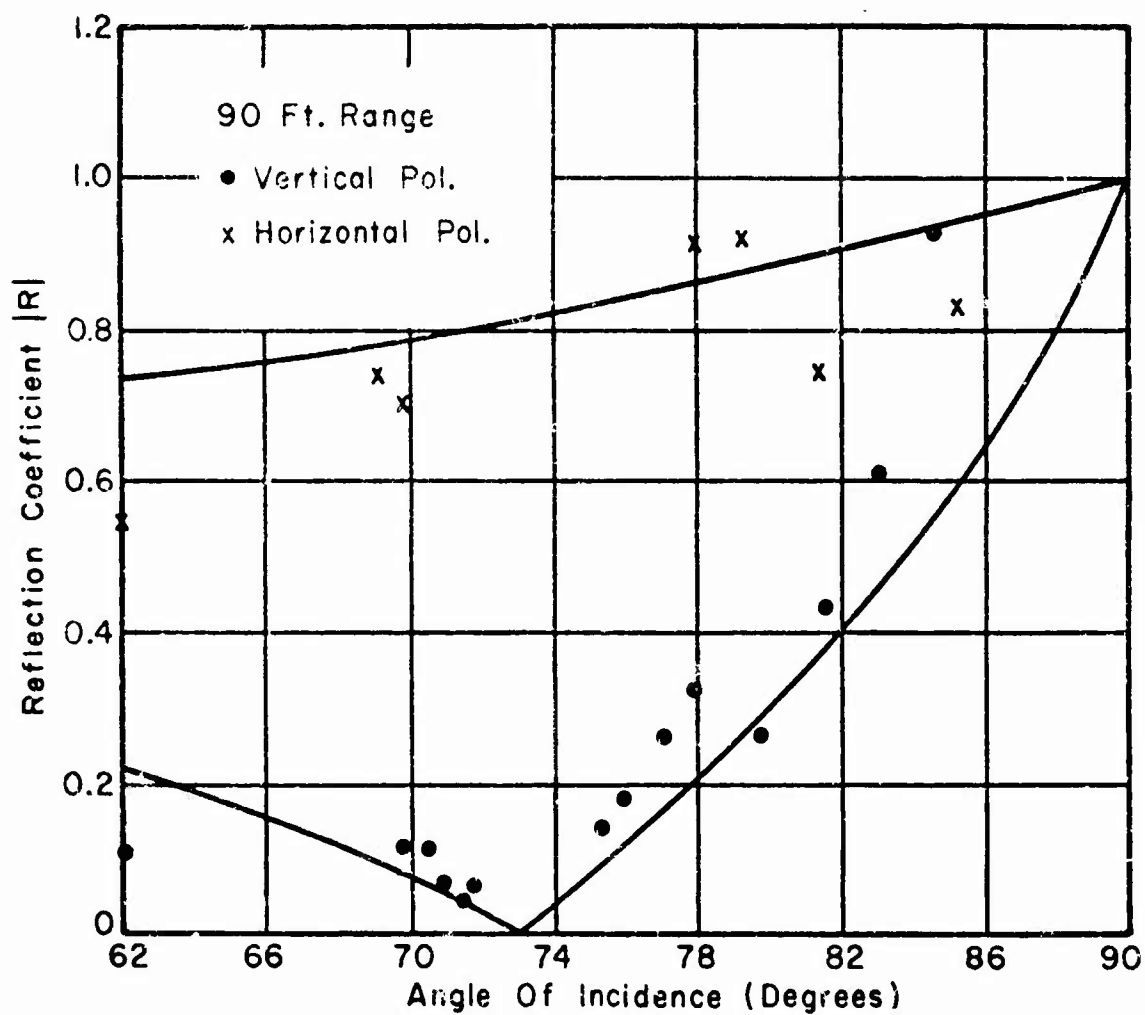


Fig. 26. Reflection coefficients measured by Sherwood and Ginzton for a tidal flat with some organic material; solid curves are theoretical for $\epsilon_r = 10$ - Reference 9.

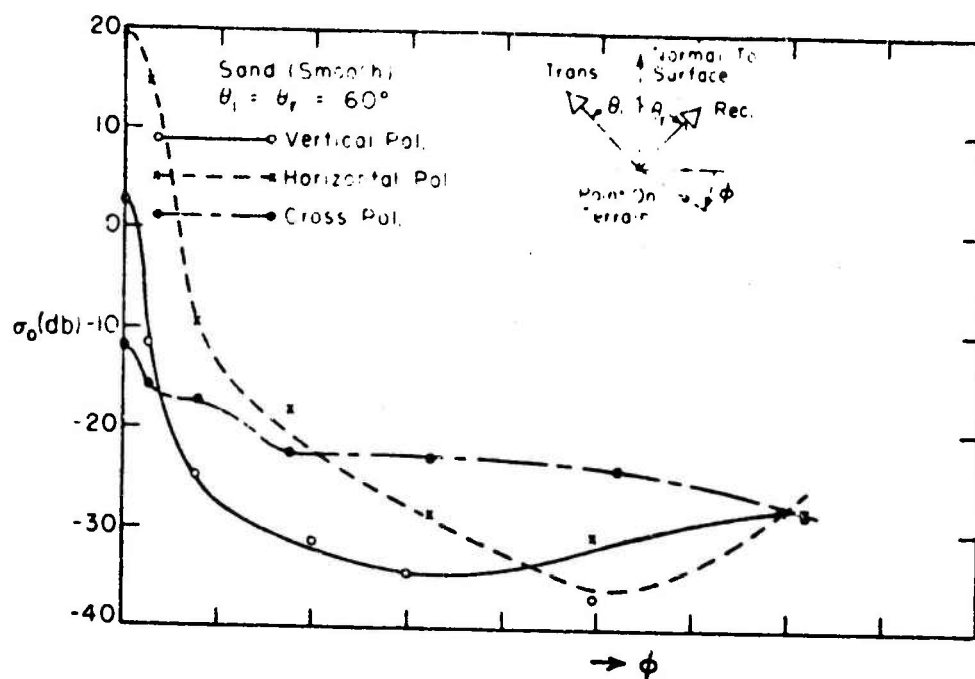


Fig. 27. Effects of polarization on the azimuthal bistatic scattering pattern for smooth sand.

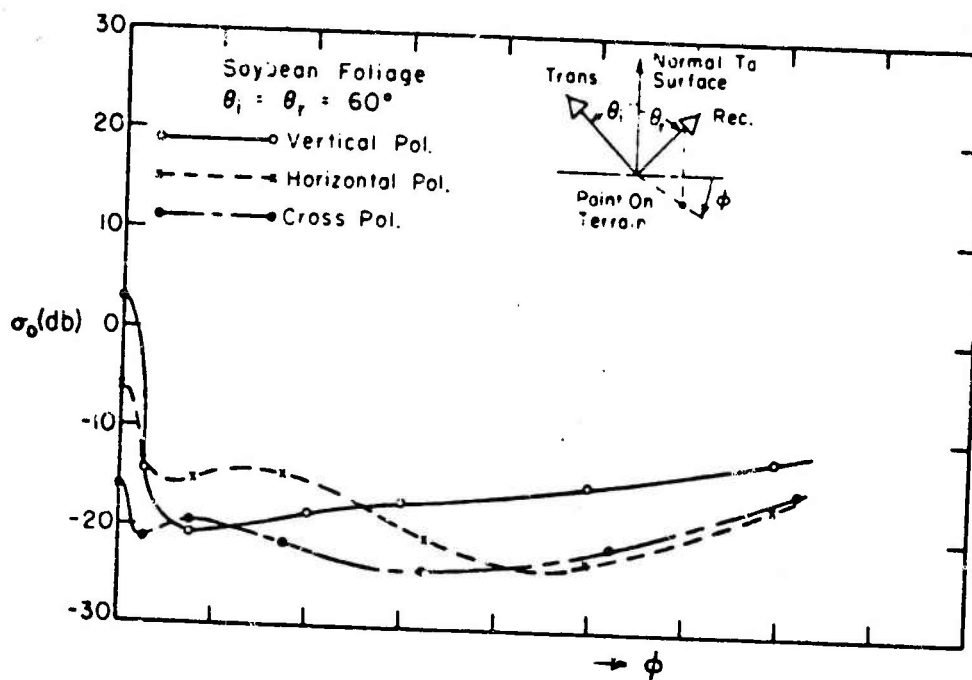


Fig. 28. Effects of polarization on the azimuthal bistatic scattering pattern for soybean foliage.

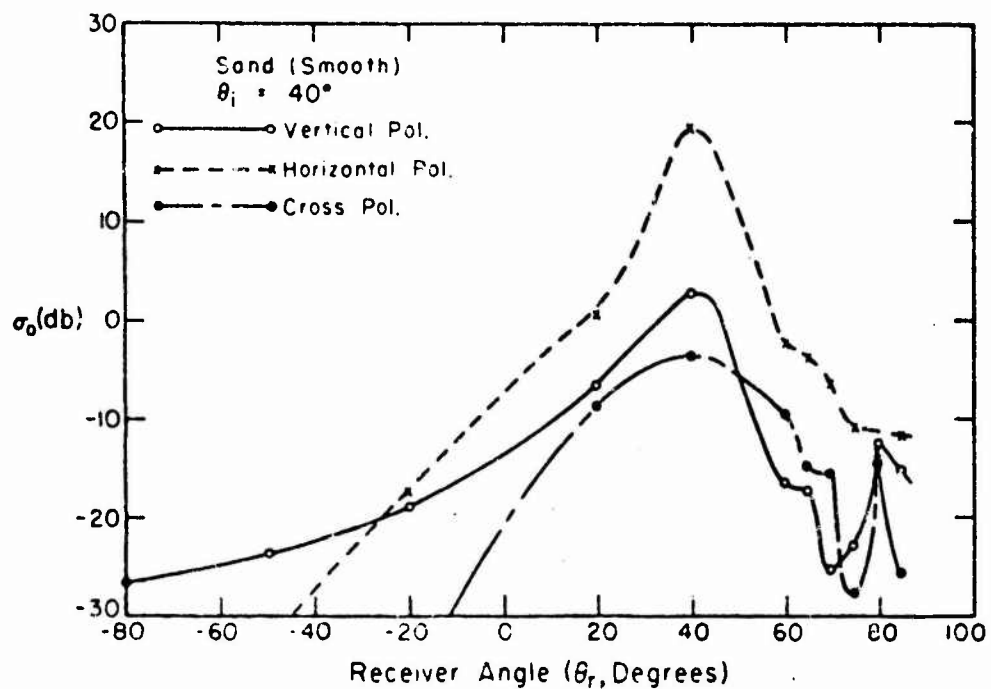


Fig. 29. Effects of polarization on the bistatic cross section, in the plane of incidence, for smooth sand.

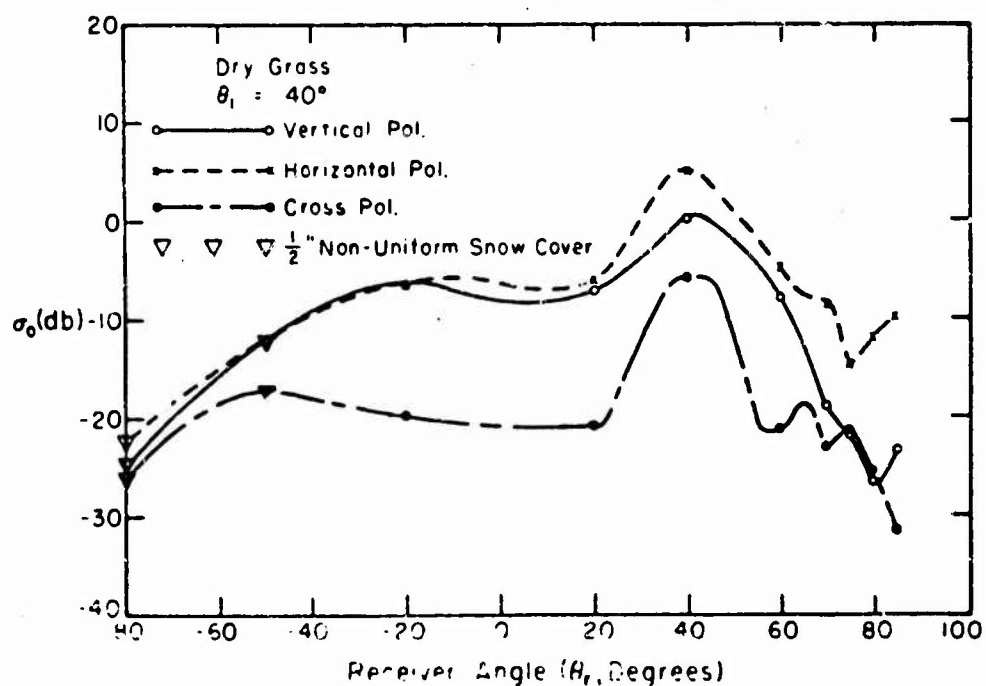


Fig. 30. Effects of polarization on the bistatic cross section, in the plane of incidence, for dry grass.

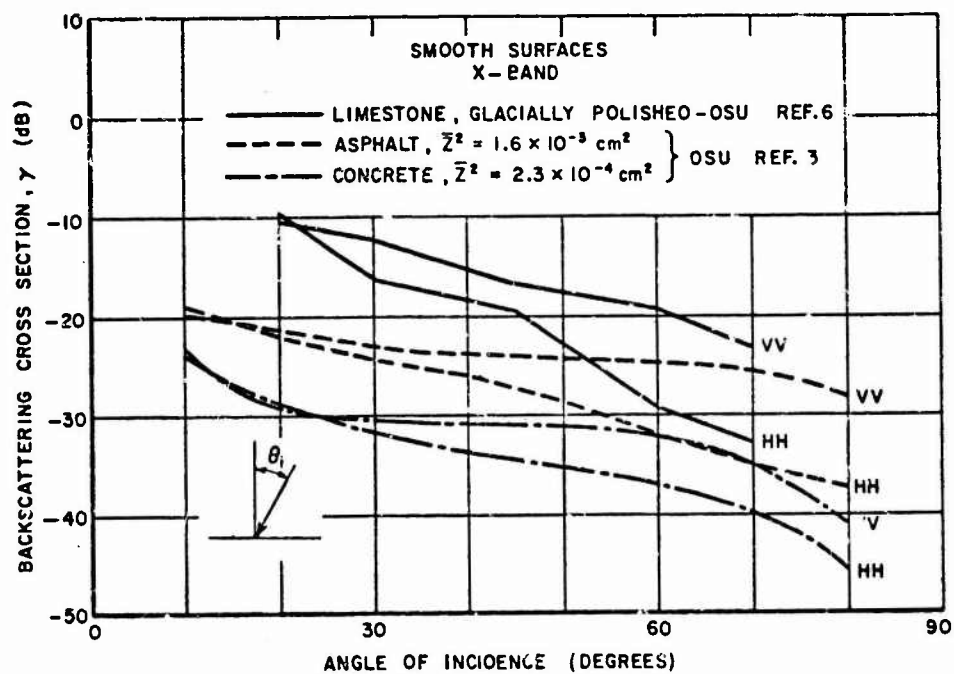


Fig. 31. Radar backscattering cross sections for three smooth surfaces (limestone, asphalt, and concrete) at X-band.

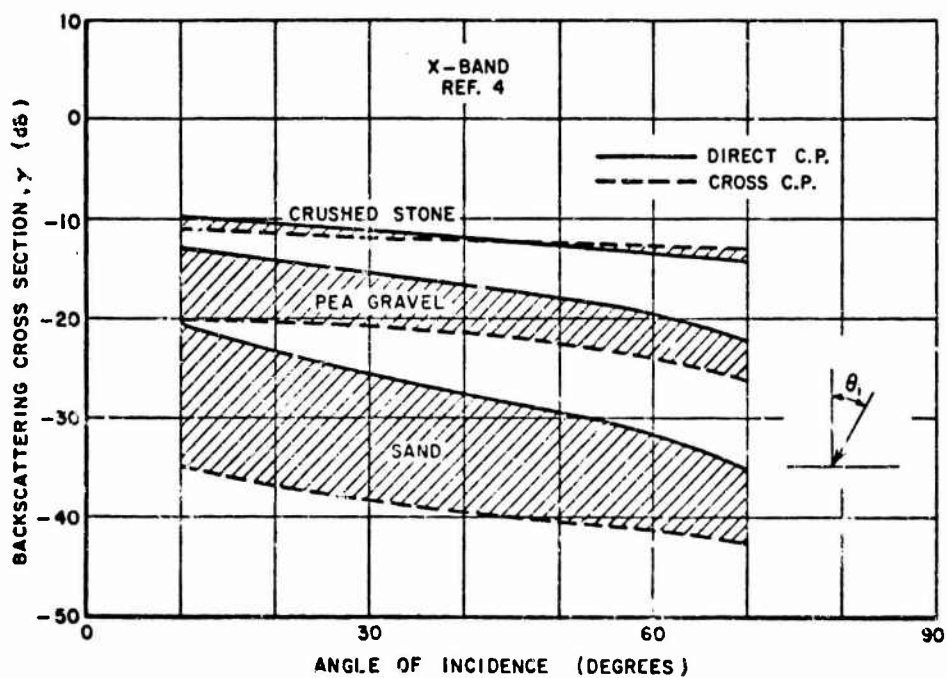


Fig. 32. Radar backscattering cross sections for three rubble type surfaces (sand, pea gravel, and crushed stone) at X-band. C.P. (Circular Polarization)

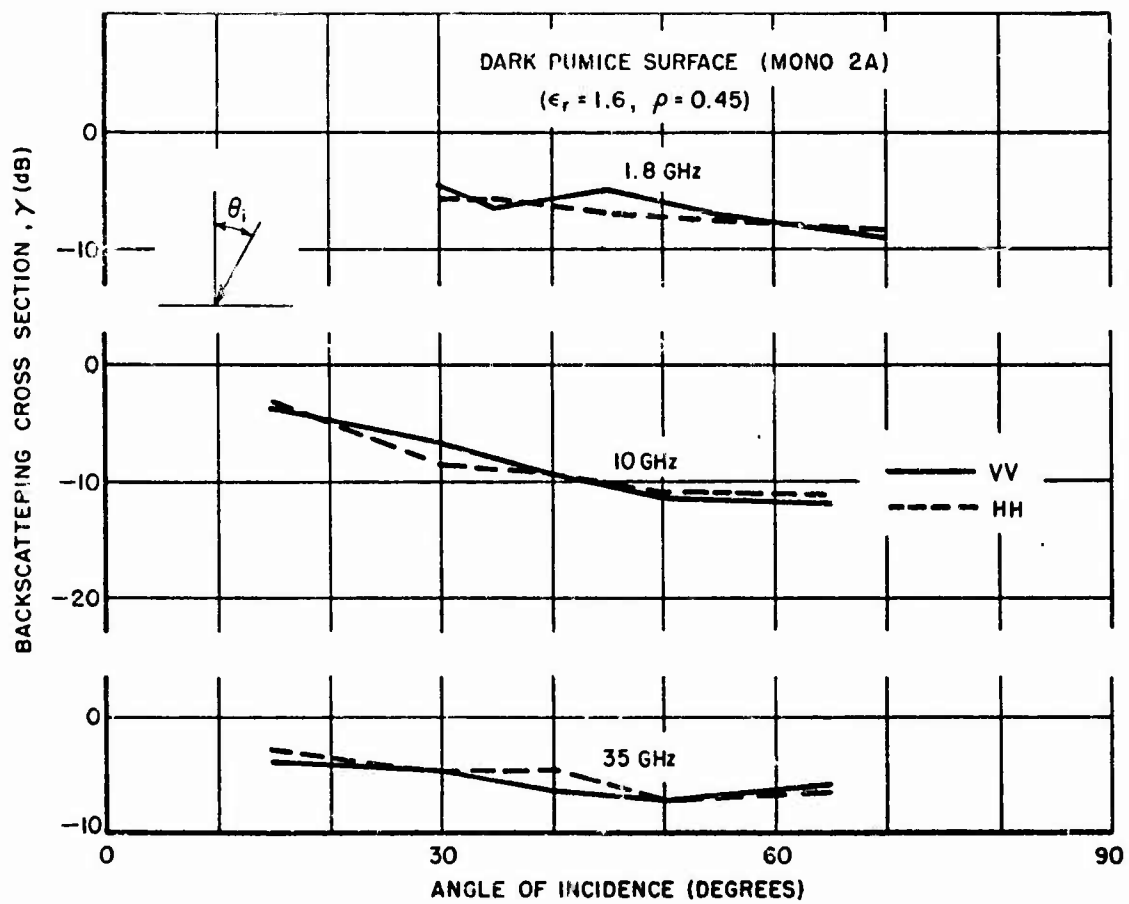
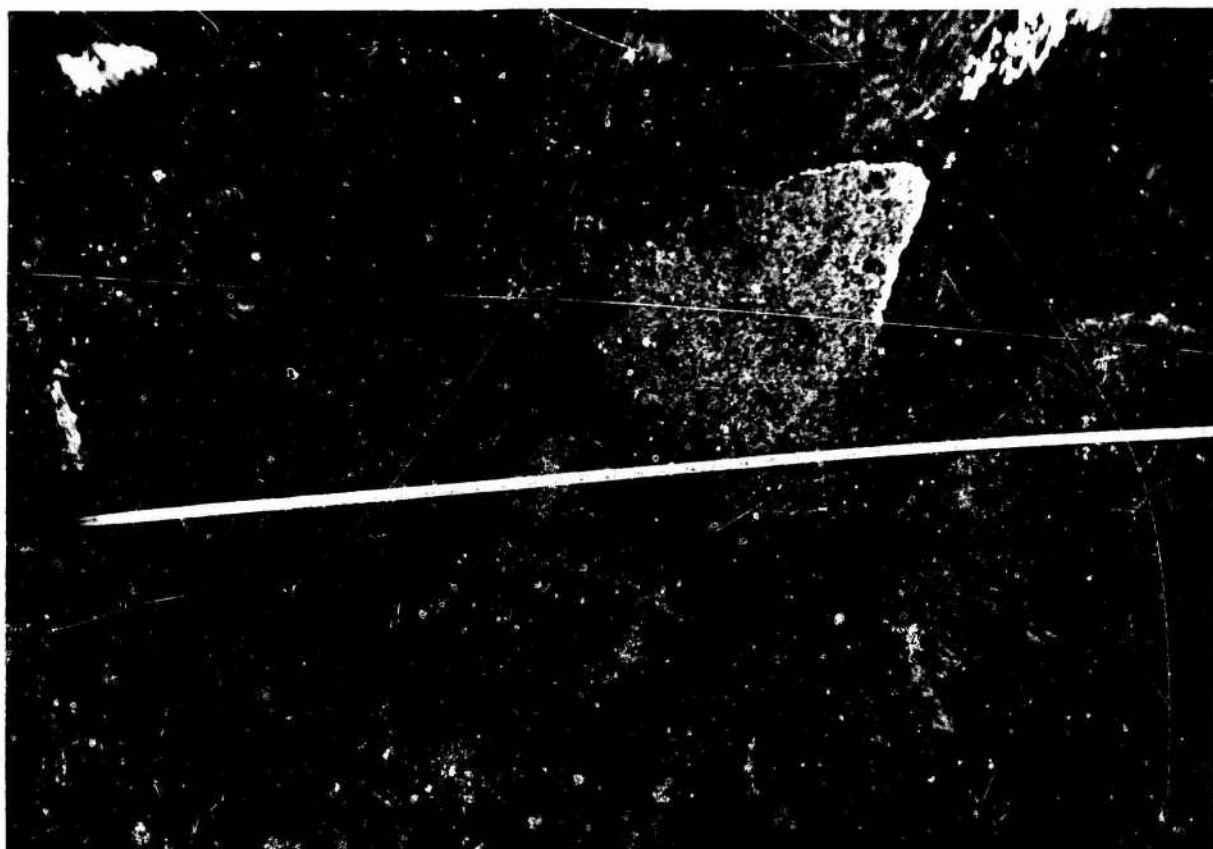


Fig. 33. Radar backscattering cross section for large blocks of pumice at Mono Crater, California. (ρ = density)



NOT REPRODUCIBLE

Fig. 34. Pumice blocks at Mono Crater. The photograph shows the large angular blocks of pumice that underlie the rugged topography near the summit of one of the Mono Craters. Note the large size of the vesicles. The scale is in inches.

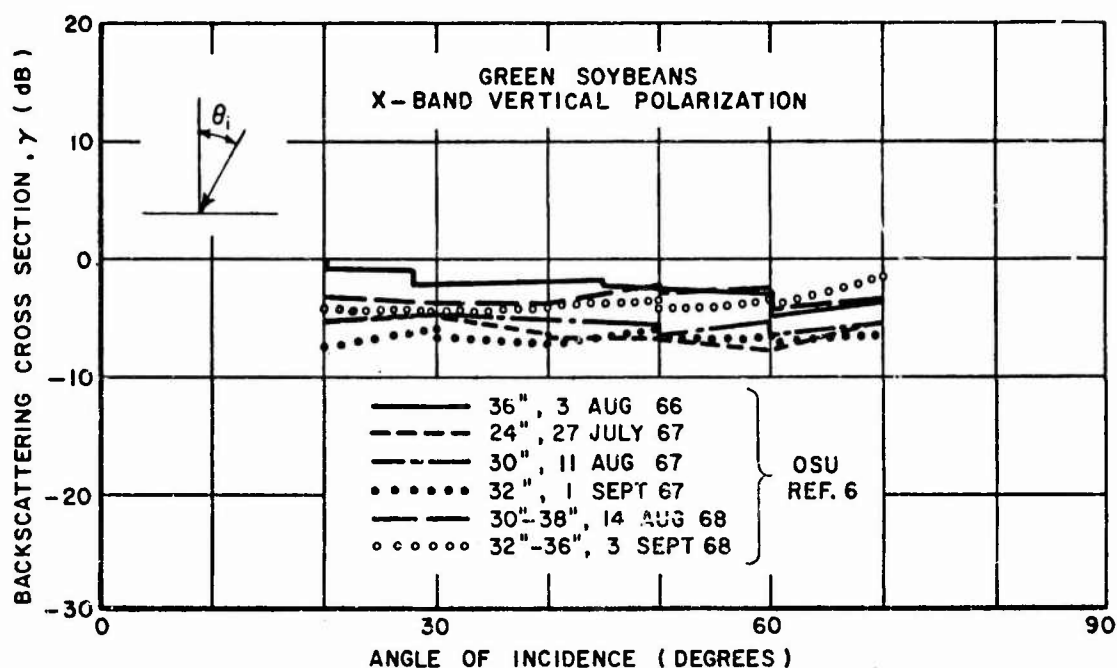


Fig. 35. Radar backscatter for green soybeans at X-band.

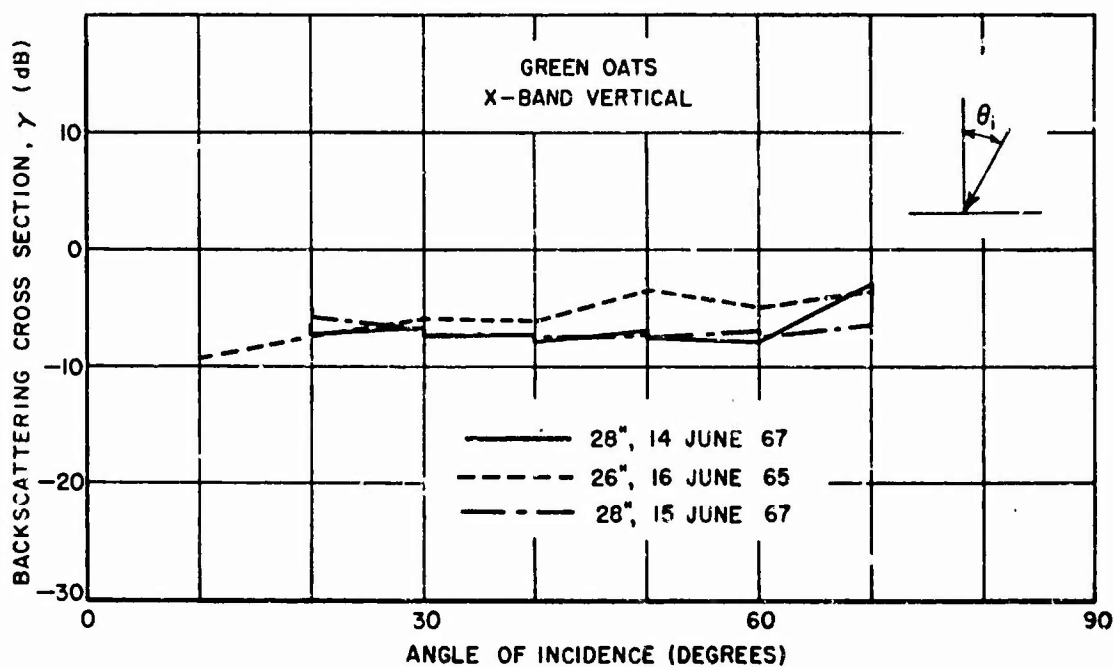


Fig. 36. Radar backscatter for green oats at X-band - Reference 6. (Stepped data indicates variability of measurements made on same day)

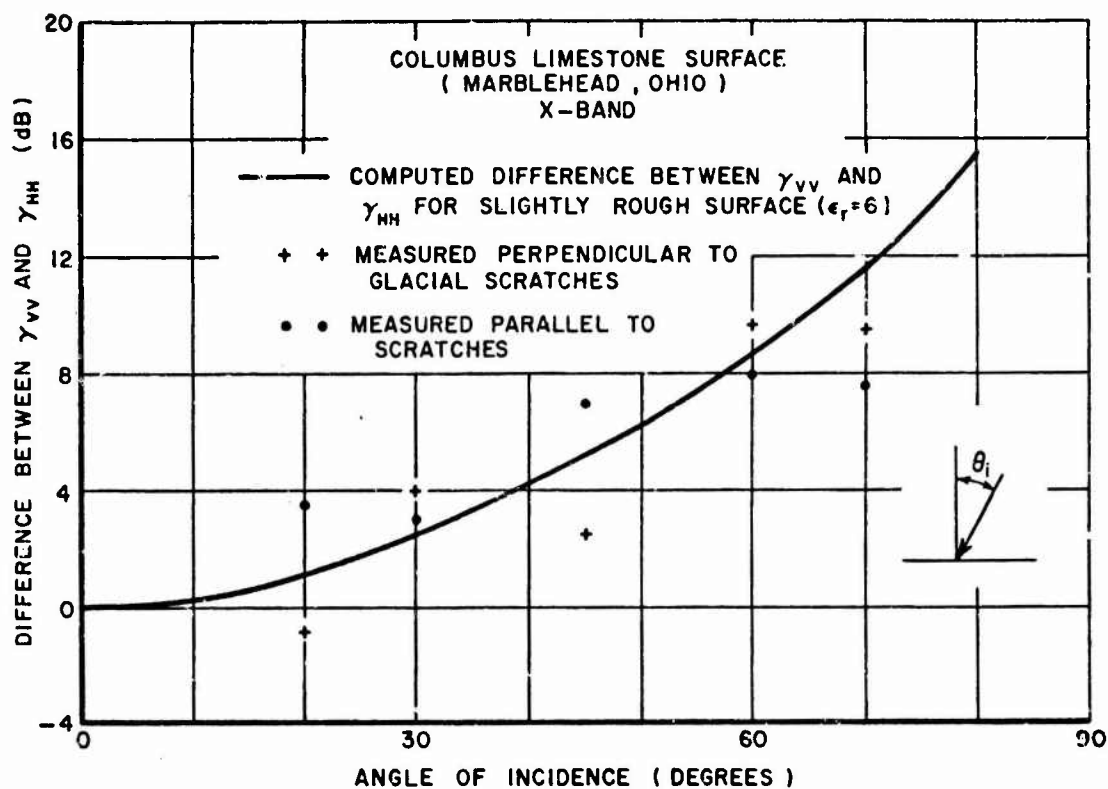


Fig. 37. Measured and computed difference between vertical and horizontal backscatter for "smooth" limestone at X-band.

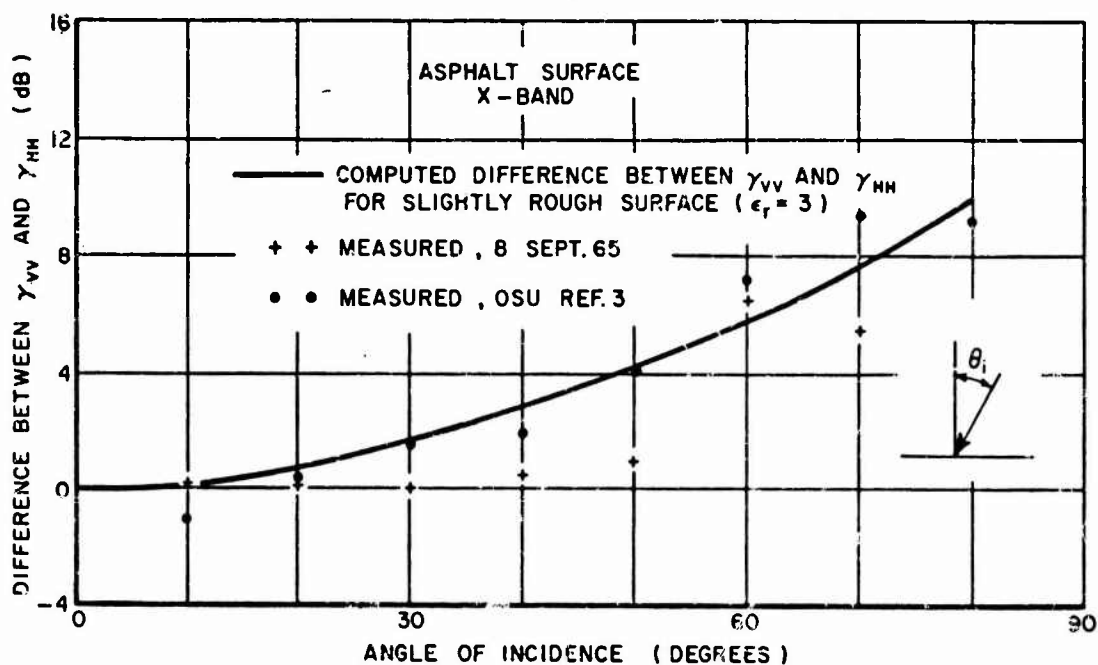


Fig. 38. Measured and computed difference between vertical and horizontal backscatter for "smooth" asphalt at X-band.

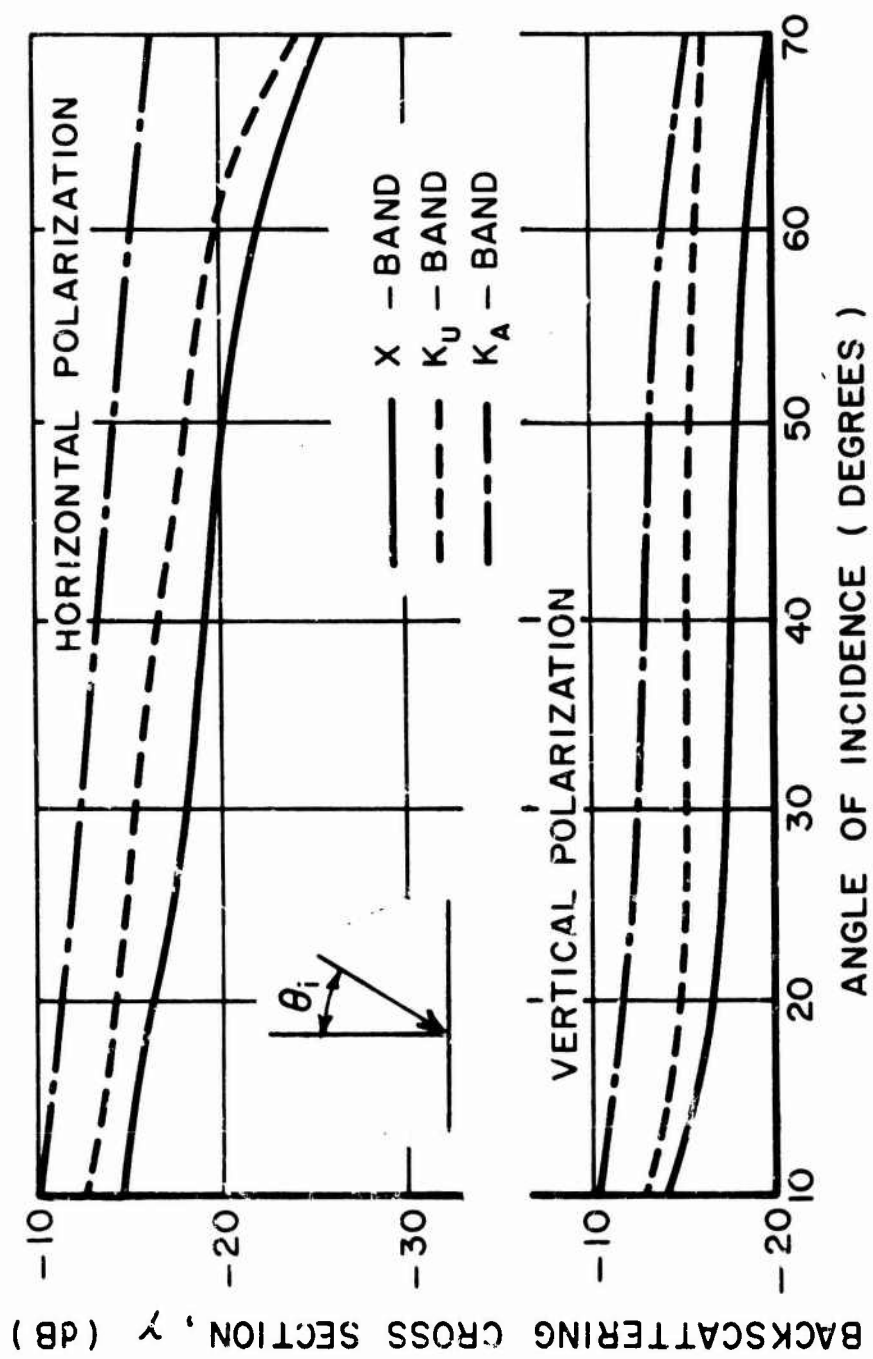


Fig. 39. Angular dependence of the radar backscatter for slightly rough gravel; average diameter of rounded gravel ≈ 1 cm. - Reference 4.

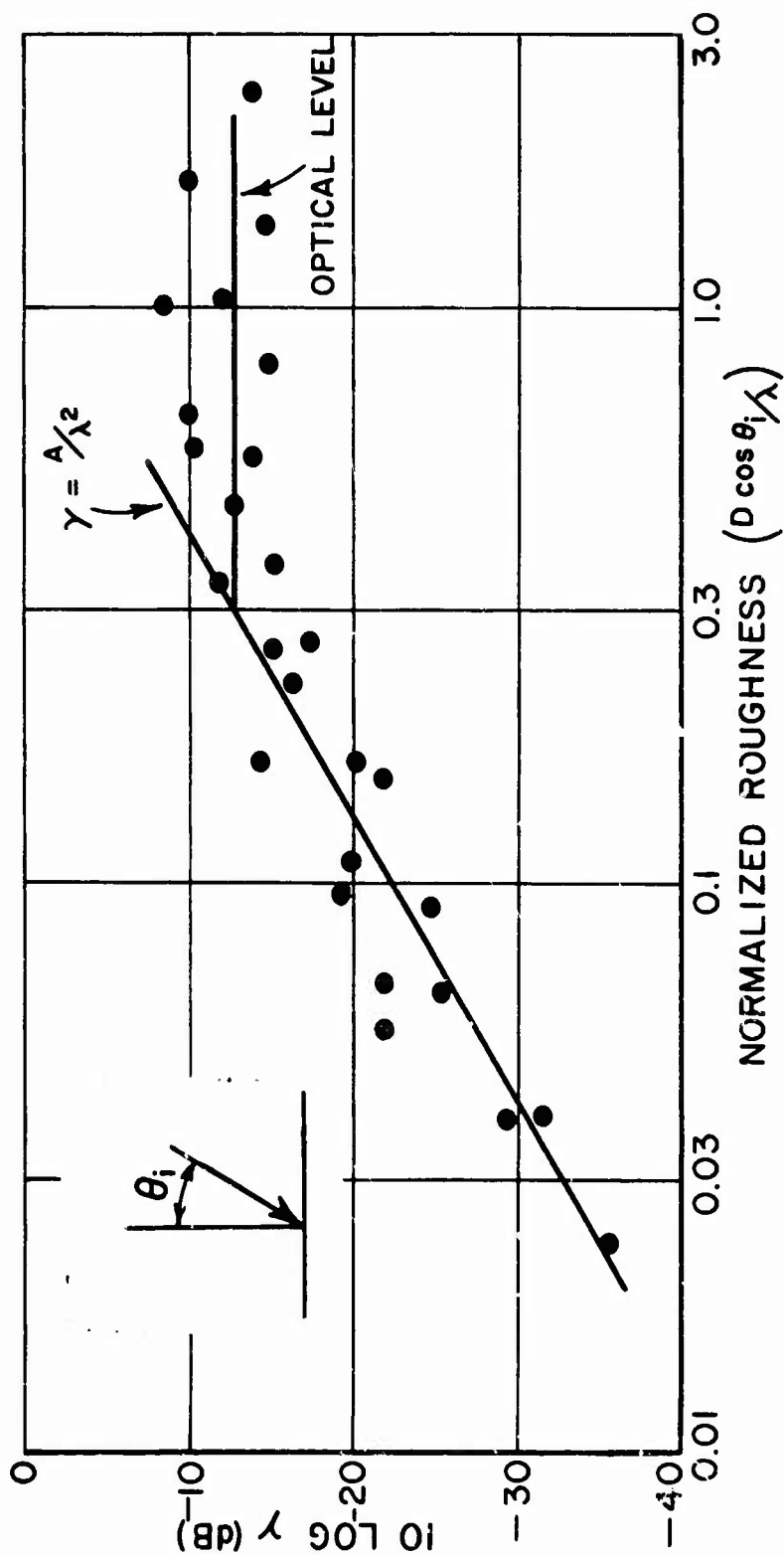


Fig. 40. Radar return vs. normalized roughness for crushed stone, gravel, and sand surfaces at X-, K_u-, and K_a-bands - Reference 4.

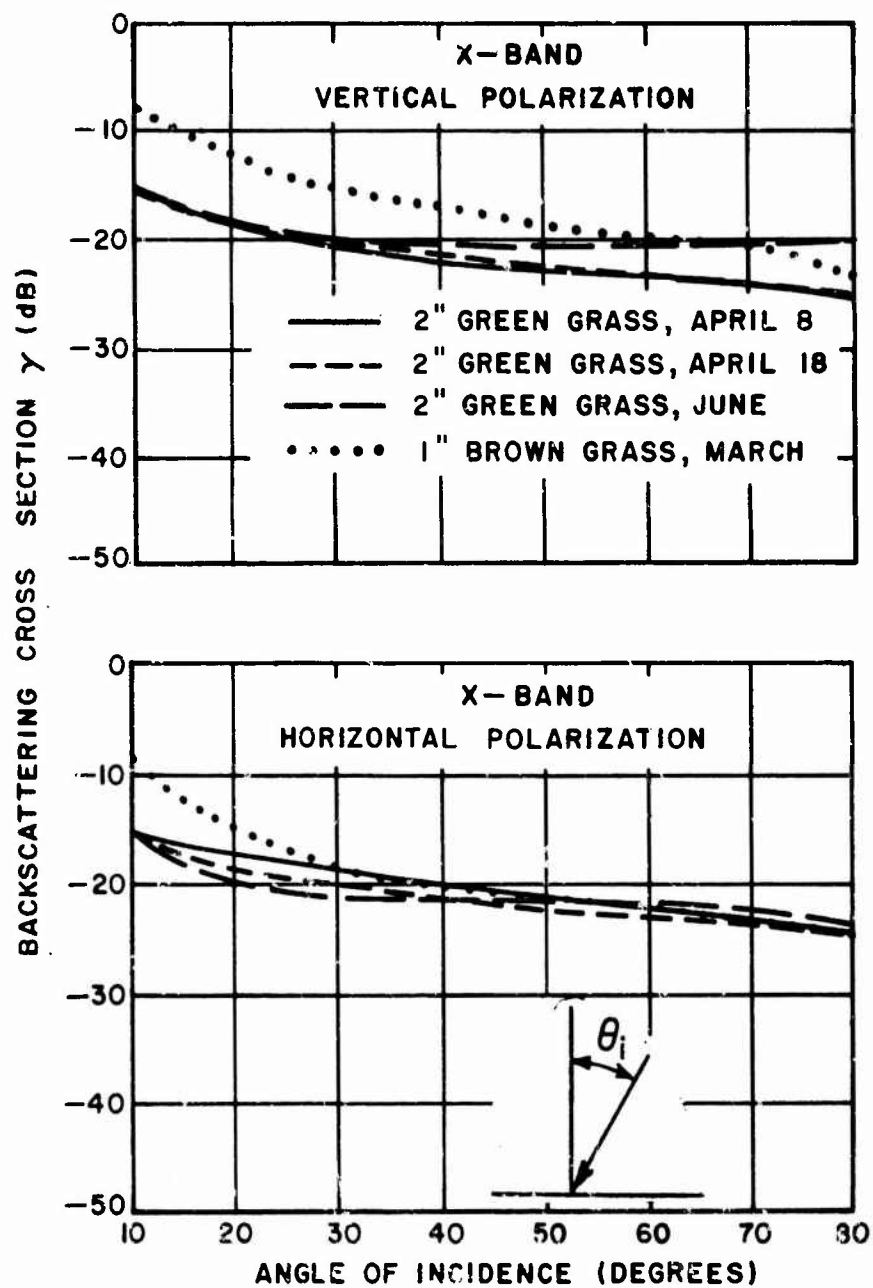


Fig. 41. Seasonal changes of grass at X-band - Reference 3.

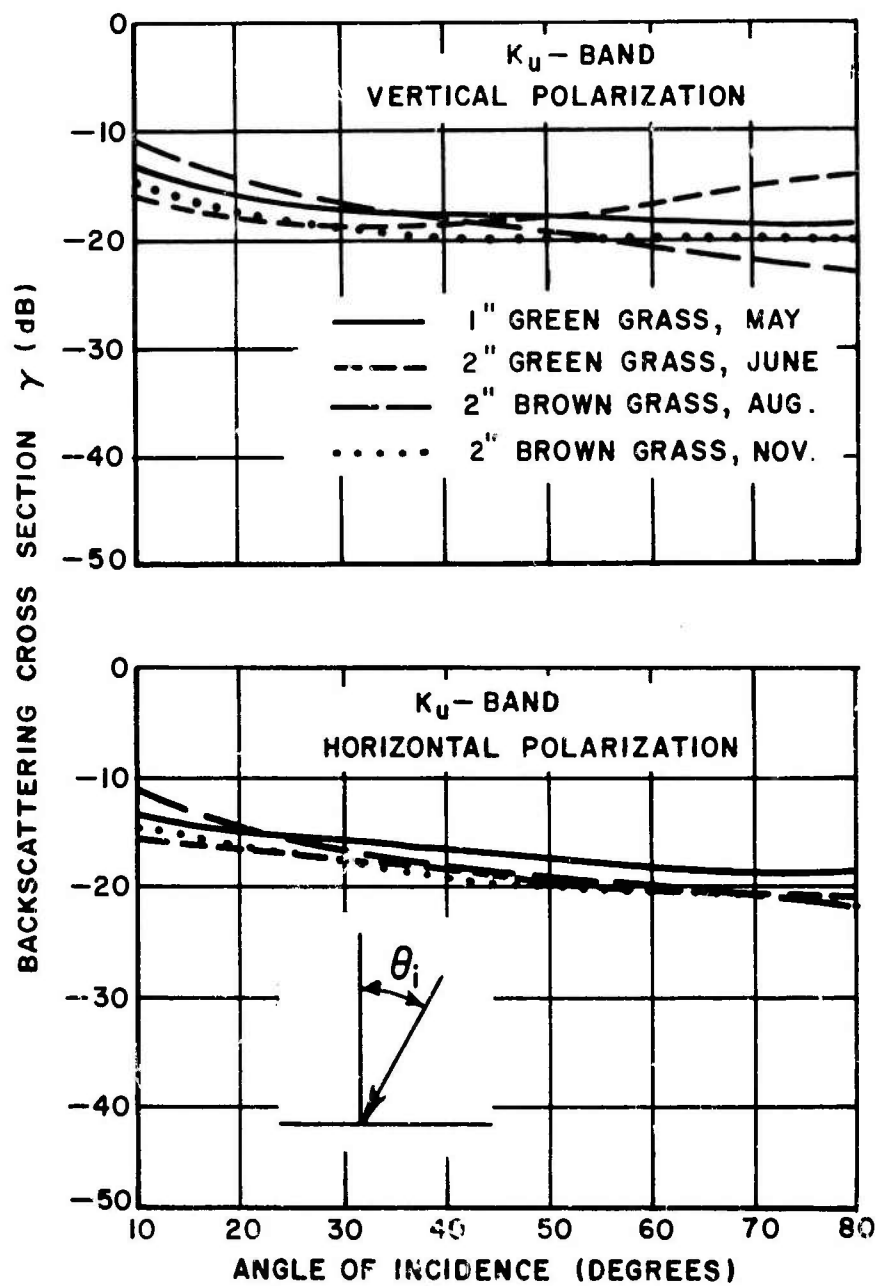


Fig. 42. Seasonal changes of grass at K_u-band - Reference 3.

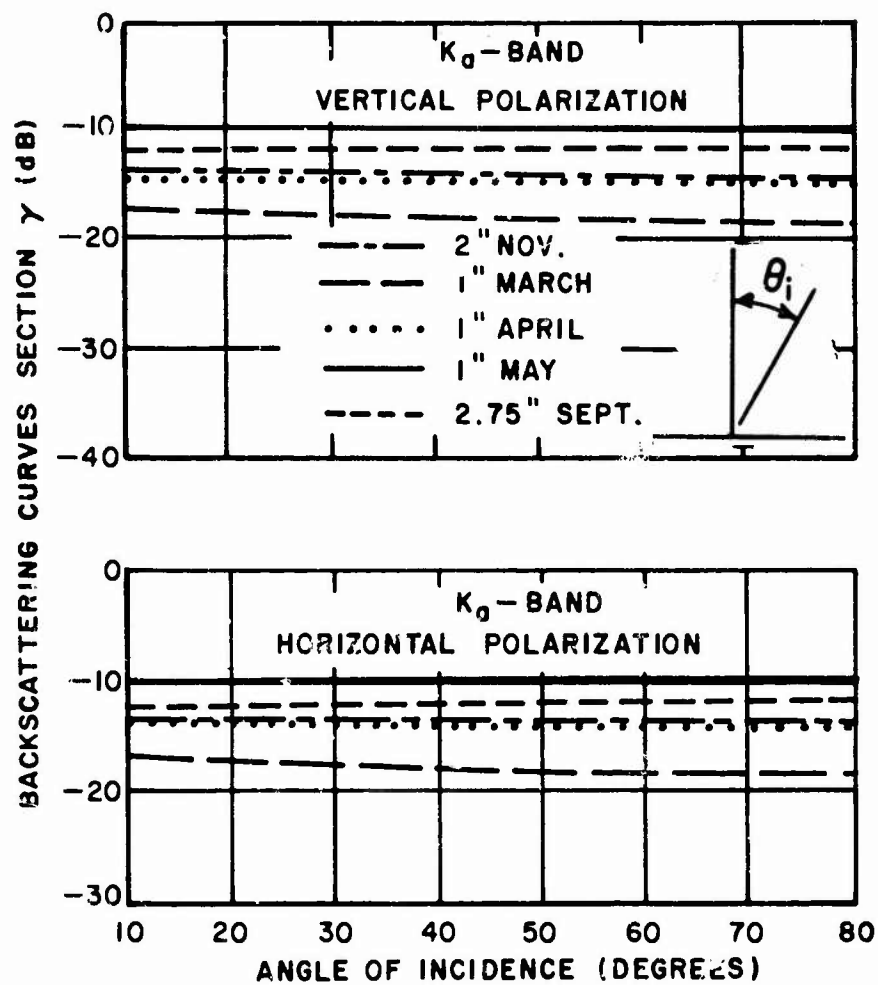


Fig. 43. Seasonal changes of grass at K_a-band - Reference 3.

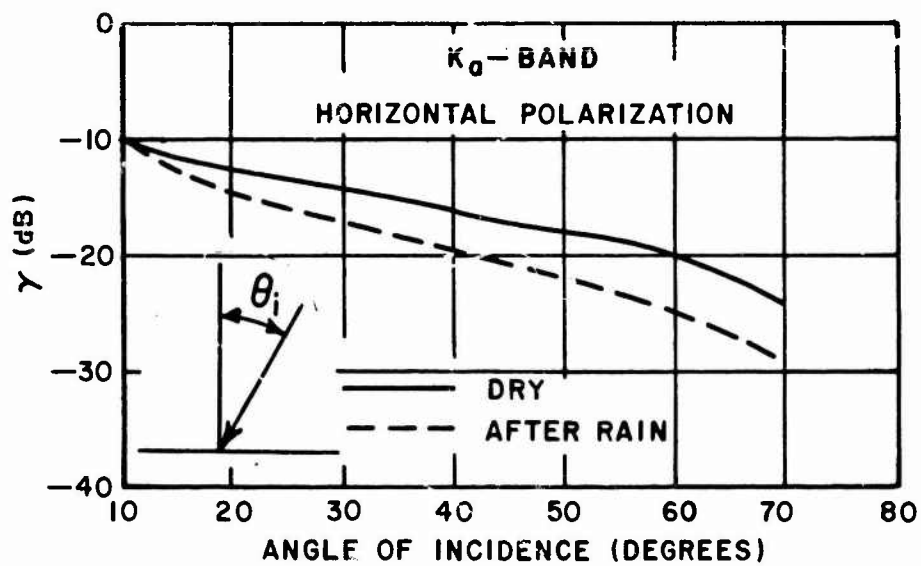


Fig. 44. Effects of rain on a smooth asphalt road at K_a-band - Reference 3.

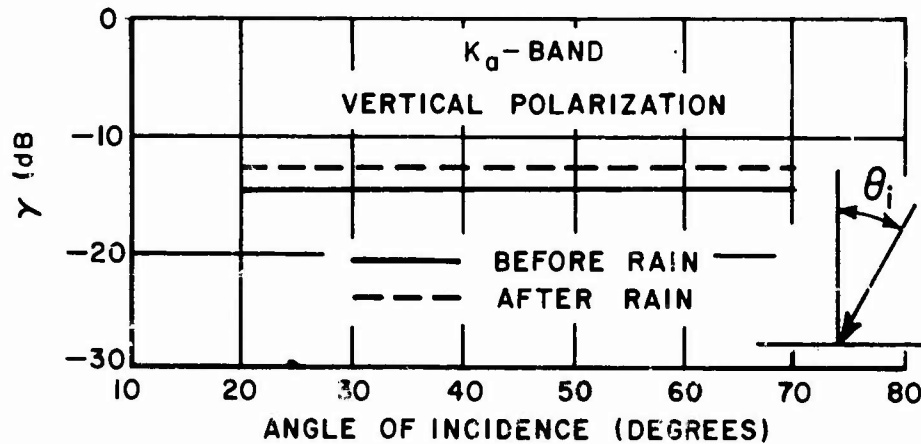


Fig. 45. Effects of rain on two-inch grass at K_a-band - Reference 3.

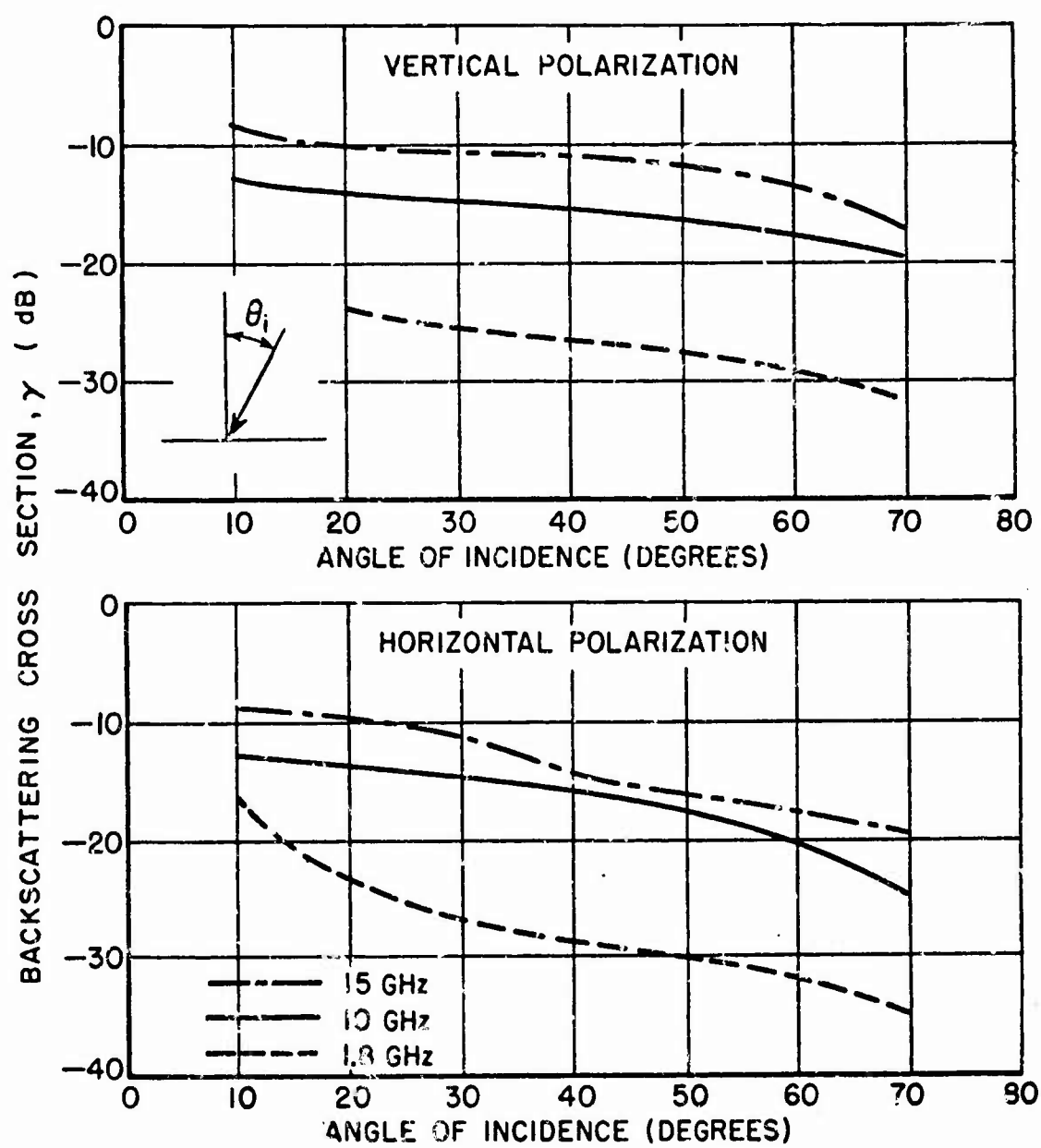


Fig. 46. Frequency dependence of radar backscattering for a smooth asphalt surface. (Roughness $\approx 0.3\text{mm}$)

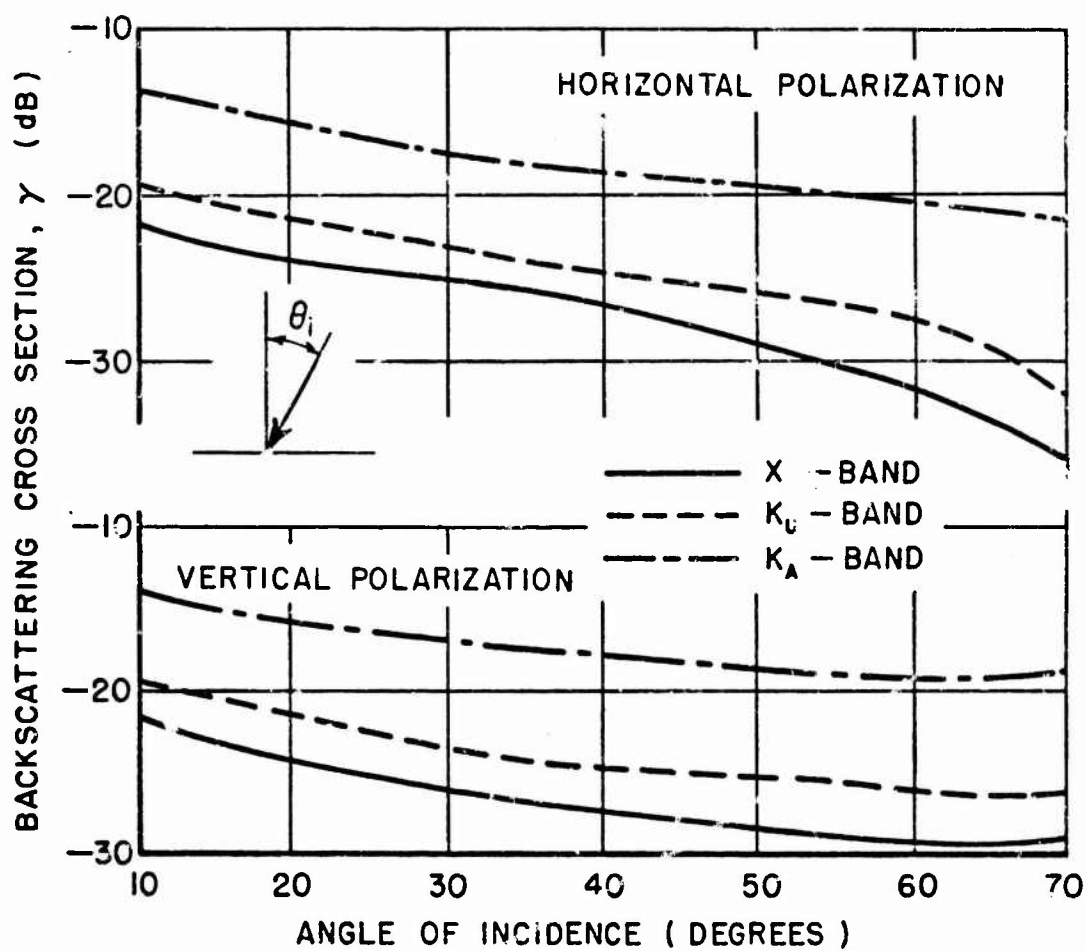


Fig. 47. Frequency dependence of radar backscattering for a smooth sand surface - Reference 4.

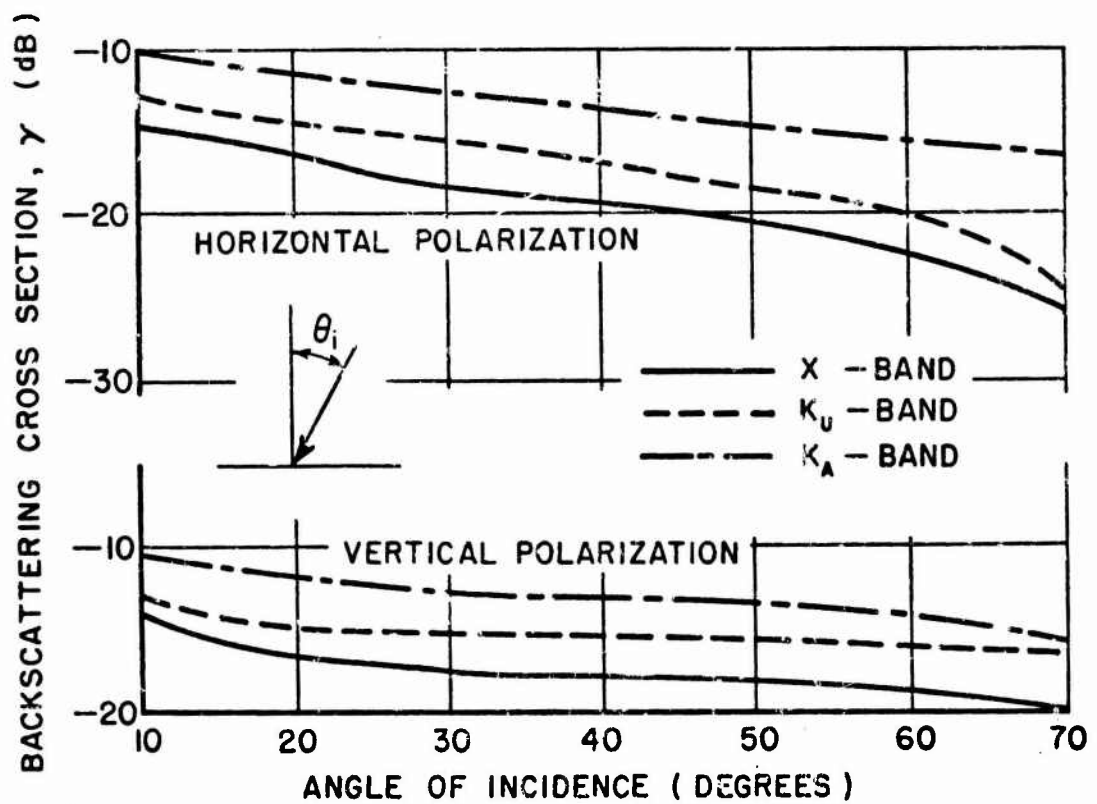


Fig. 48. Frequency dependence of radar backscattering for a slightly rough gravel surface; average diameter of rounded gravel ≈ 1 cm - Reference 4.

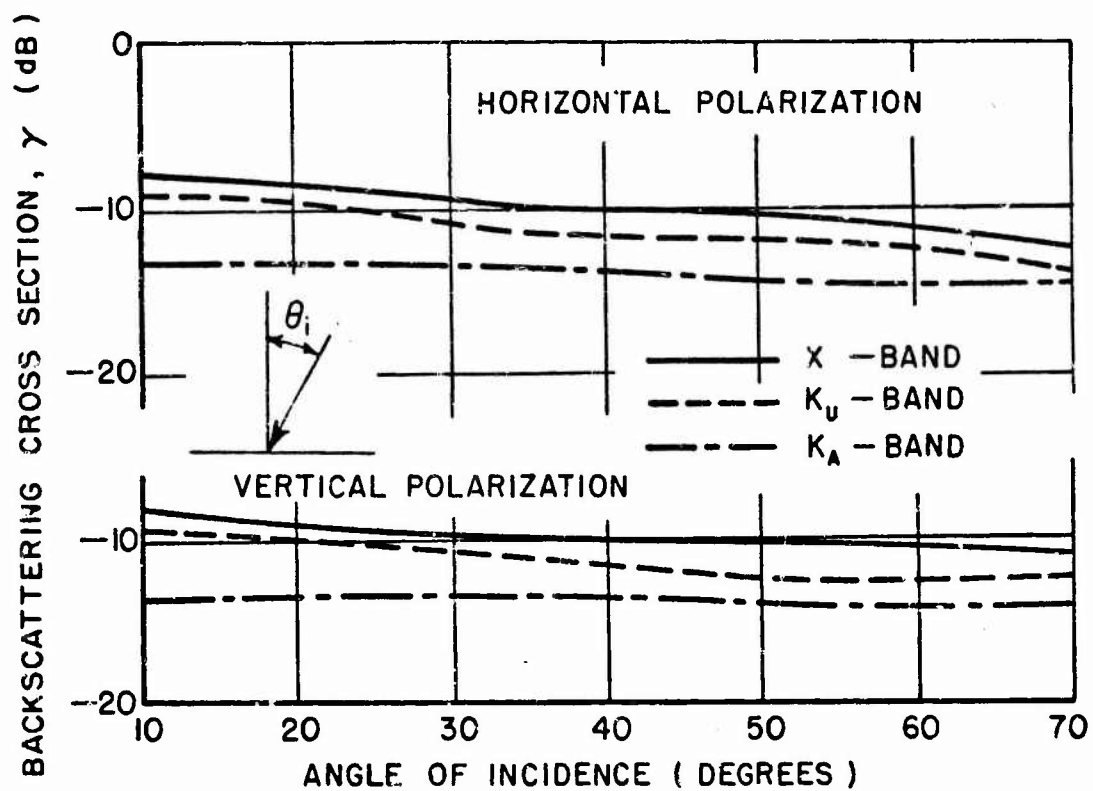


Fig. 49. Frequency dependence of radar backscattering for a rough crushed stone surface; average diameter of stone = 3 to 5 cm - Reference 4.

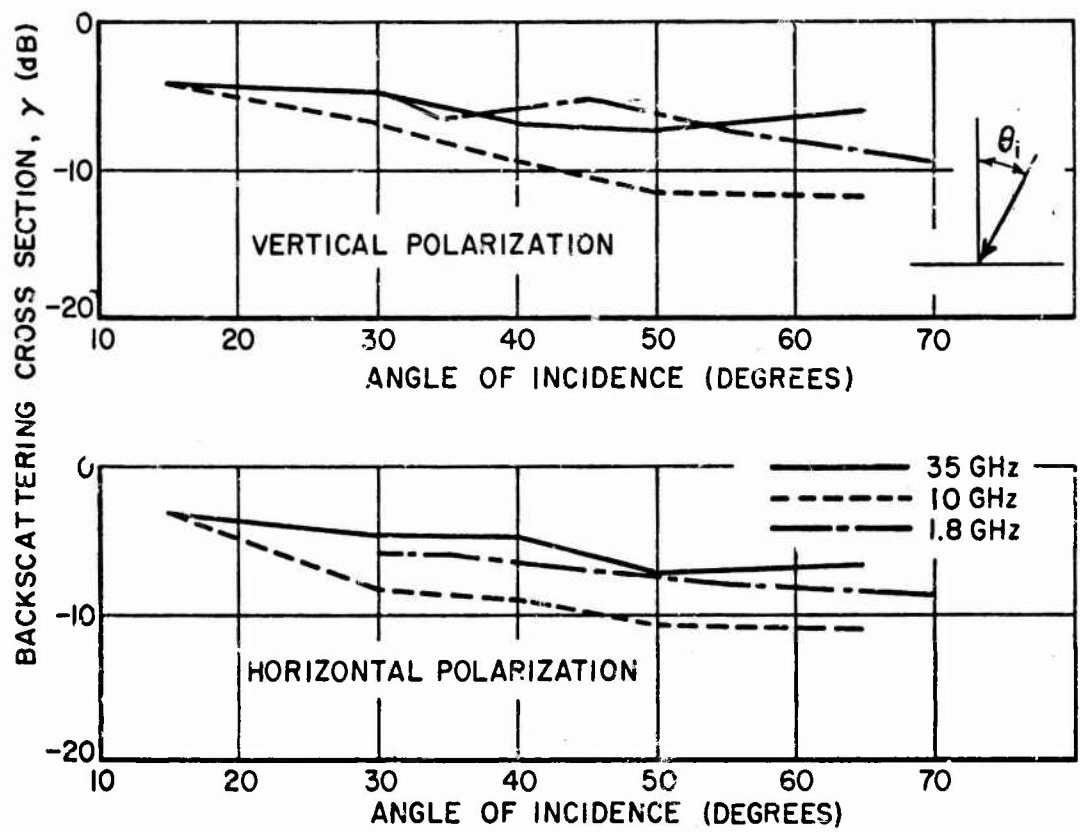


Fig. 50. Frequency dependence of radar backscattering for a rough grey pumice surface.

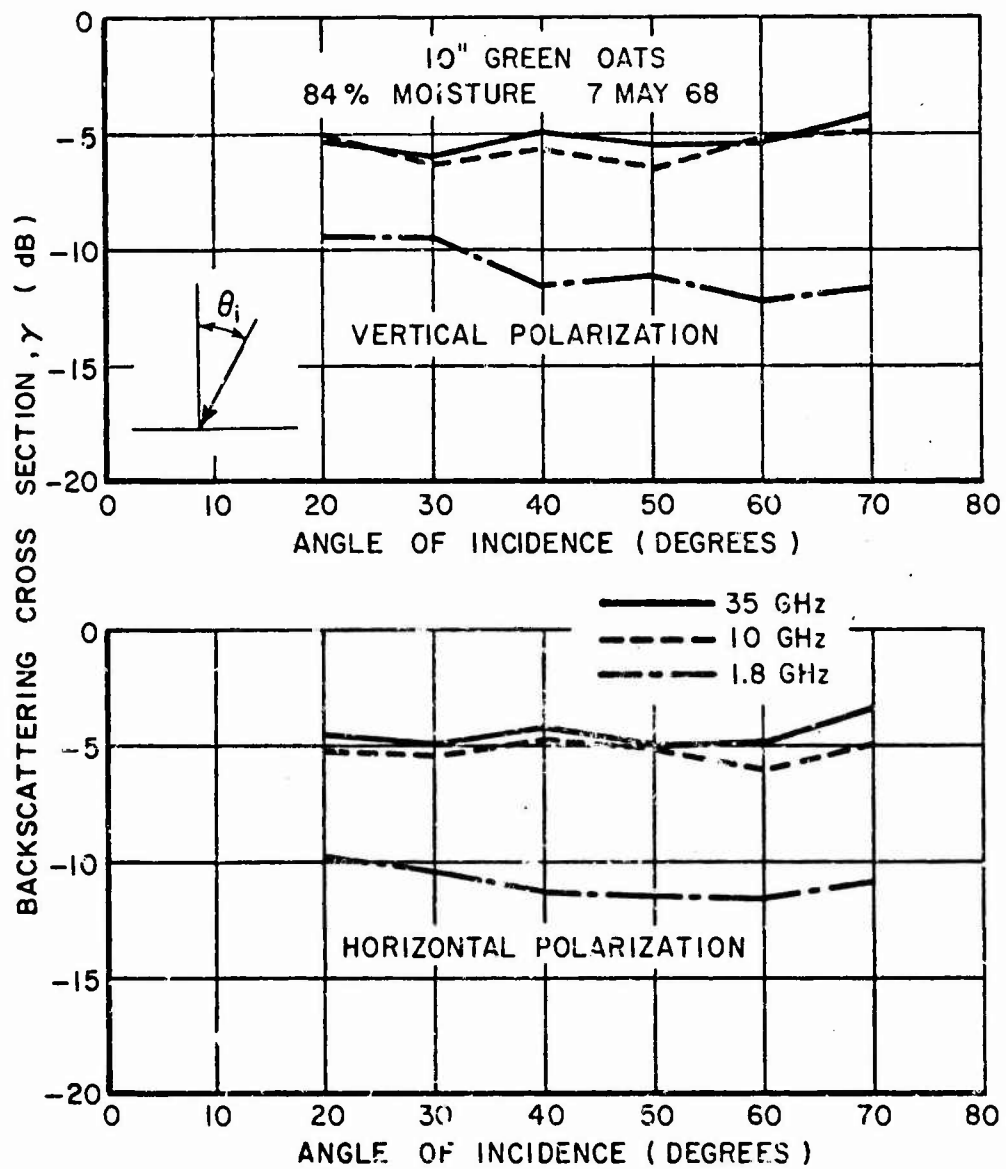


Fig. 51. Frequency dependence of radar backscattering for a vegetated surface (oats).

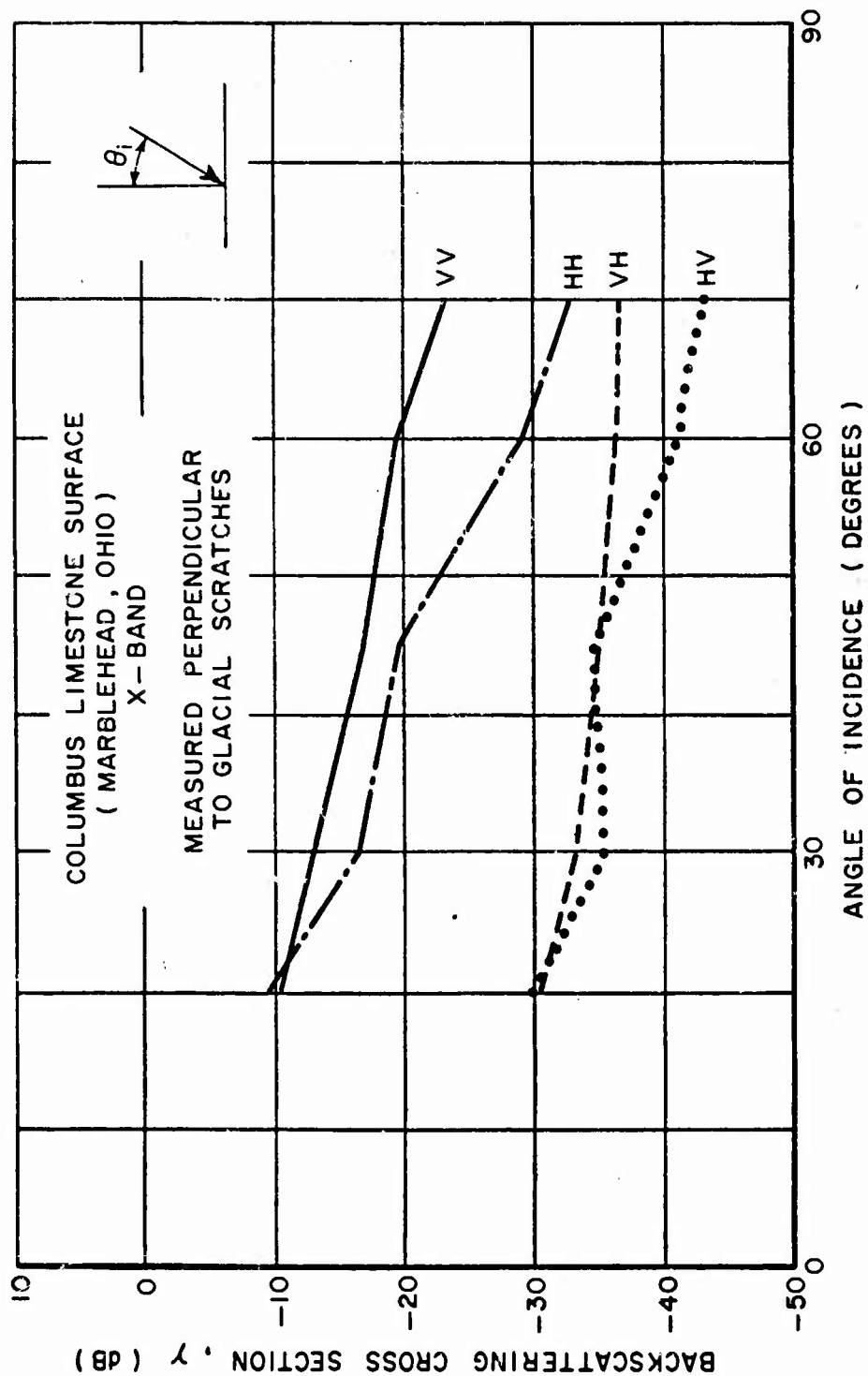


Fig. 52: Polarization dependence of the radar backscattering for a "smooth" limestone surface at X-band - Reference 5.

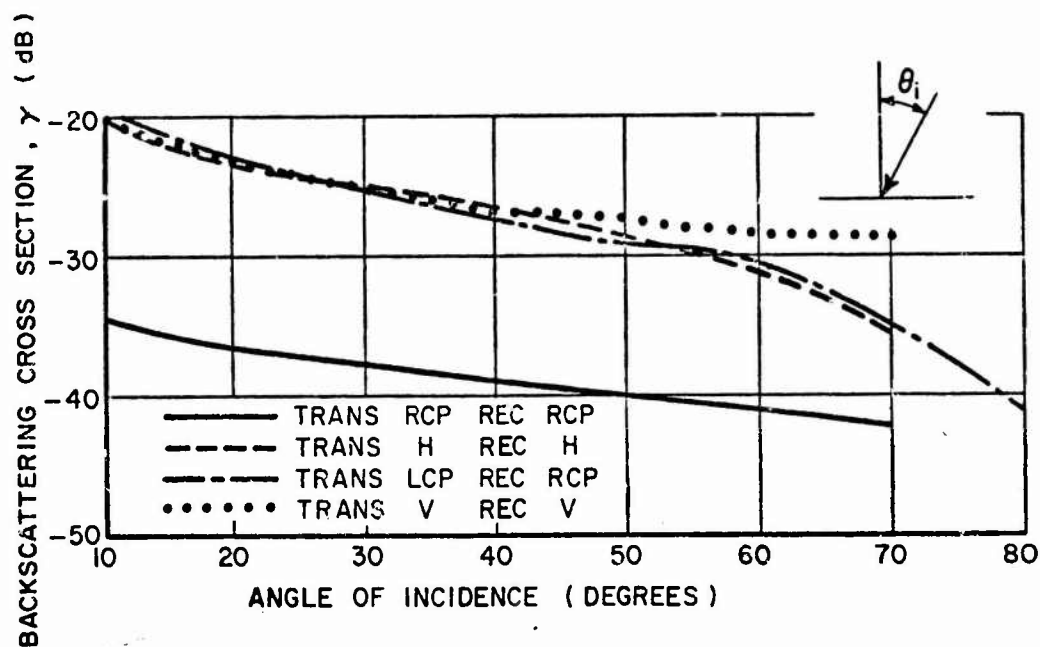


Fig. 53. Polarization dependence of the radar backscattering for a smooth sand surface at X-band - Reference 4.

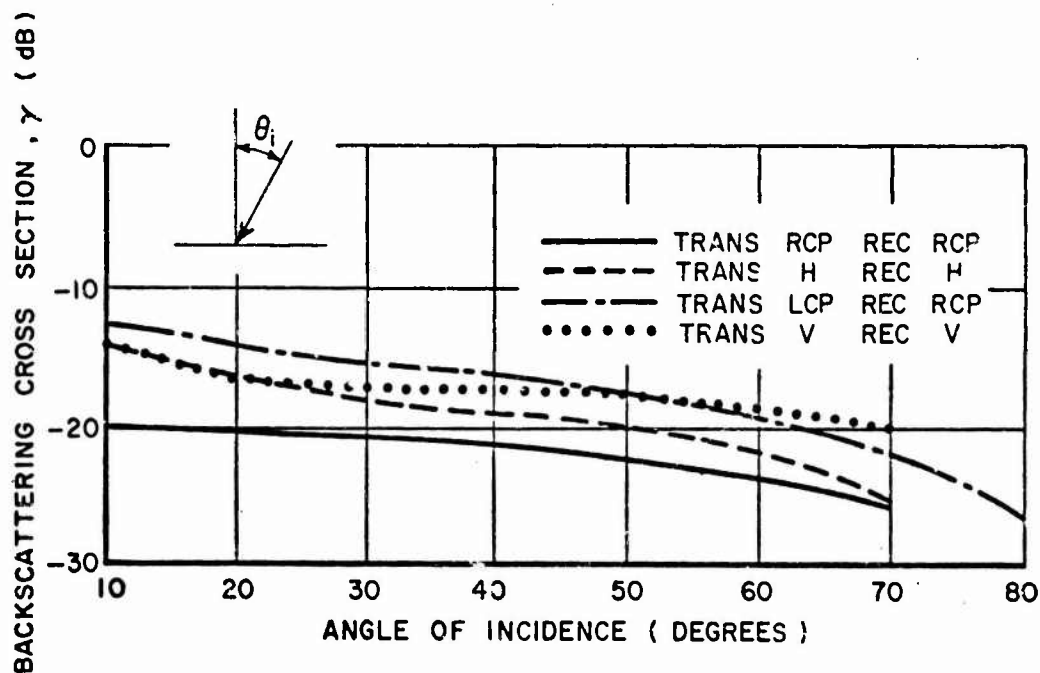


Fig. 54. Polarization dependence of the radar backscattering for a slightly rough gravel surface at X-band - Reference 4.

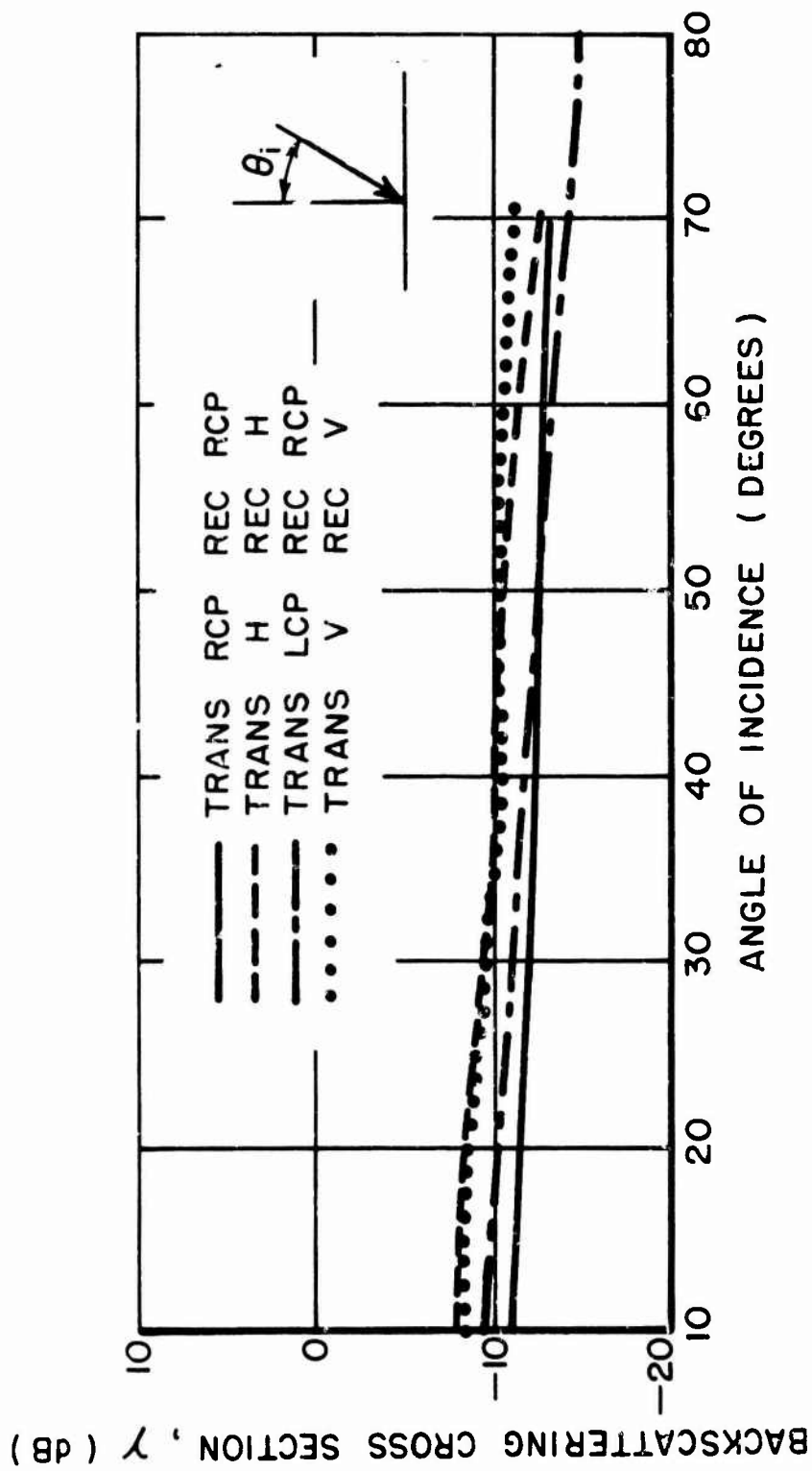


Fig. 55. Polarization dependence of the radar backscattering for a rough stone surface at X-band - Reference 4.

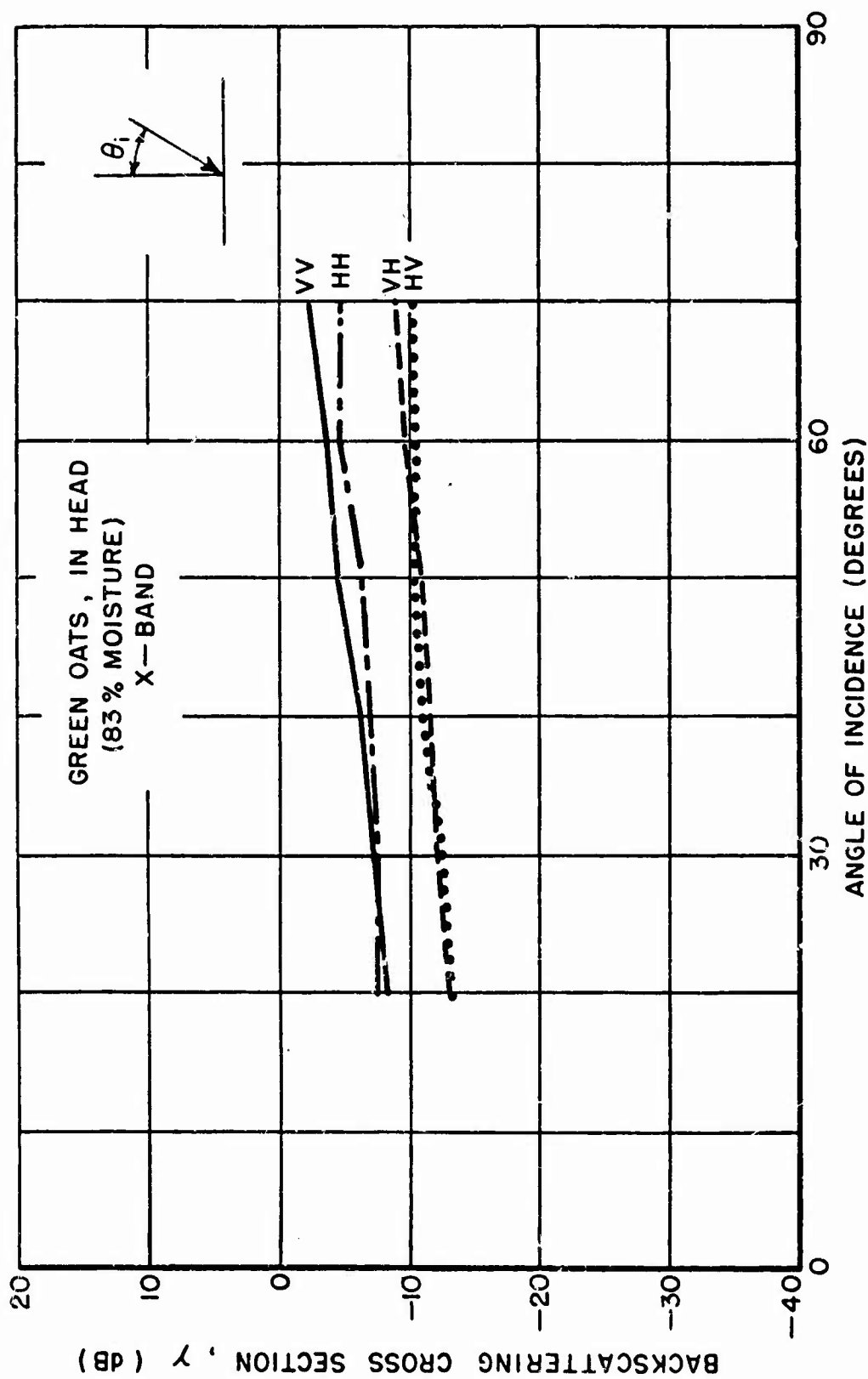


Fig. 56. Polarization dependence of the radar backscattering for a vegetated surface (oats) at X-band - Reference 6.

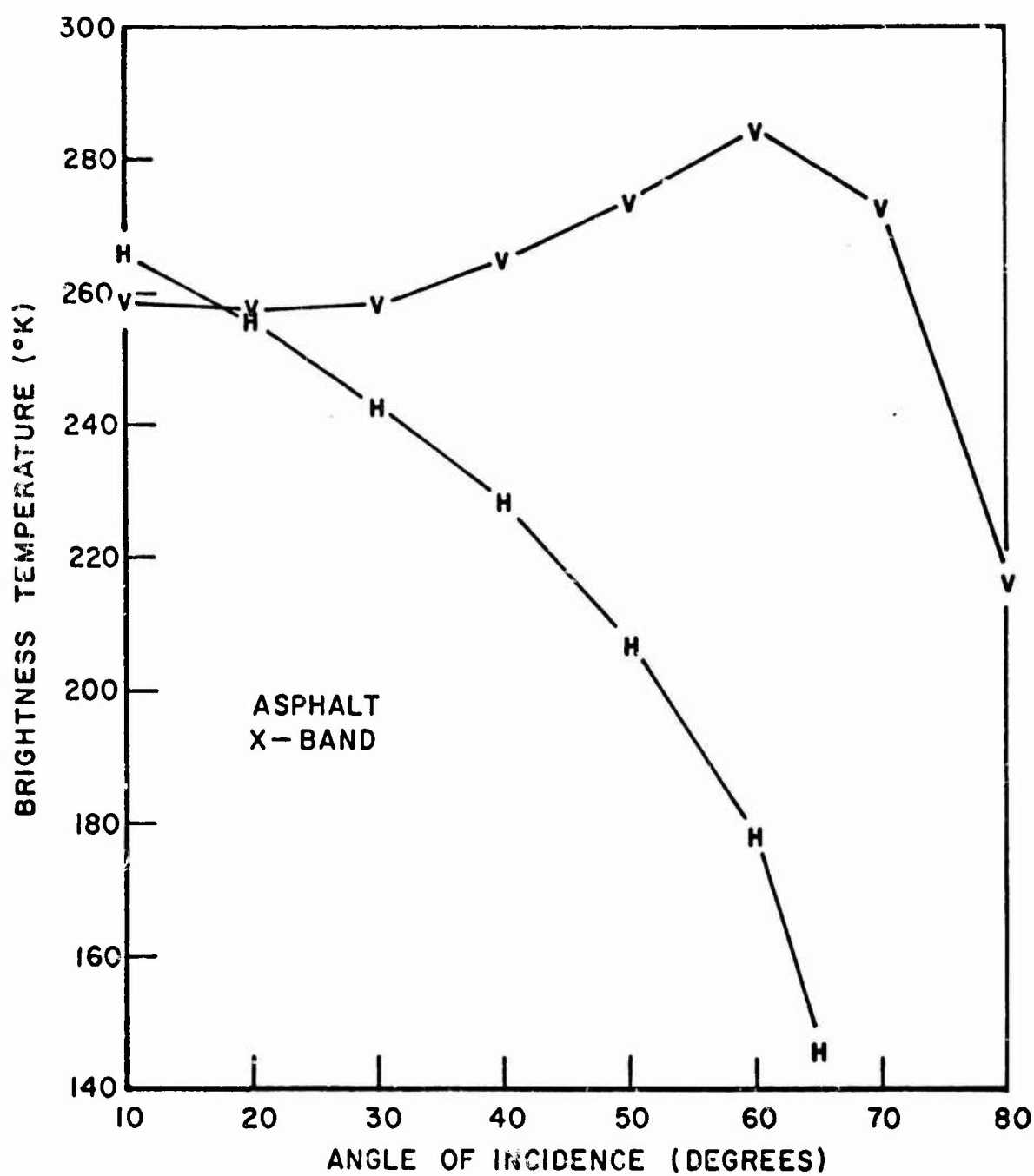


Fig. 57. Brightness temperature of smooth asphalt at 10 GHz.

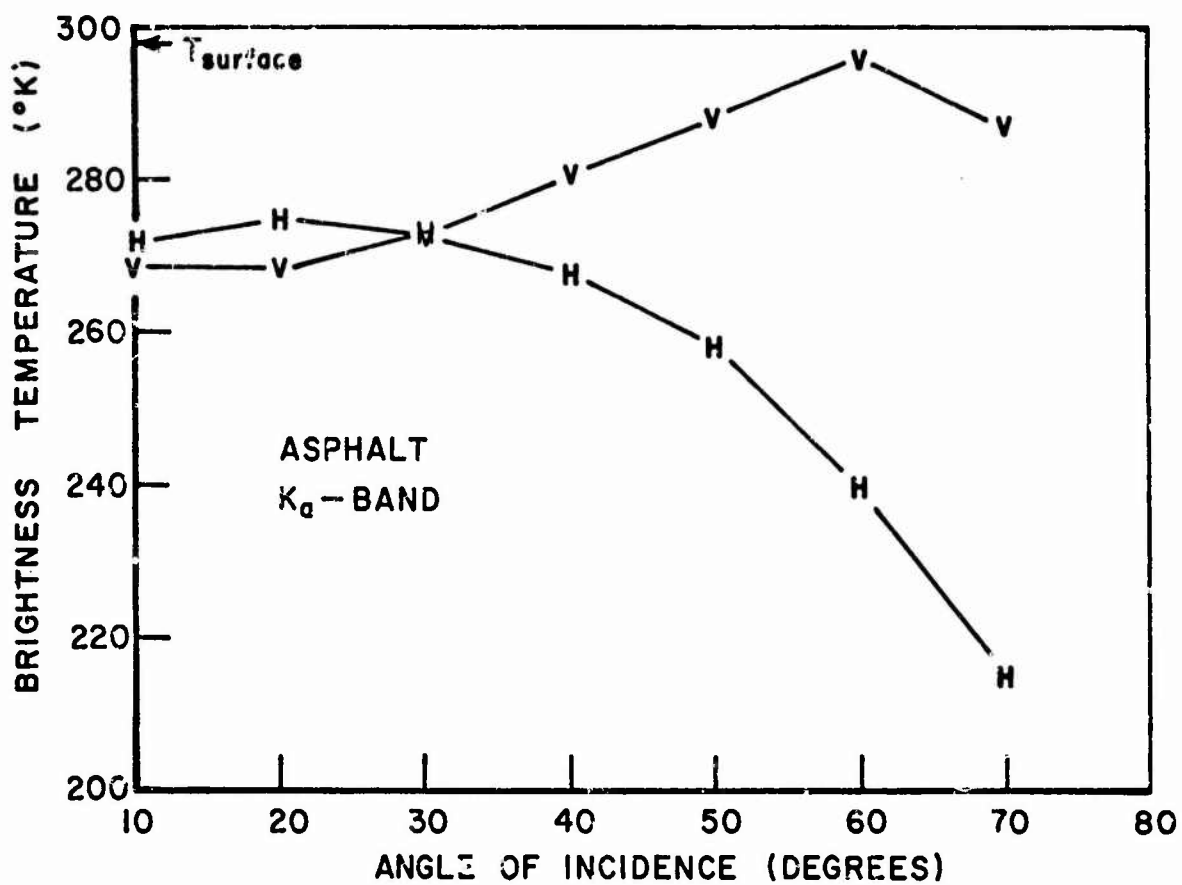


Fig. 58. Brightness temperature of smooth asphalt at 35 GHz.

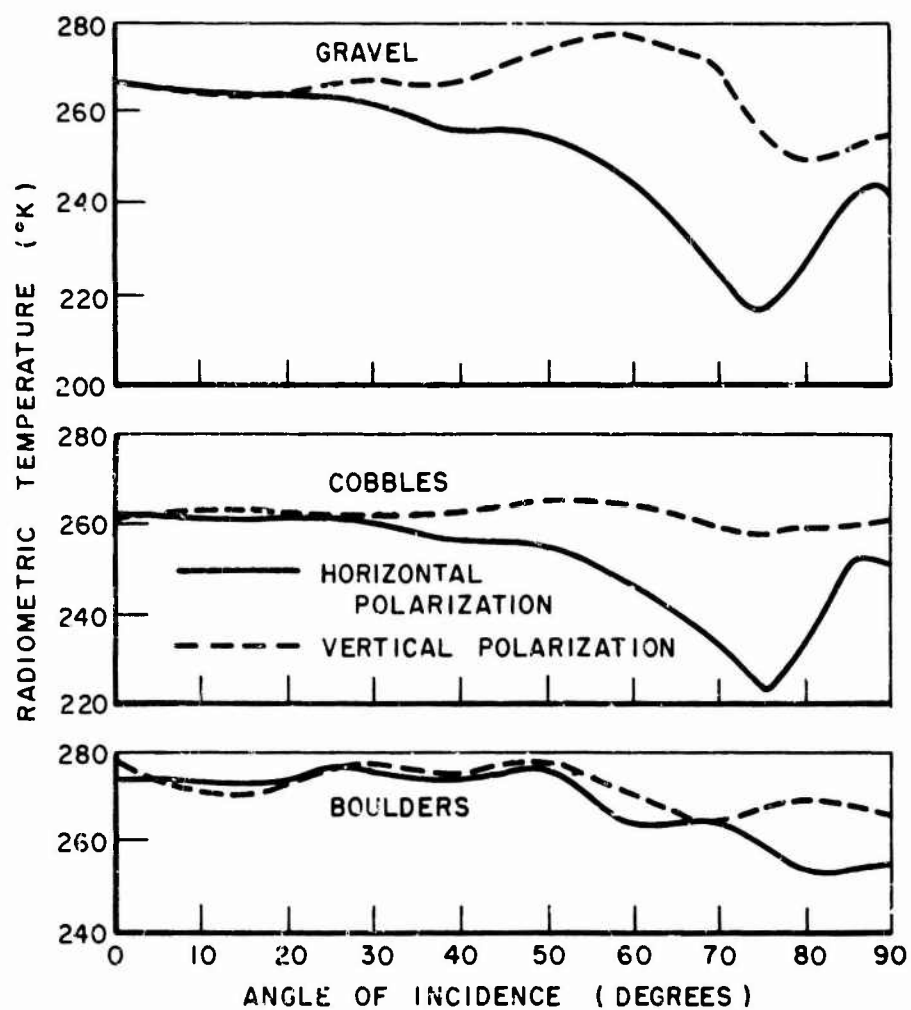


Fig. 59. Brightness temperatures for different size fractions of limestone at 13.5 GHz. - Reference 11.

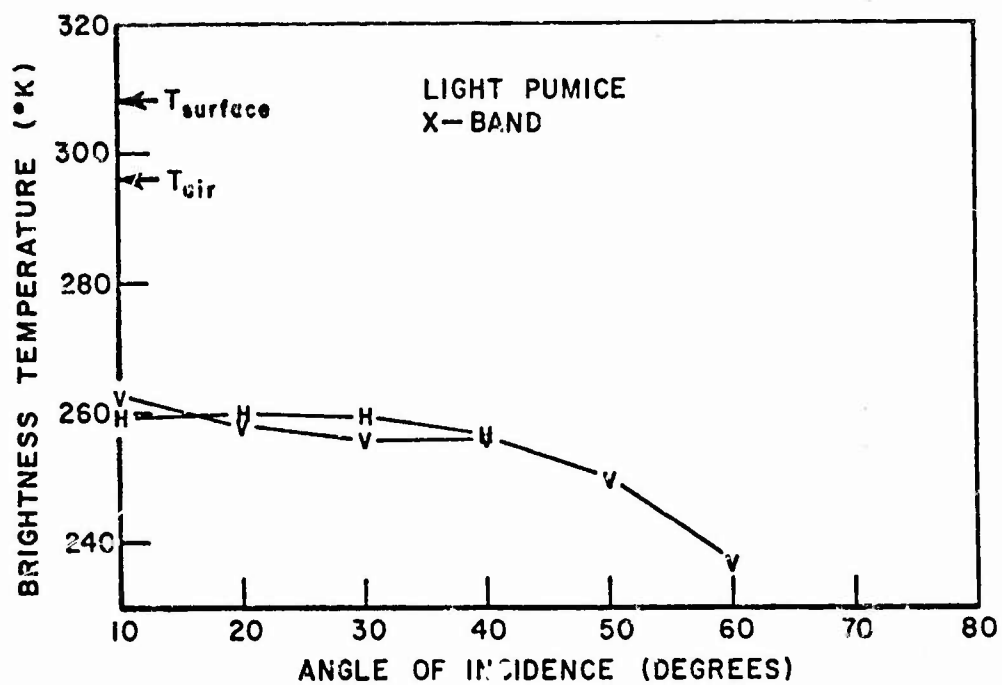


Fig. 60. Brightness temperature for dense, broken, grey pumice at 10 GHz. ($\rho = 1.9$; $\epsilon \approx 2.7$)

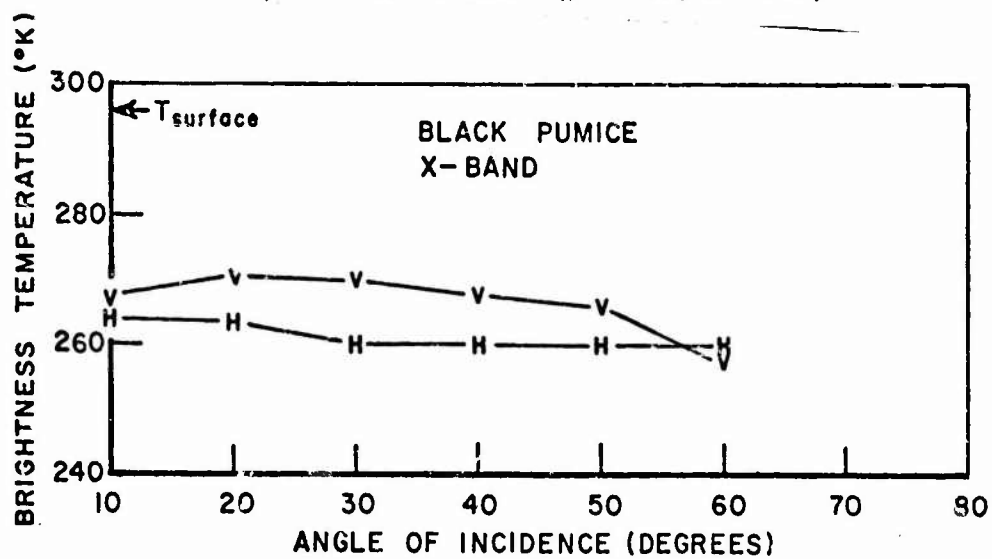


Fig. 61. Brightness temperature for light weight, dark pumice at 10 GHz. ($\rho = 0.45$)

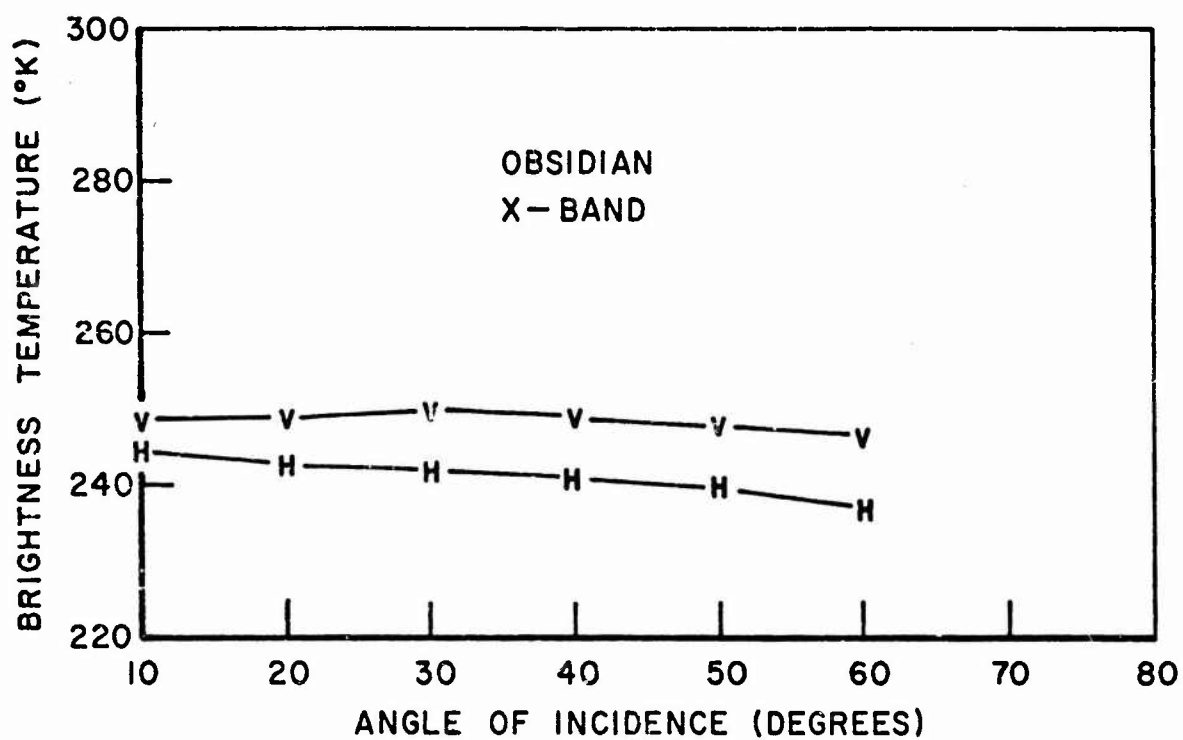


Fig. 62. Brightness temperature for large blocks of obsidian at 10 GHz. ($\rho = 2.3$; $\epsilon \approx 4.7$)



DARK PUMICE
NOT REPRODUCIBLE



OBSIDIAN

Fig. 63. Photographs of volcanic materials at Mono Craters, California - Reference 7.

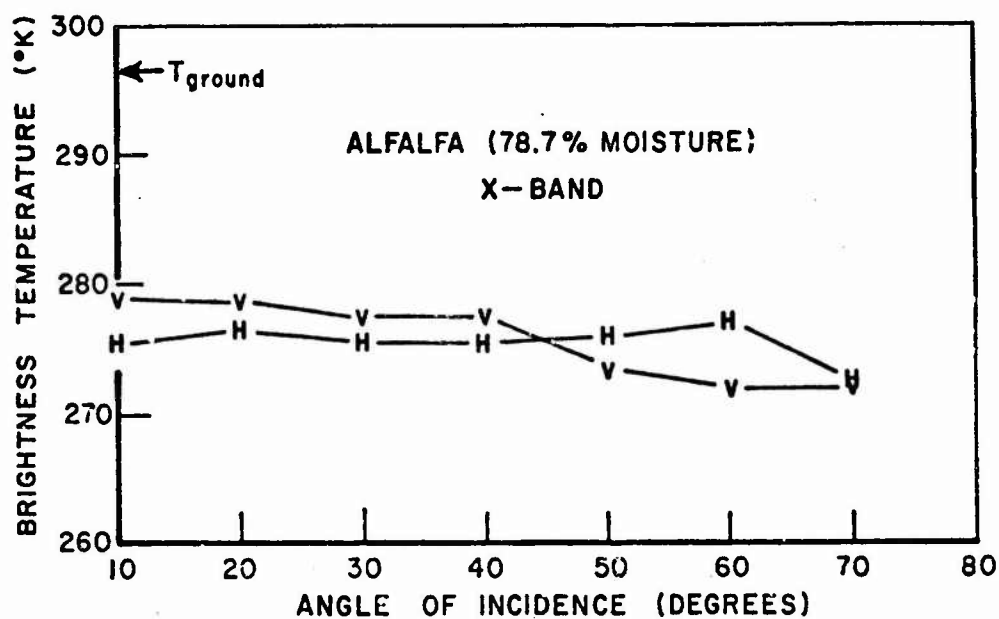


Fig. 64. Brightness temperature of alfalfa at 10 GHz.

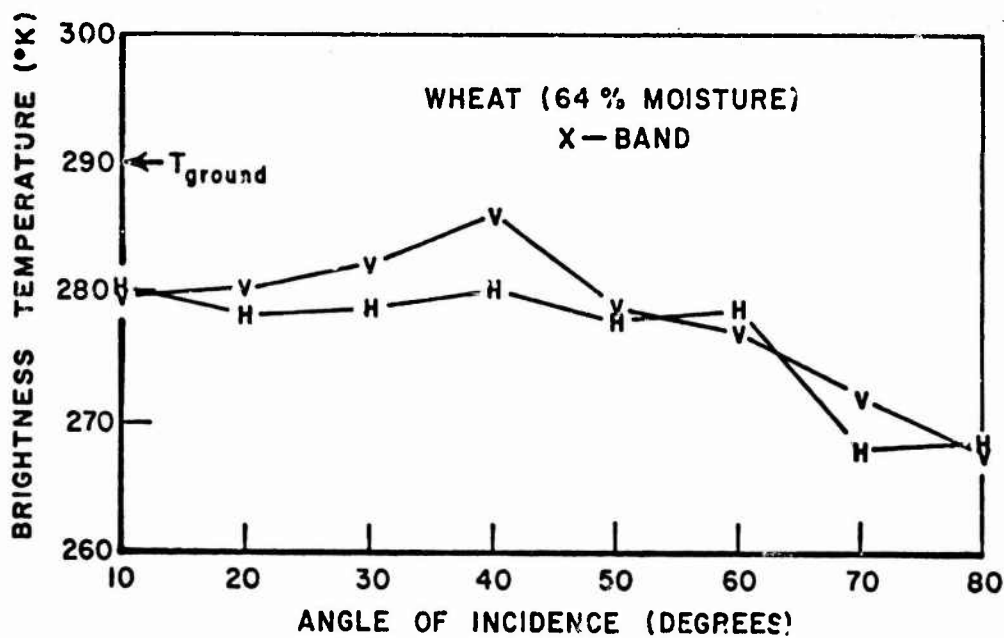


Fig. 65. Brightness temperature of green wheat, in head, at 10 GHz.

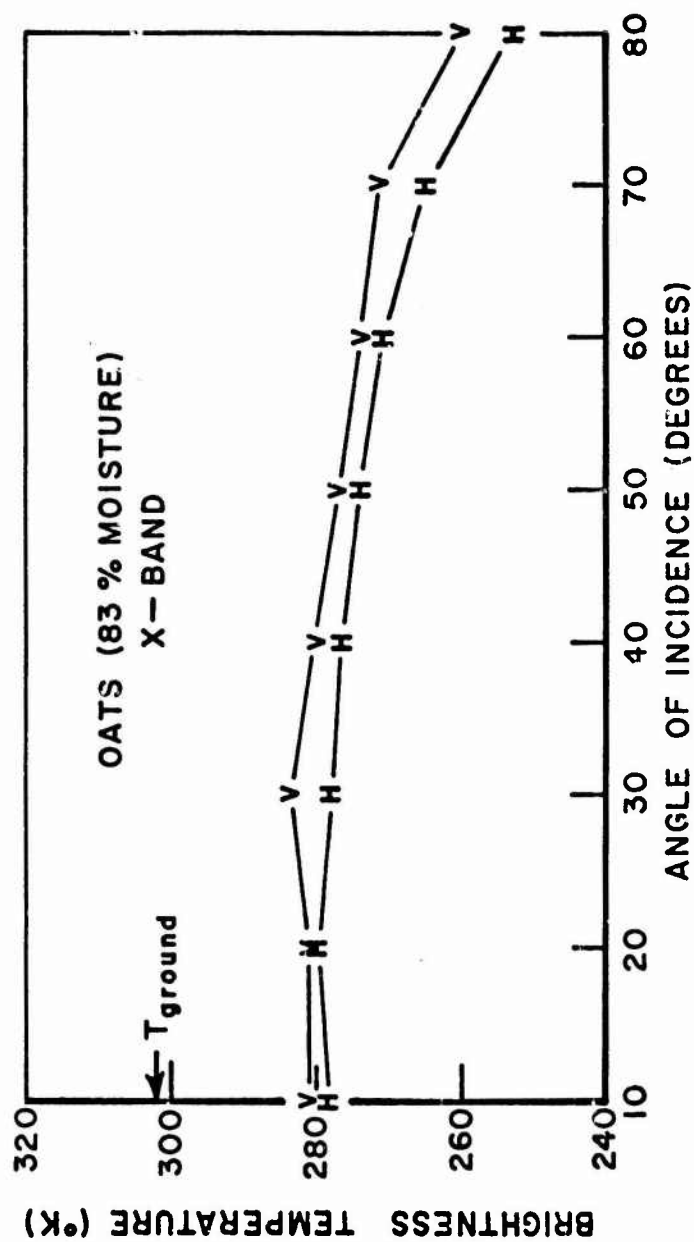


Fig. 66. Brightness temperature of green oats, in head, at 10 GHz.

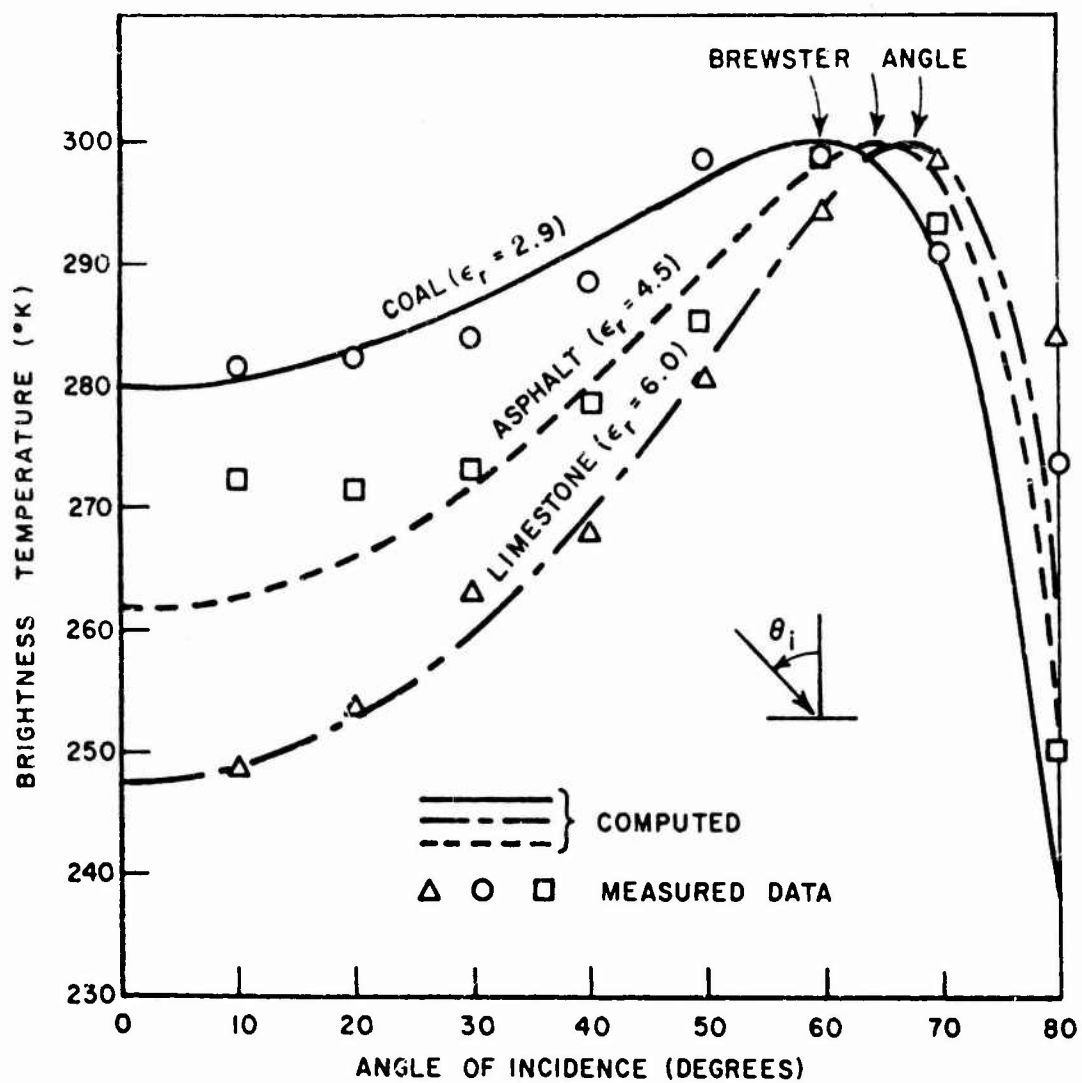


Fig. 67. Computed and measured brightness temperatures for coal (near Cadiz, Ohio), limestone (near Marblehead, Ohio), and asphalt surfaces at 10 GHz, vertical polarization. (Data normalized to 300°K at the Brewster Angle).

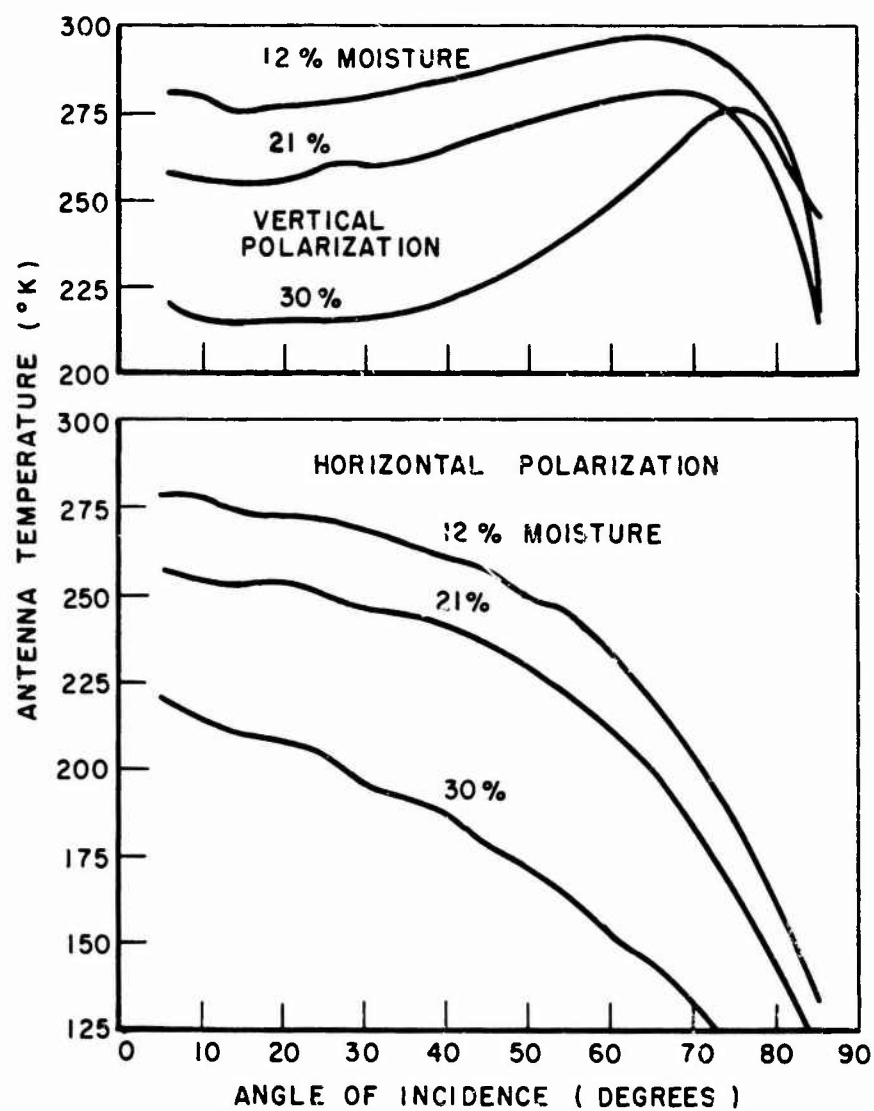


Fig. 68. Brightness temperatures of playa sediments, with variable moisture, at 13.4 GHz - Reference 11.

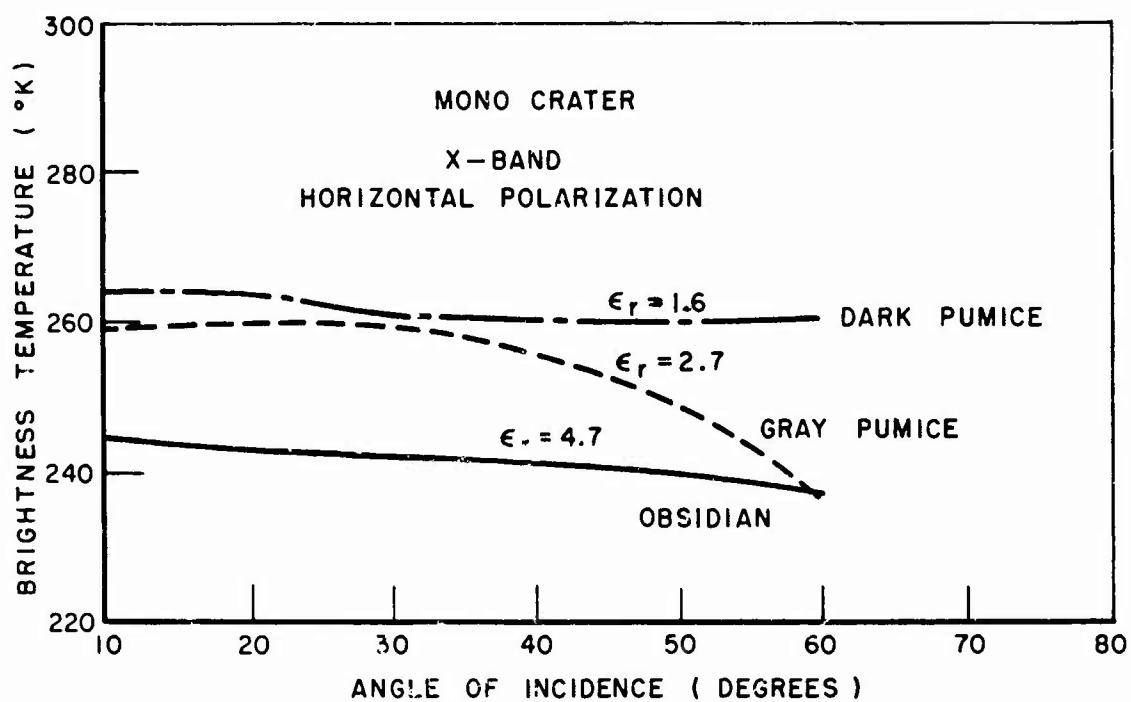


Fig. 69. Brightness temperature of three pumices (Mono Crater, California) at X-band.

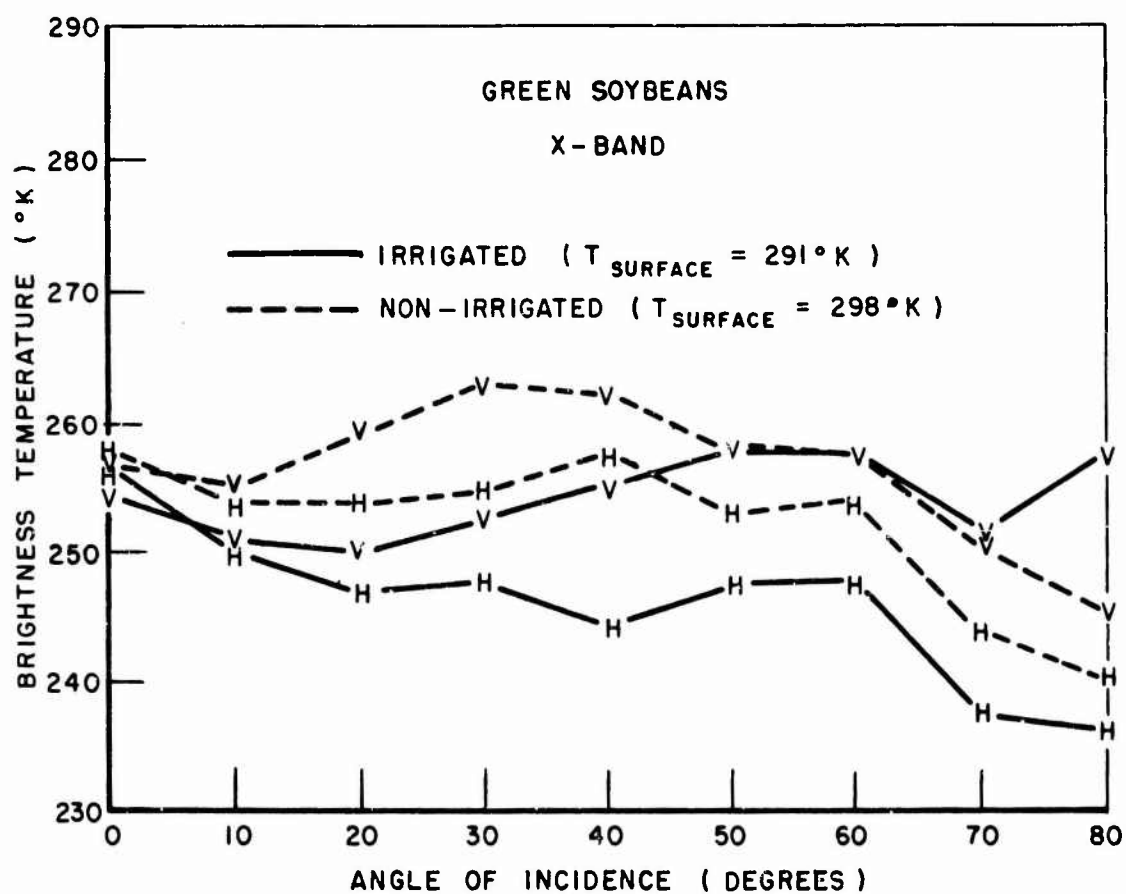


Fig. 70. Brightness temperatures for irrigated and non-irrigated soybeans at X-band.

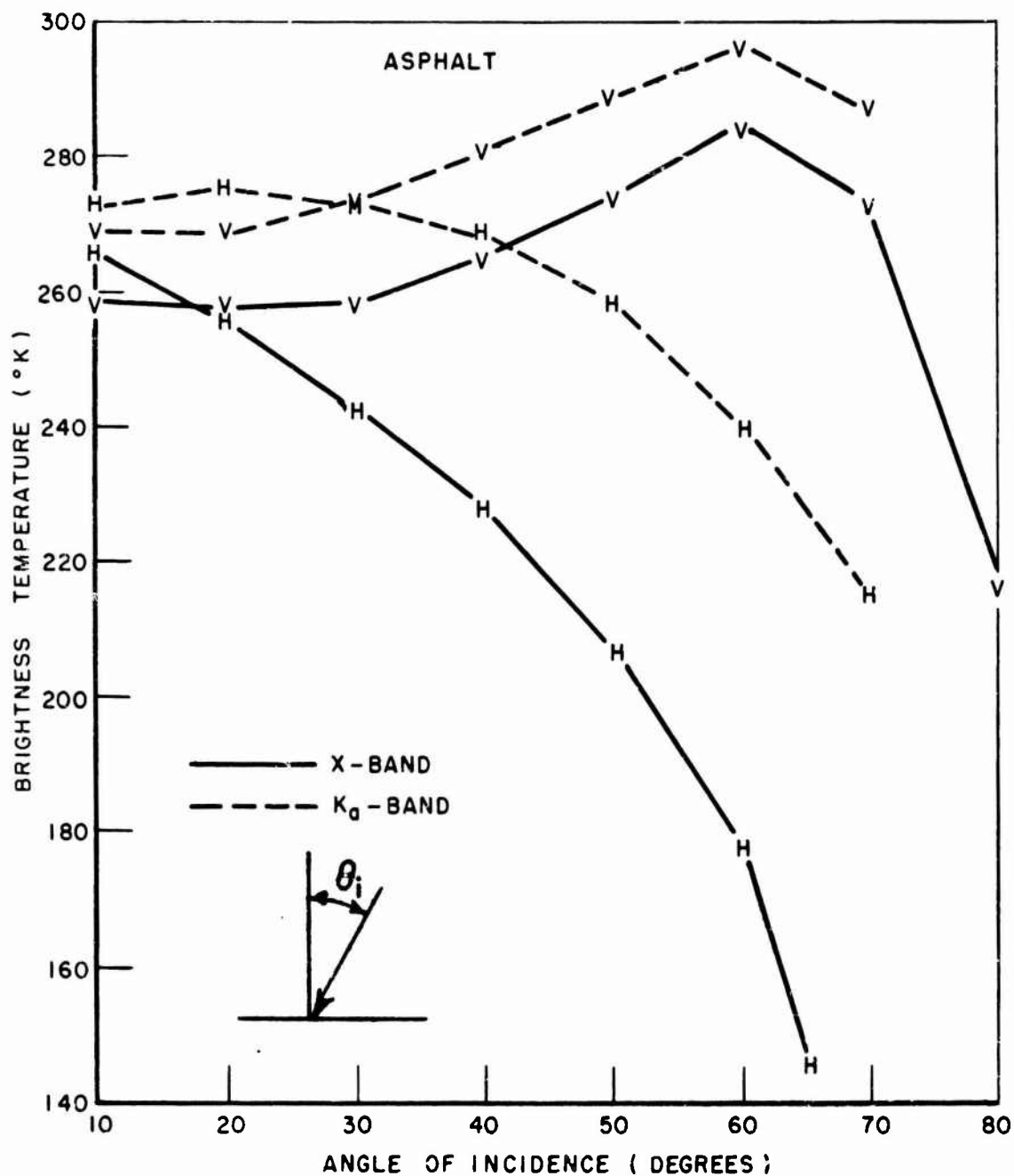


Fig. 7. Brightness temperature of smooth asphalt at 10 GHz and 35 GHz.

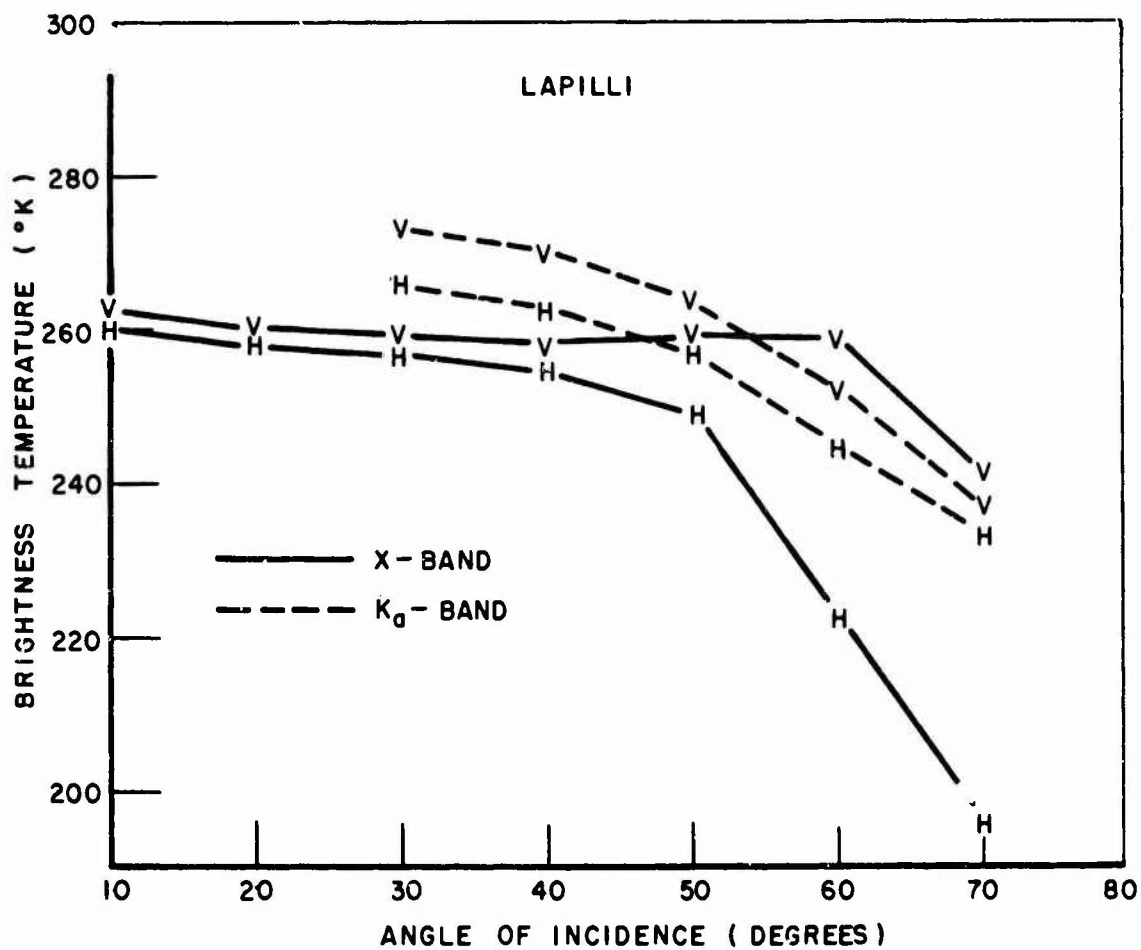


Fig. 72. Brightness temperature of lapilli (volcanic ash) at 10 GHz and 35 GHz (Mono Crater, California).

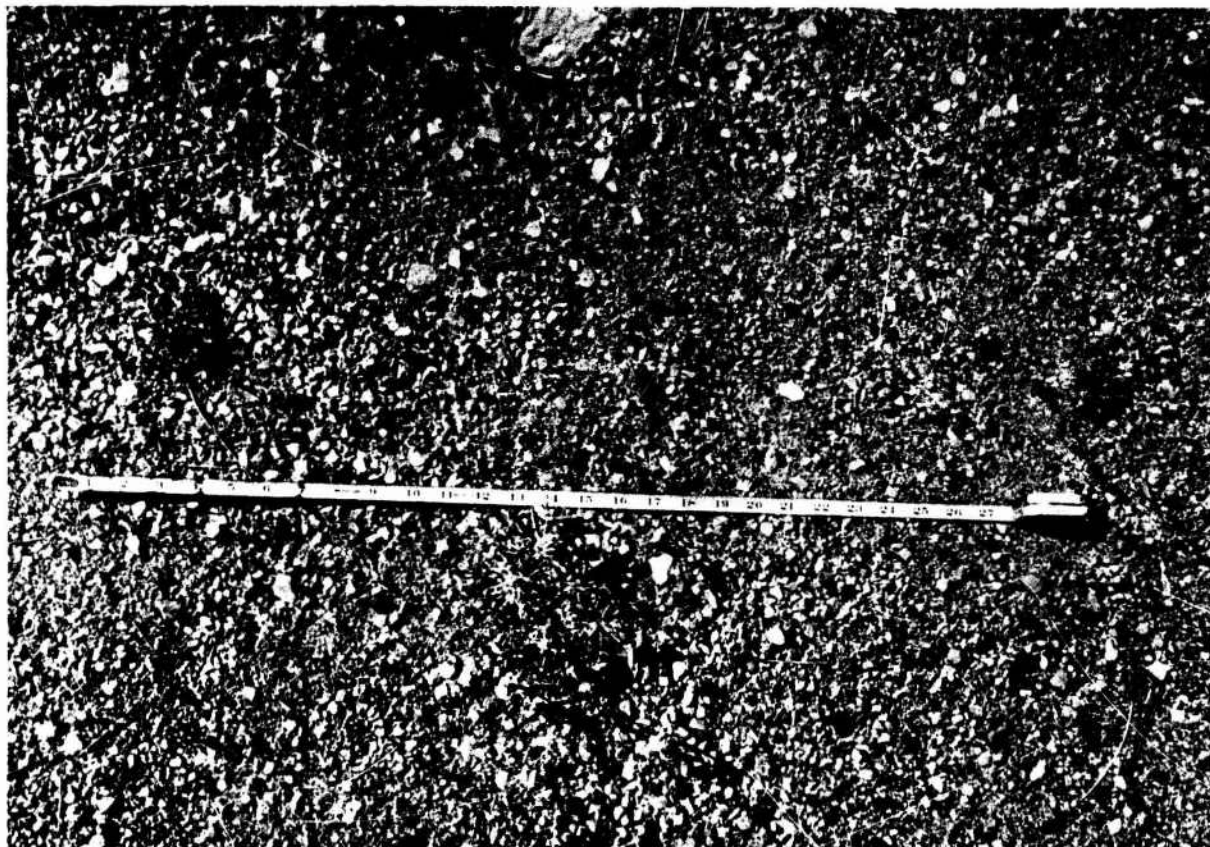


Fig. 73. Close-up of lapilli surface. Note the concentration of coarse pumice lapilli in botches and bands, and the sparse ground vegetation and scattered pine needles. Scale is in inches.

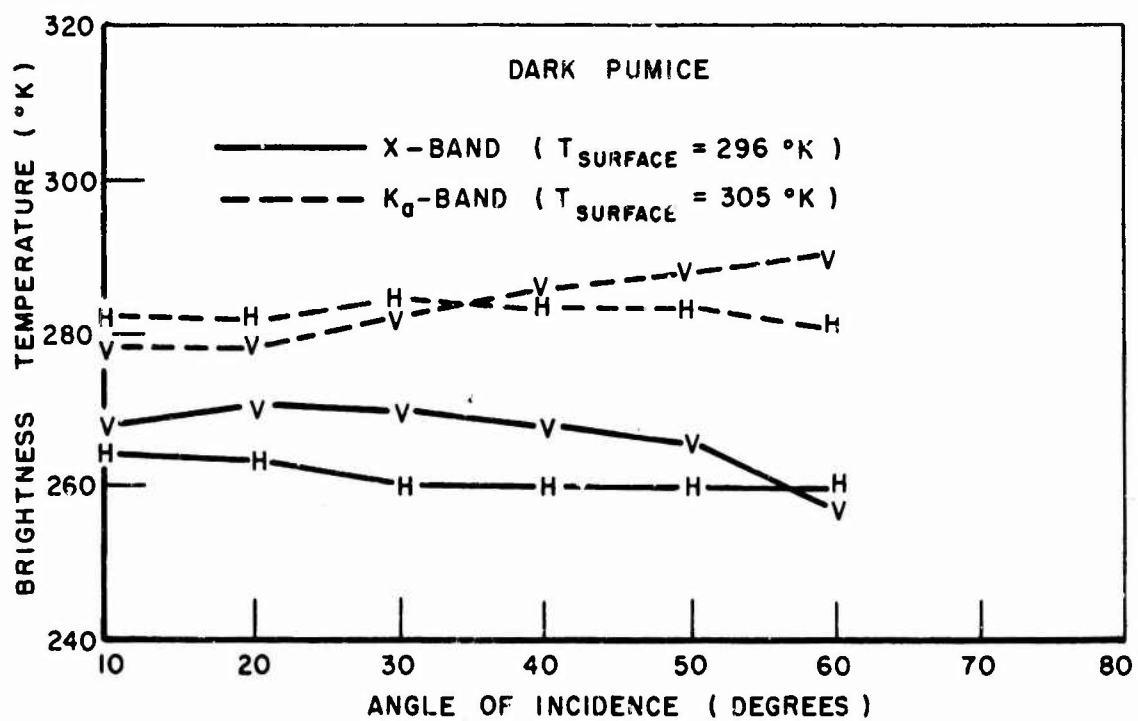
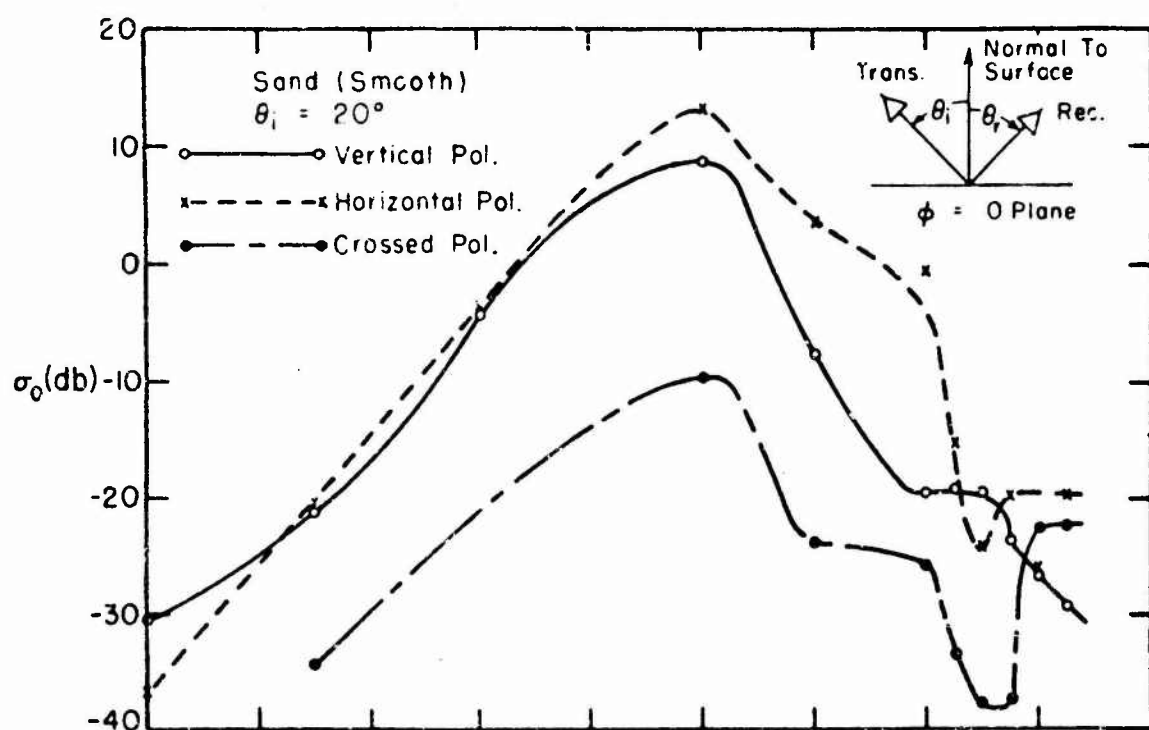
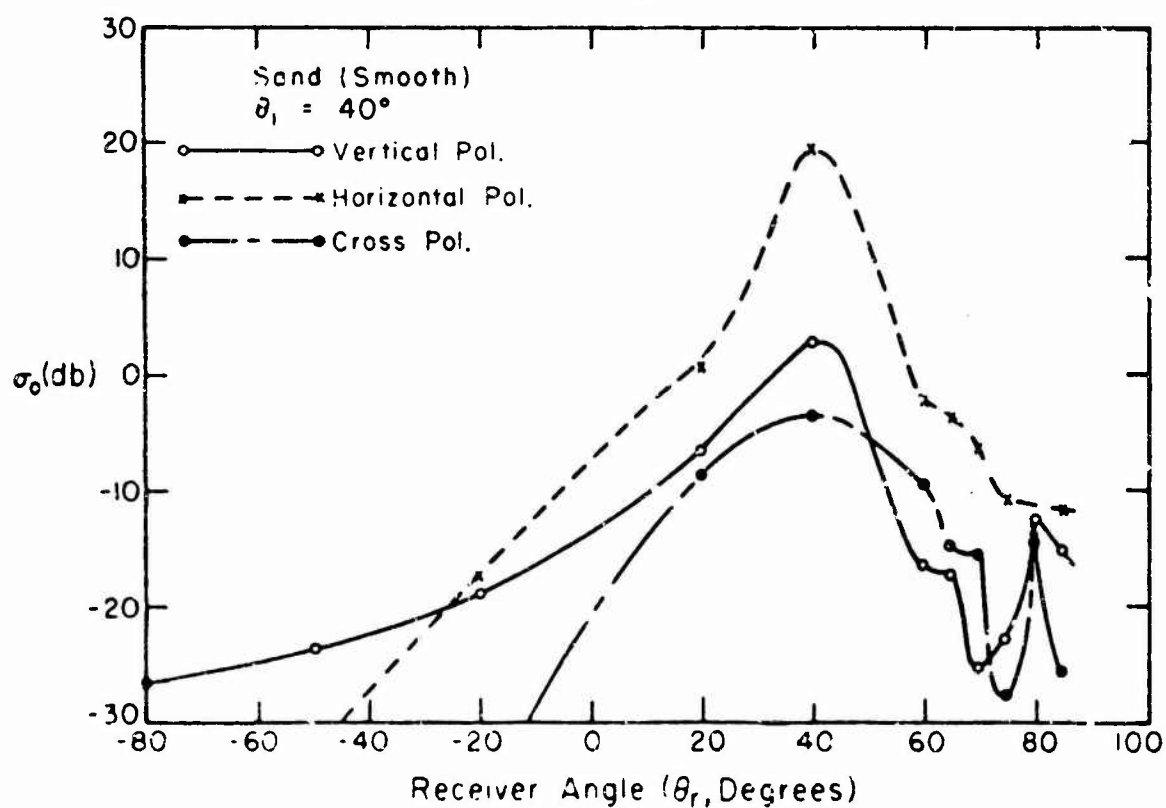


Fig. 74. Brightness temperature of "rough" dark pumice at 10 GHz and 35 GHz (Moro Crater, California).

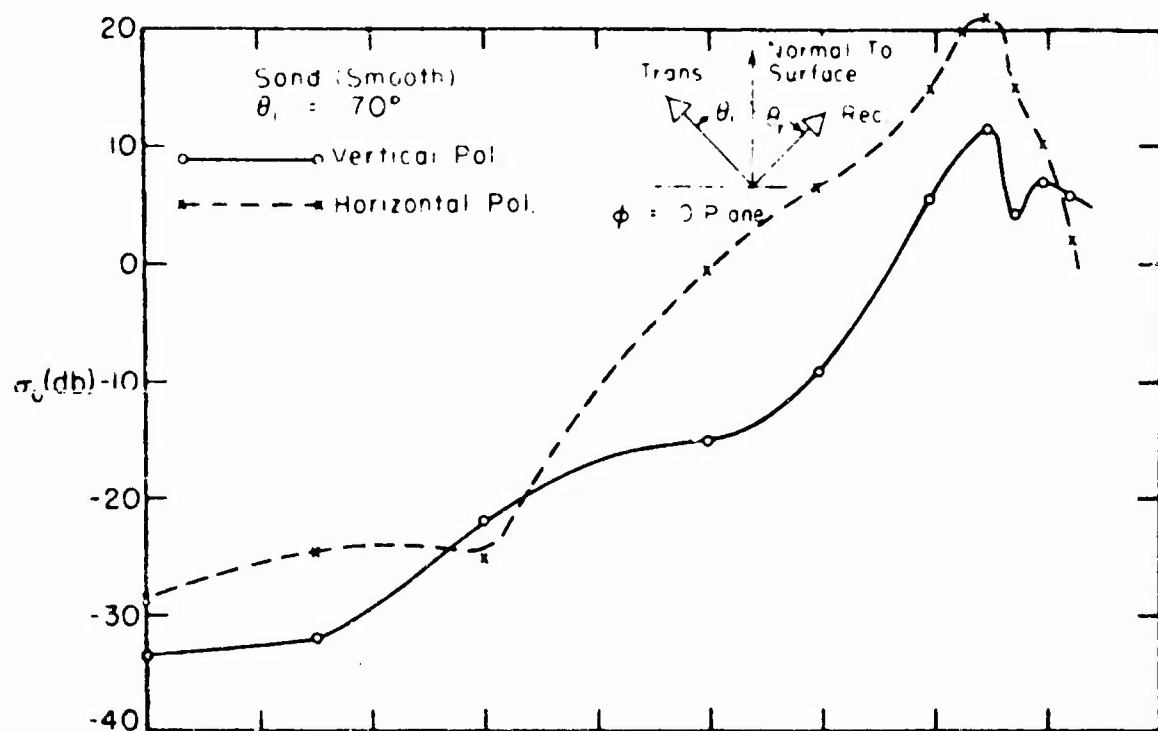


(a)

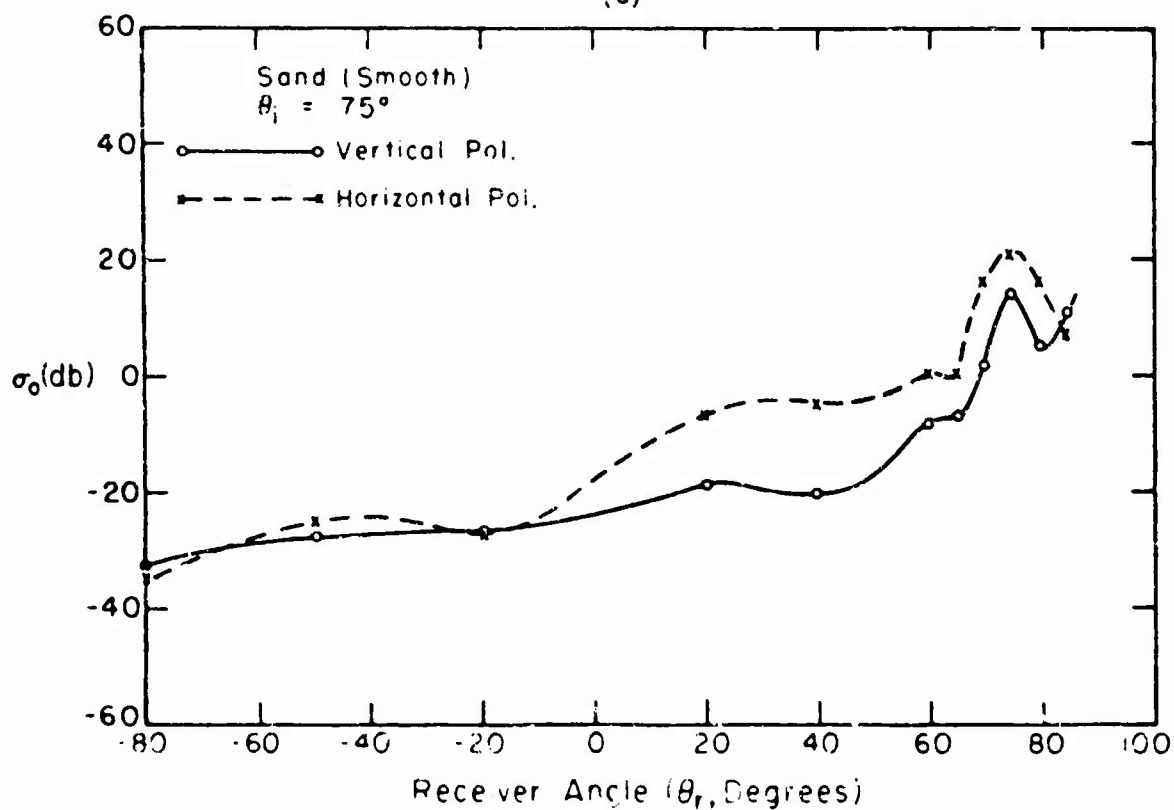


(b)

Fig. 75. Bistatic scattering cross section, in the plane of incidence, for smooth sand at X-band.



(c)



(d)

Fig. 75. (Continued)

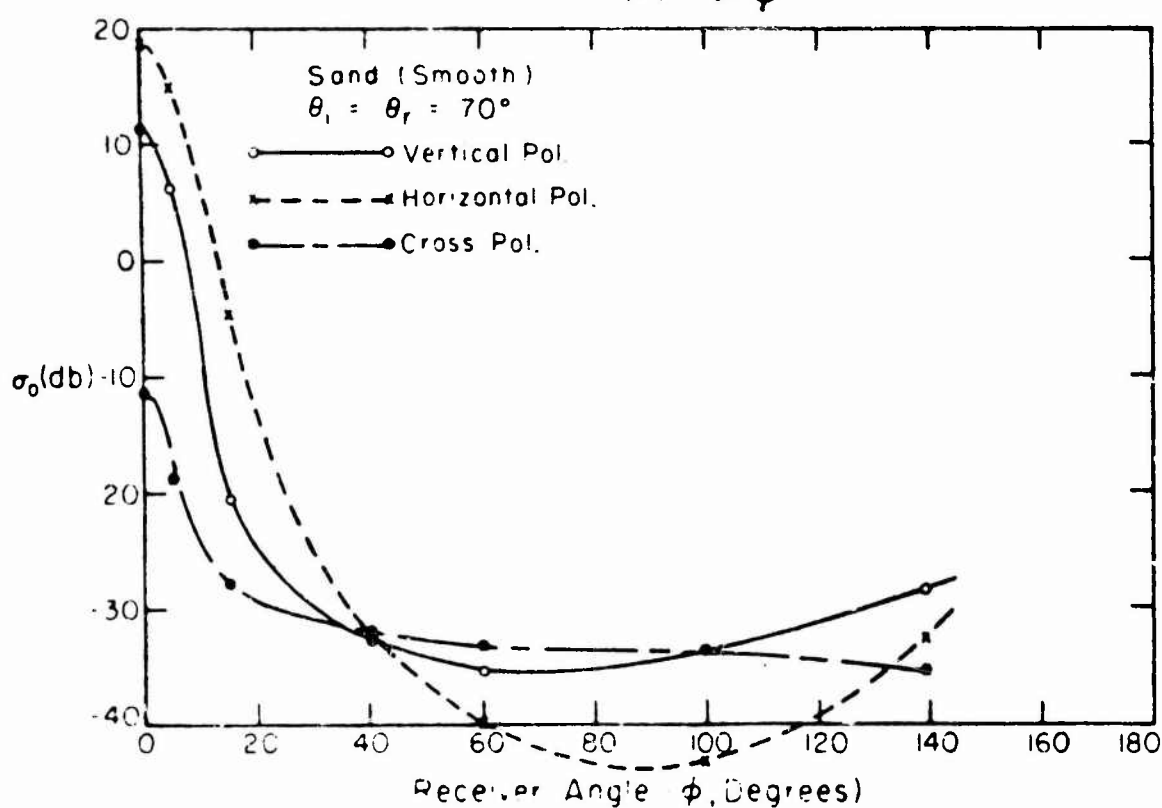
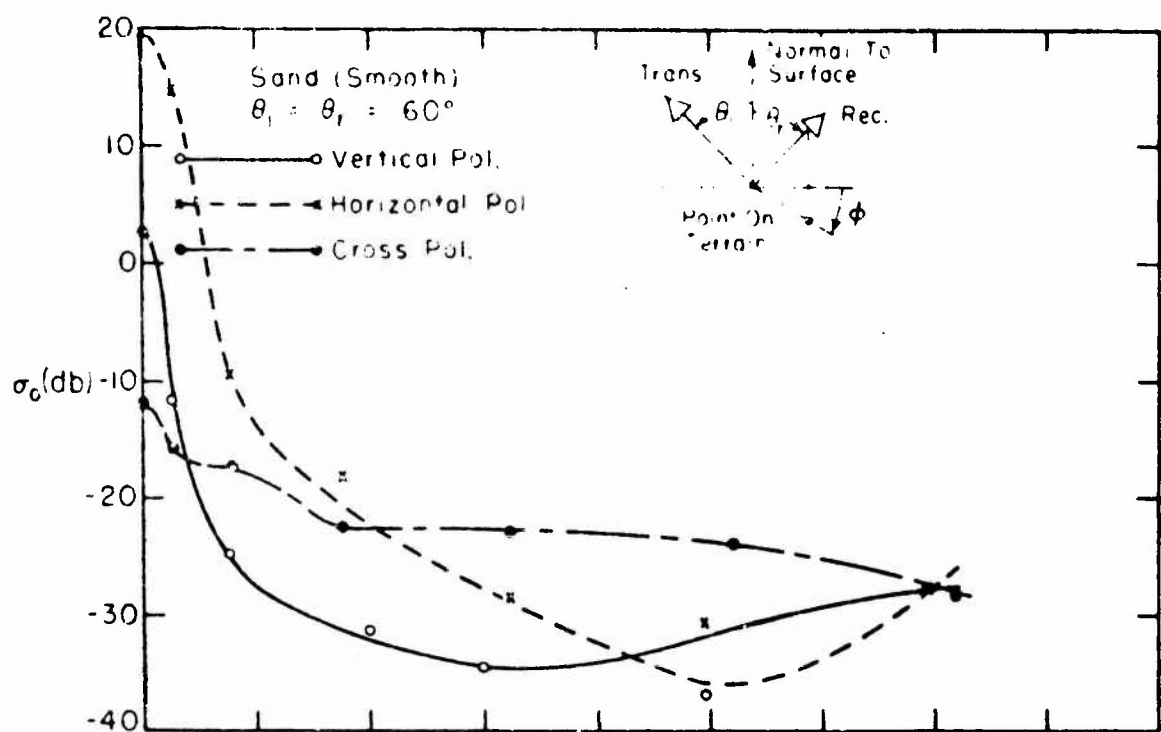
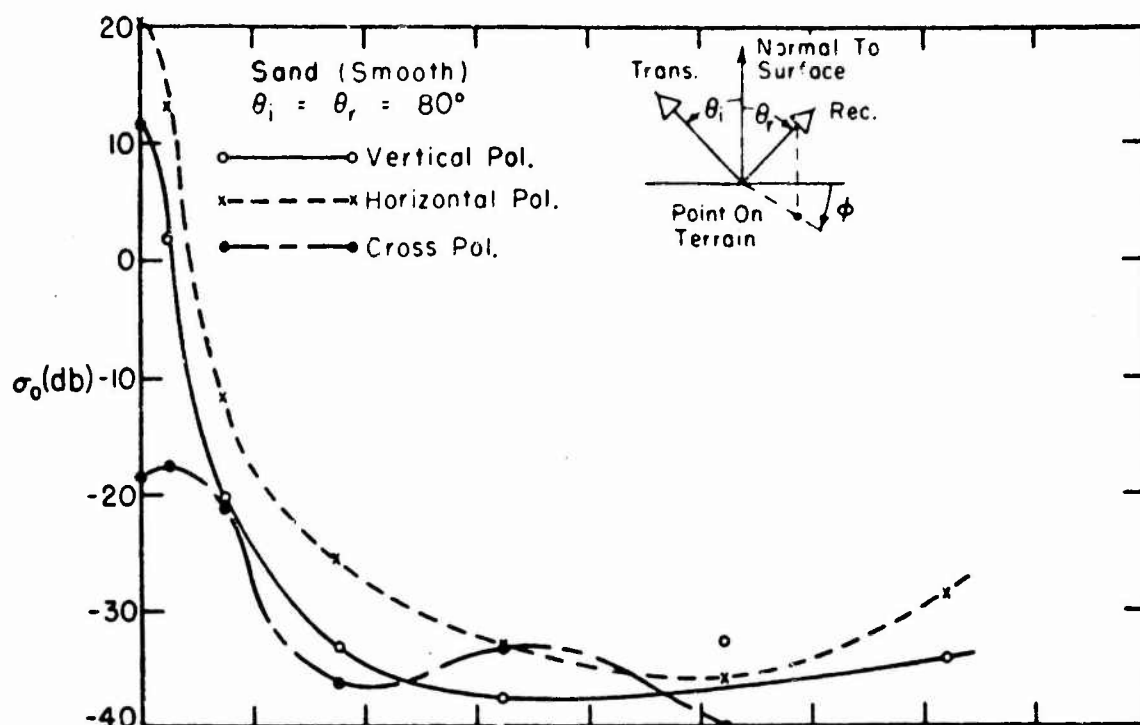
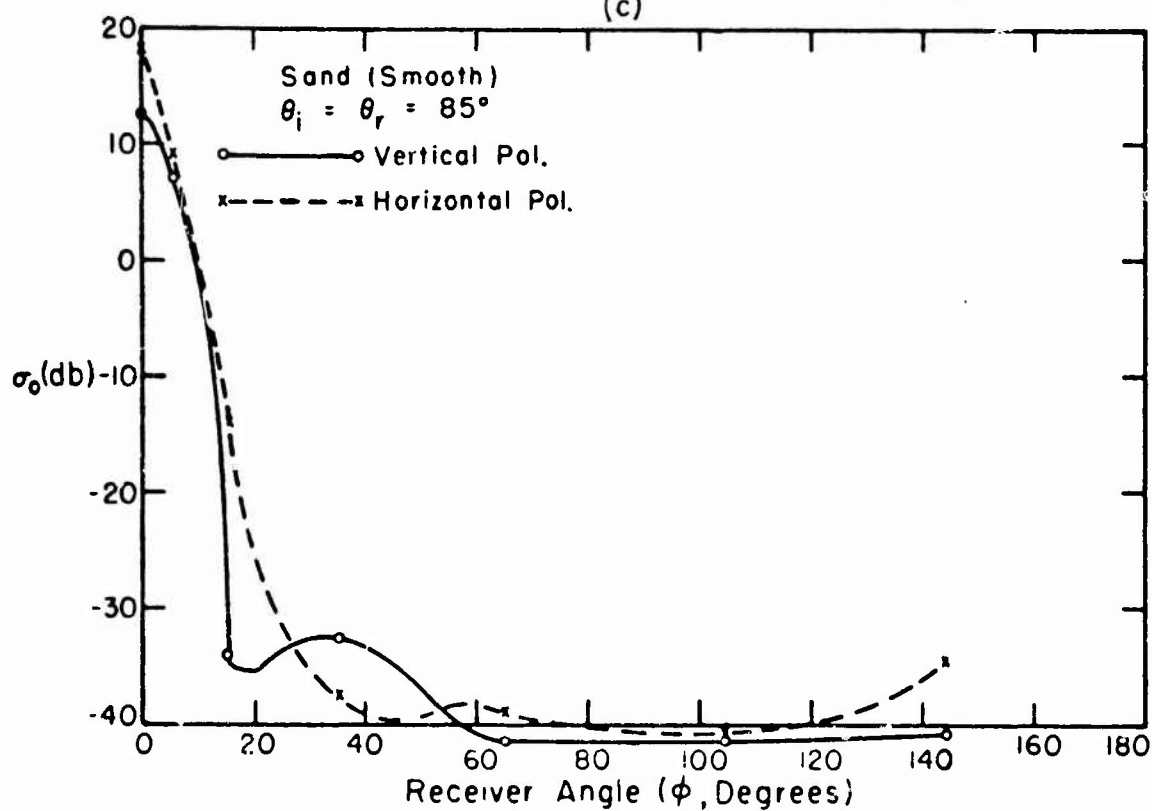


Fig. 76. Bistatic scattering cross section, in the azimuth cone, for smooth sand at X-band.



(c)



(d)

Fig. 76. (Continued)

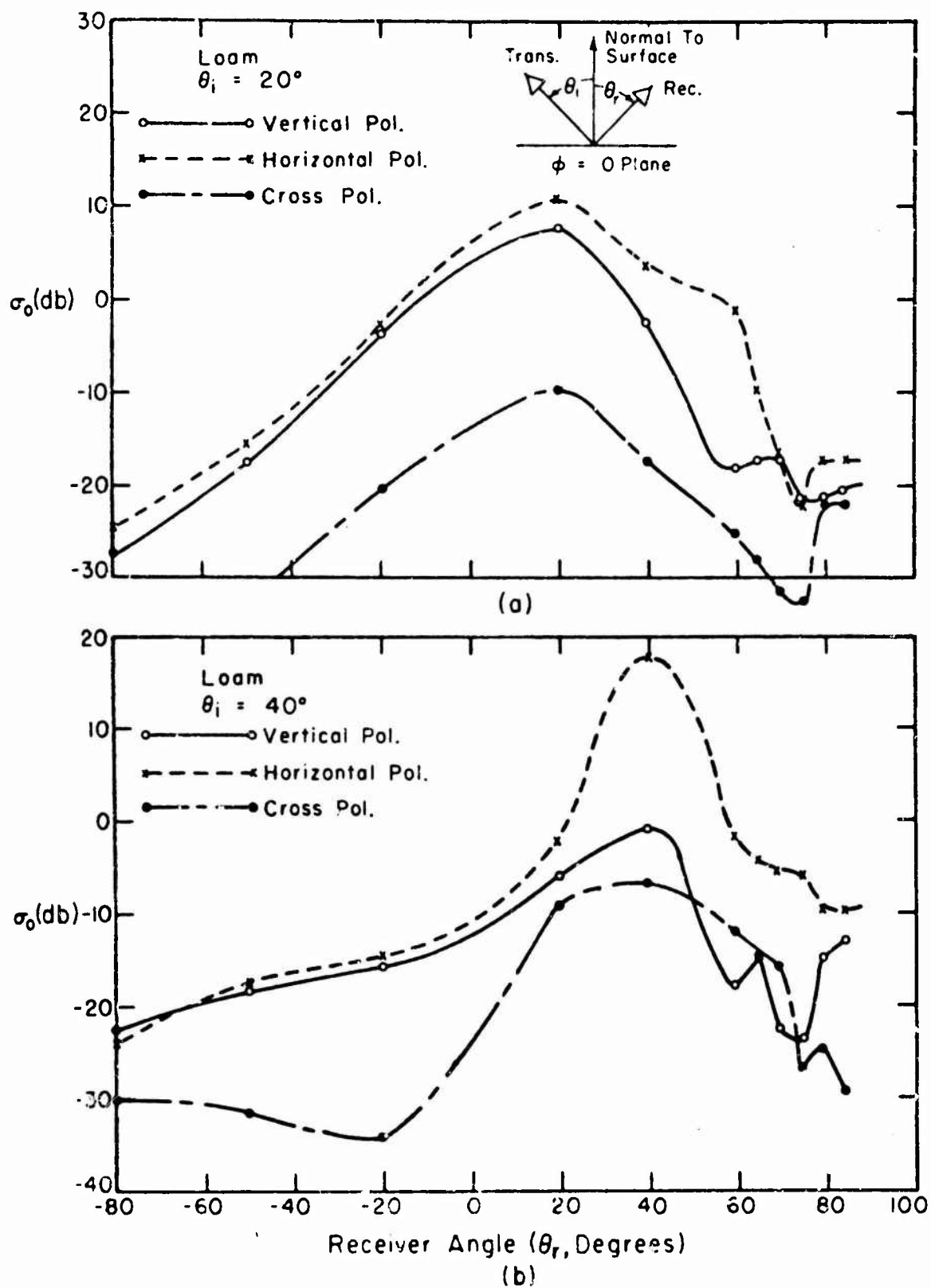
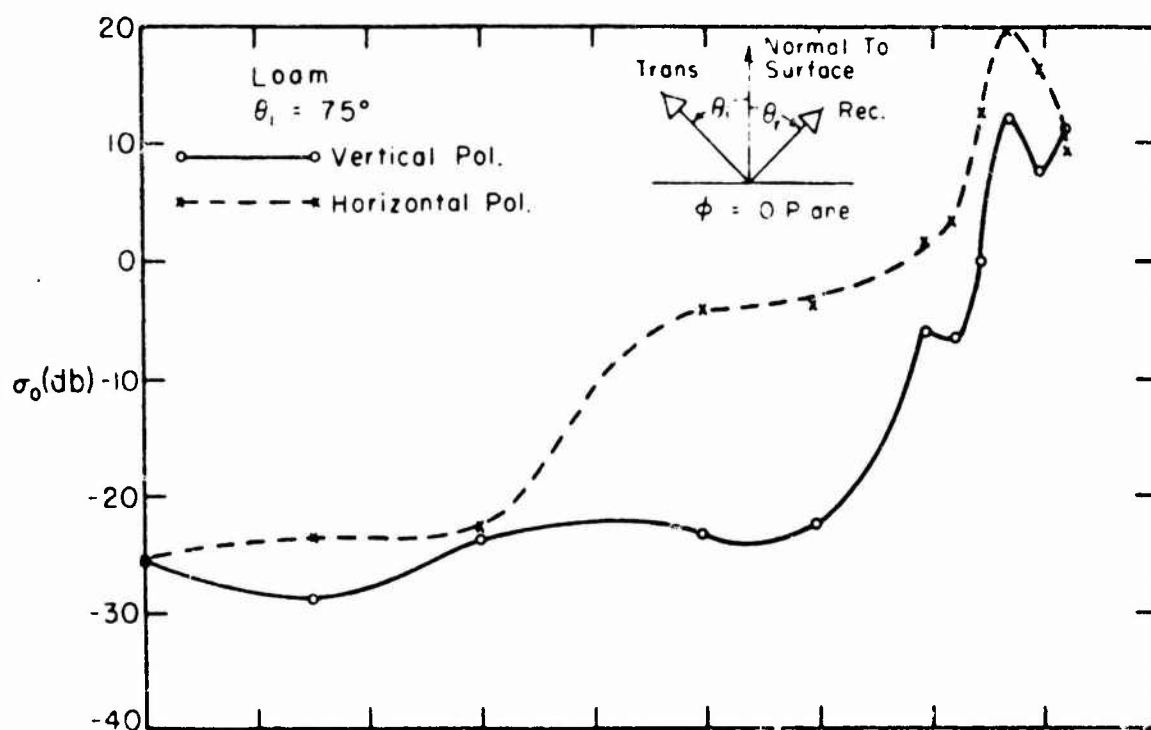


Fig. 77. Bistatic scattering cross section, in the plane of incidence, for smooth loam at X-band.



(c)

Fig. 77. (Continued)

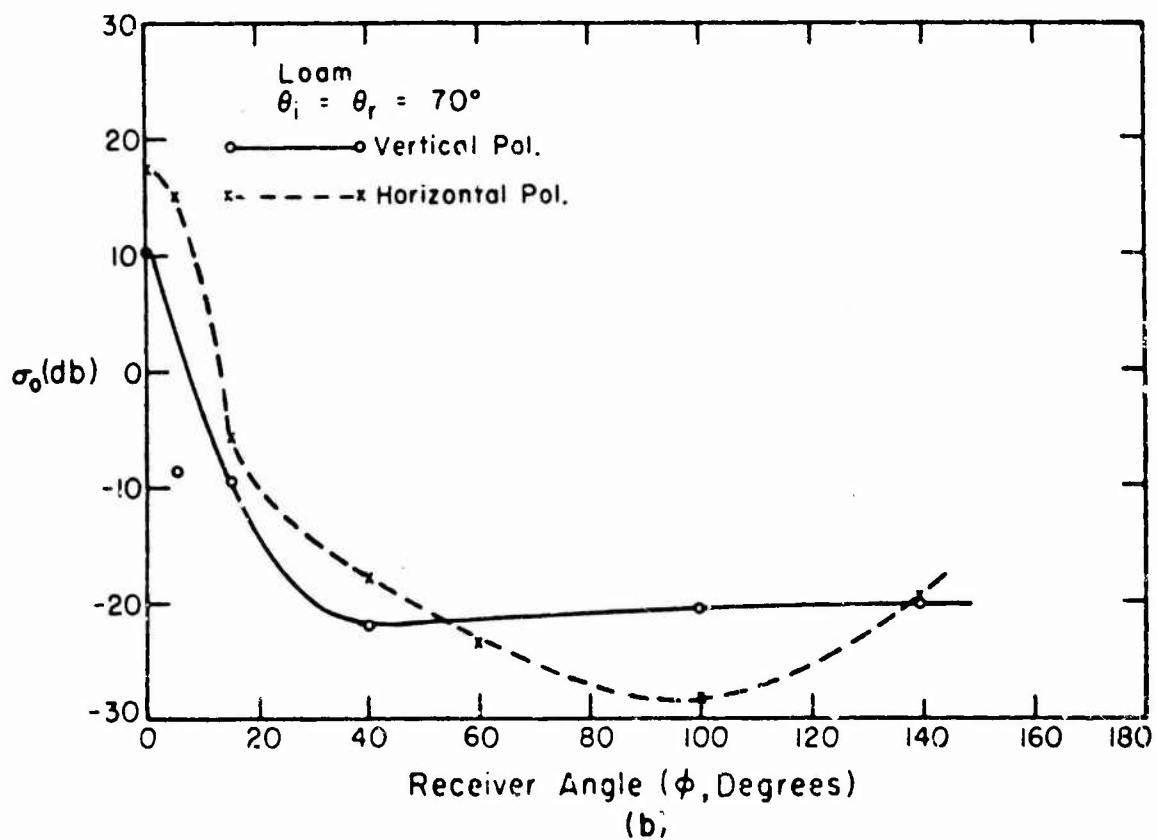
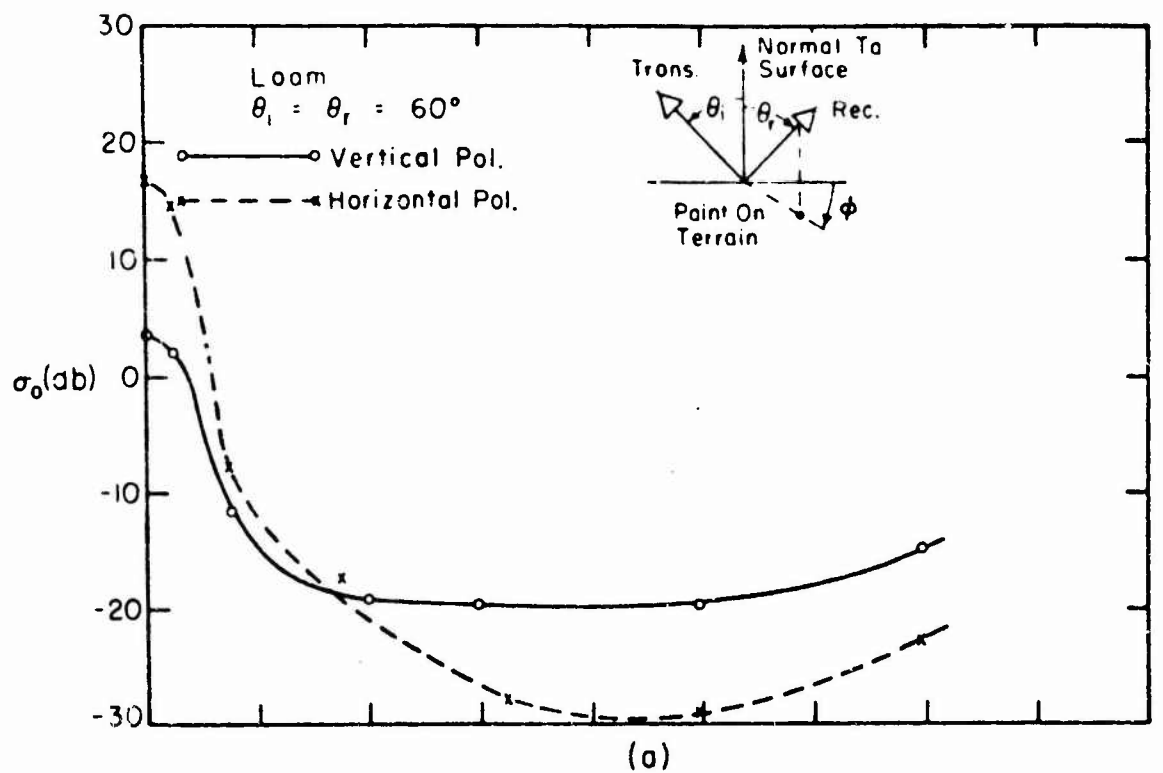
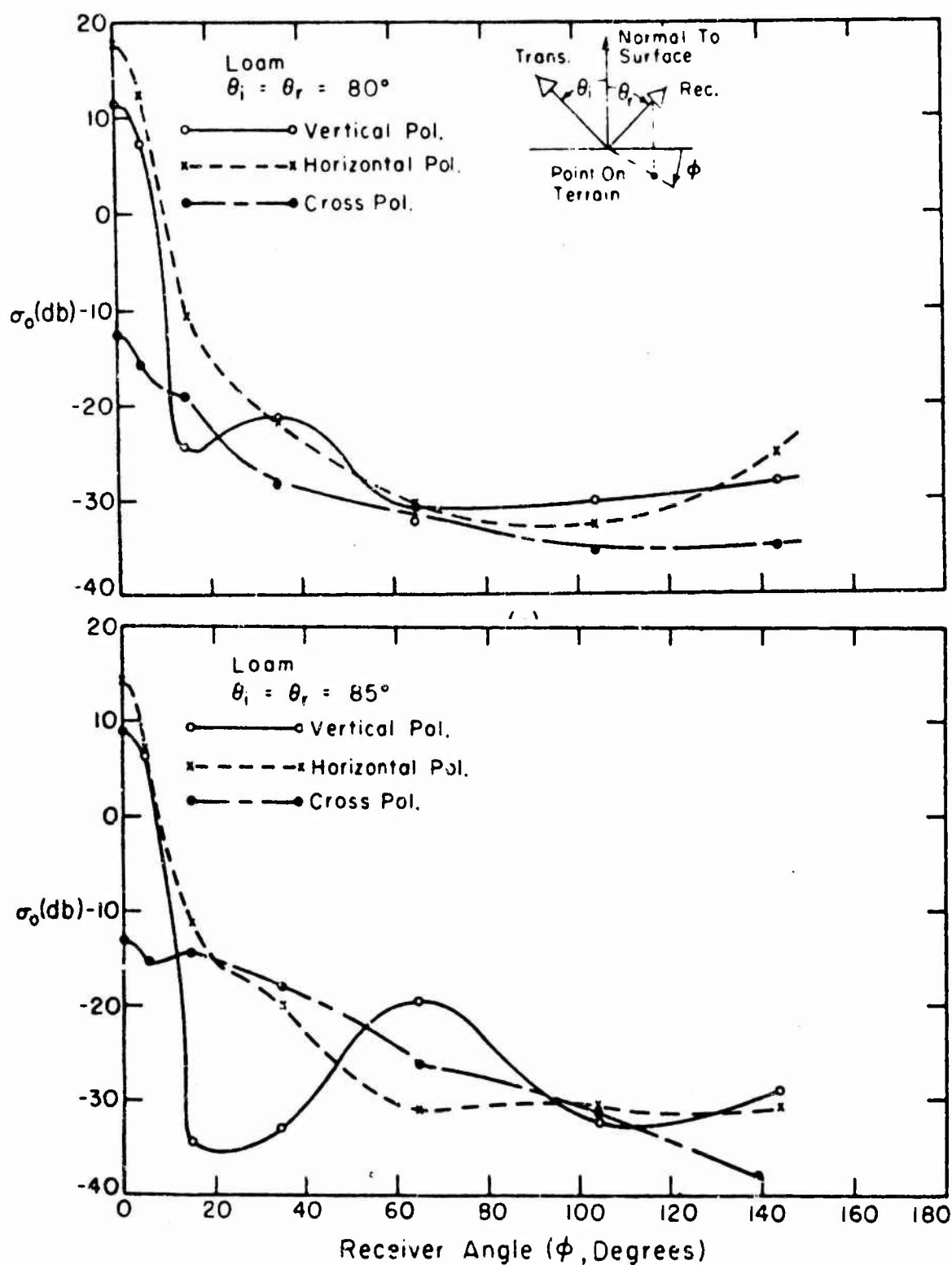


Fig. 78. Bistatic scattering cross section, in the azimuth cone, for smooth loam at X-band.



(d)

Fig. 78. (Continued)

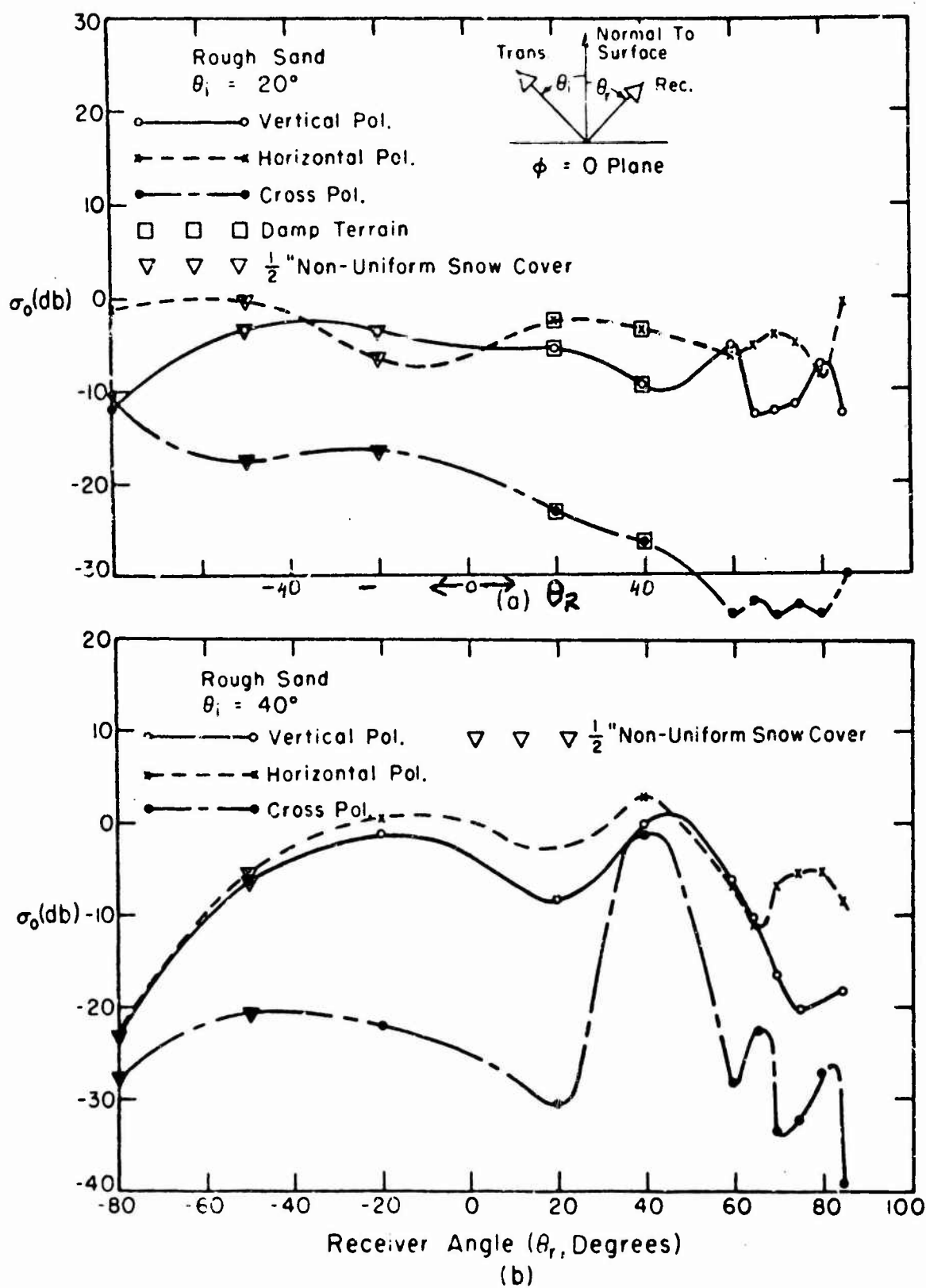
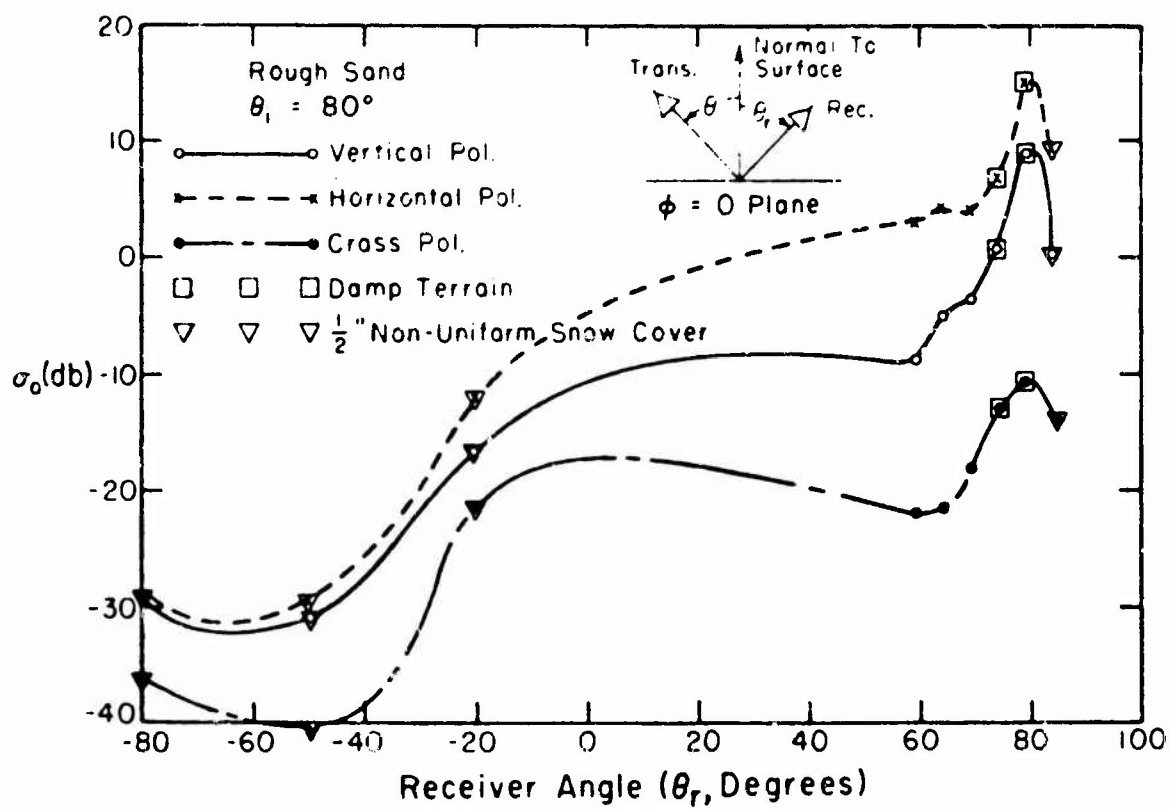


Fig. 79. Bistatic scattering cross section, in the plane of incidence, for rough sand at X-band.



(c)

Fig. 79. (Continued)

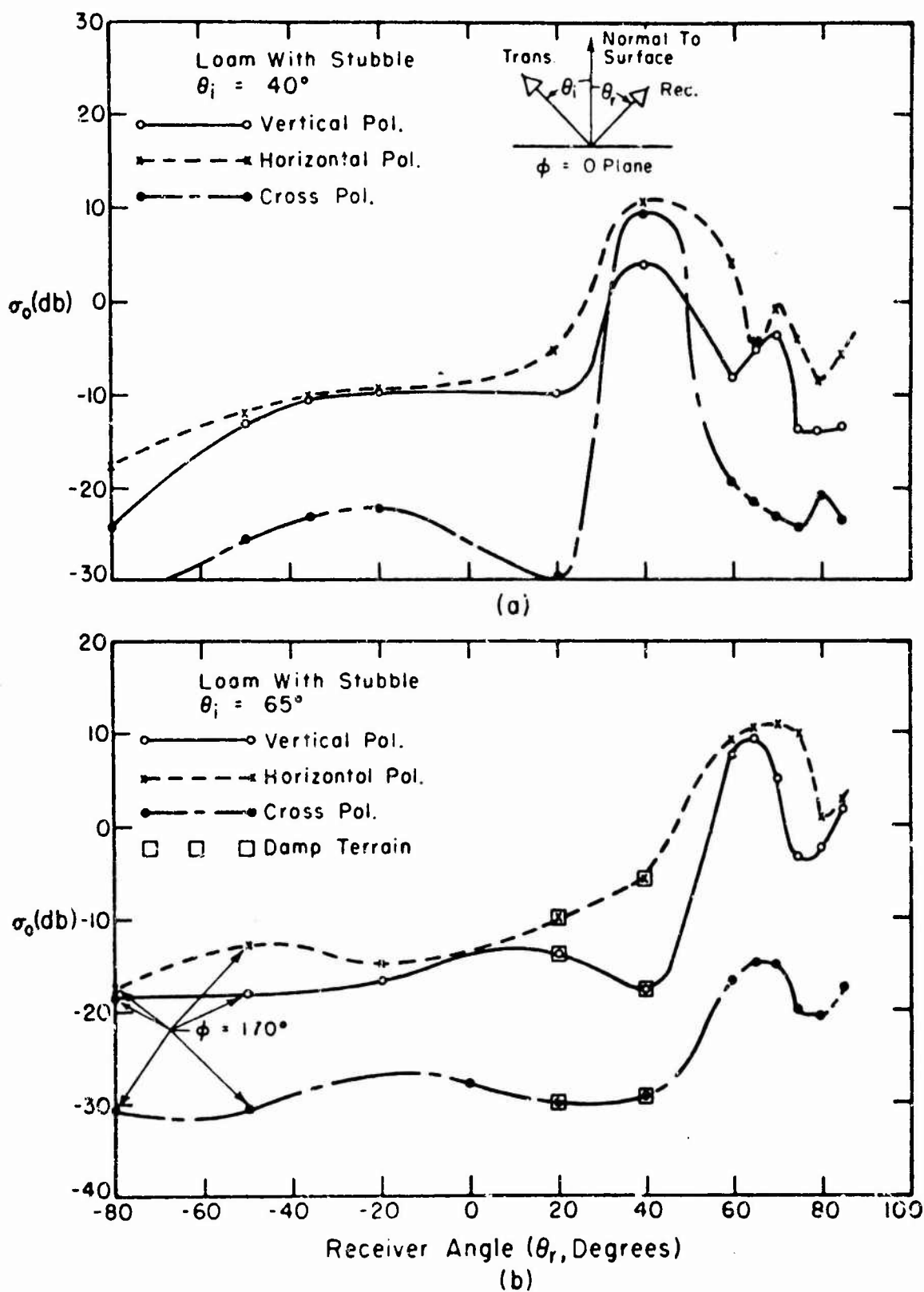
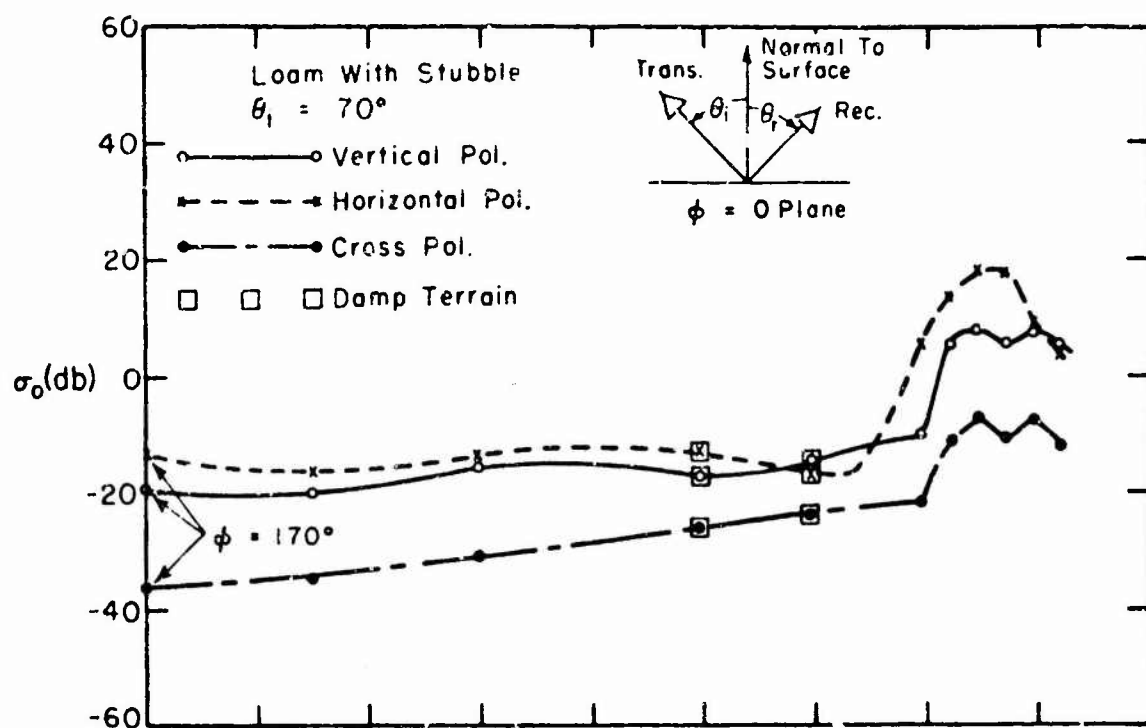
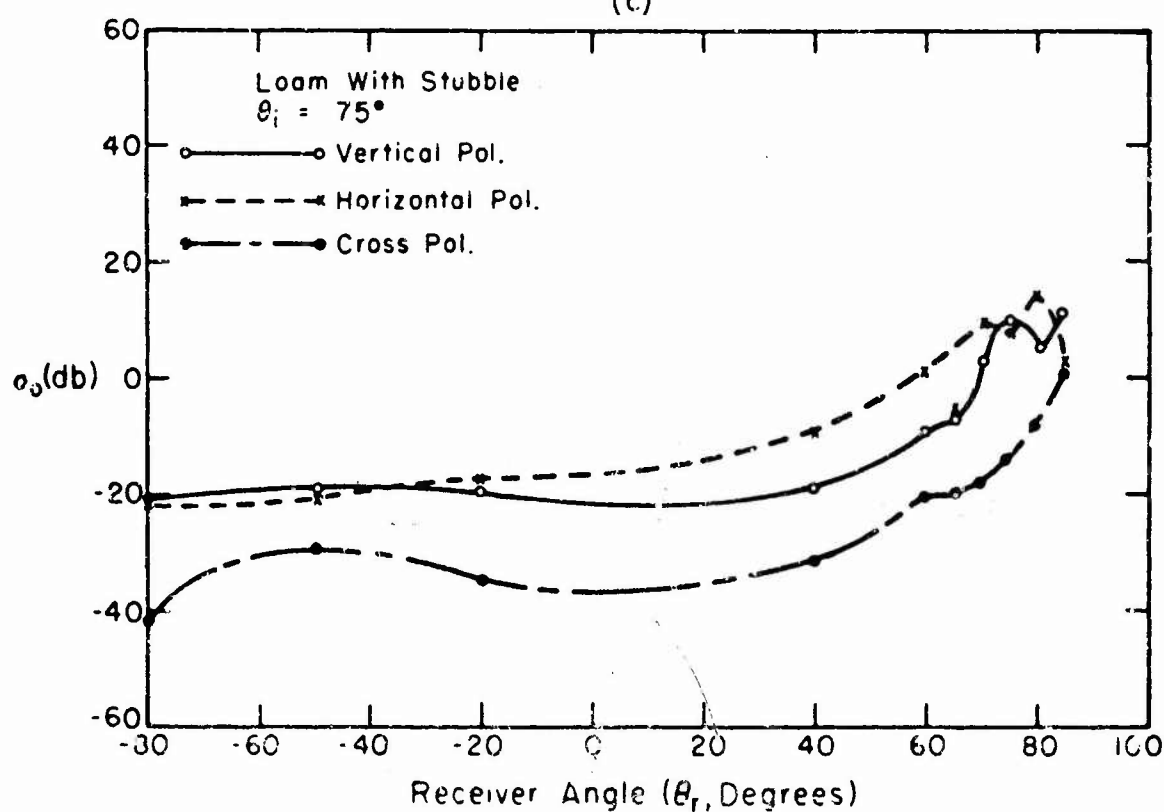


Fig. 80. Bistatic scattering cross section, in the plane of incidence, for stubble at X-band. ($\phi = 0$ or 180° except where marked)

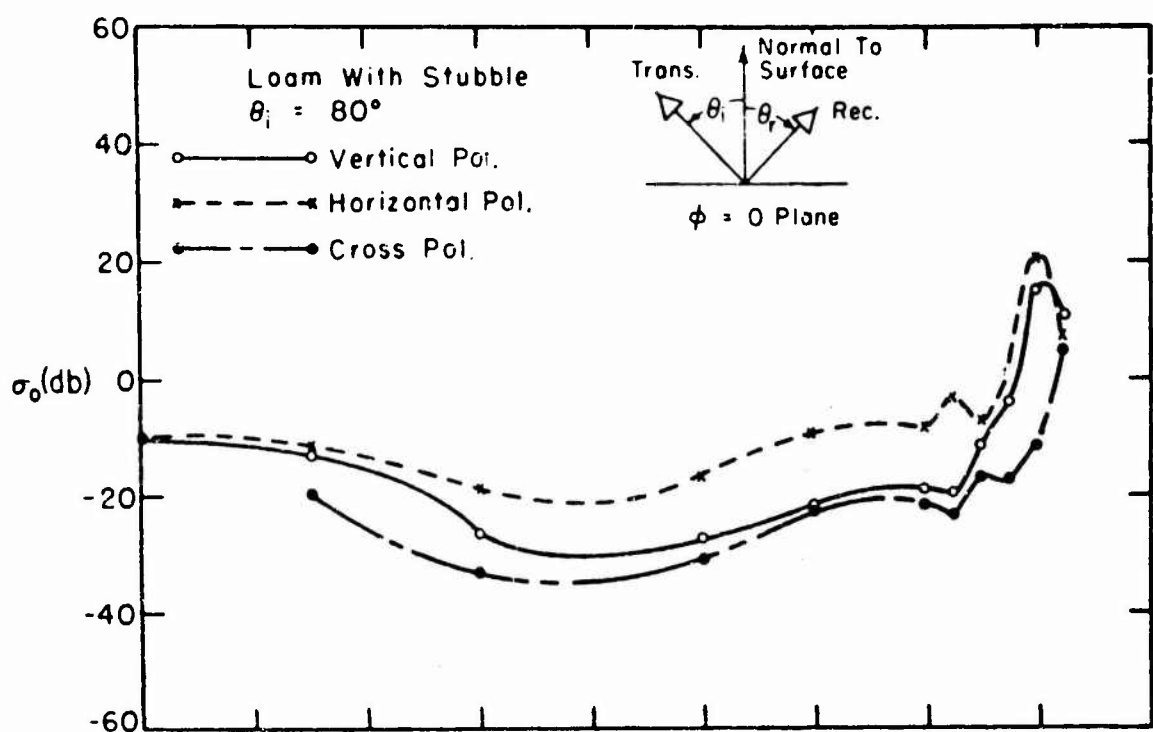


(c)

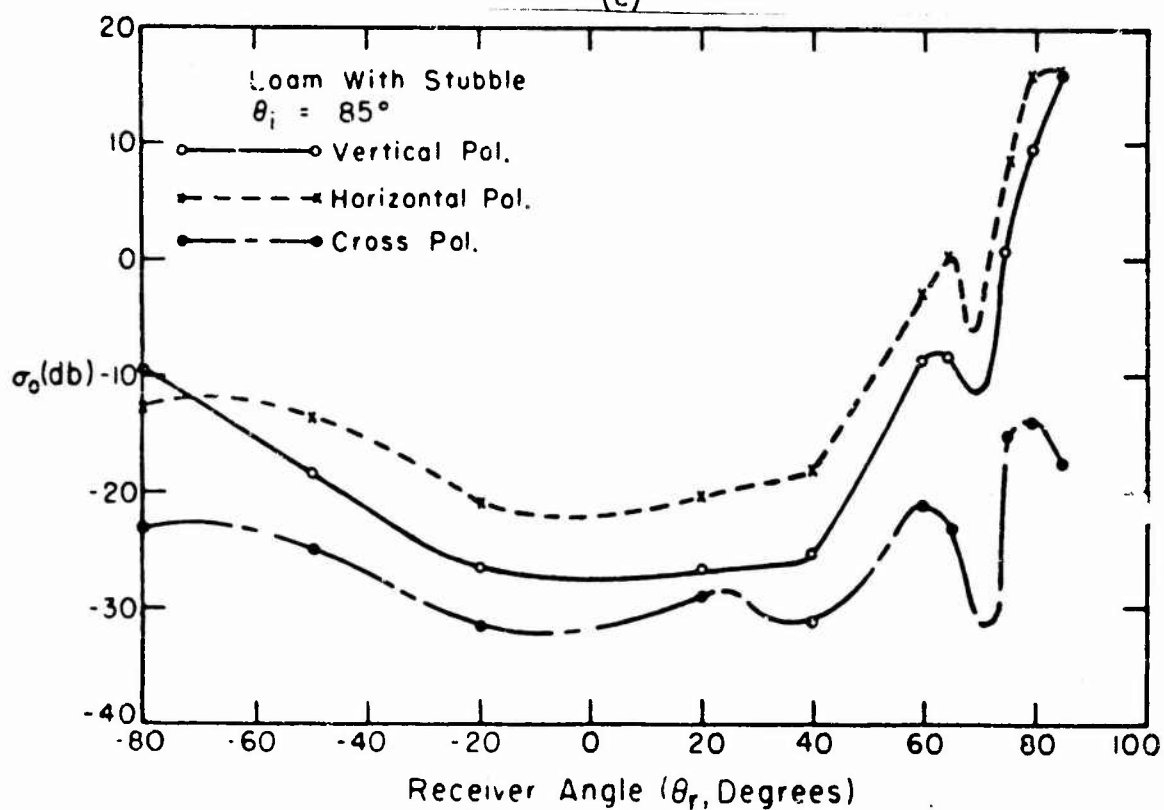


(d)

Fig. 80. (Continued)

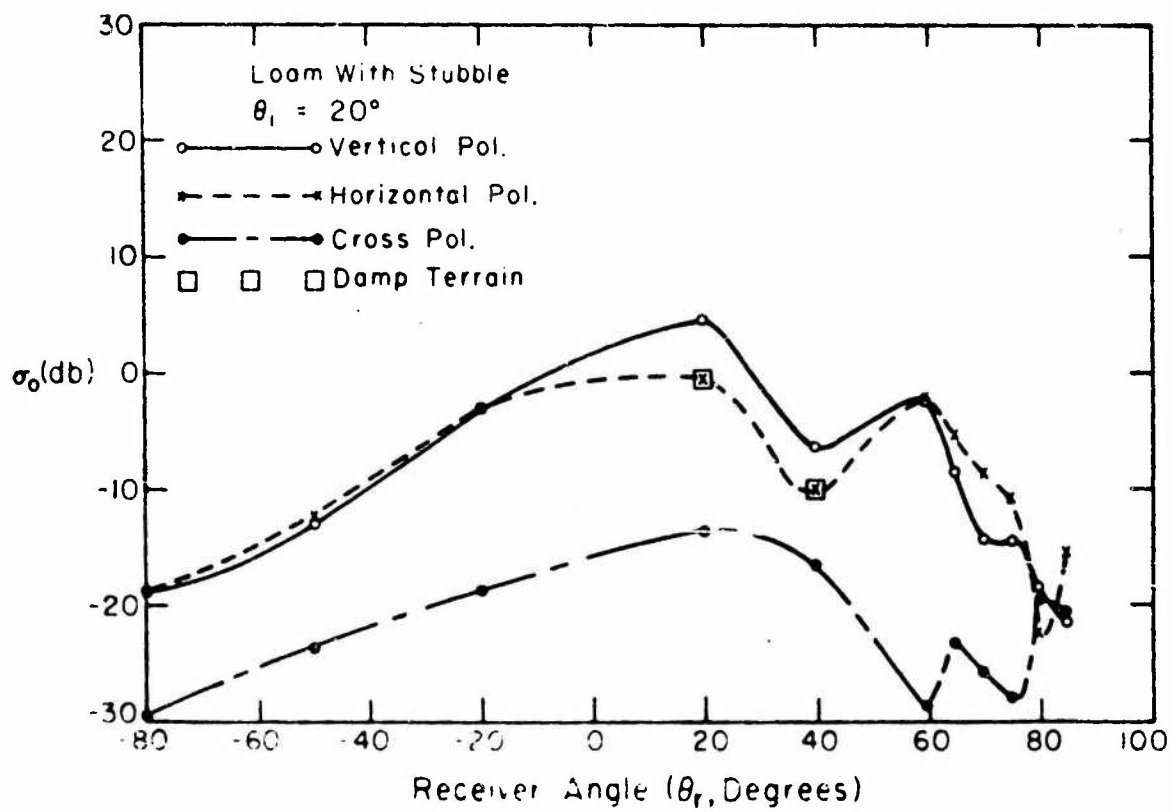


(e)



(f)

Fig. 80. (Continued)



(g)

Fig. 80. (Continued)

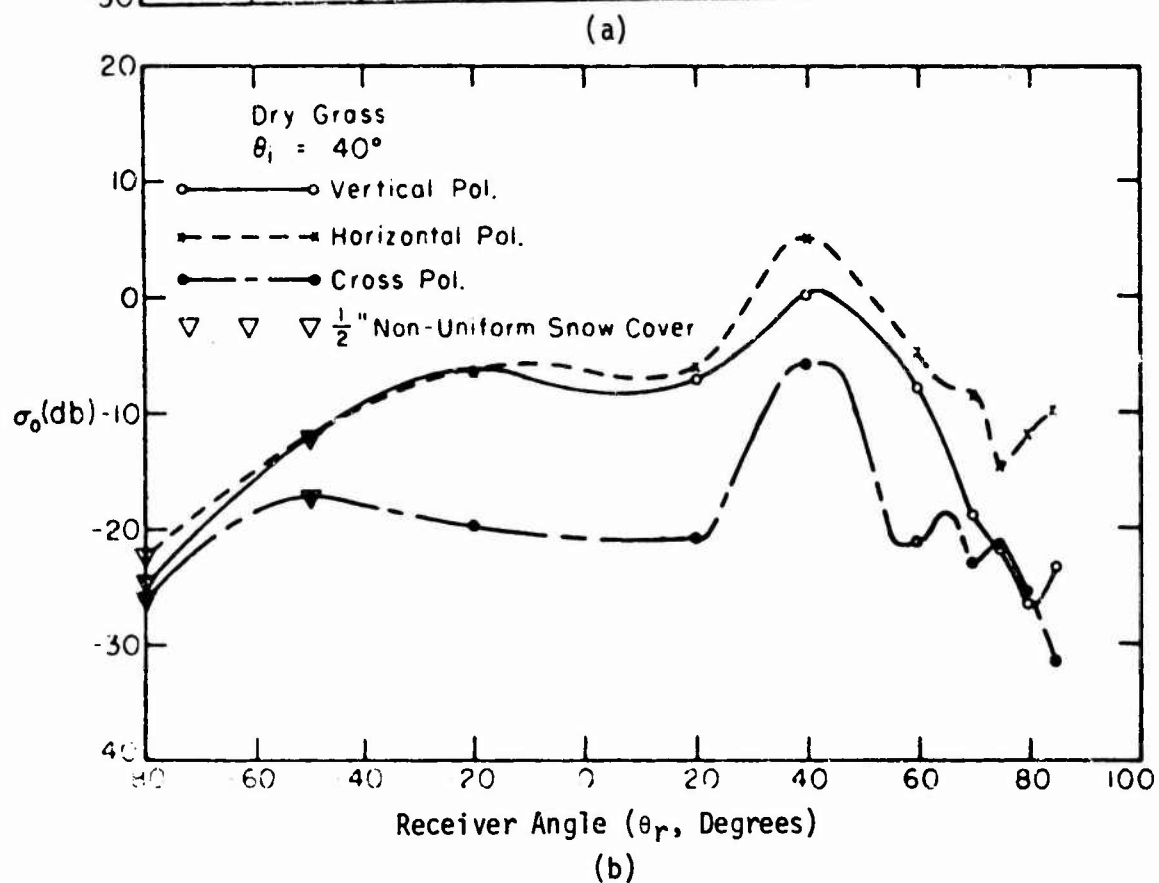
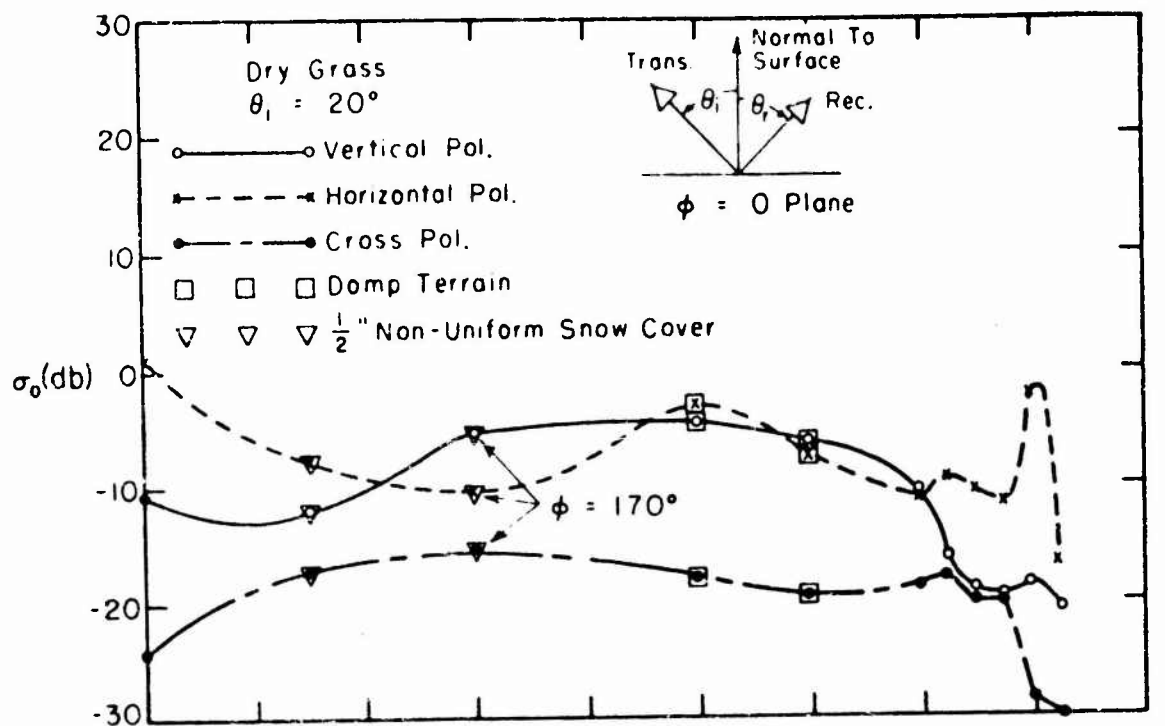
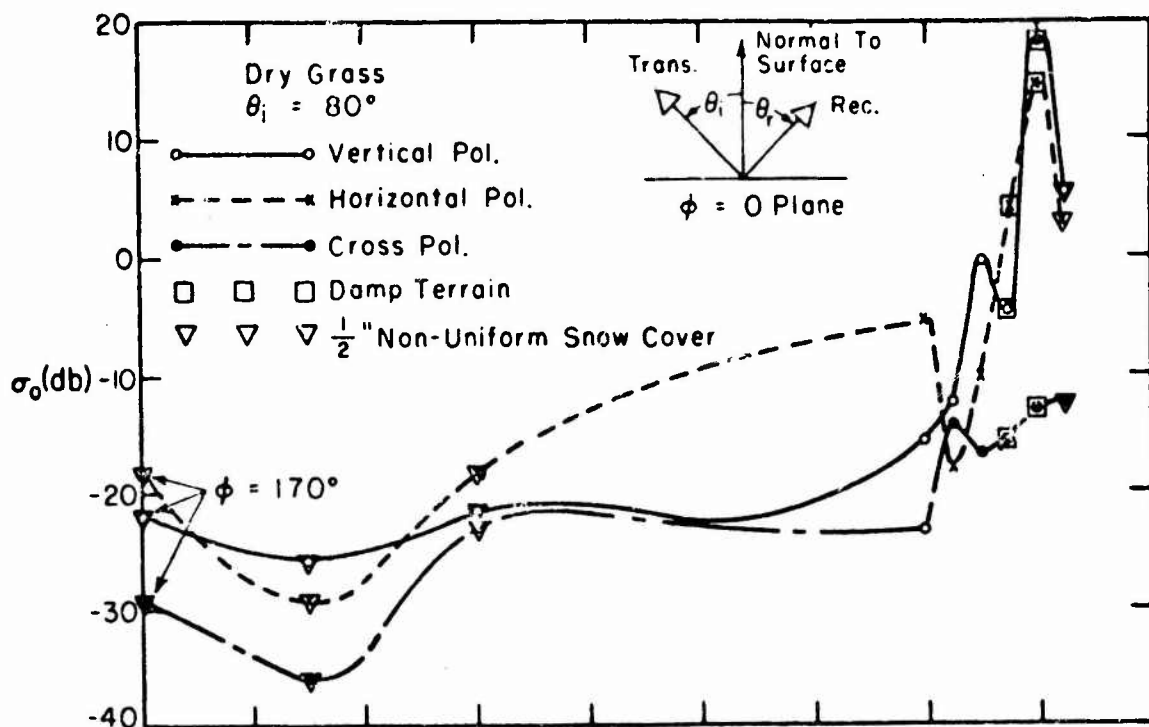
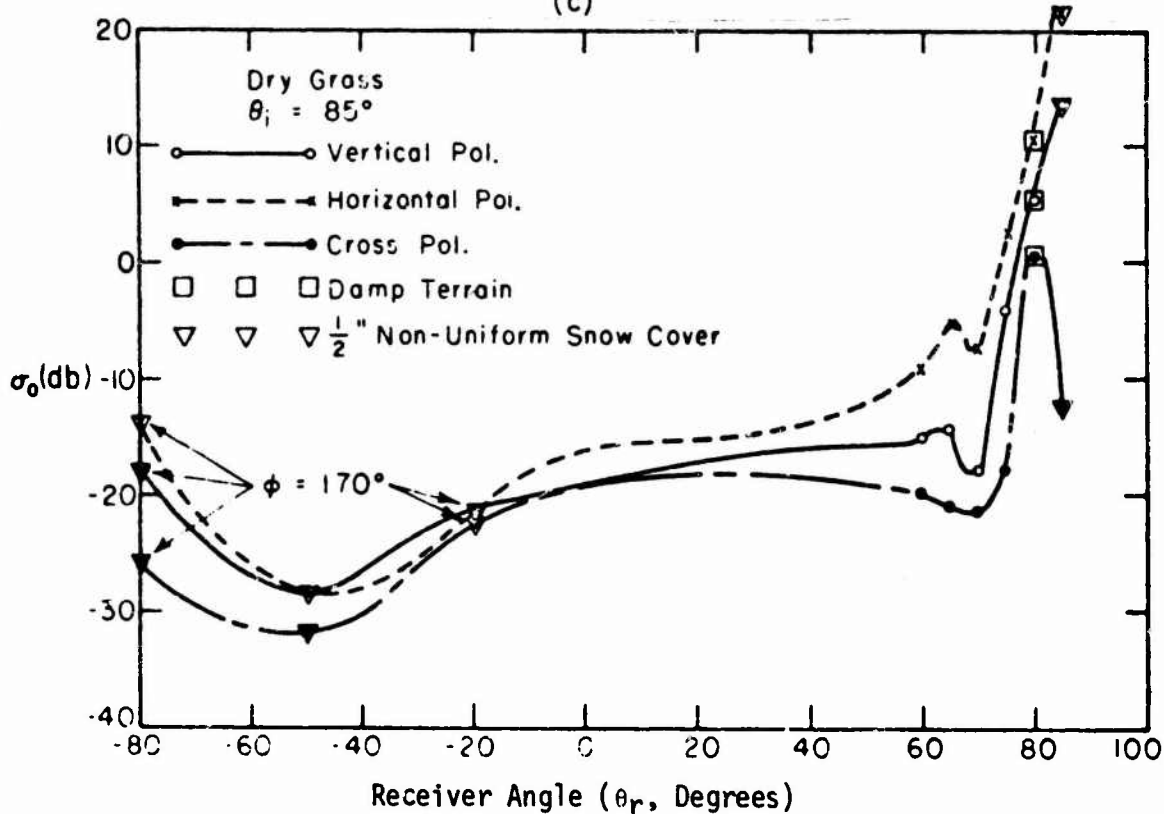


Fig. 81. Bistatic scattering cross section, in the plane of incidence, for dry grass at X-band.



(c)



(d)

Fig. 81. (Continued)

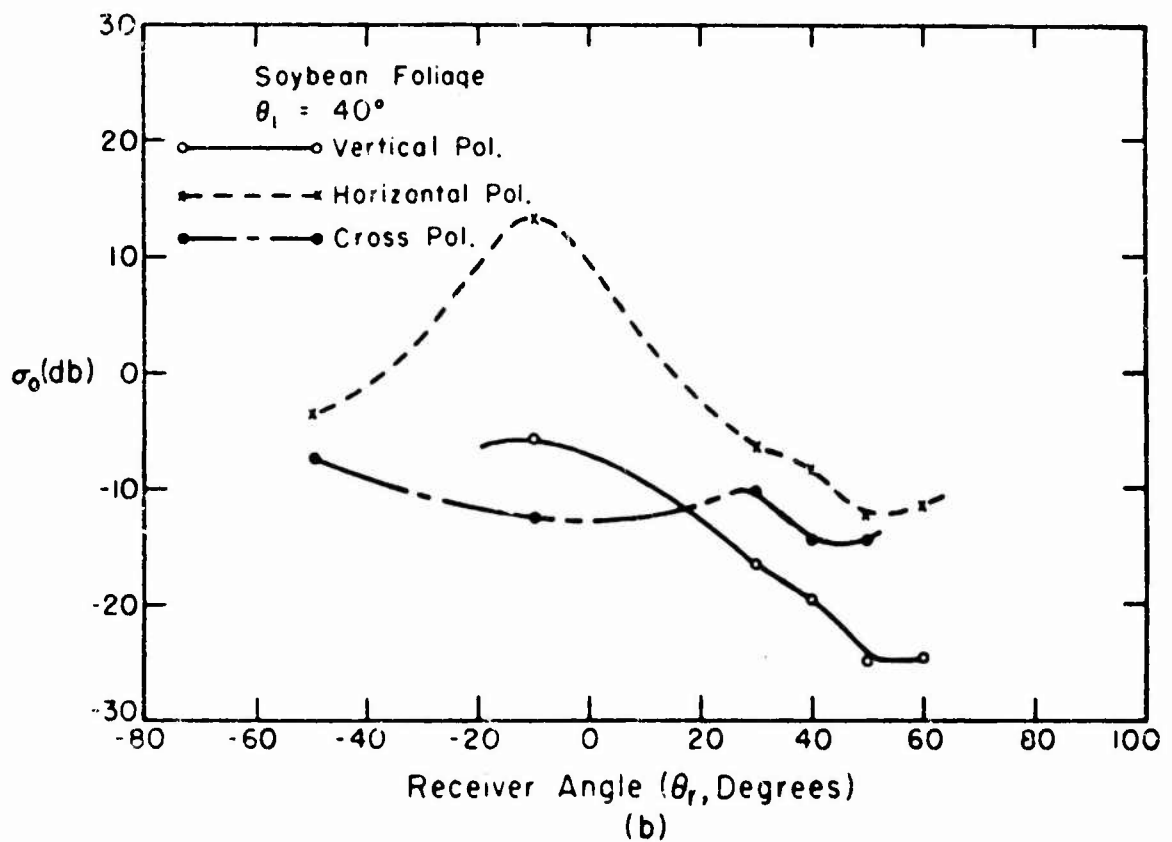
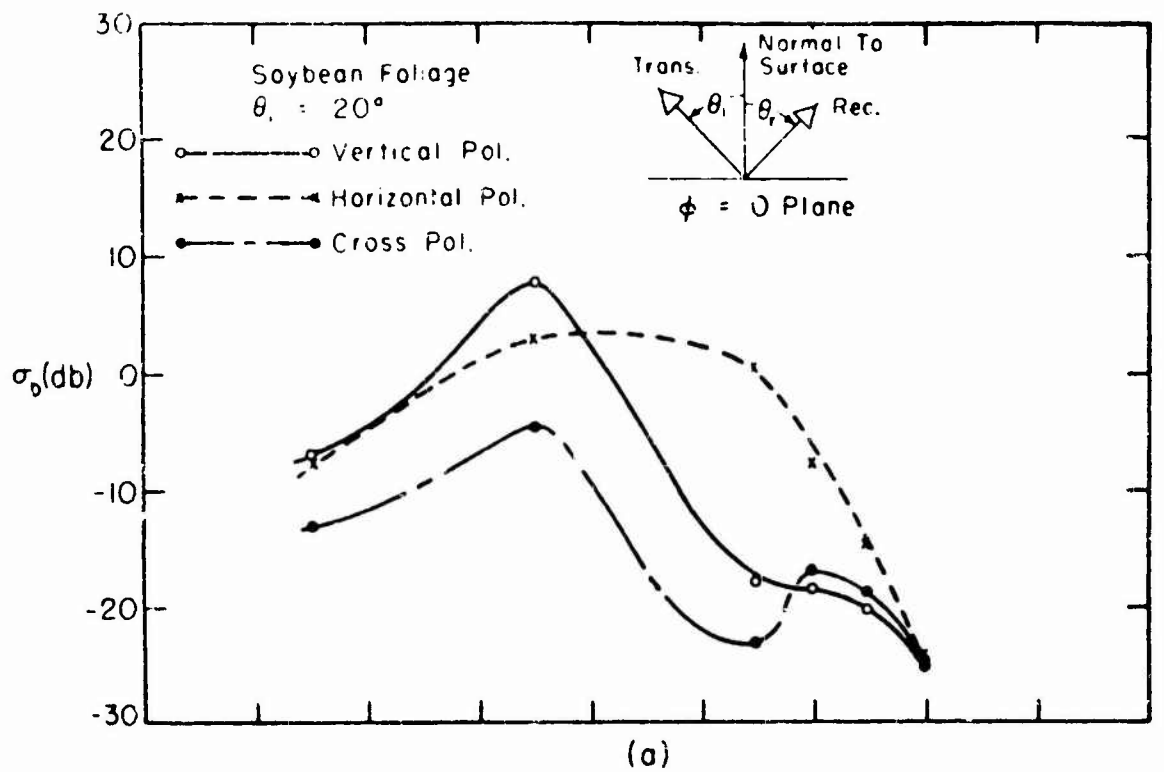


Fig. 82. Bistatic scattering cross section, in the plane of incidence, for soybean foliage at X-band.

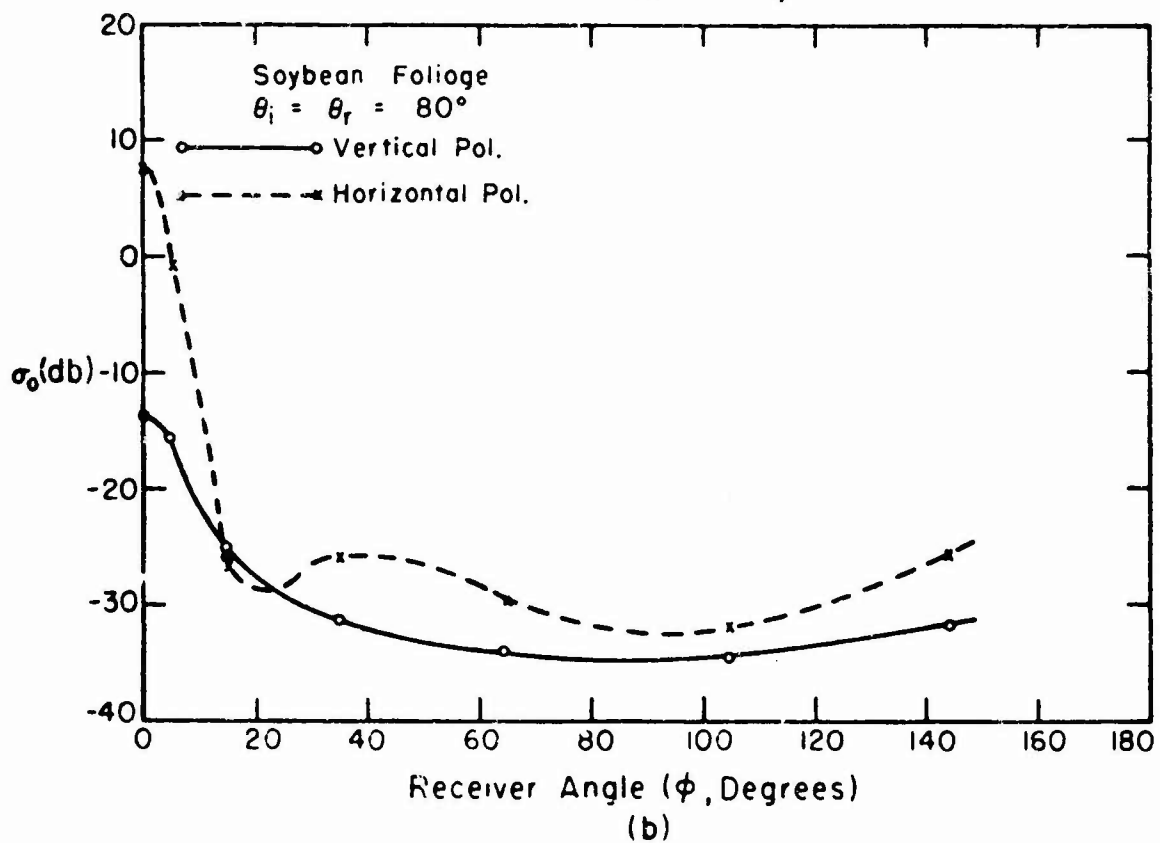
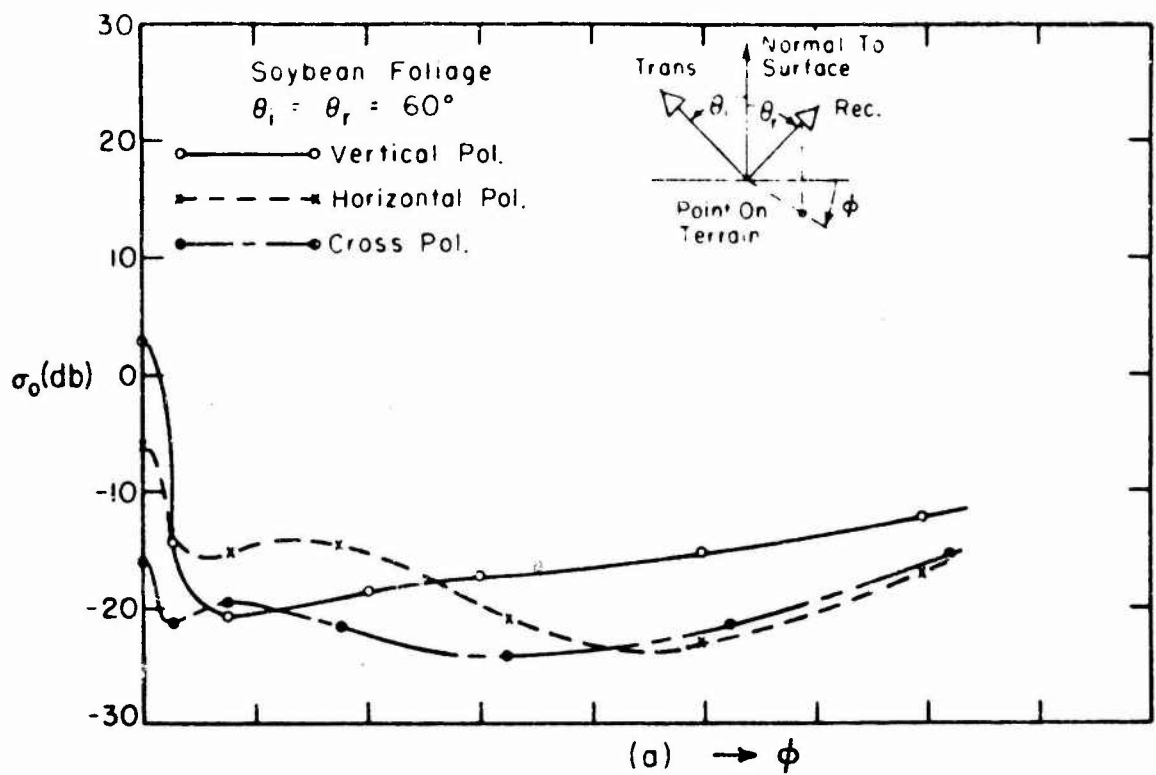


Fig. 83. Bistatic scattering cross section, in the azimuth cone, for soybean foliage at X-band.

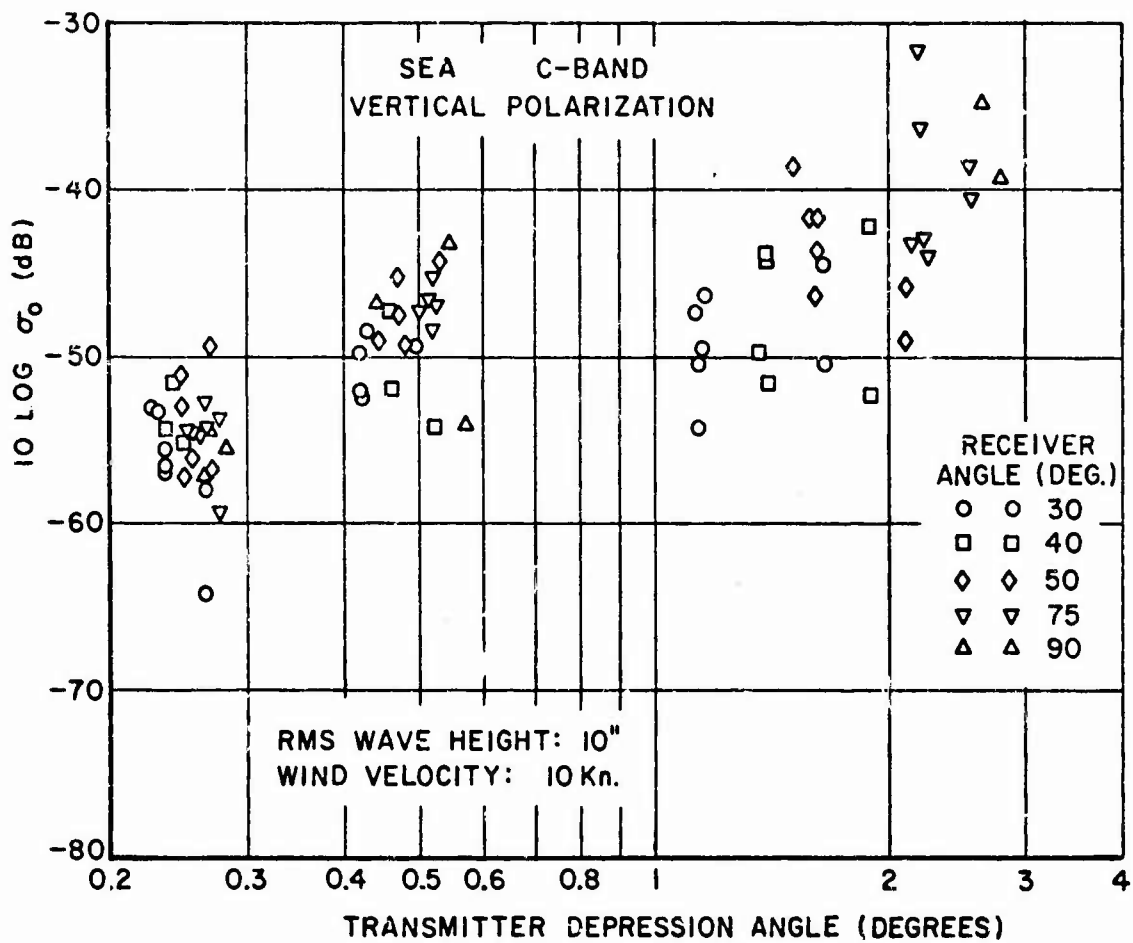


Fig. 84. Bistatic scattering cross section of the sea (sea state 3) at C-band, vertical polarization - Reference 13.

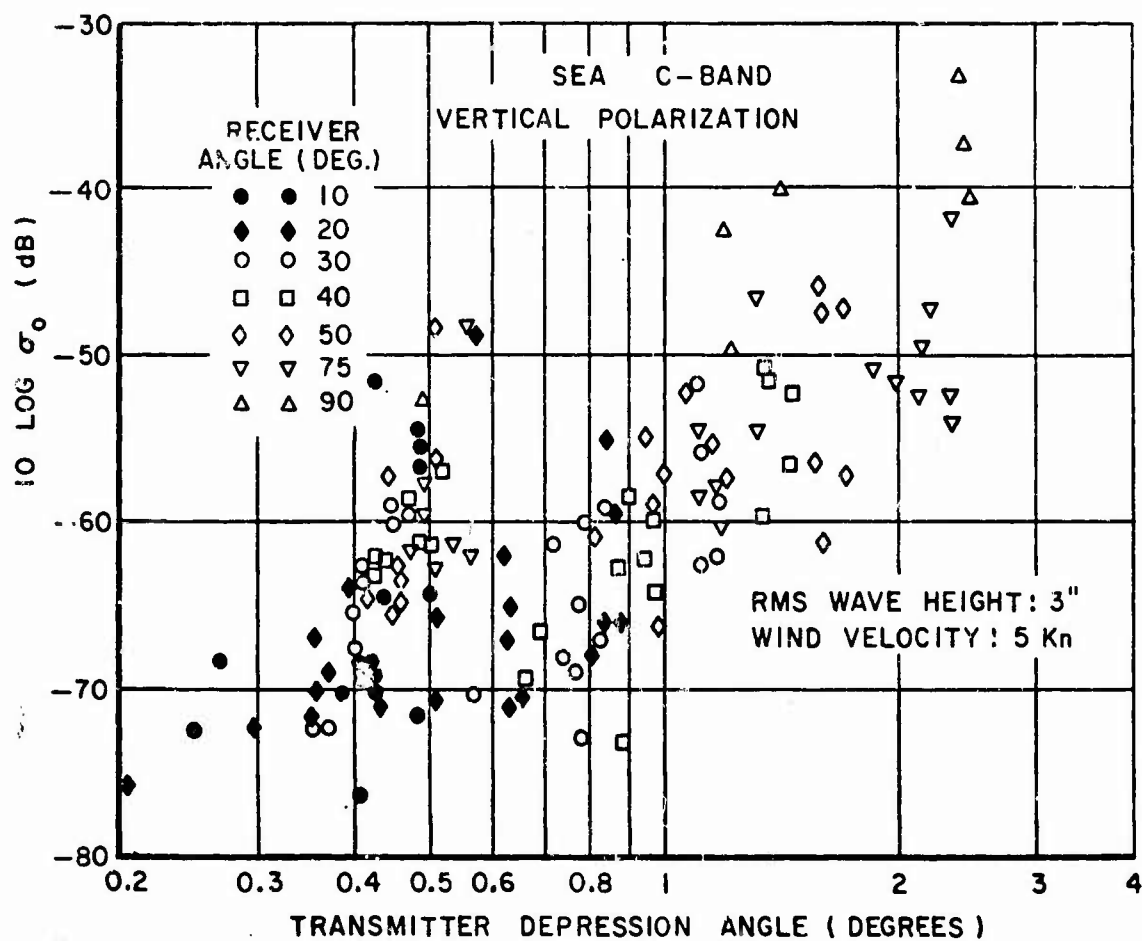


Fig. 85. Bistatic scattering cross section of the sea (sea state 1) at C-band, vertical polarization - Reference 13. (Depression angle = grazing angle = $90^\circ - \theta_i$.)

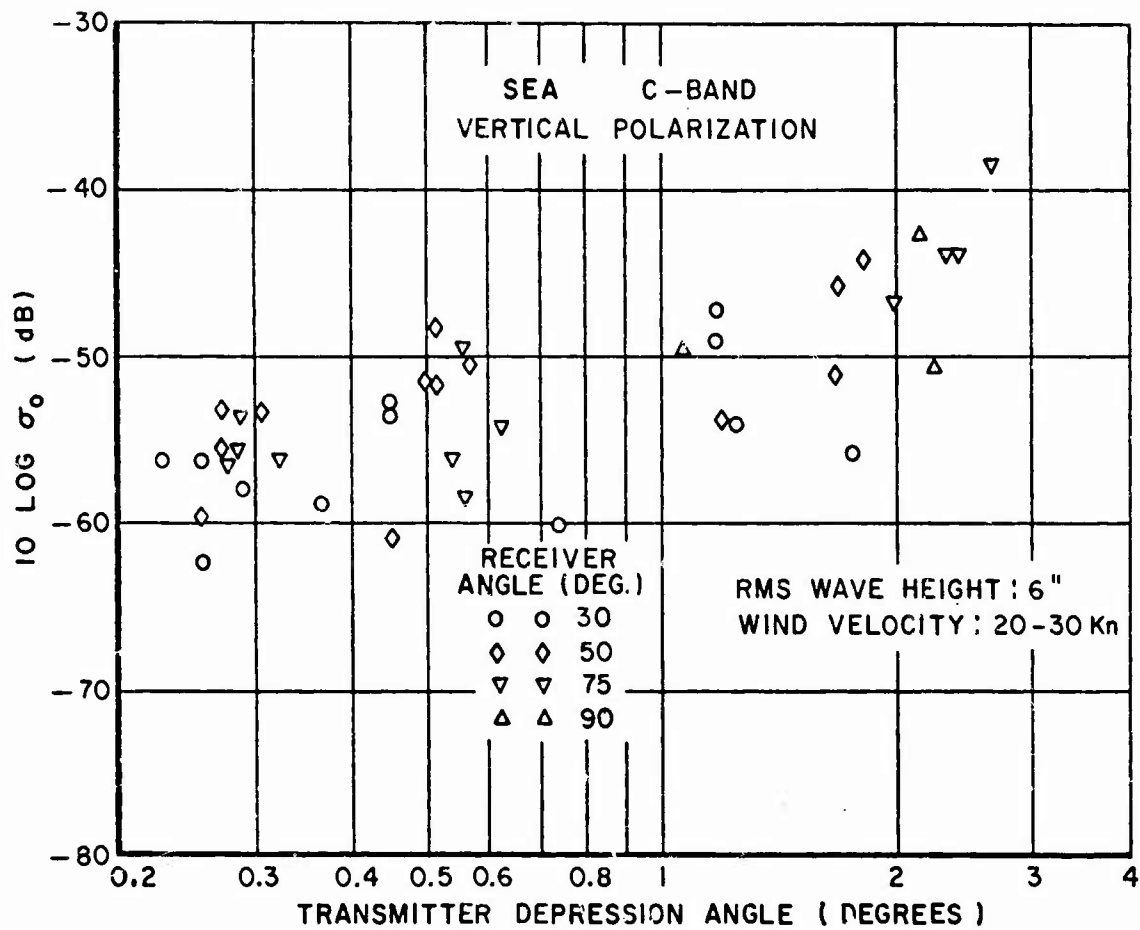


Fig. 86. Bistatic scattering cross section of the sea (sea state 2) at C-band, vertical polarization - Reference 13.

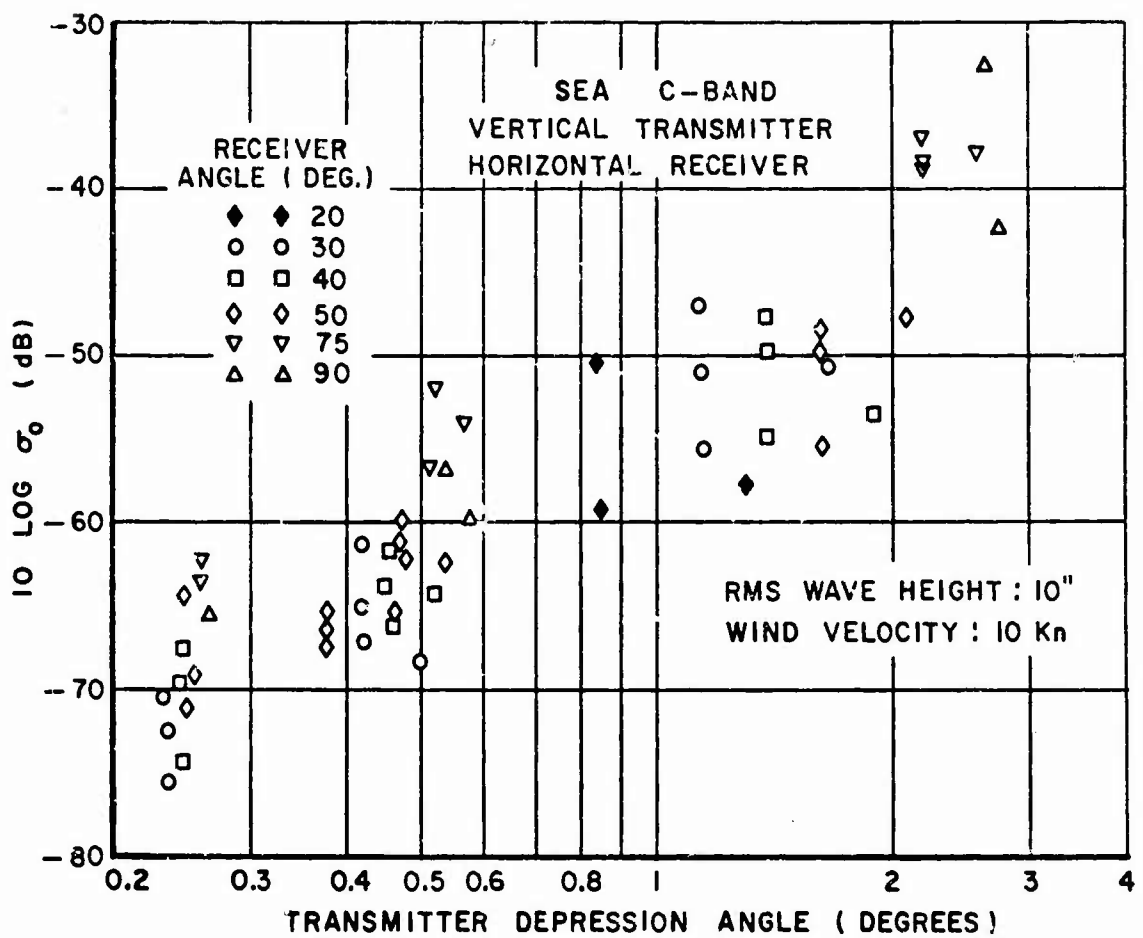


Fig. 87. Bistatic scattering cross section of the sea (sea state 3) at C-band, vertically-polarized transmitter and horizontally-polarized receiver - Reference 13.

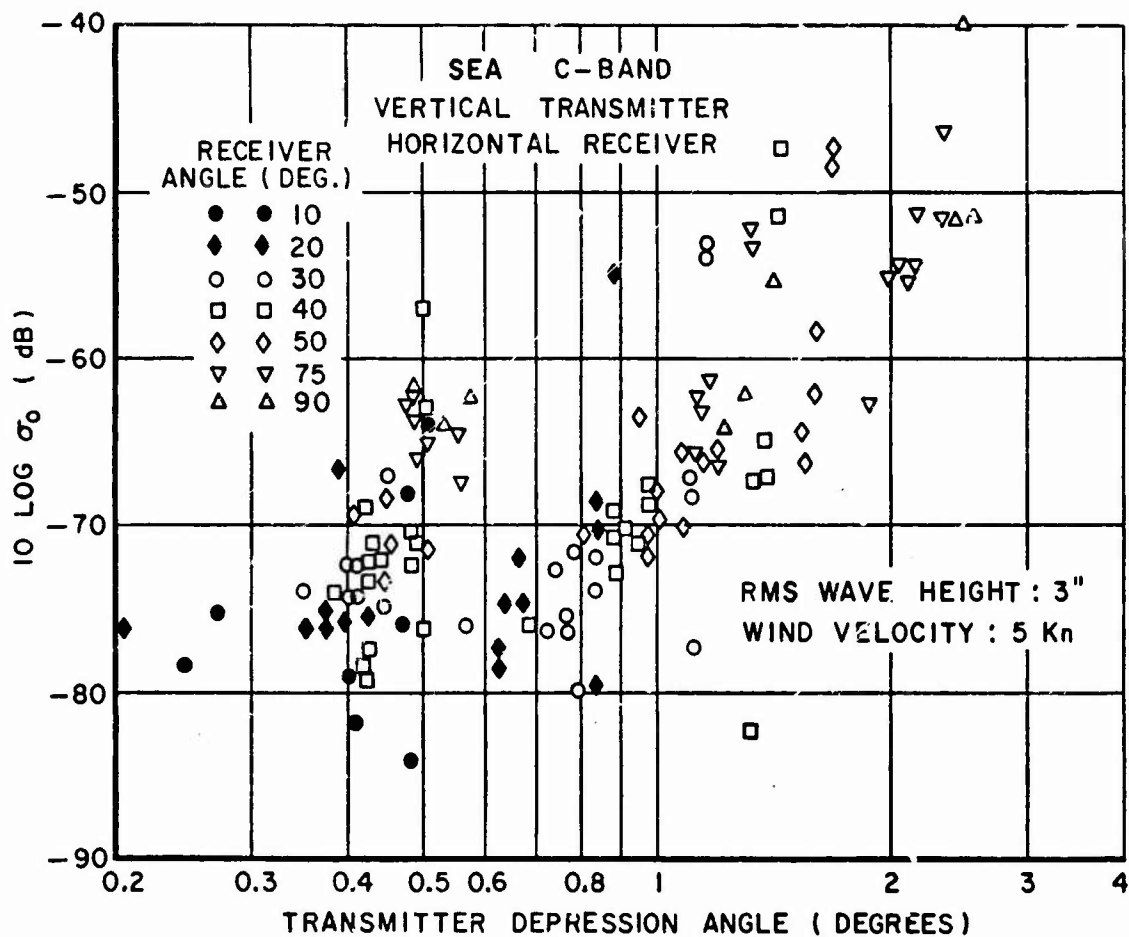


Fig. 88. Bistatic scattering cross section of the sea (sea state 1) at C-band, vertically-polarized transmitter and horizontally-polarized receiver - Reference 13.

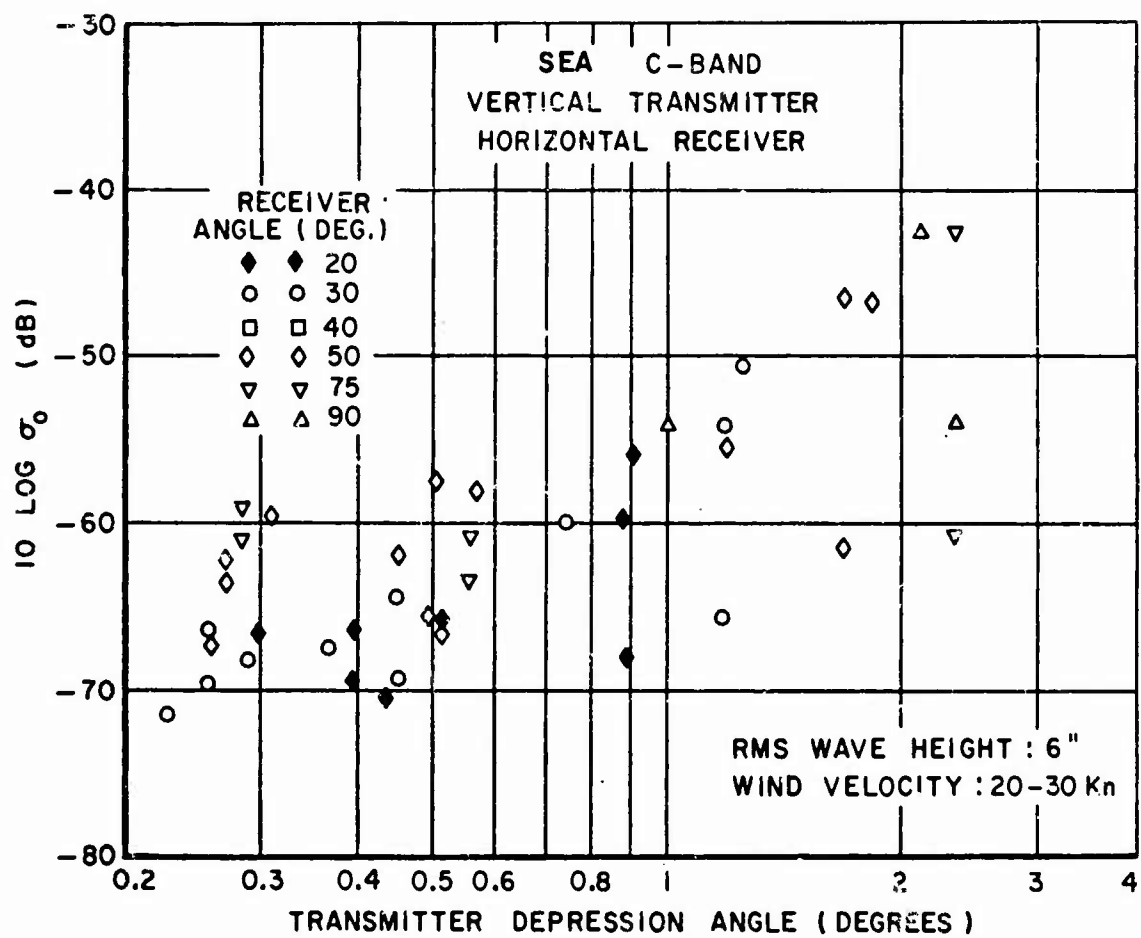


Fig. 89. Bistatic scattering cross section of the sea (sea state 2) at C-band, vertically-polarized transmitter and horizontally-polarized receiver - Reference 13.

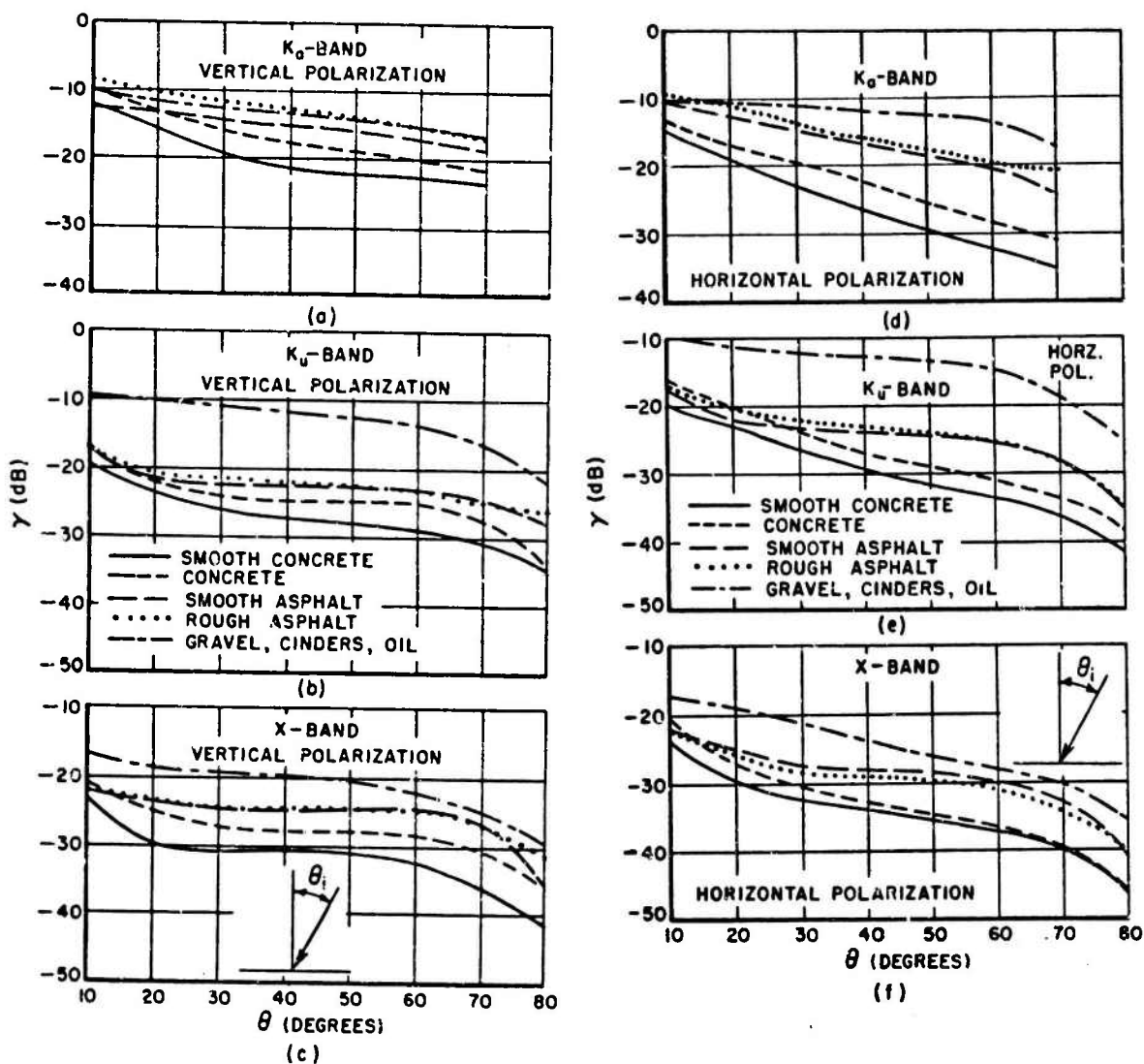


Fig. 90. Radar backscattering cross sections for several slightly rough surfaces - Reference 3.

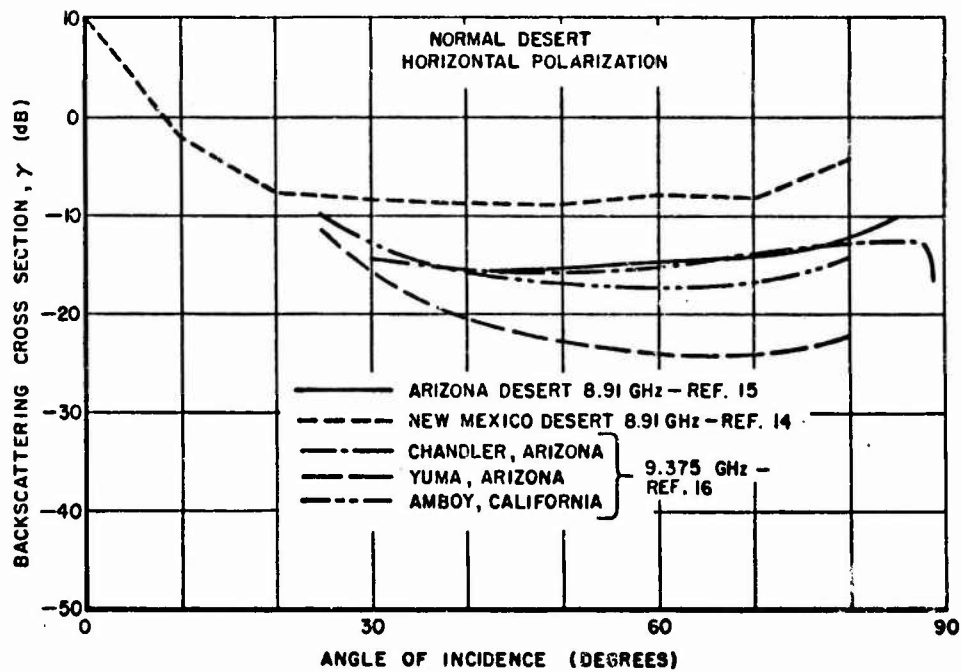


Fig. 91. Radar backscattering cross section for normal desert at X-band.

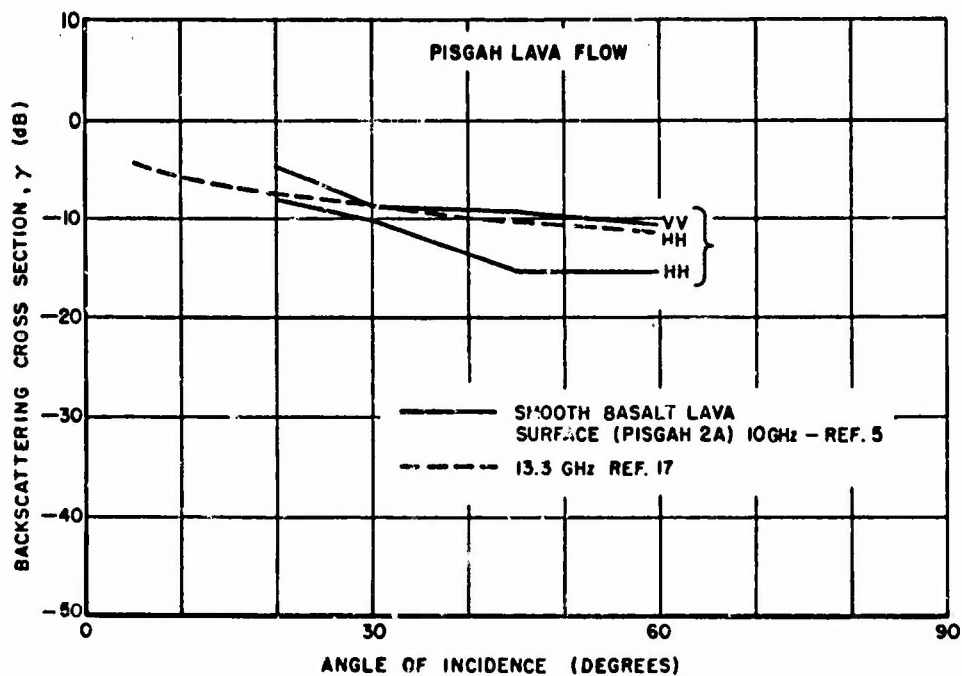


Fig. 92. Radar backscattering cross section for Pissgah Lava Flow at X-band and K_u -band.

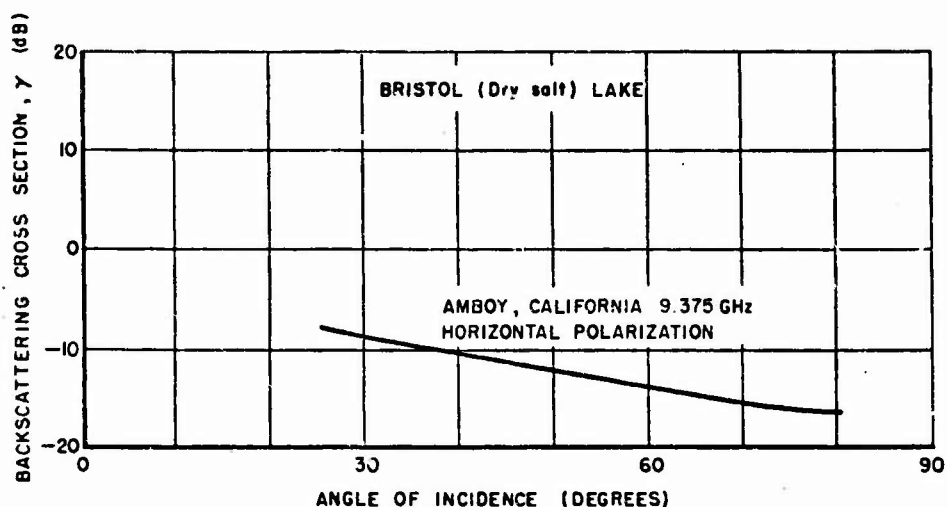


Fig. 93. Radar backscattering cross section for Bristol (Dry Salt) Lake at X-band - Reference 16.

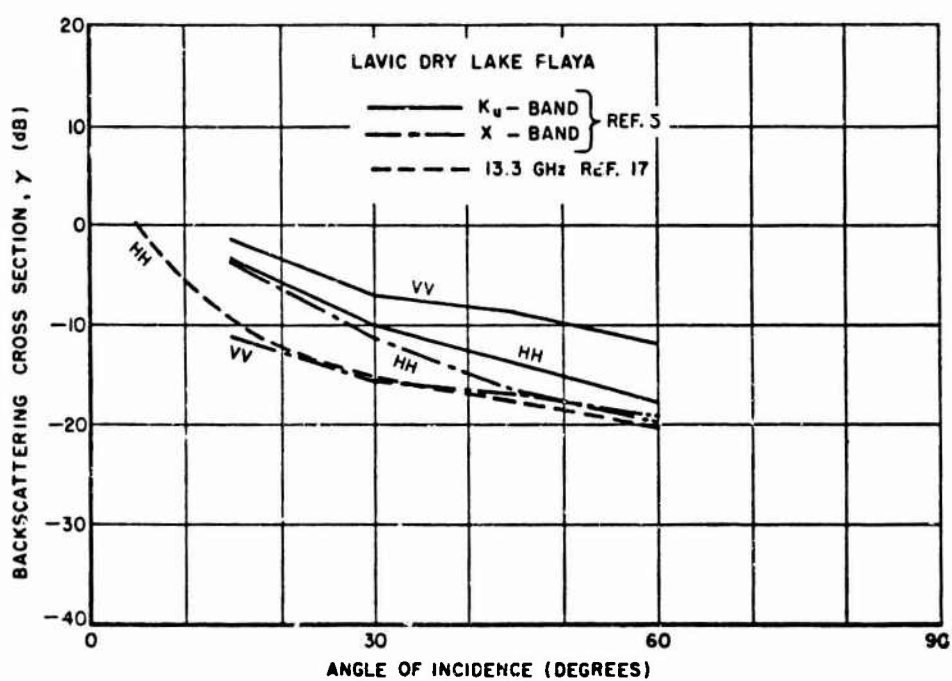


Fig. 94. Radar backscattering cross section for Lavic Dry Lake playa at X-band and K_u -band.



NOT REPRODUCIBLE

Fig. 95. Lavić Lake Playa. The surface of the playa is almost perfectly flat except for small scale roughness generated by contraction (dessication) cracks. These cracks break the playa surface into polygons of three distinct sizes: A - measured in terms of 10's of feet; B - measured in terms of a few feet; and C - measured in terms of a few inches. In the intermediate distance is the radar truck being used to make calibration measurements and in the far distance to the left are the black basalt lava flows from Sunshine Crater. The view is to the northwest.

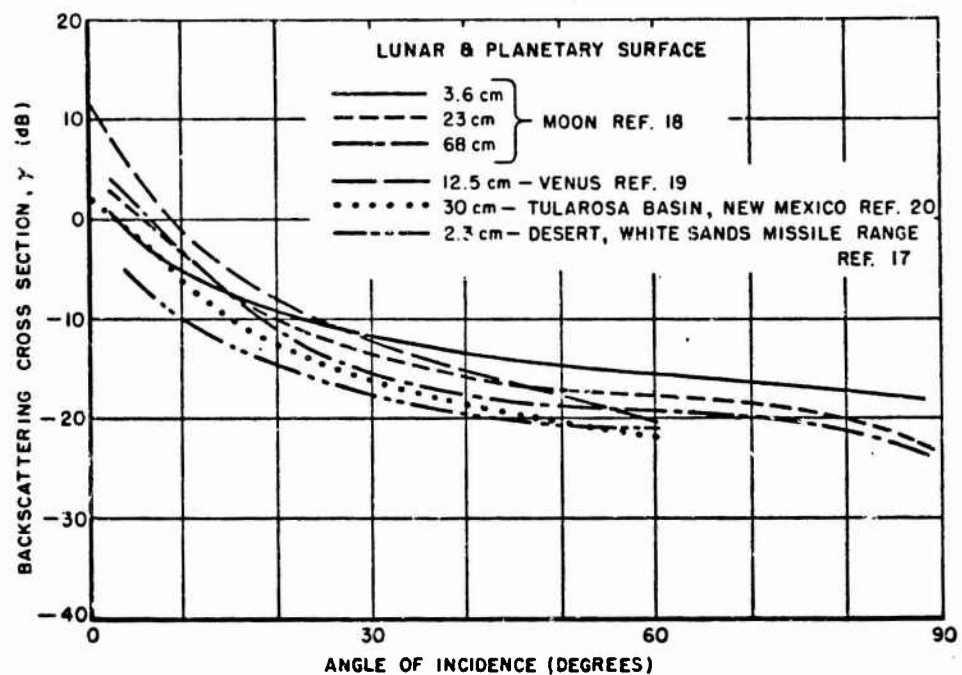


Fig. 96. Radar backscattering cross sections for the lunar and planetary surfaces.

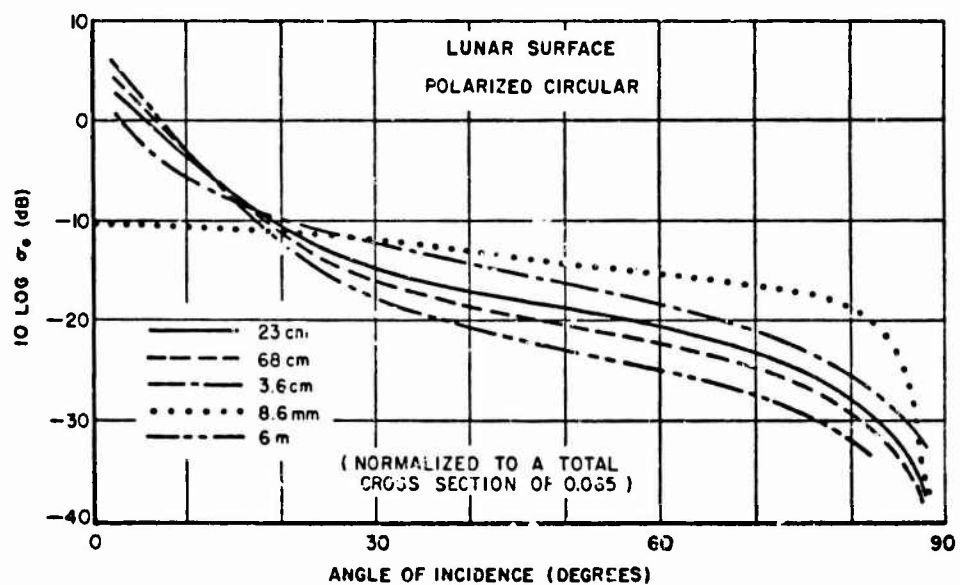


Fig. 97. Frequency dependence of the radar backscattering cross section for the Moon - Reference 21.

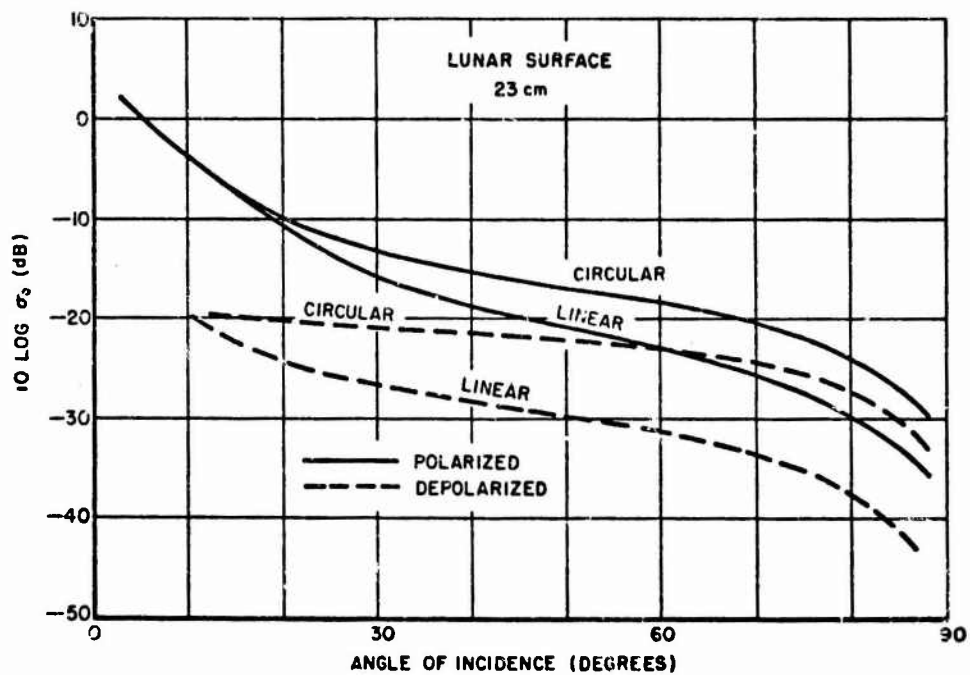


Fig. 98. Polarization dependence of the radar backscattering cross section for the Moon at 23 cm - Reference 22.

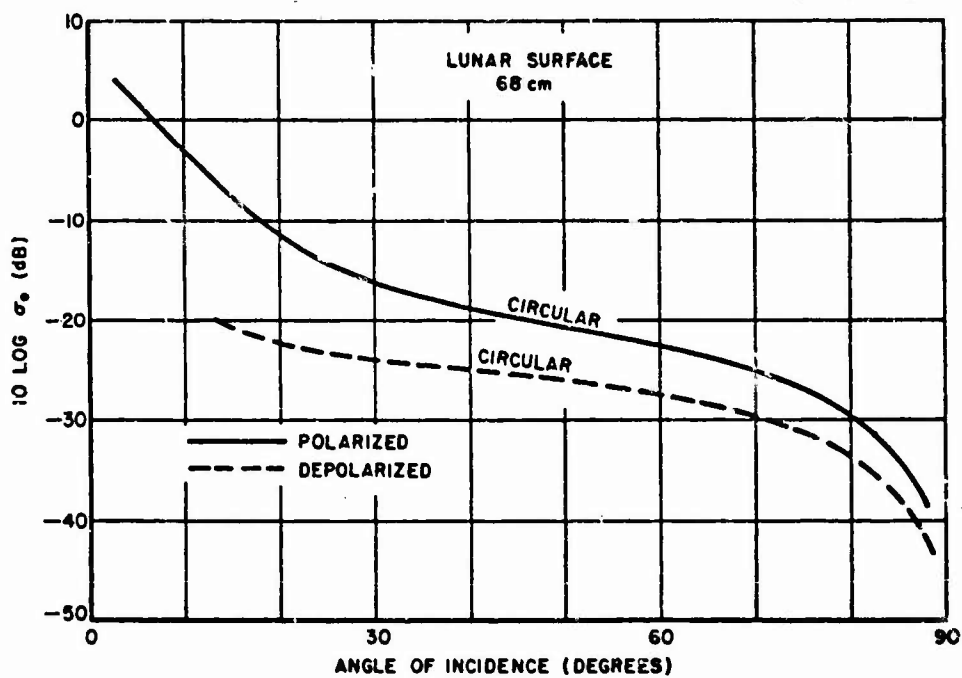


Fig. 99. Polarization dependence of the radar backscattering cross section for the Moon at 68 cm - Reference 22.

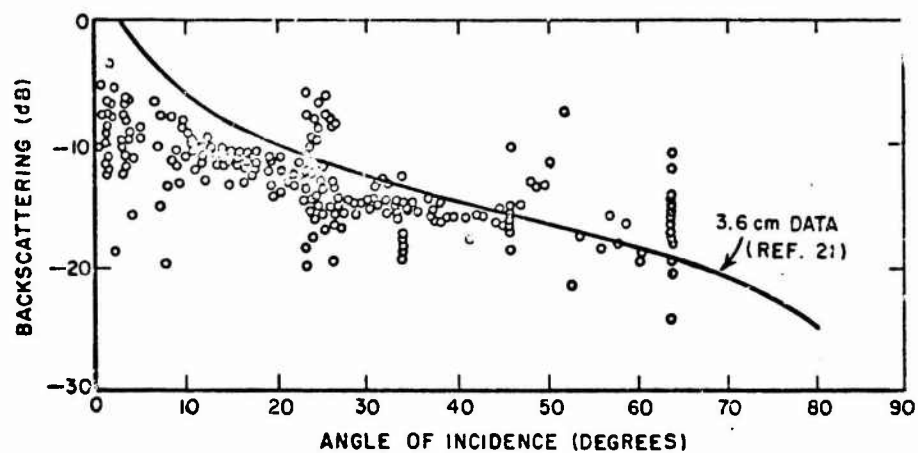


Fig. 100. Radar cross section of the lunar surface vs. angle of incidence for Surveyor V (13.3 GHz).

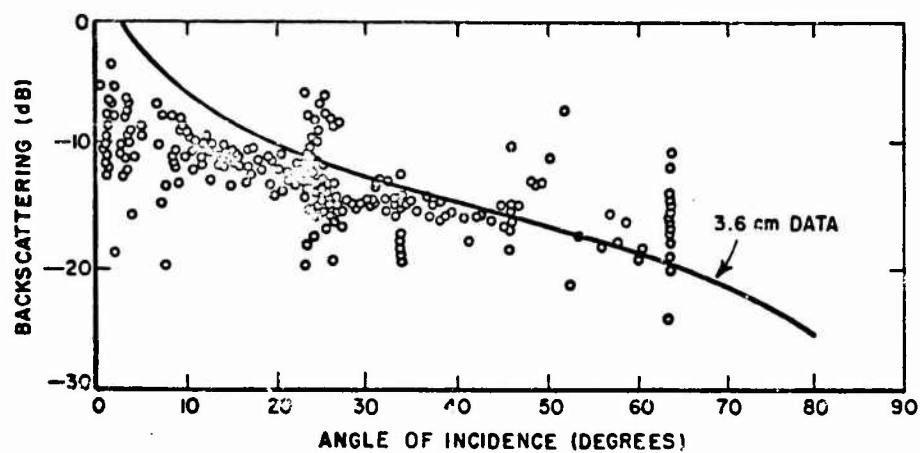


Fig. 101. Radar cross section of the lunar surface vs. angle of incidence for Surveyor VI (13.3 GHz).

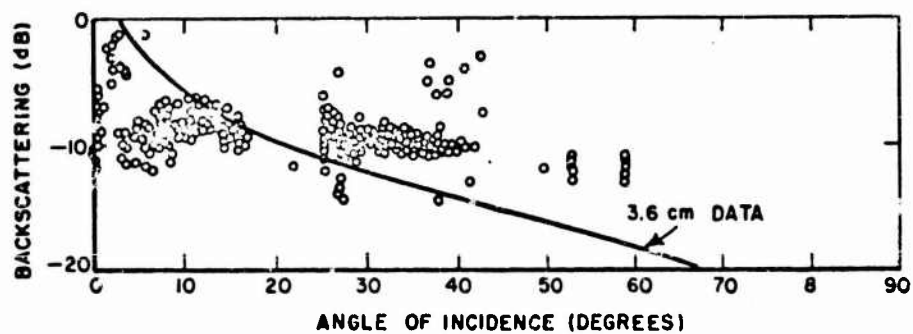


Fig. 102. Radar cross section for the lunar surface vs. angle of incidence for Surveyor VII (13.3 GHz). (Data from Ref. 23)

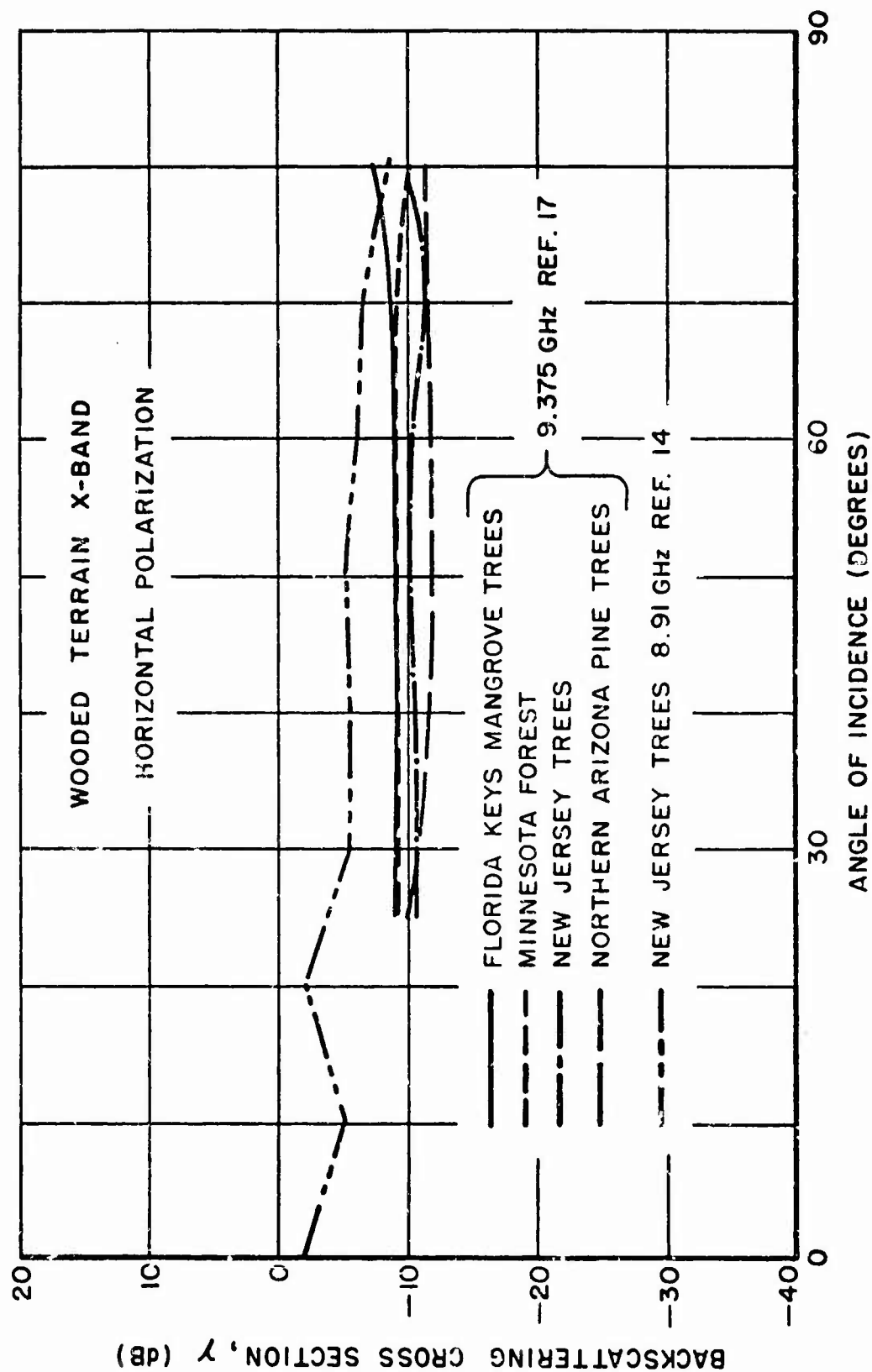


Fig. 103. Radar backscattering cross section for wooded terrain at X-band.

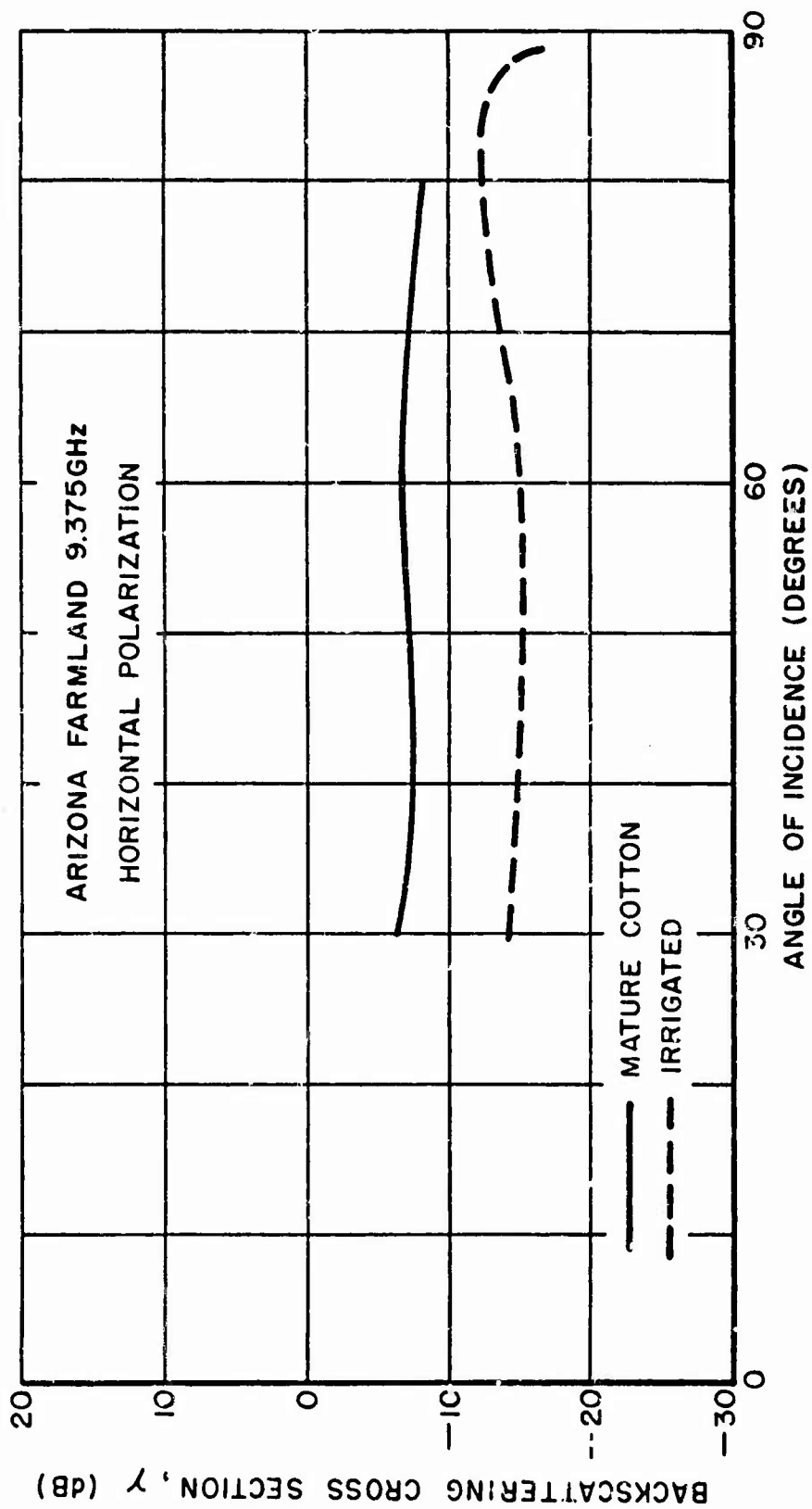


Fig. 104. Radar backscattering cross section for Arizona farmland at X-band - Reference 16.

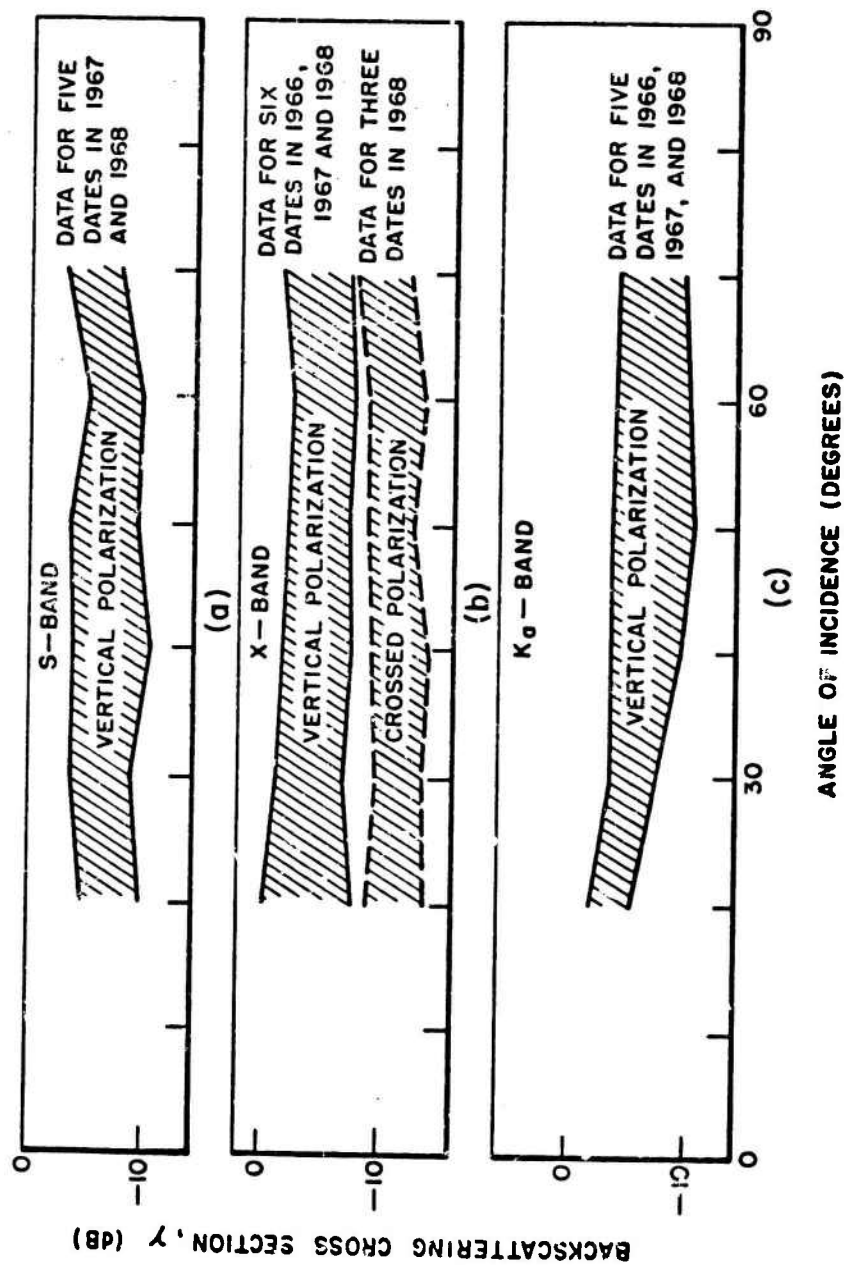


Fig. 105. Radar backscattering cross section for 24"-36" green soybeans at S-, X-, and K α -bands. Shaded Area is envelope of measured curves.

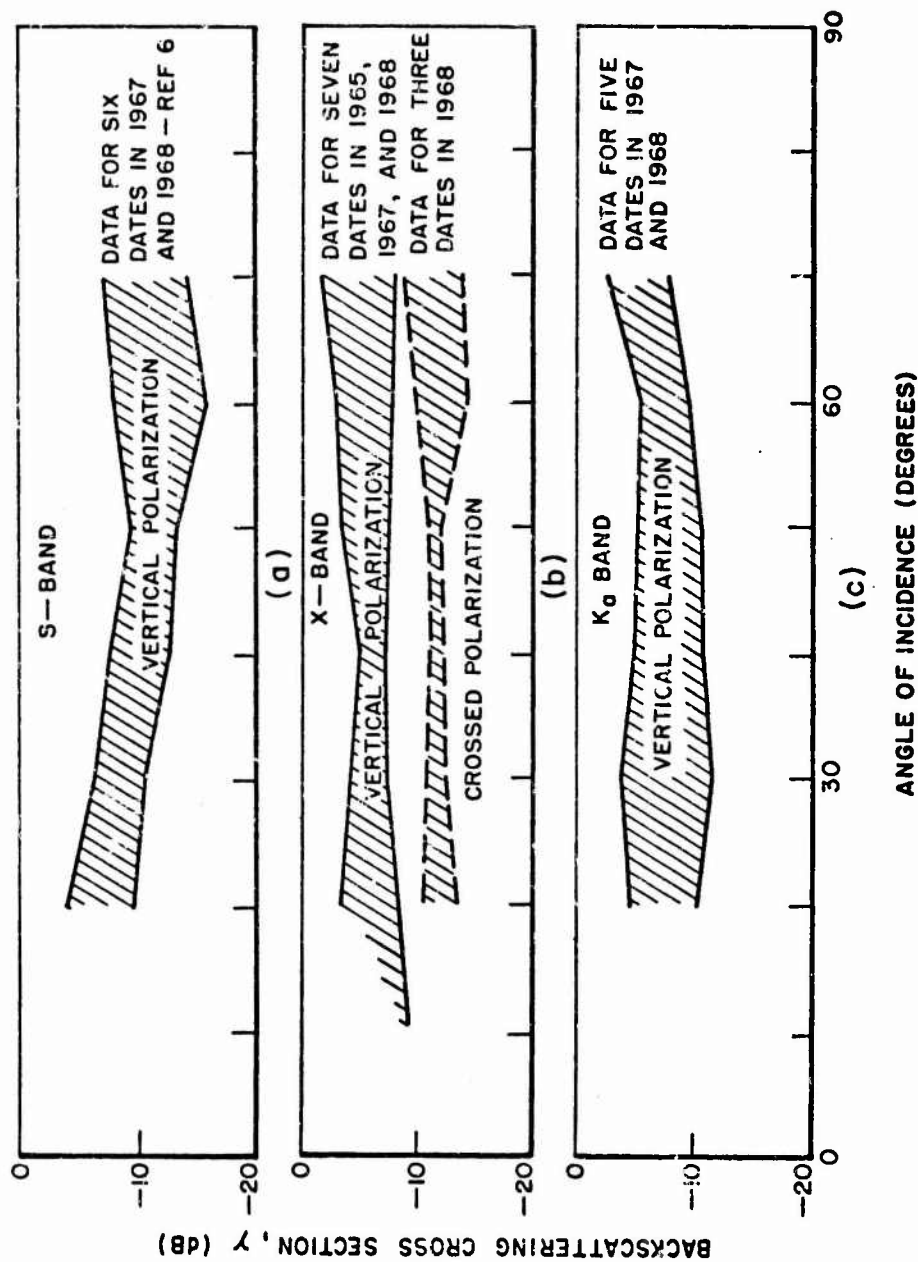


Fig. 106. Radar backscattering cross section for 10"-36" oats at S-, X-, and K_u-bands. Shaded area is envelope of measured curves.

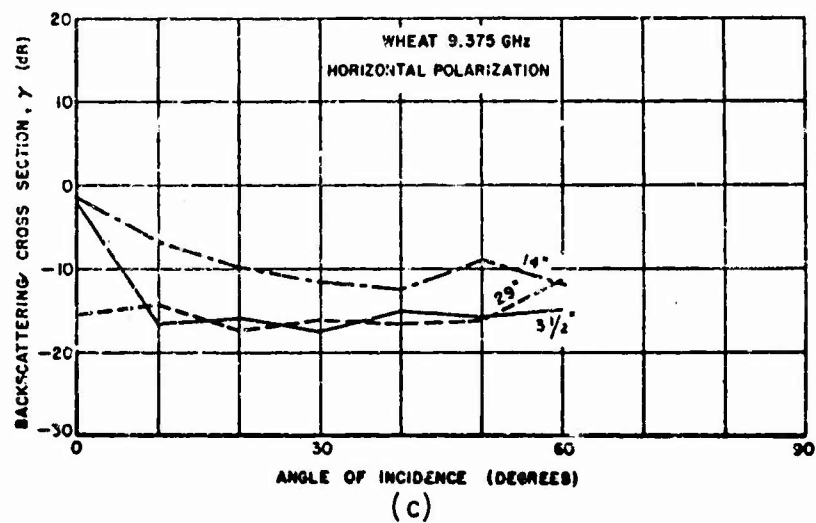
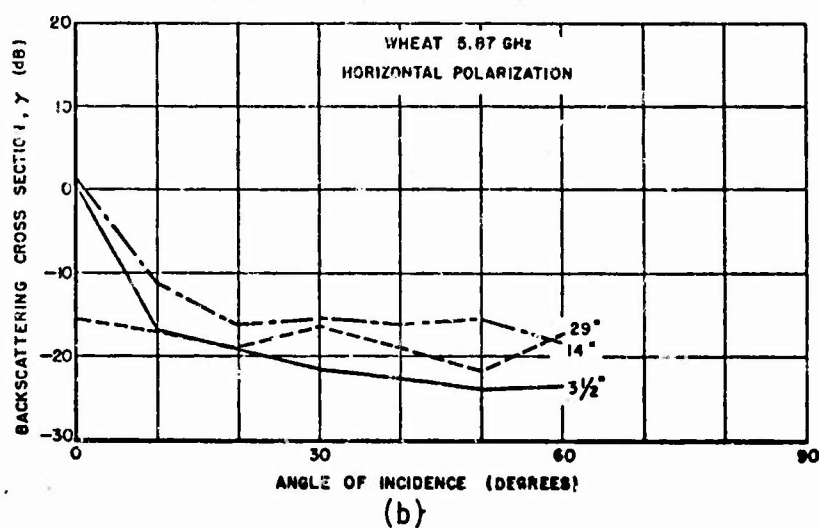
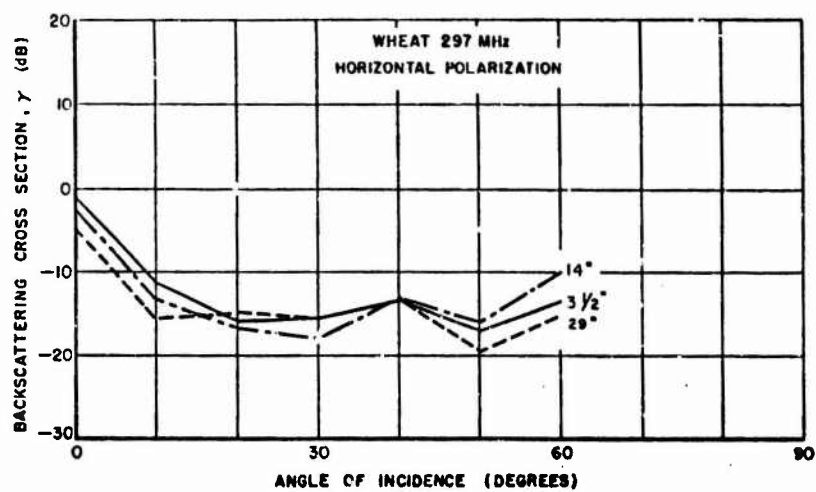


Fig. 107. Radar backscattering cross section for wheat at 297 MHz, 5.87 GHz, and 9.375 GHz - Reference 25.

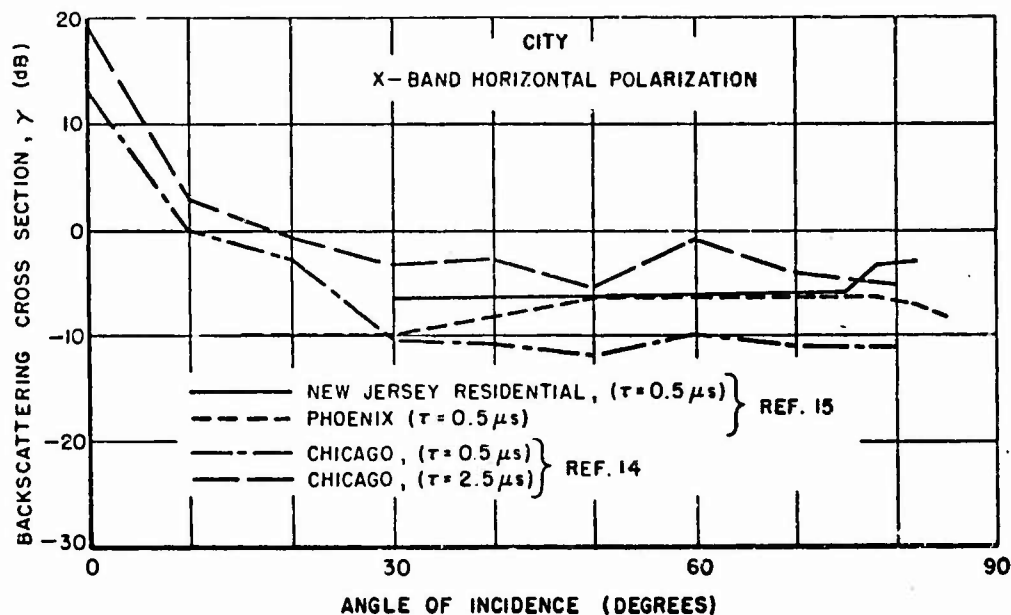


Fig. 108. Radar backscattering cross section for cities at 220 MHz and 428 MHz.

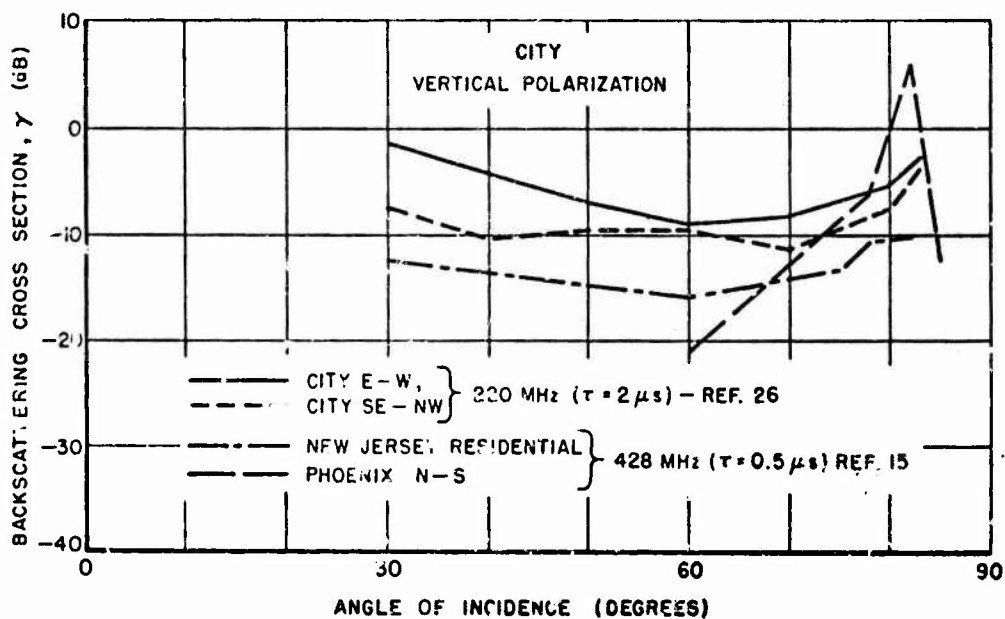


Fig. 109. Radar backscattering cross section for cities at X-band.

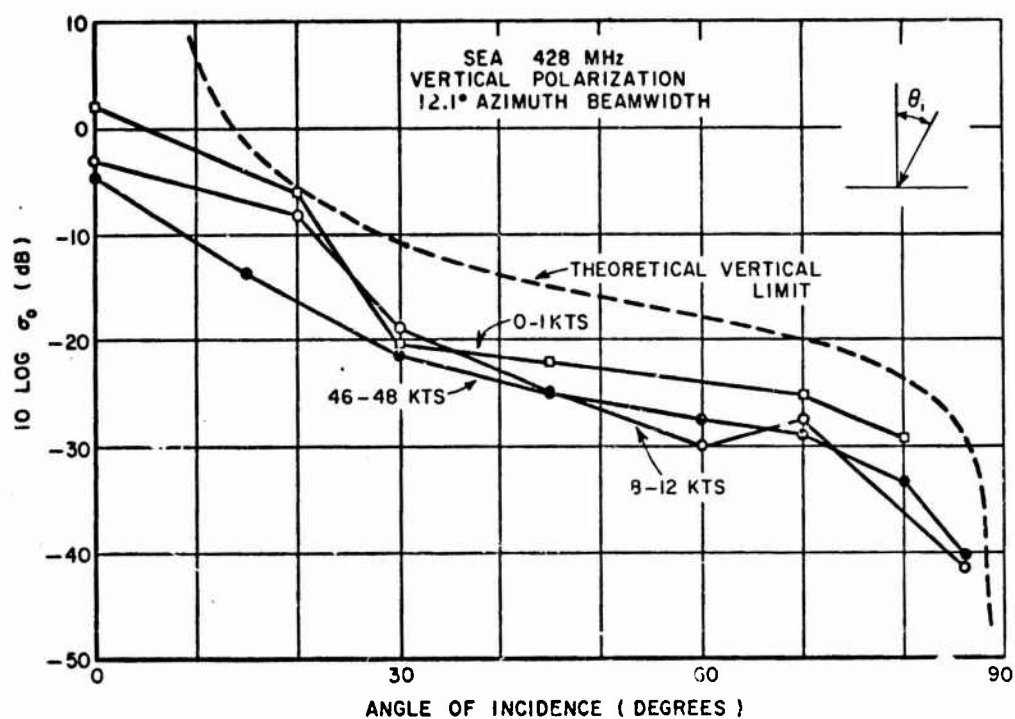


Fig. 110. Radar backscattering cross section for the sea at 428 MHz, vertical polarization - Reference 27.

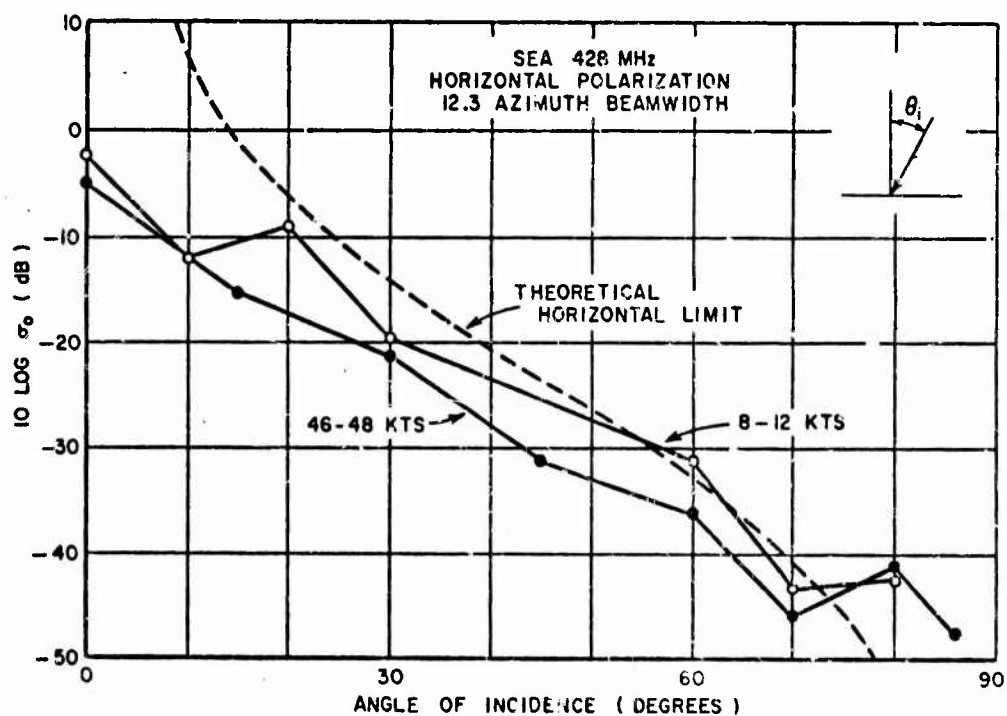


Fig. 111. Radar backscattering cross section for the sea at 428 MHz, horizontal polarization - Reference 27.

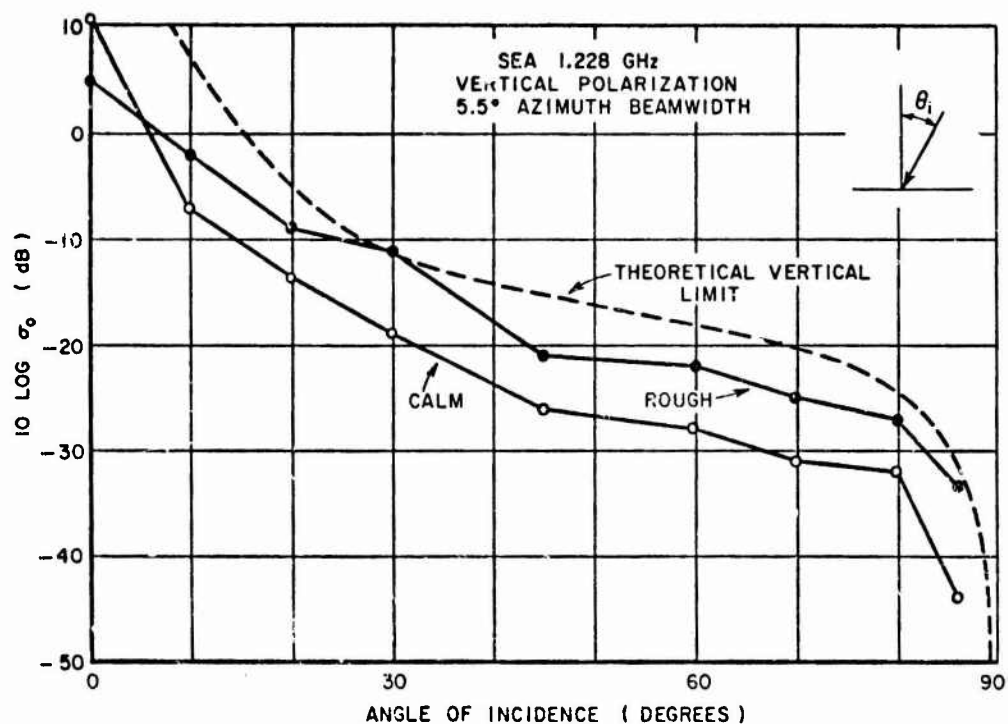


Fig. 112. Radar backscattering cross section for the sea at 1.228 GHz, vertical polarization - Reference 27.

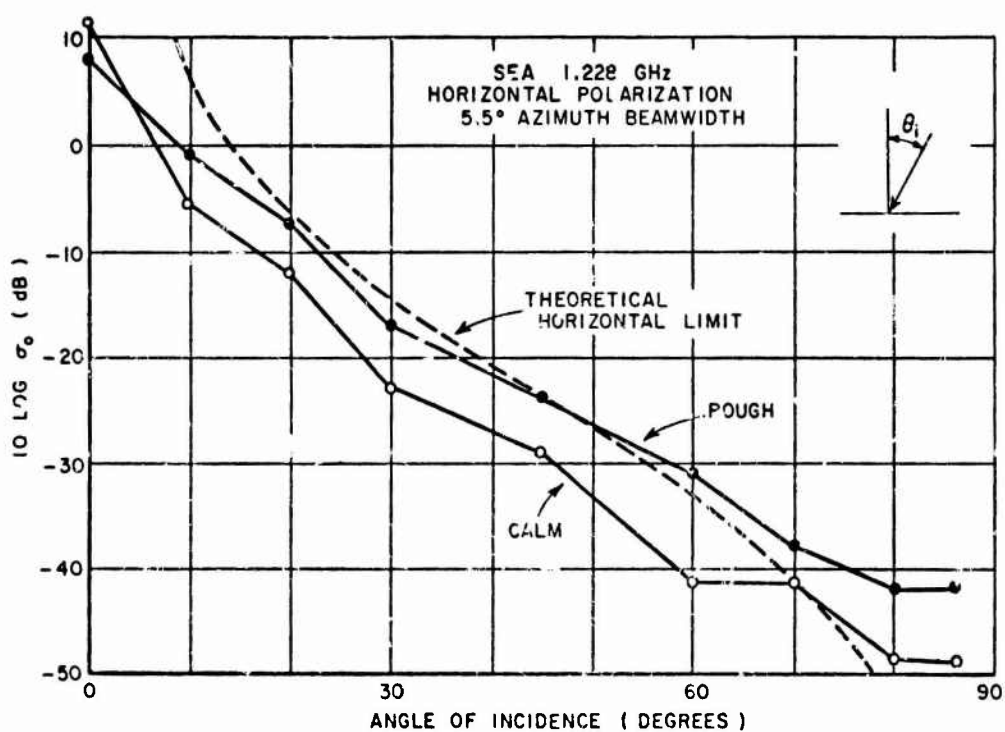


Fig. 113. Radar backscattering cross section for the sea at 1.228 GHz, horizontal polarization - Reference 27.

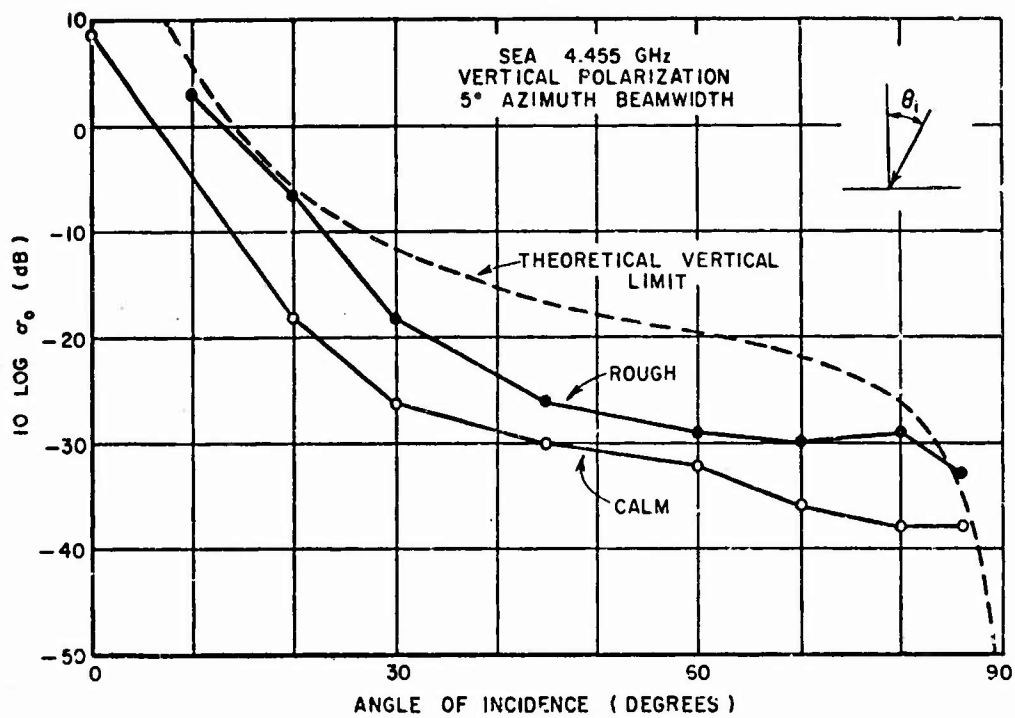


Fig. 114. Radar backscattering cross section for the sea at 4.455 GHz, vertical polarization - Reference 27.

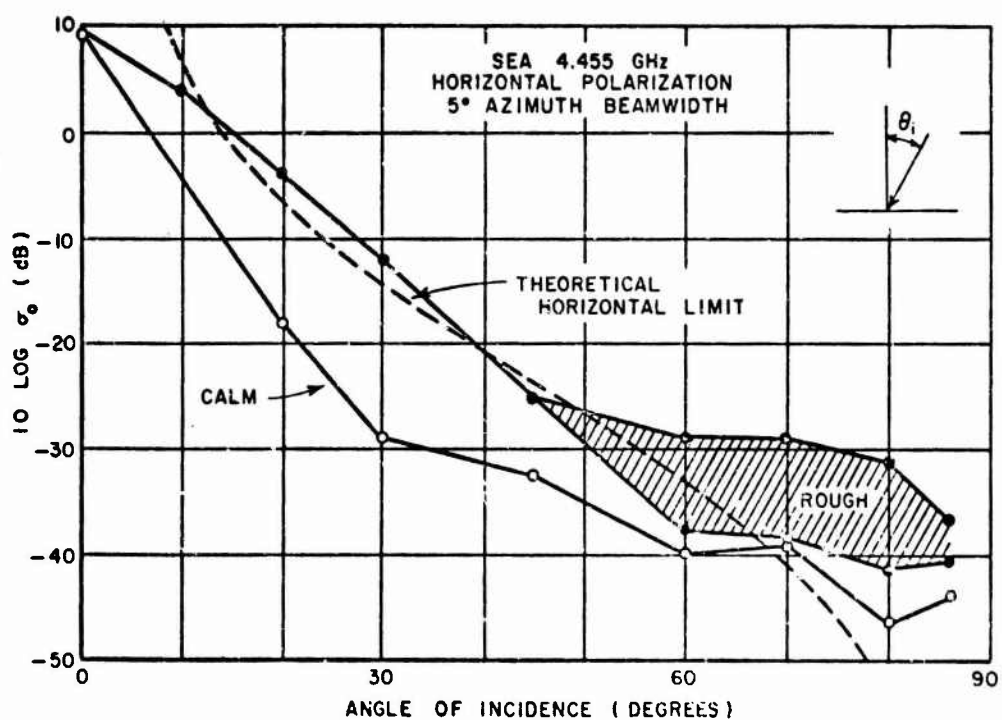


Fig. 115. Radar backscattering cross section for the sea at 4.455 GHz, horizontal polarization - Reference 27.

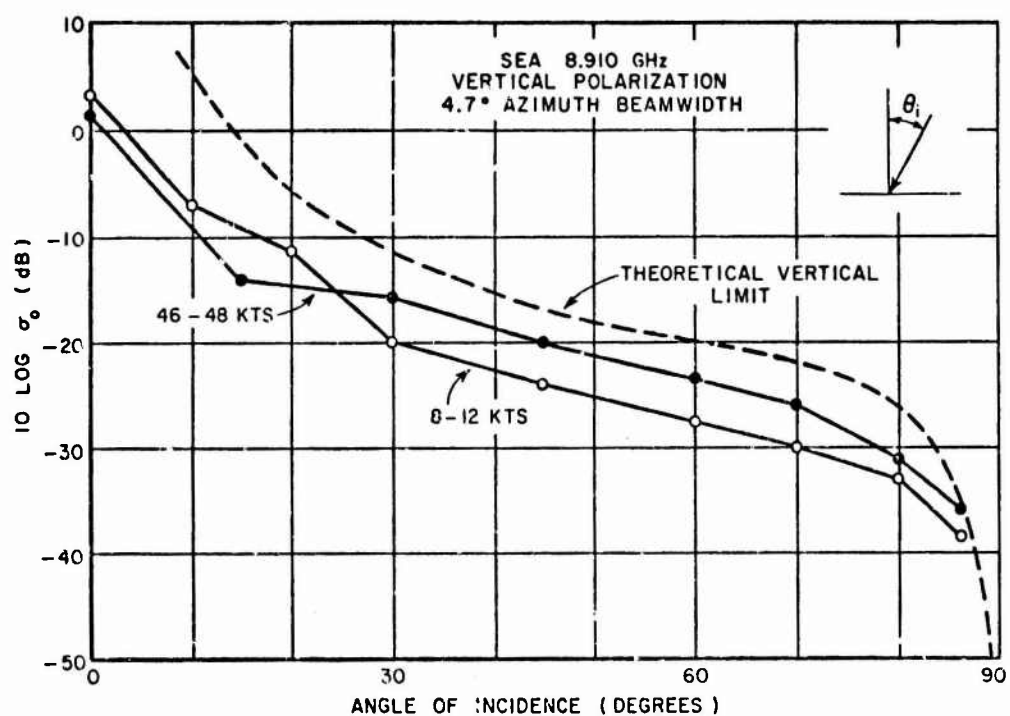


Fig. 116. Radar backscattering cross section for the sea at 8.91 GHz, vertical polarization - Reference 27.

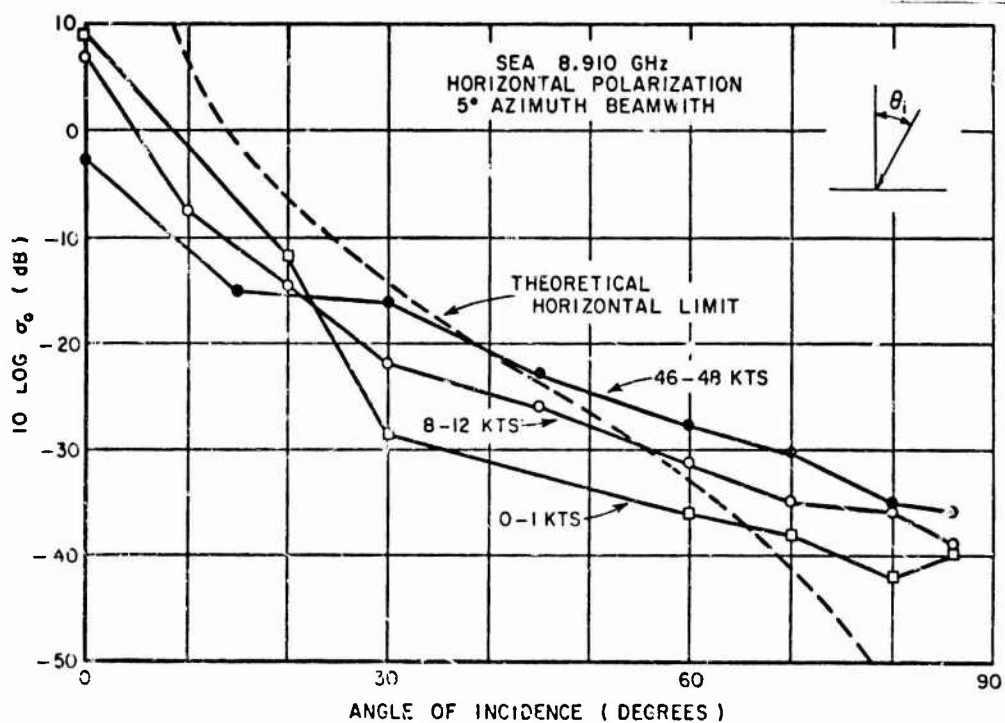


Fig. 117. Radar backscattering cross section for the sea at 8.91 GHz, horizontal polarization - Reference 27.

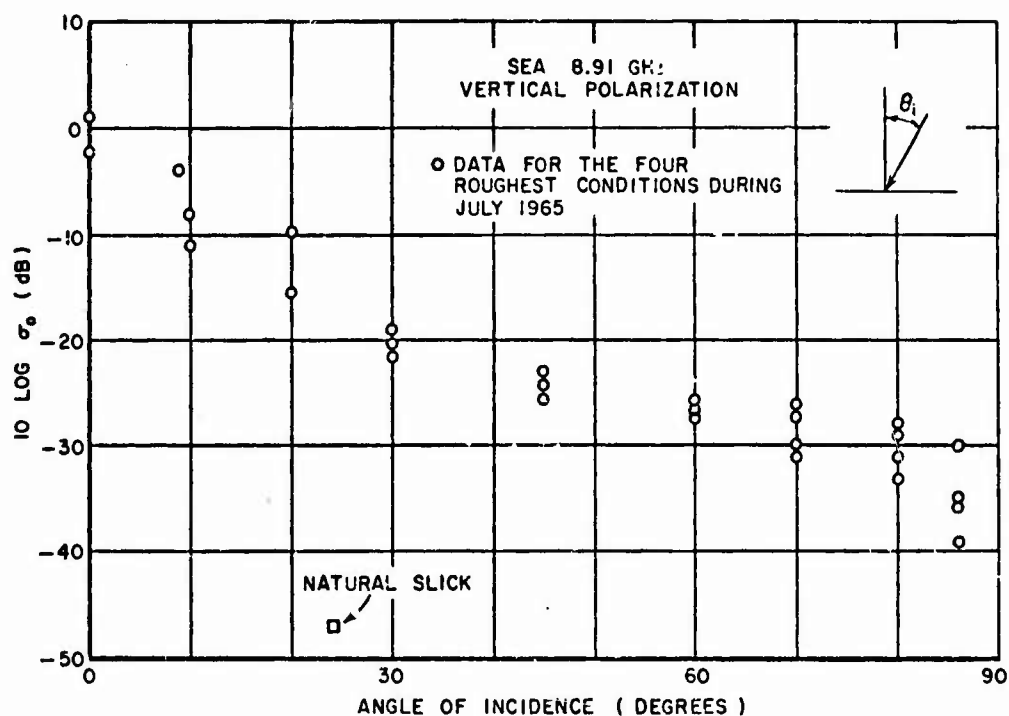


Fig. 118. Radar backscattering cross section for the sea with slicks at 8.91 GHz, vertical polarization - Reference 27.

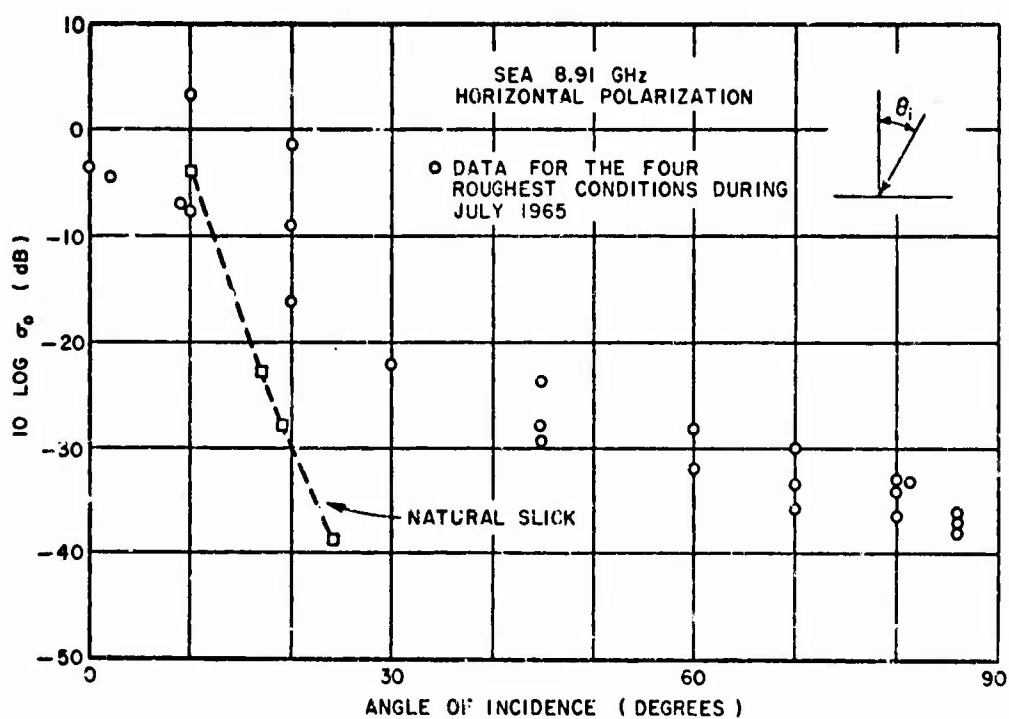


Fig. 119. Radar backscattering cross section for the sea with slicks at 8.91 GHz, horizontal polarization - Reference 27.

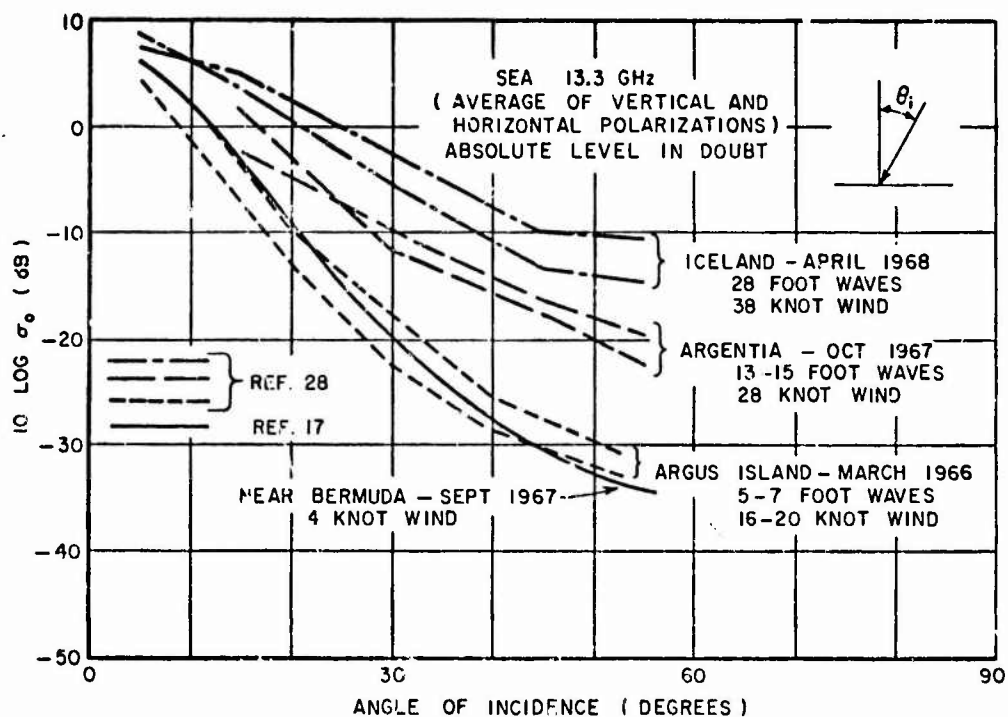


Fig. 120. Radar backscattering cross section for the sea at 13.3 GHz.

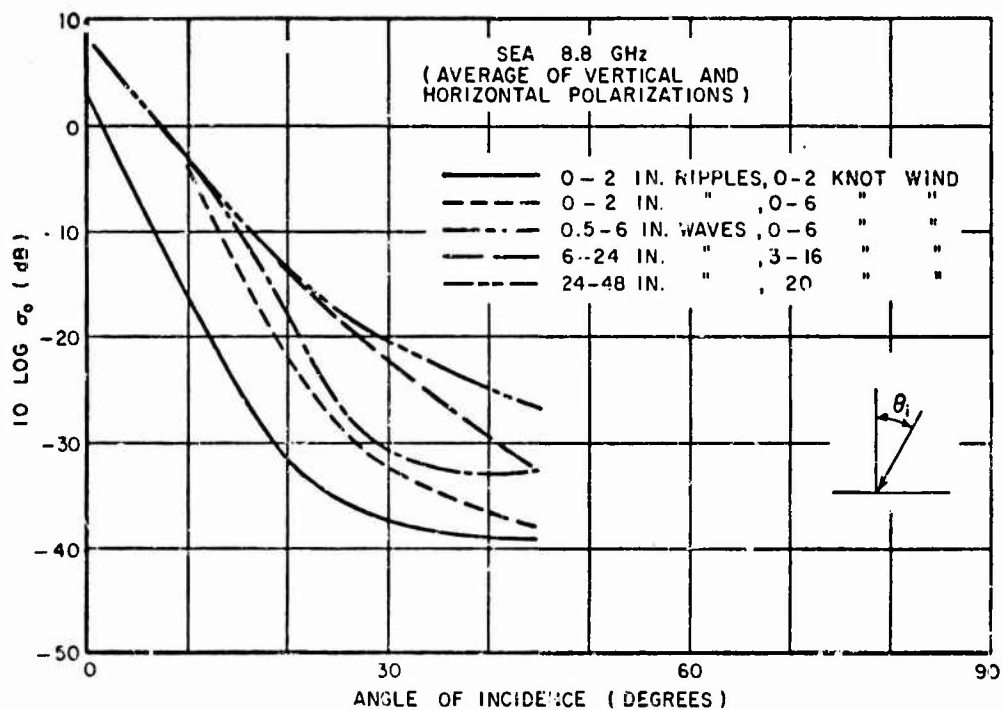


Fig. 121. Radar backscattering cross section for the sea at 8.8 GHz, (average of vertical and horizontal polarization) - Reference 29.

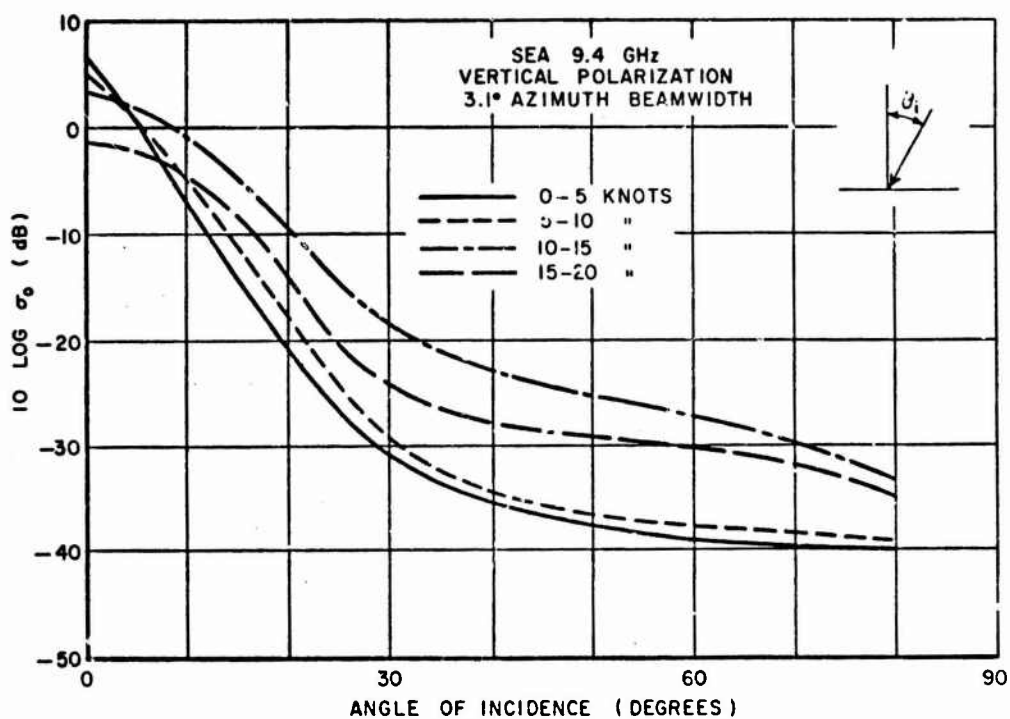


Fig. 122. Radar backscattering cross section for the sea at 9.4 GHz, vertical polarization - Reference 24.

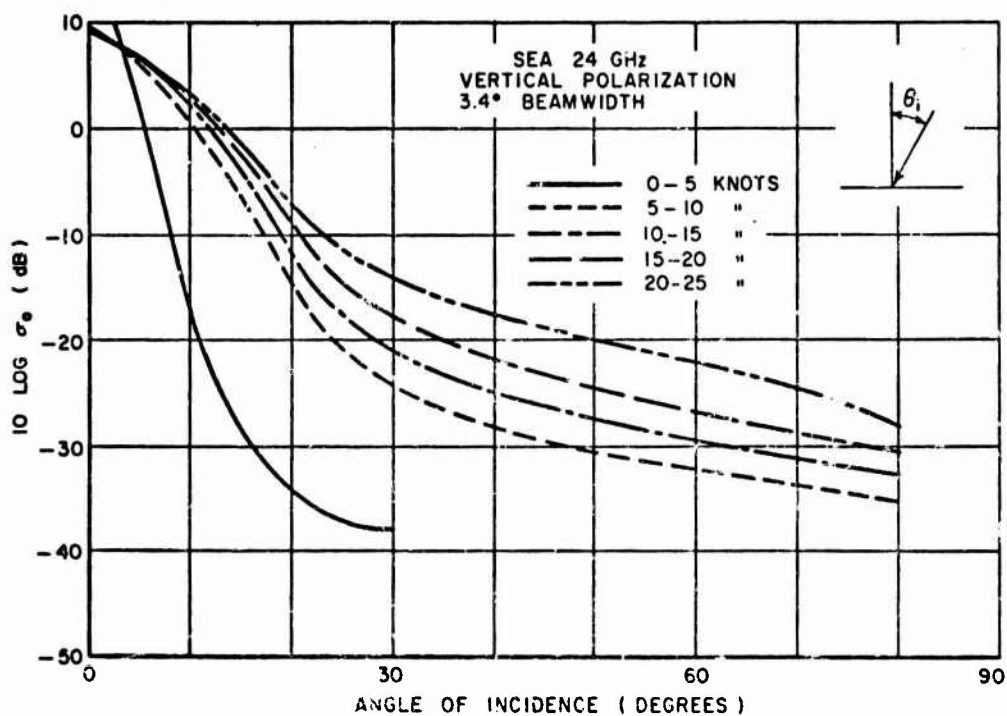


Fig. 123. Radar backscattering cross section for the sea at 24 GHz, vertical polarization - Reference 24.

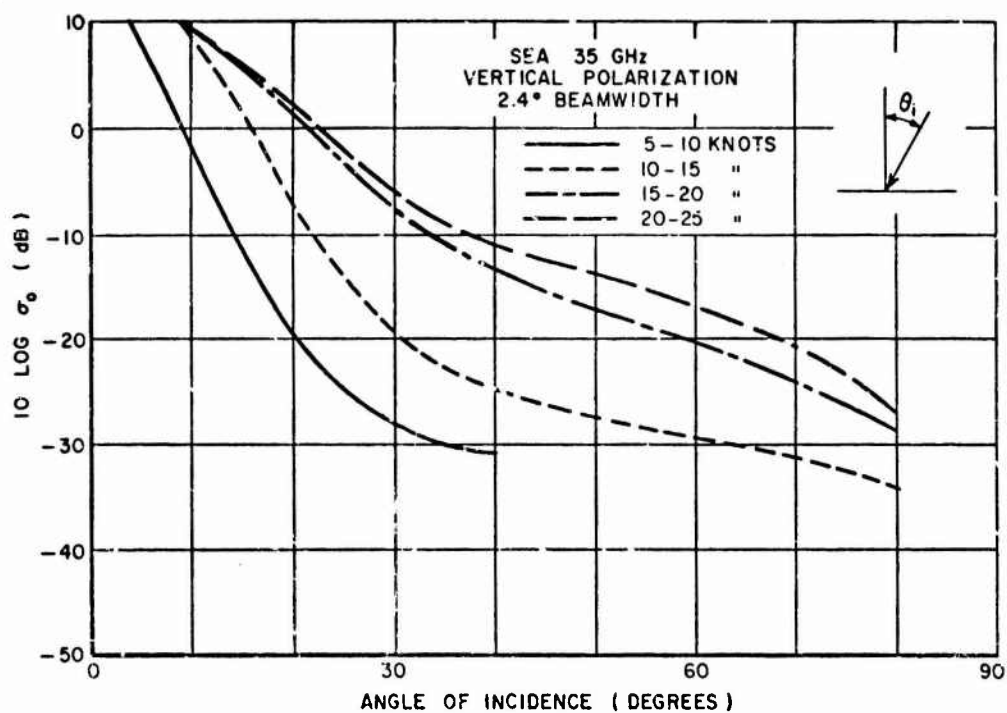


Fig. 124. Radar backscattering cross section for the sea at 35 GHz, vertical polarization - Reference 24.

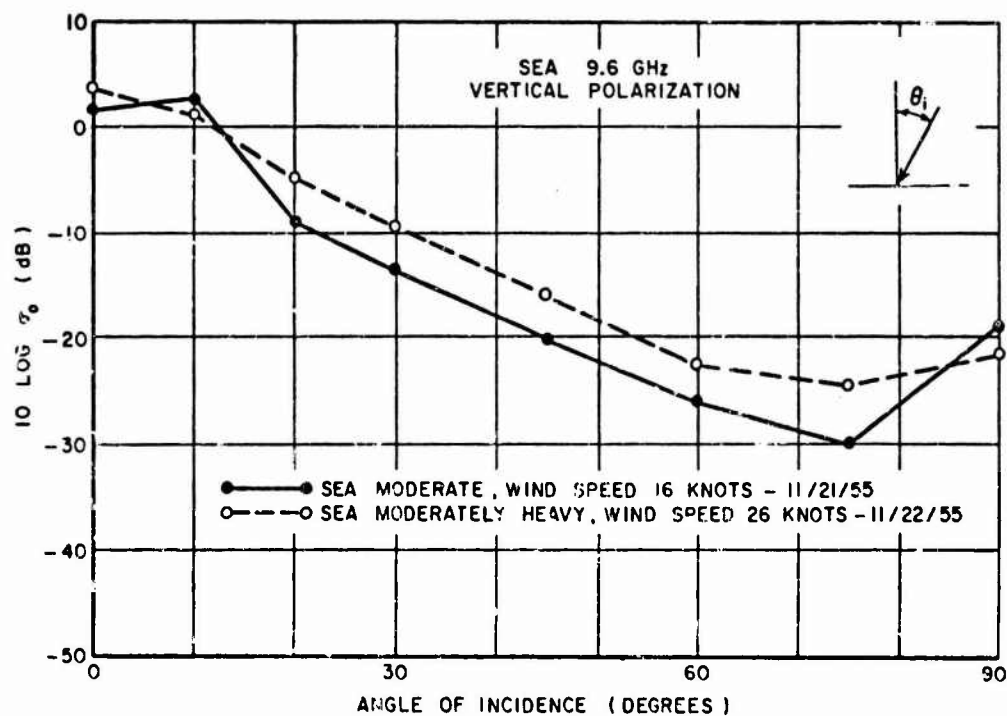


Fig. 125. Radar backscattering cross section for the sea at 9.6 GHz, vertical polarization - Reference 30.

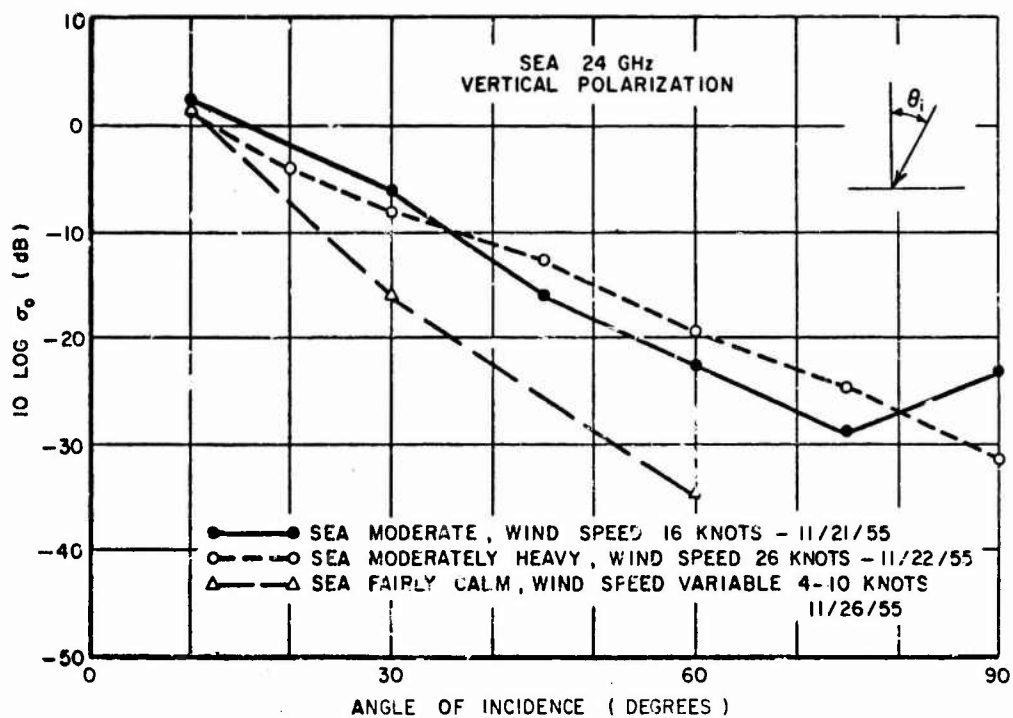


Fig. 126. Radar backscattering cross section for the sea at 24 GHz, vertical polarization - Reference 30.

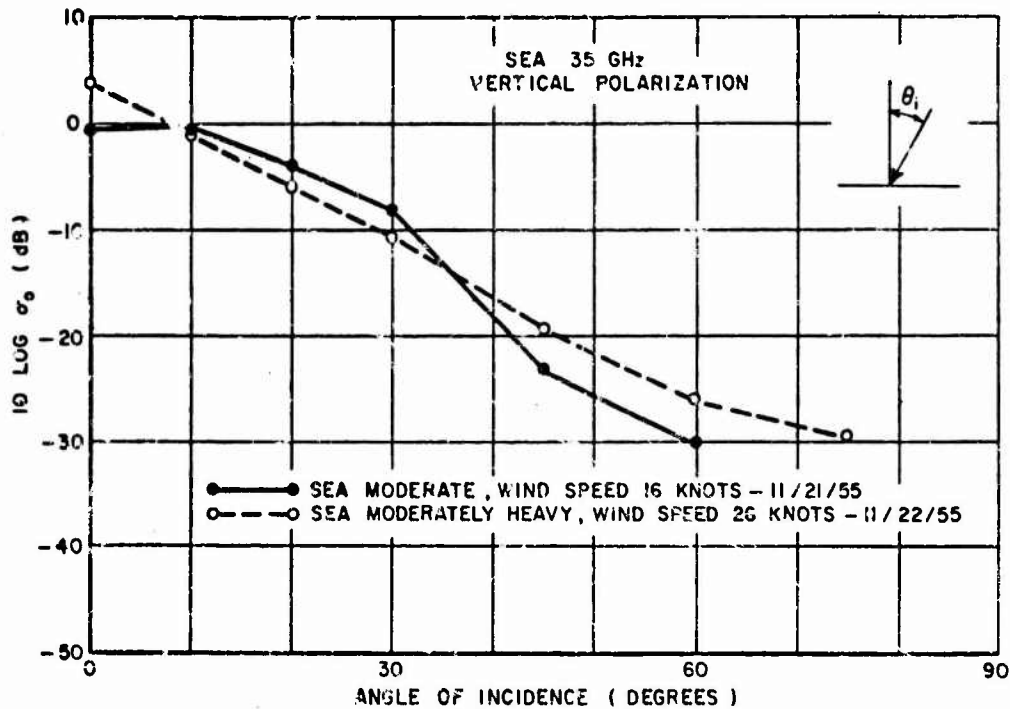


Fig. 127. Radar backscattering cross section for the sea at 35 GHz, vertical polarization - Reference 30.

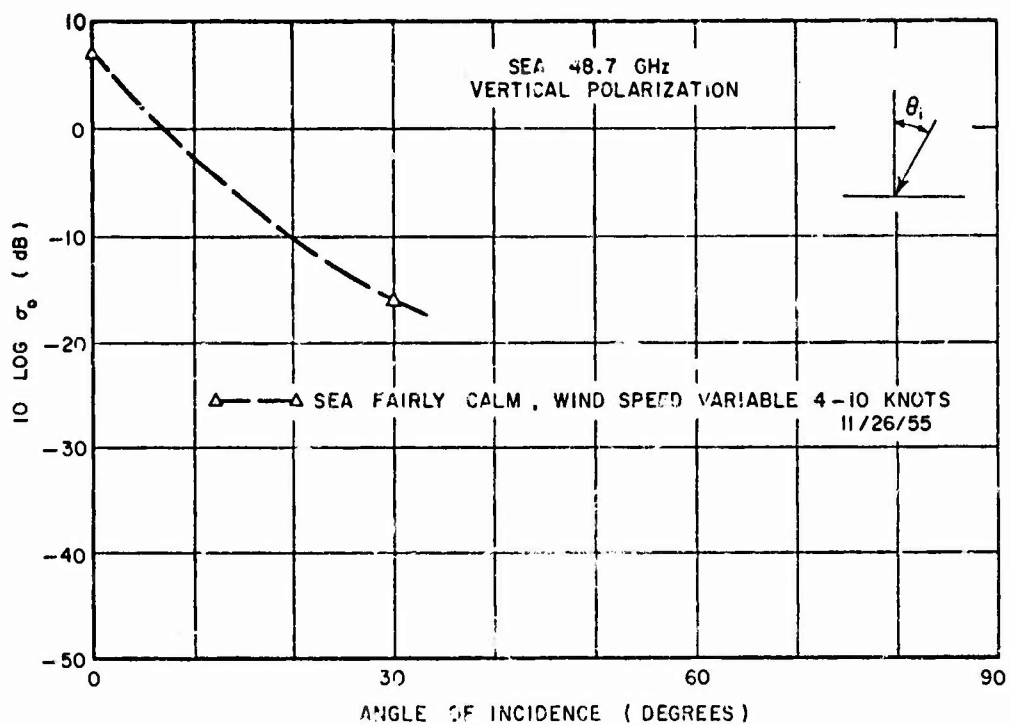


Fig. 128. Radar backscattering cross section for the sea at 48.7 GHz, vertical polarization - Reference 30.

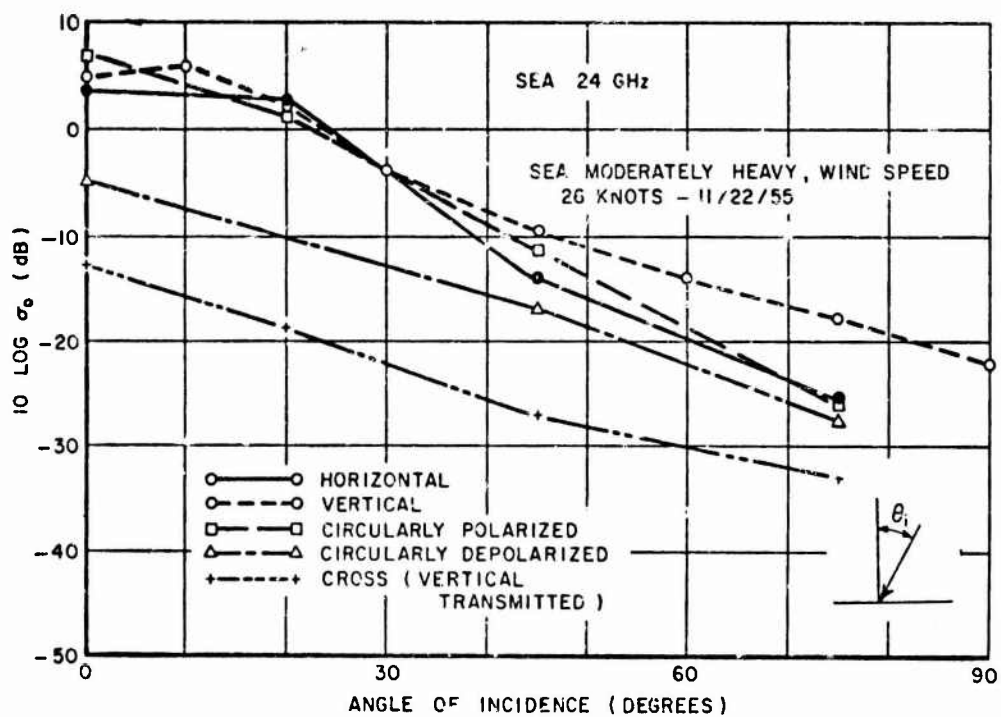


Fig. 129. Effects of polarization on the radar backscattering for the sea at 24 GHz - Reference 30.

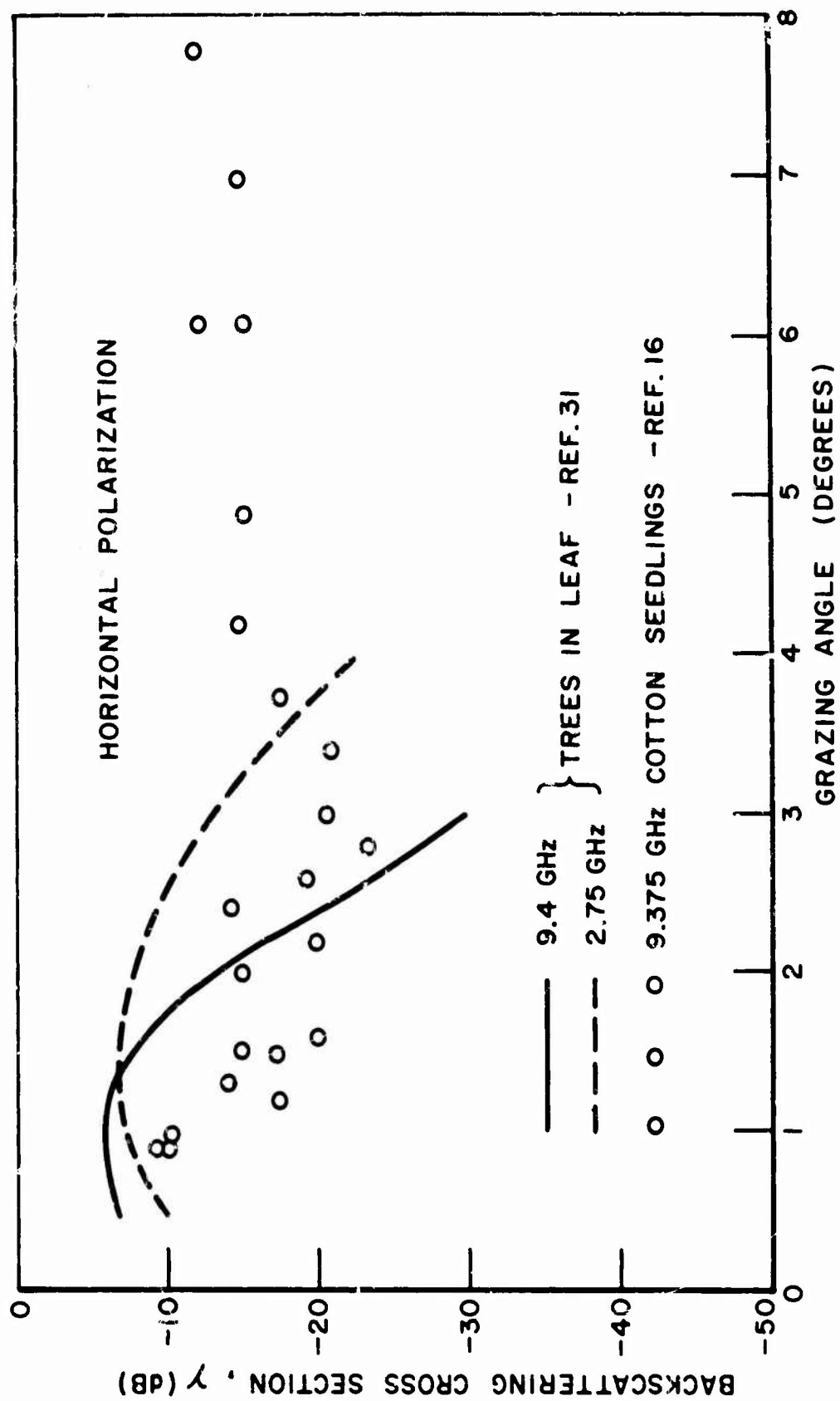


Fig. 130. Near-grazing radar backscatter for trees (X-band and S-band) and cotton seedlings (X-band).

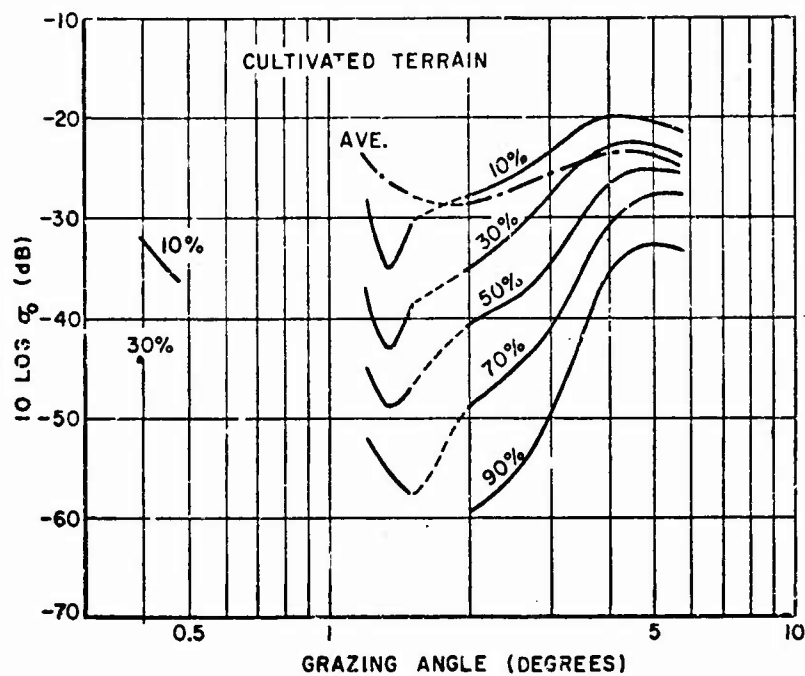


Fig. 131. Near-grazing radar backscatter for cultivated terrain at 10 GHz - Reference 32. Parameter is per cent of returns exceeding given ordinate.

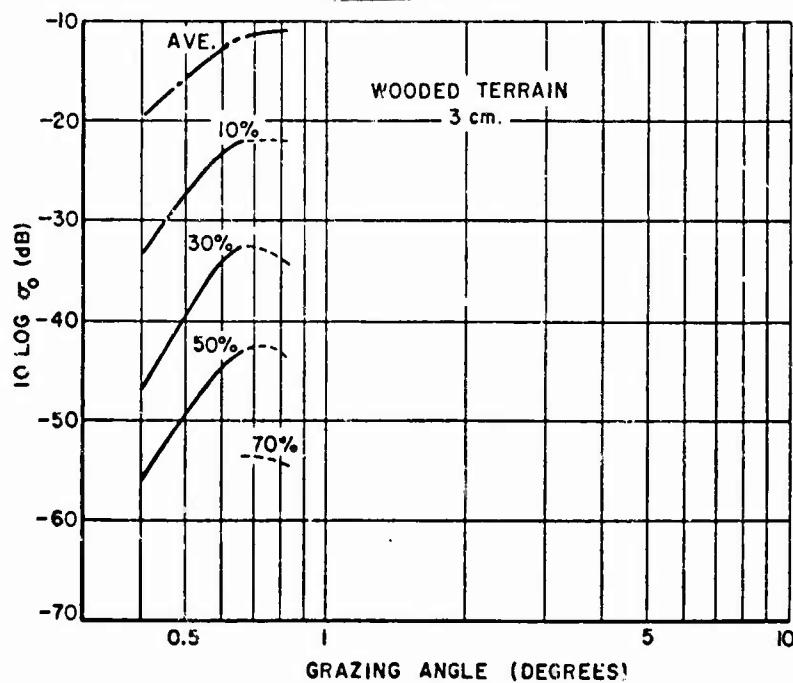


Fig. 132. Near-grazing radar backscatter for wooded terrain at 10 GHz - Reference 32. Parameter is per cent of returns exceeding given ordinate.

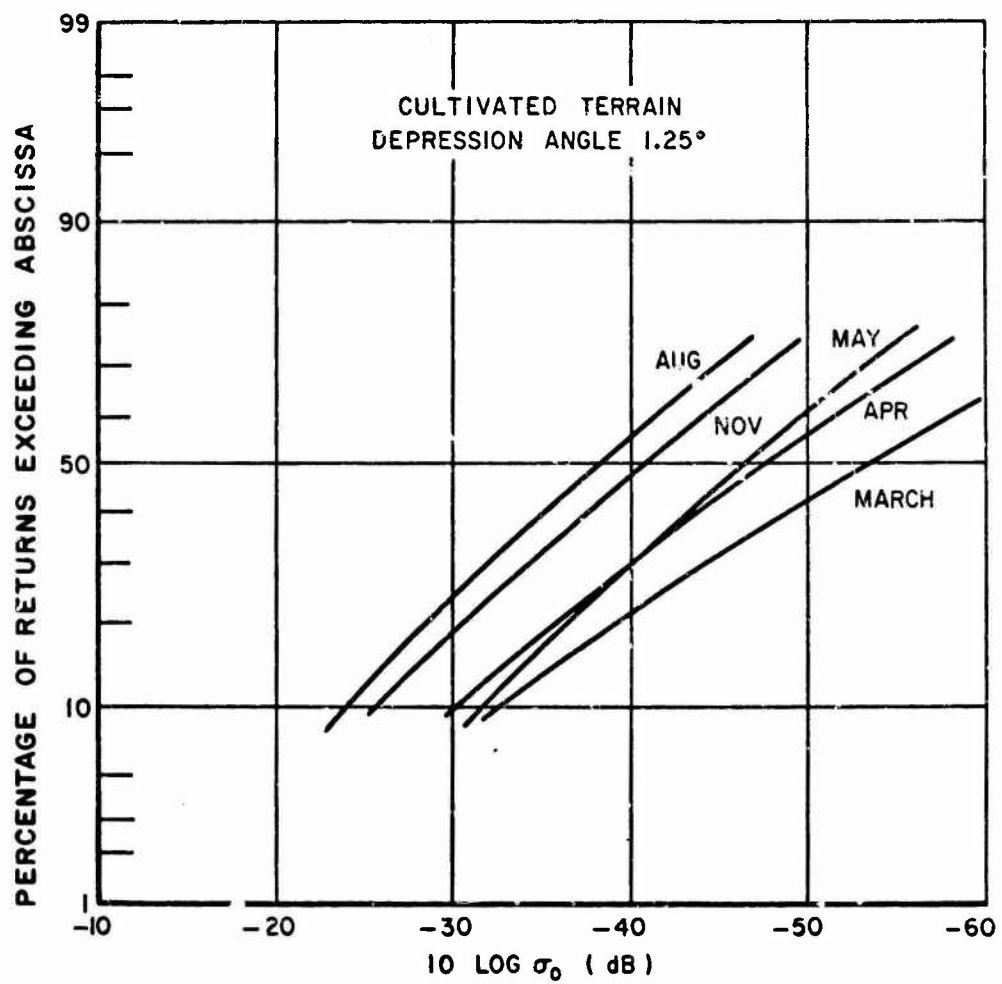


Fig. 133. Seasonal variation in the radar backscatter distribution for cultivated terrain, at 10 GHz, for a 1.25° depression angle - Reference 32.

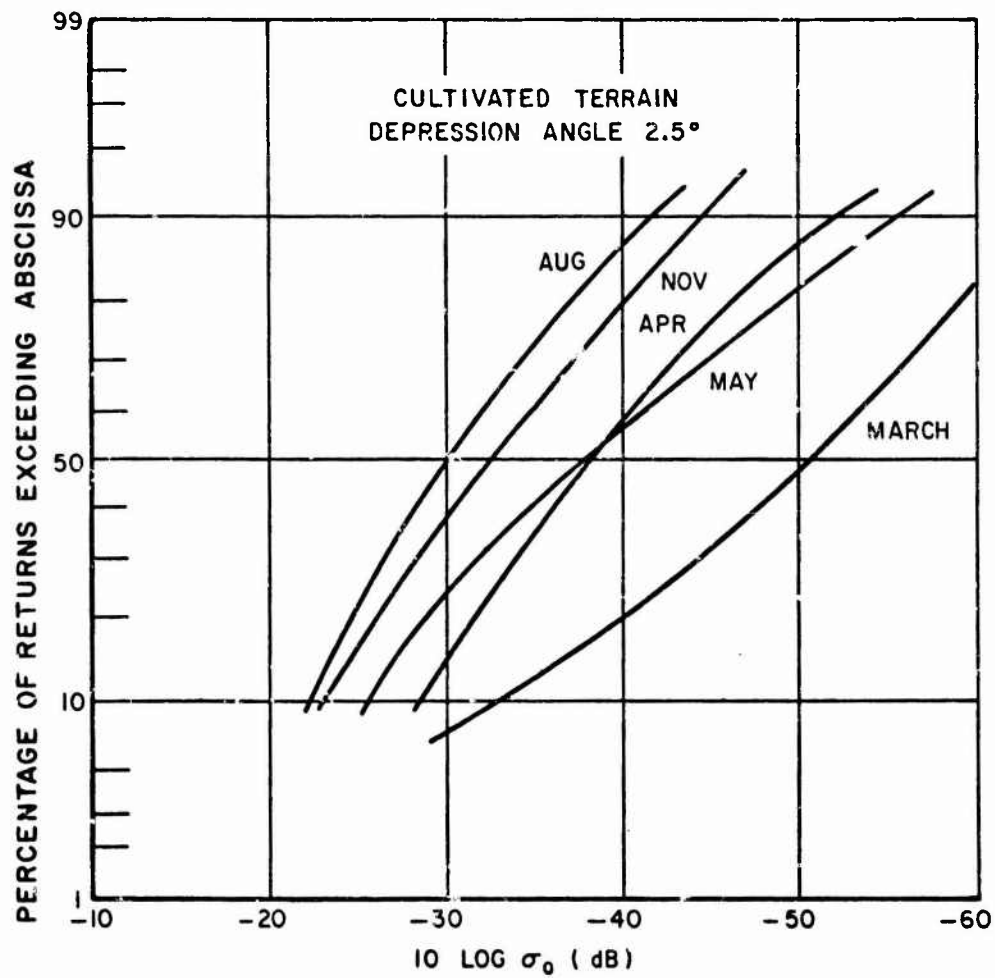


Fig. 134. Seasonal variation in the radar backscatter distribution for cultivated terrain, at 10 GHz, for a 2.5° depression angle - Reference 32.

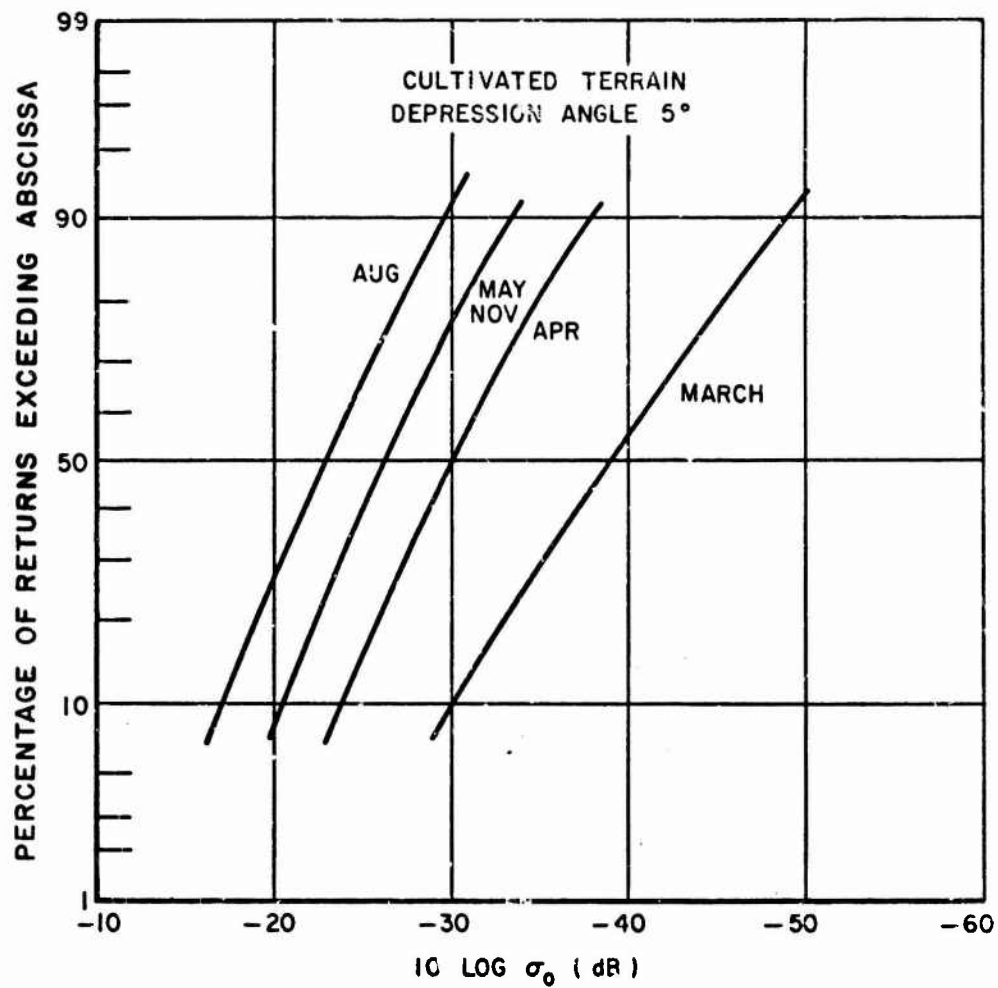


Fig. 135. Seasonal variation in the radar backscatter distribution for cultivated terrain, at 10 GHz, for a 5° depression angle - Reference 32.

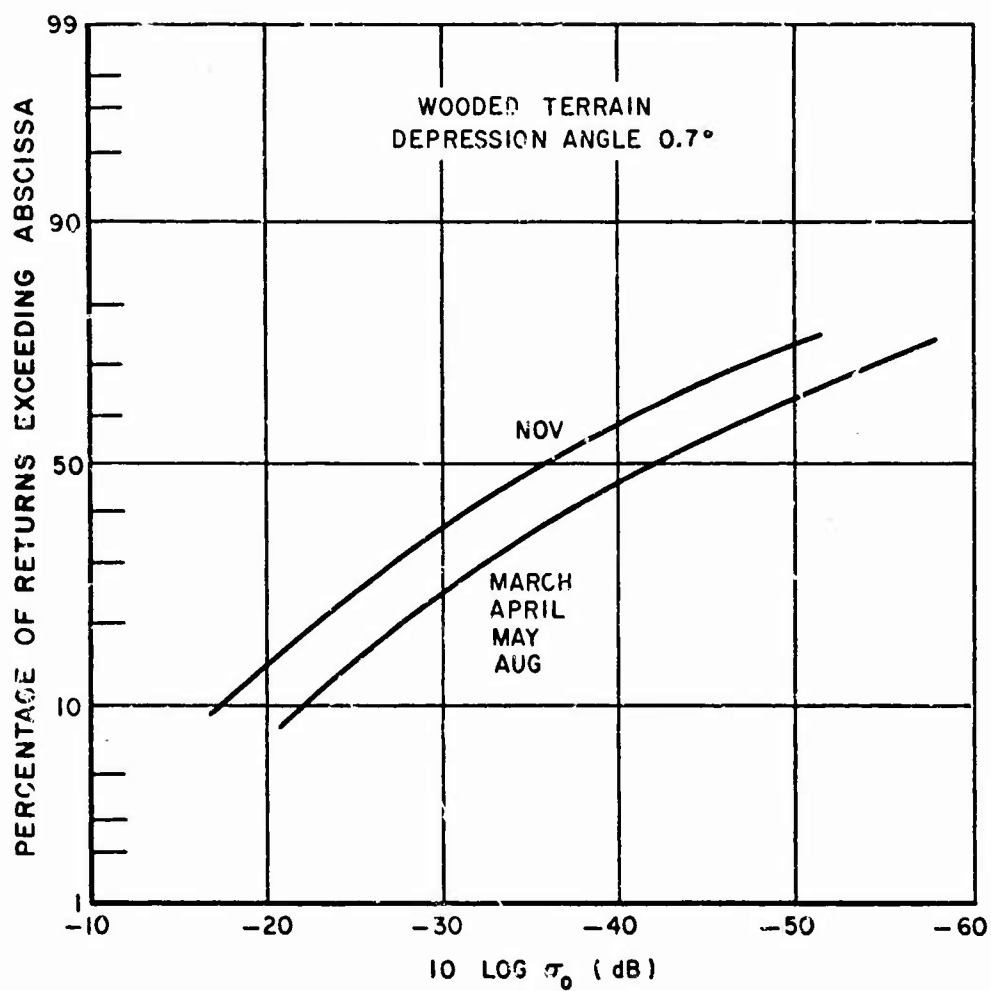


Fig. 136. Seasonal variation in the radar backscatter distribution for wooded terrain, at 10 GHz, for a 0.7° depression angle - Reference 32.

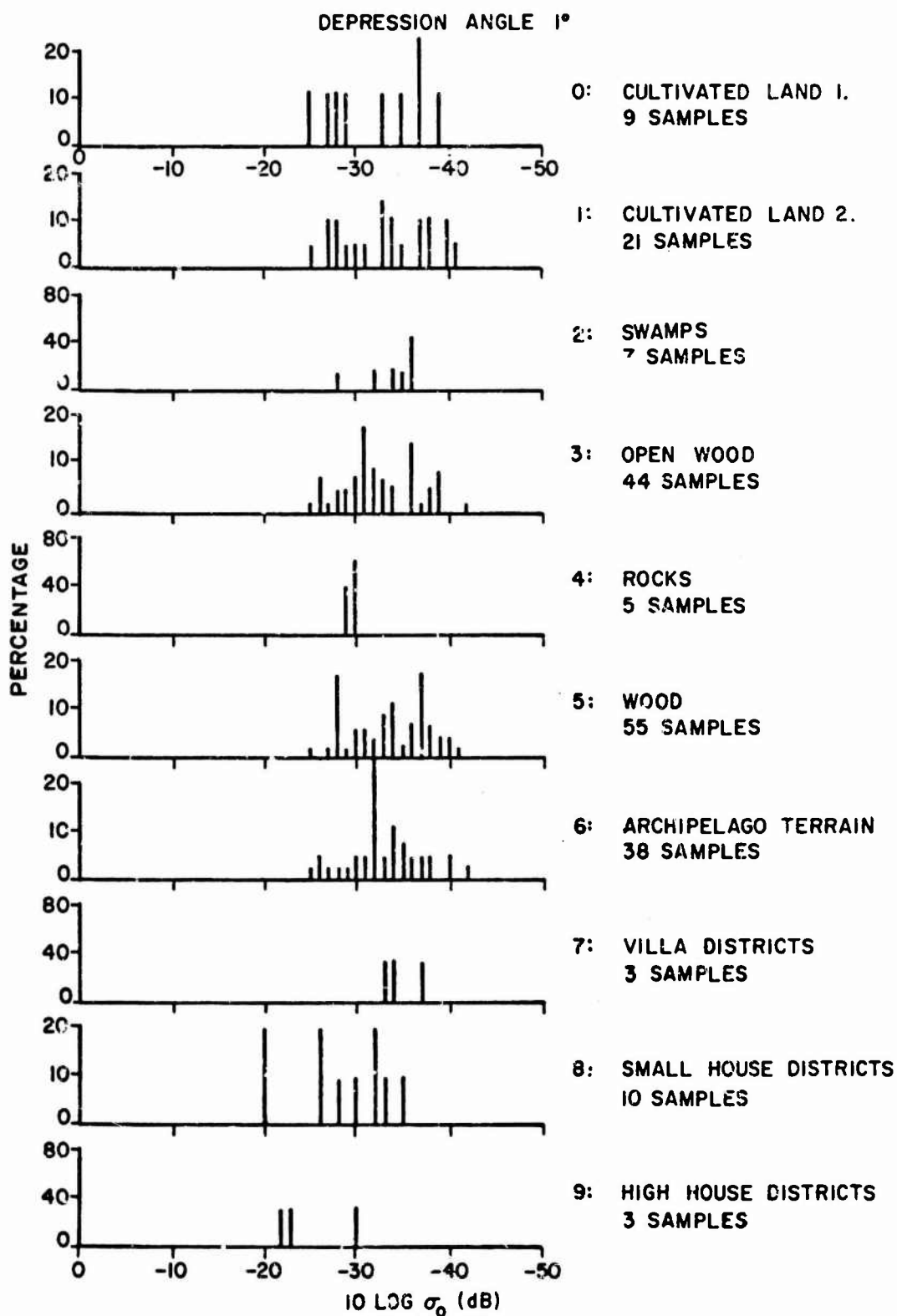


Fig. 137. Distribution of average values of σ_0 for different types of terrain, at X-band, horizontal polarization, for a 1° depression angle - Reference 33.

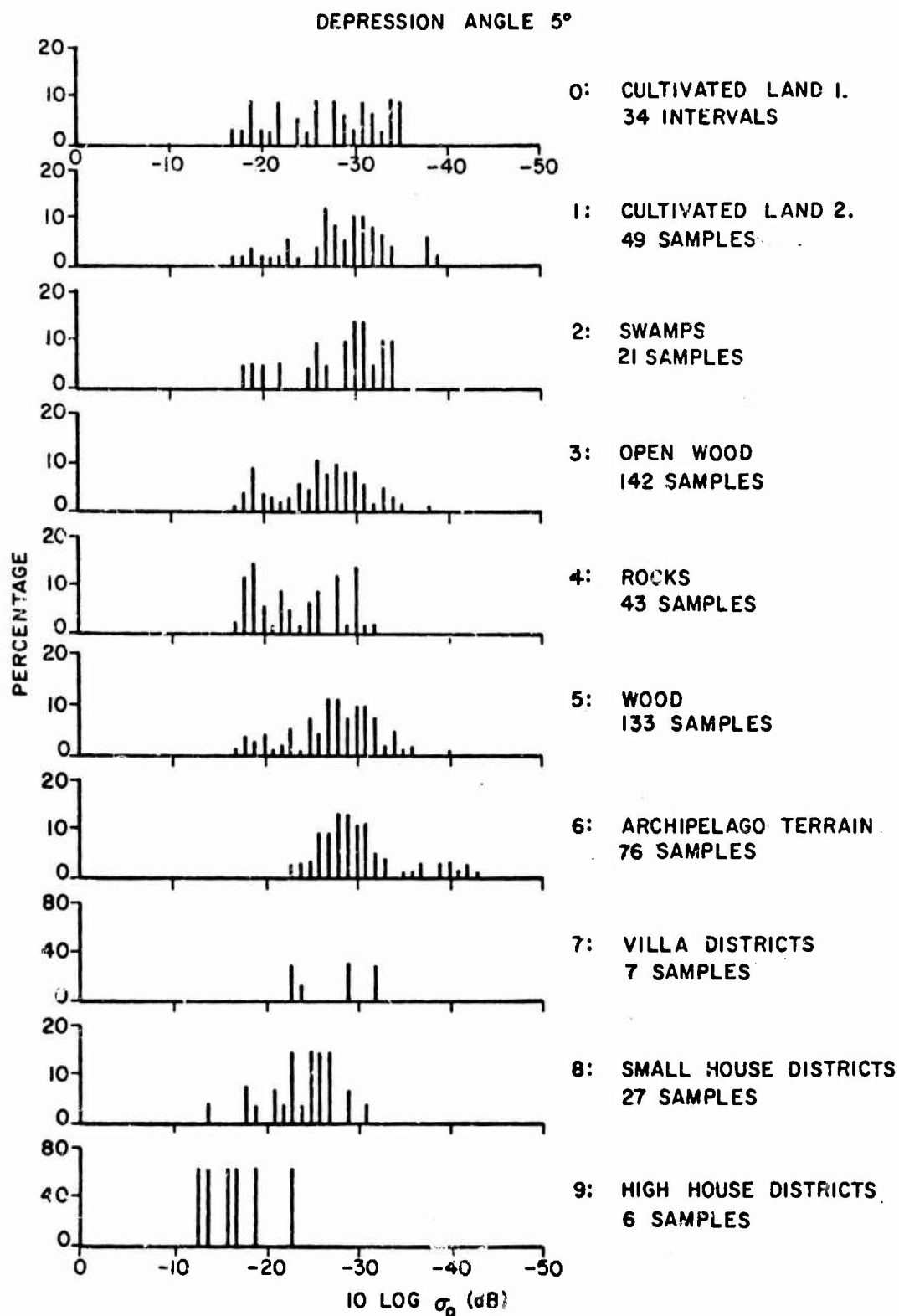


Fig. 138. Distribution of average values of σ_0 for different types of terrain, at X-band, horizontal polarization, for a 5° depression angle - Reference 33.

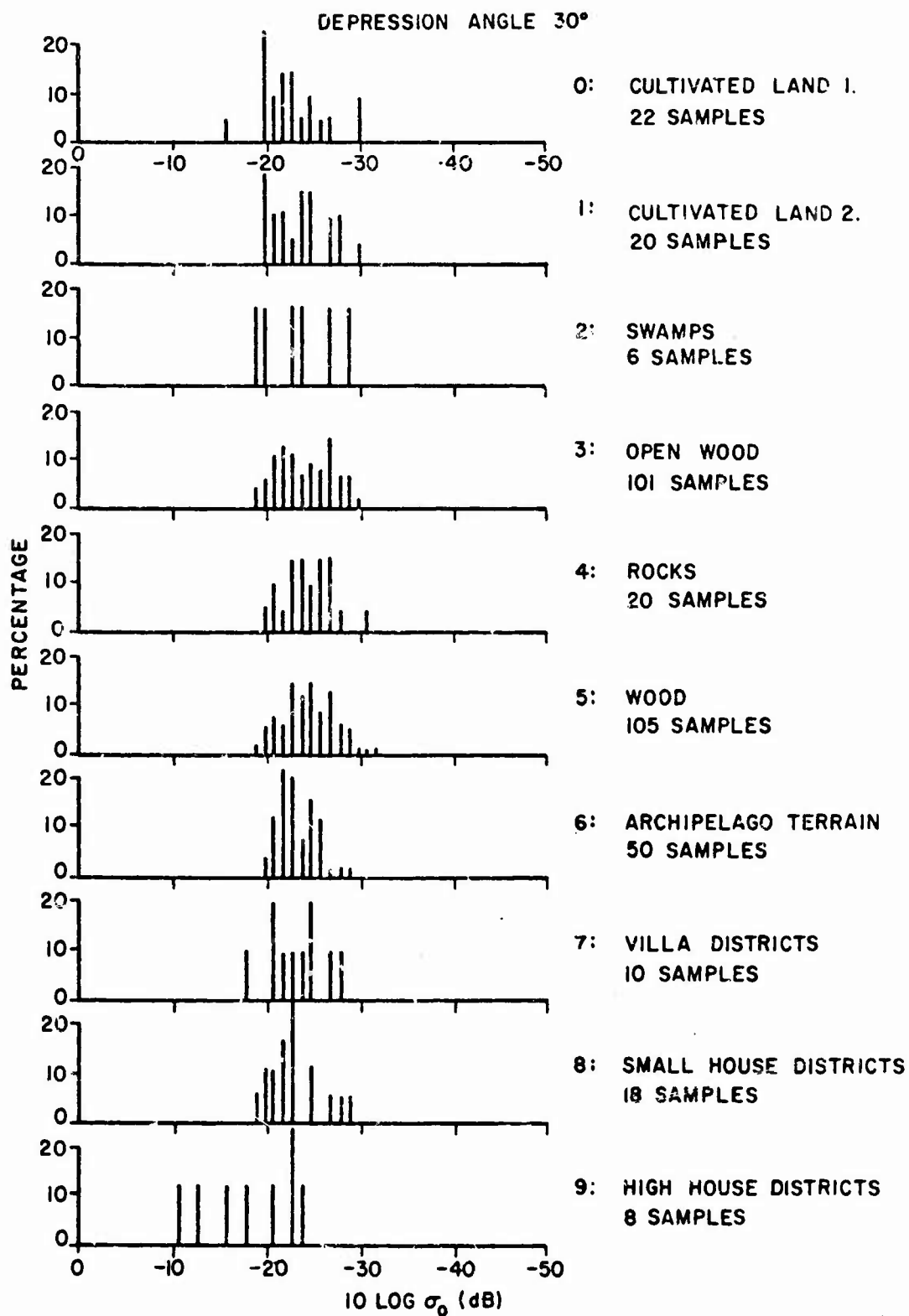


Fig. 139. Distribution of average values of σ_0 for different types of terrain, at X-band, horizontal polarization, for a 30° depression angle - Reference 33.

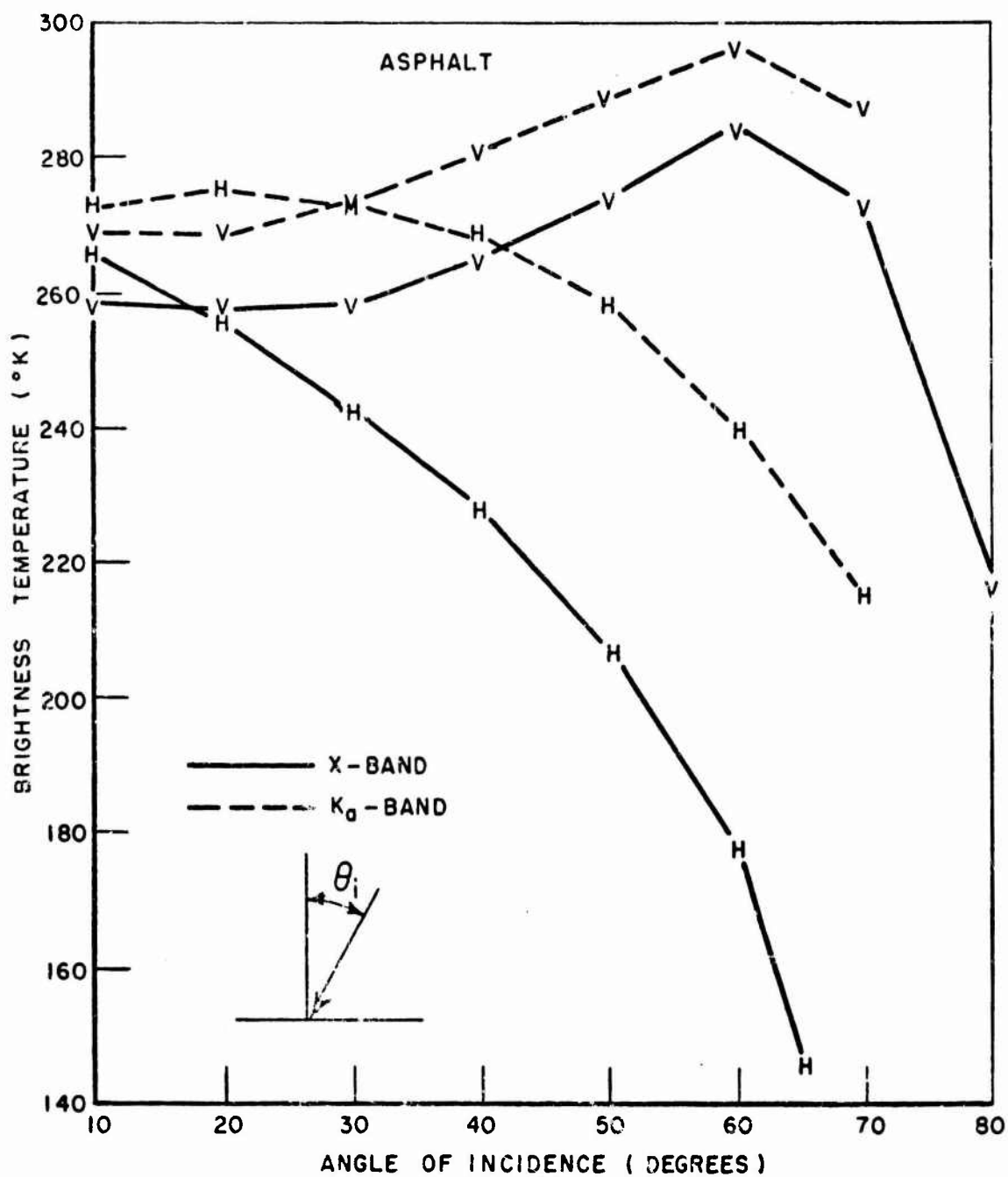


Fig. 140. Brightness temperature for asphalt at 10 GHz and 35 GHz.

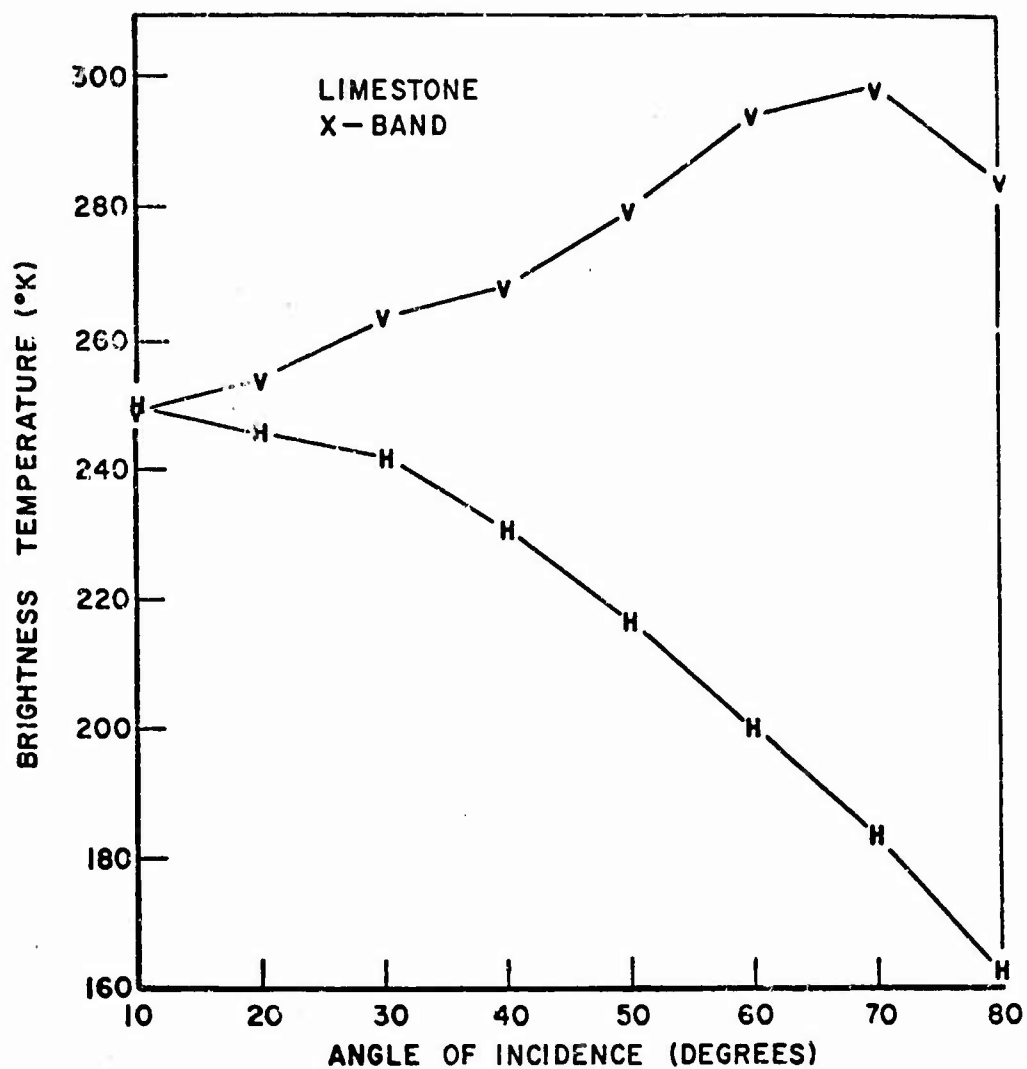


Fig. 141. Brightness temperature for glacially polished limestone at 10 GHz.

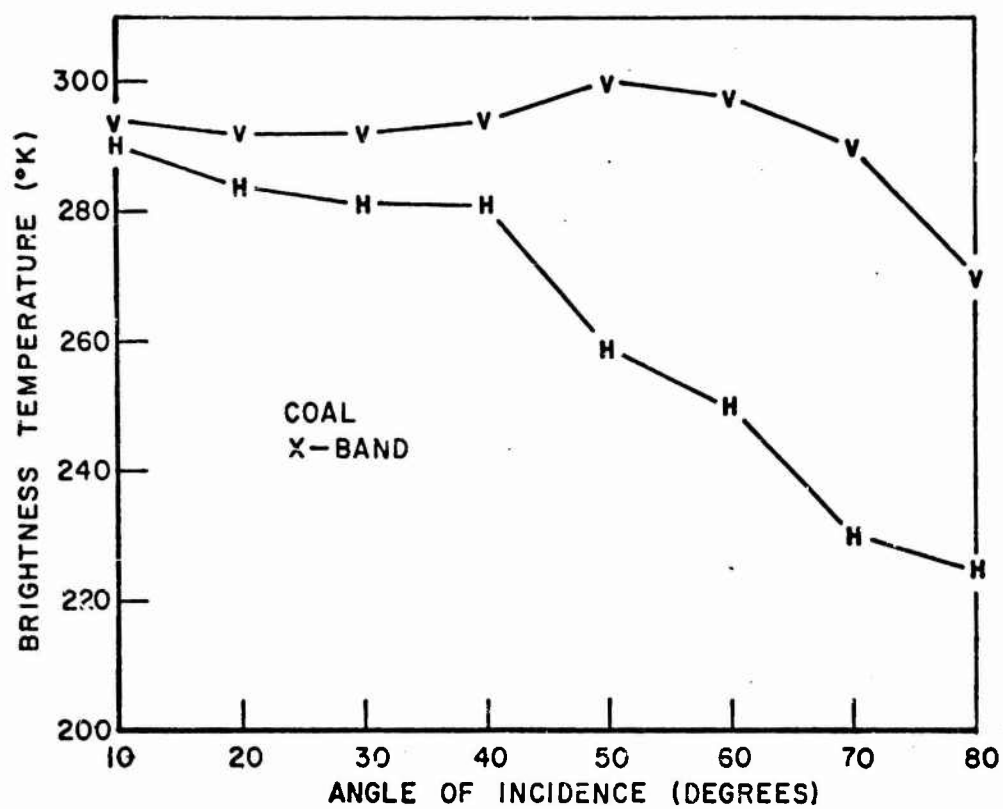


Fig. 142. Brightness temperature for Pittsburgh #8 Coal at 10 GHz.

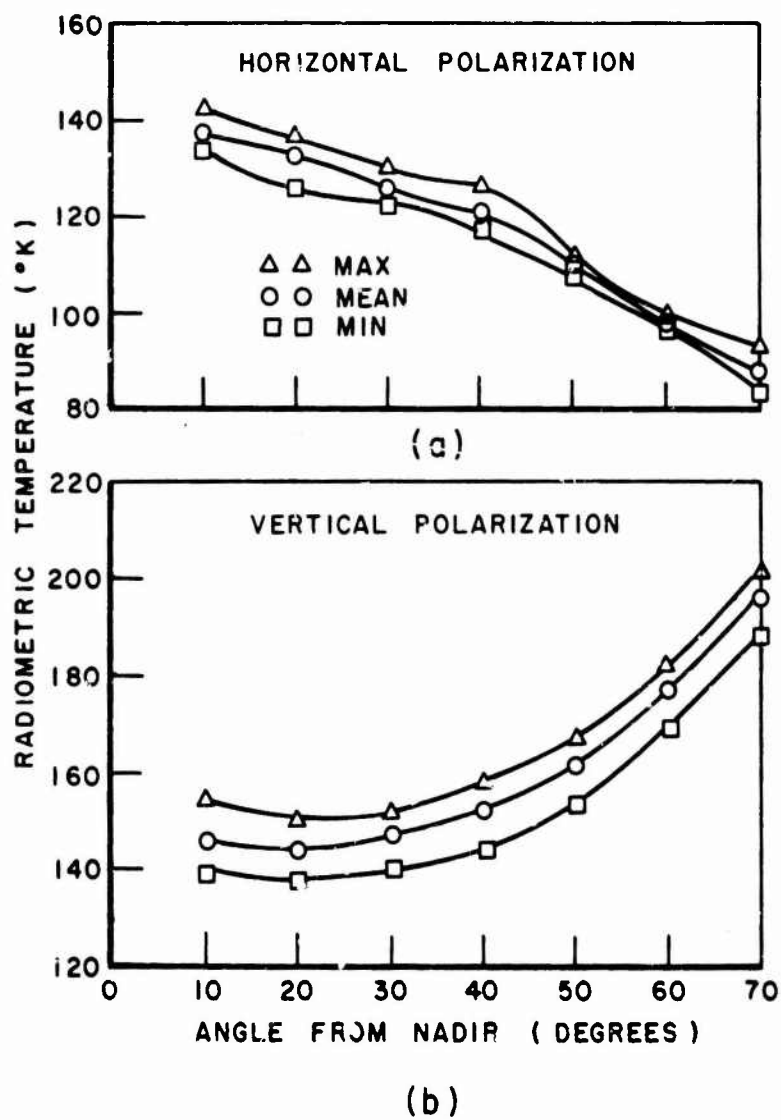


Fig. 143. Deviation envelope and mean value curve for the radiometric temperature of Palo Alto Marine mud at 13.5 GHz - Reference 34.

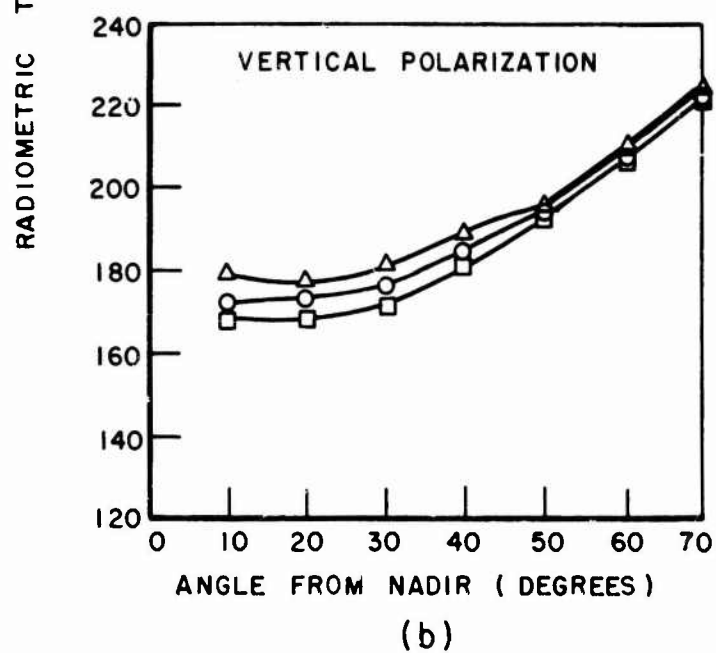
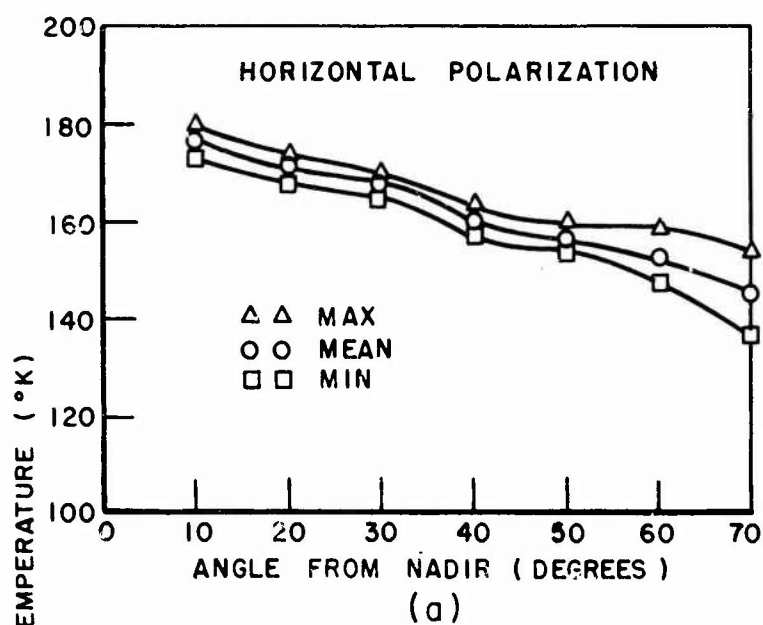


Fig. 144. Deviation envelope and mean value curve for the radiometer temperature of Palo Alto Marine mud at 37 GHz - Reference 34.

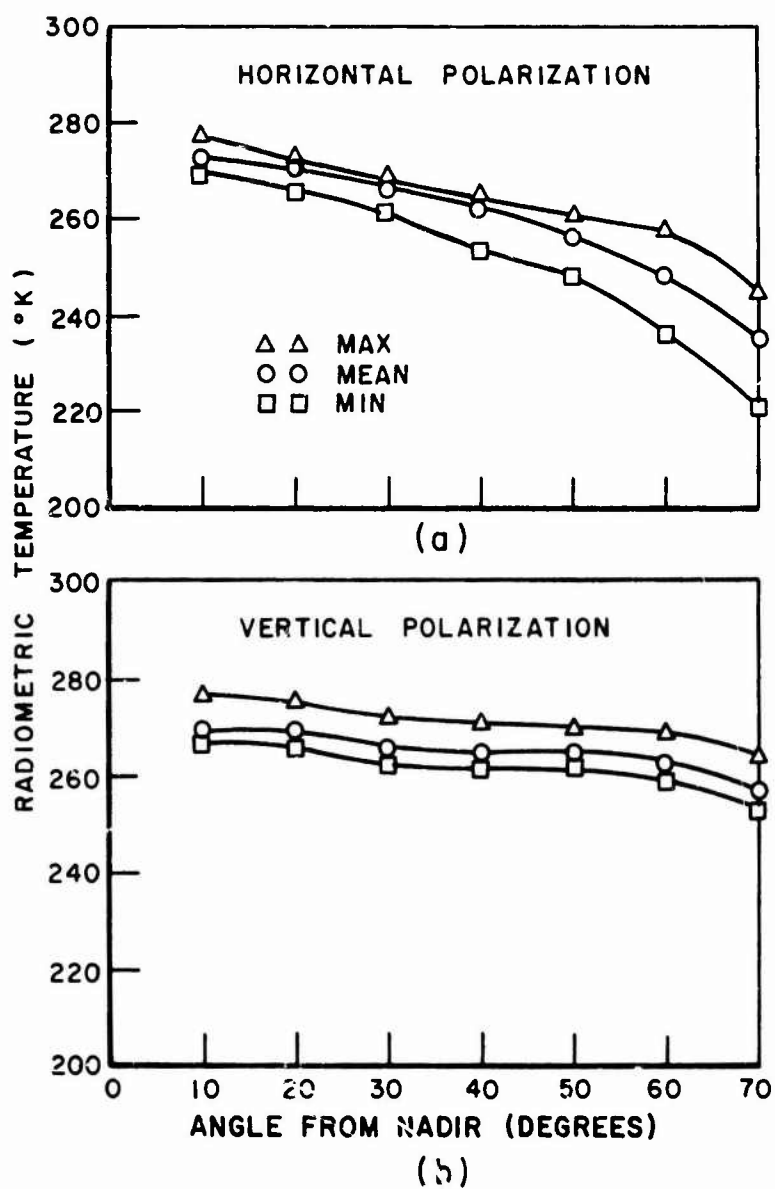


Fig. 145. Deviation envelope and mean value curve for the radiometric temperature of LaJolla Beach sand at 13.5 GHz - Reference 34.

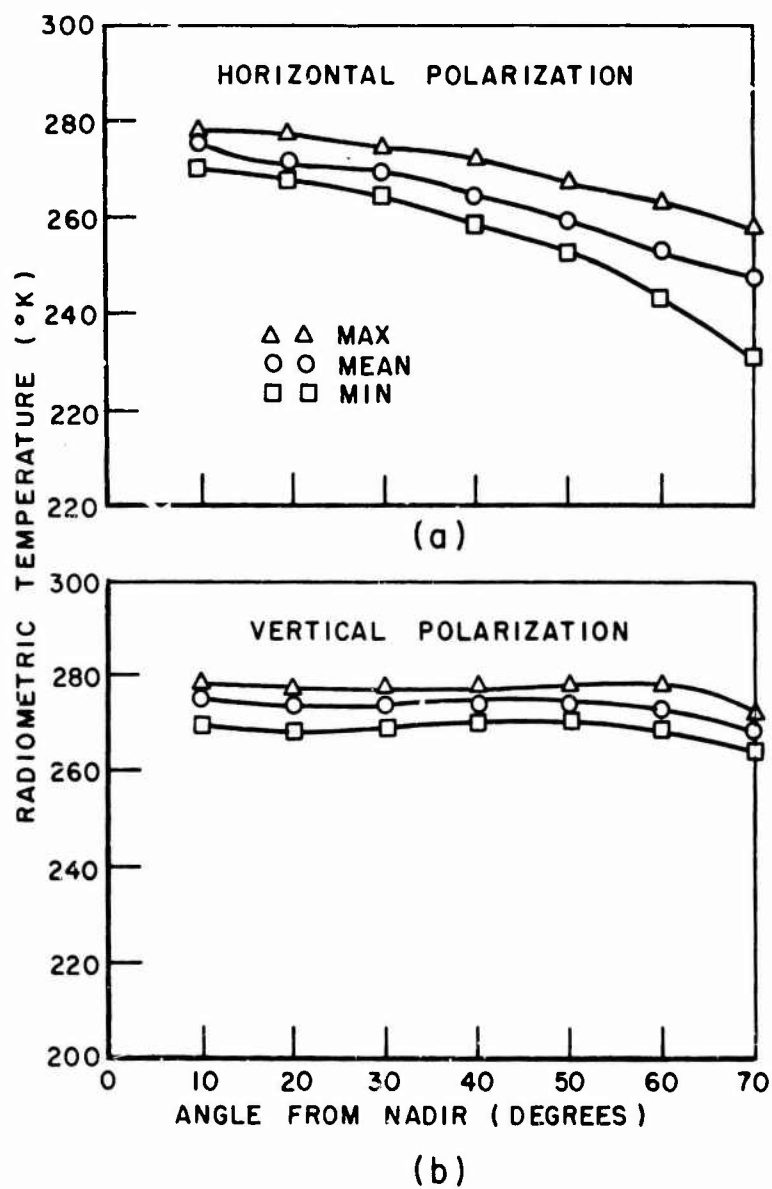


Fig. 146. Deviation envelope and mean value curve for the radiometric temperature of LaJolla Beach sand at 37 GHz - Reference 34.

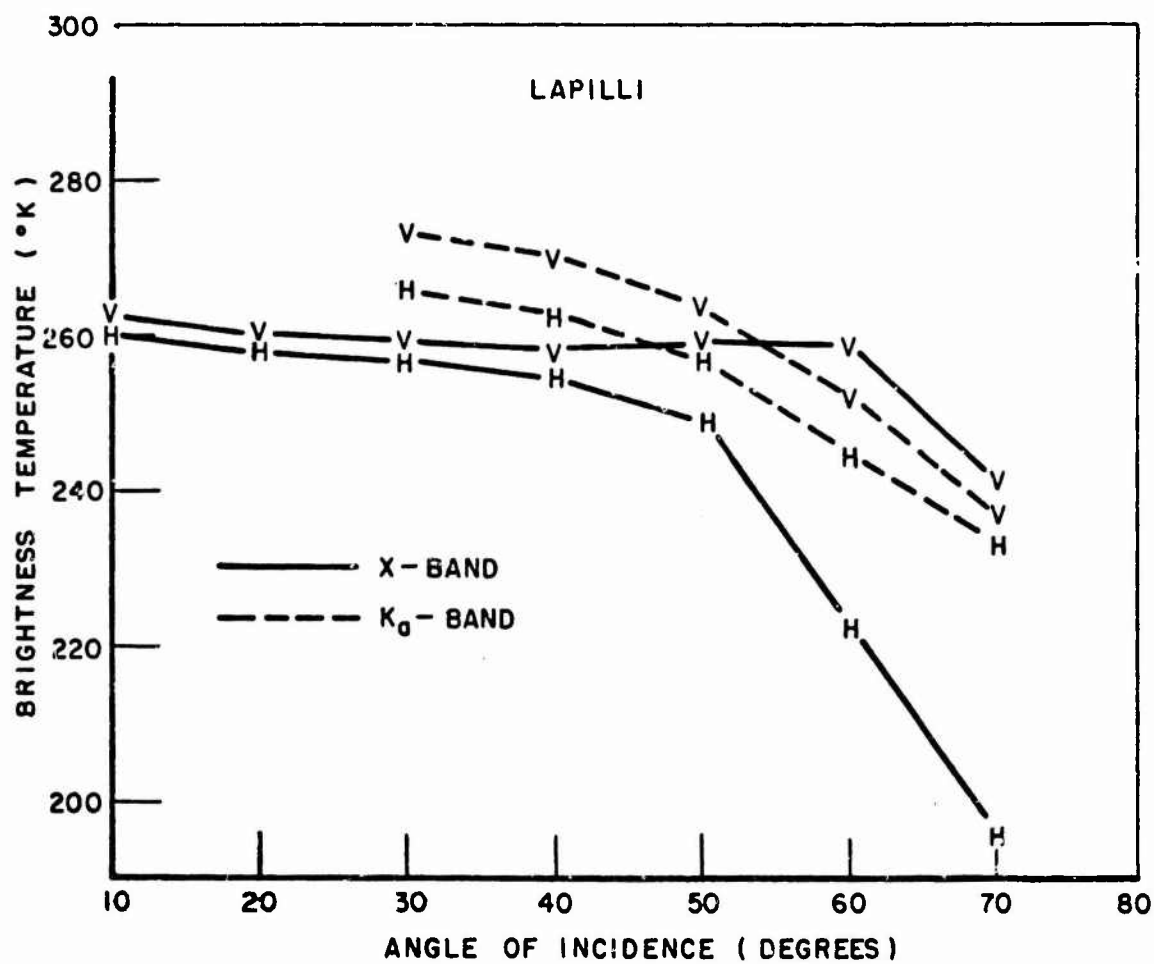


Fig. 147. Brightness temperature for lapilli (volcanic ash) at 10 GHz and 35 GHz.

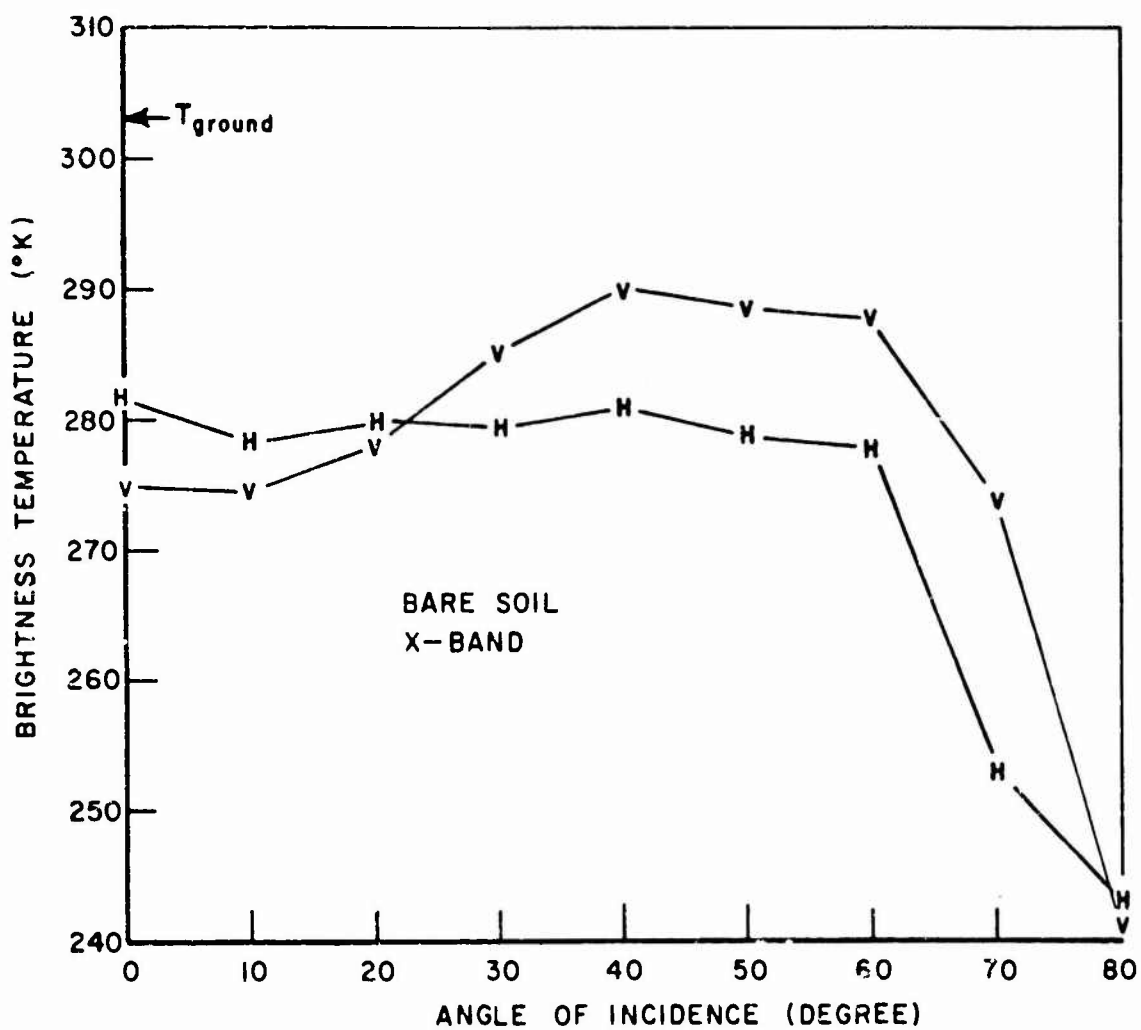


Fig. 148. Brightness temperature for disced, bare soil (2"-3" ridges) at 10 GHz.

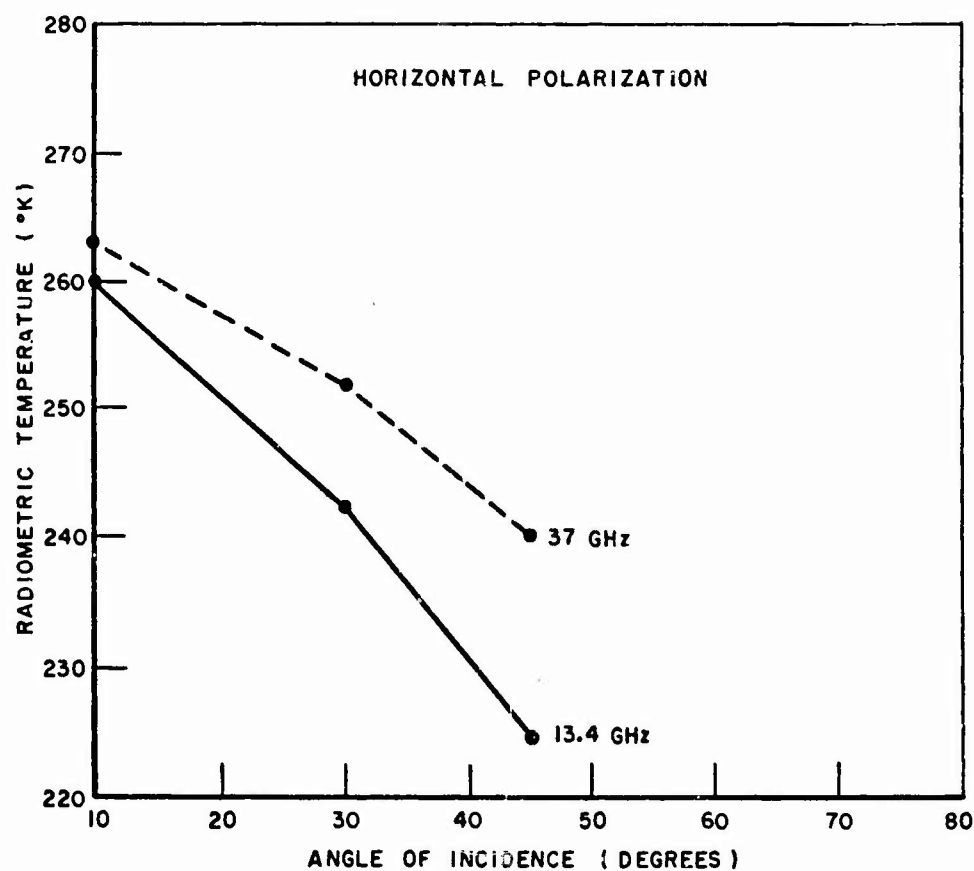


Fig. 149. Radiometric temperature for silt loam soil (Davis, California) at 13.4 GHz and 37 GHz - Reference 35.

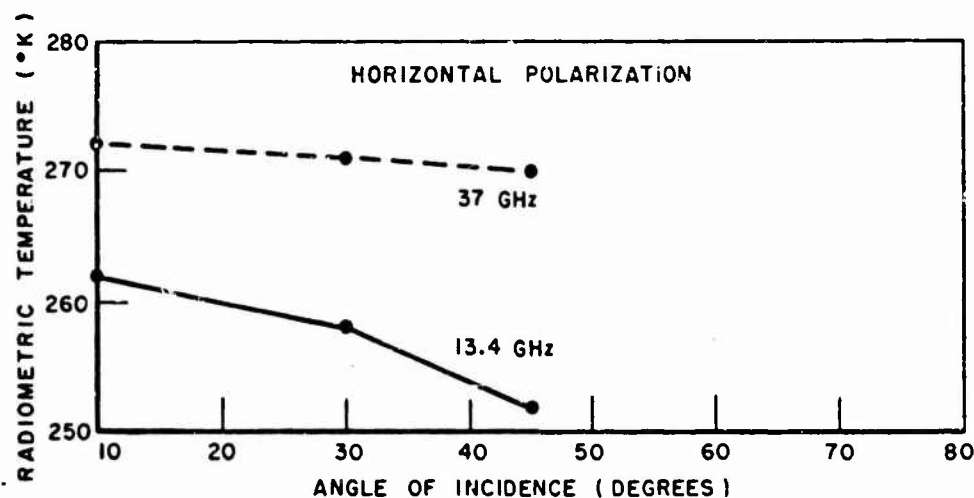


Fig. 150. Radiometric temperature for sandy loam soil with 10% vegetation cover (Rocky Mtn. Arsenal) at 13.4 GHz and 37 GHz - Reference 35.

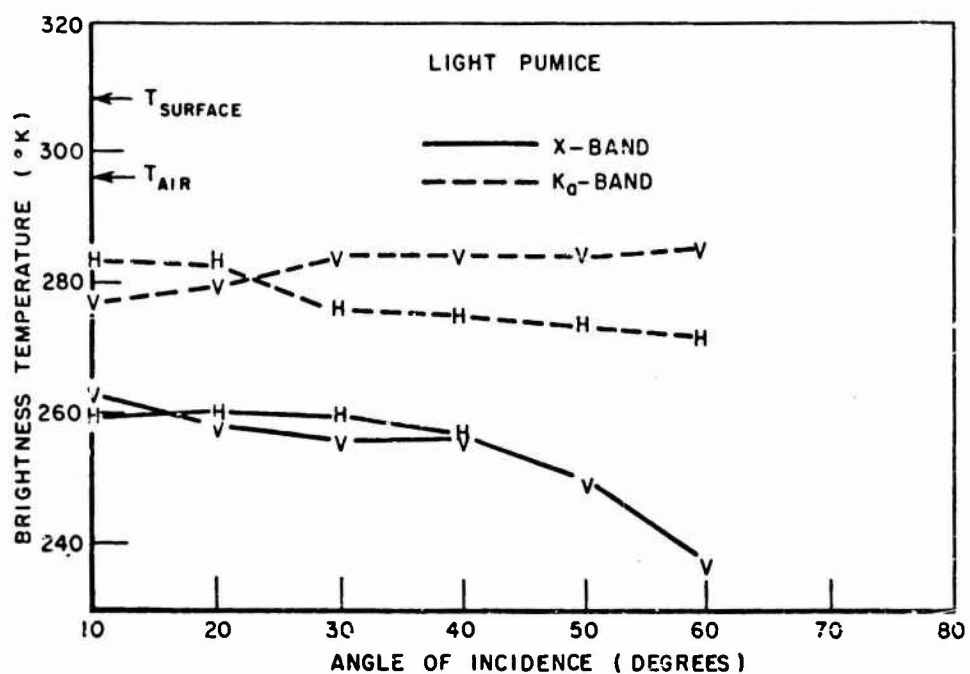


Fig. 151. Brightness temperature for dense, broken grey pumice at 10 GHz and 35 GHz.

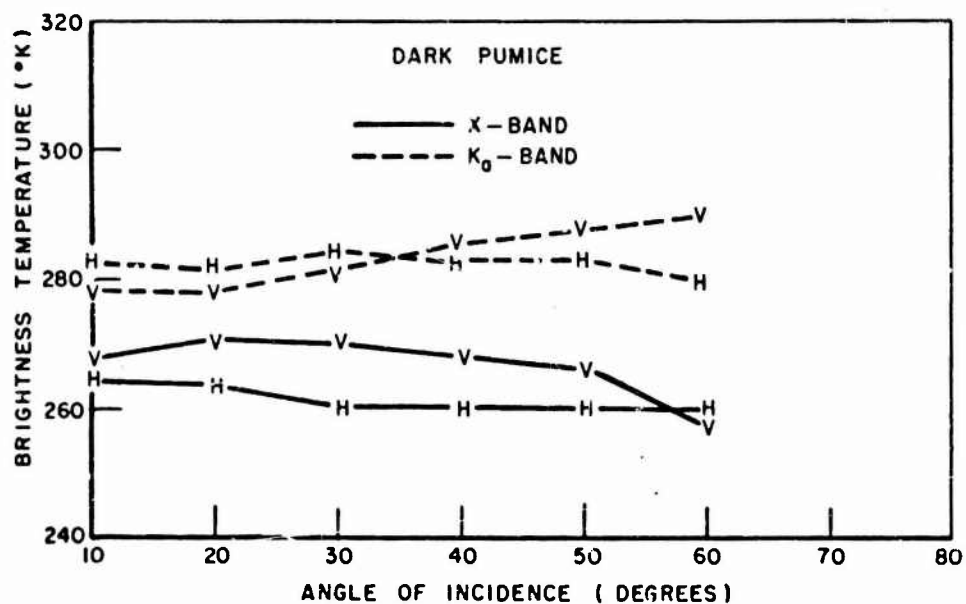


Fig. 152. Brightness temperature for light weight, dark pumice (block) at 10 GHz and 35 GHz.

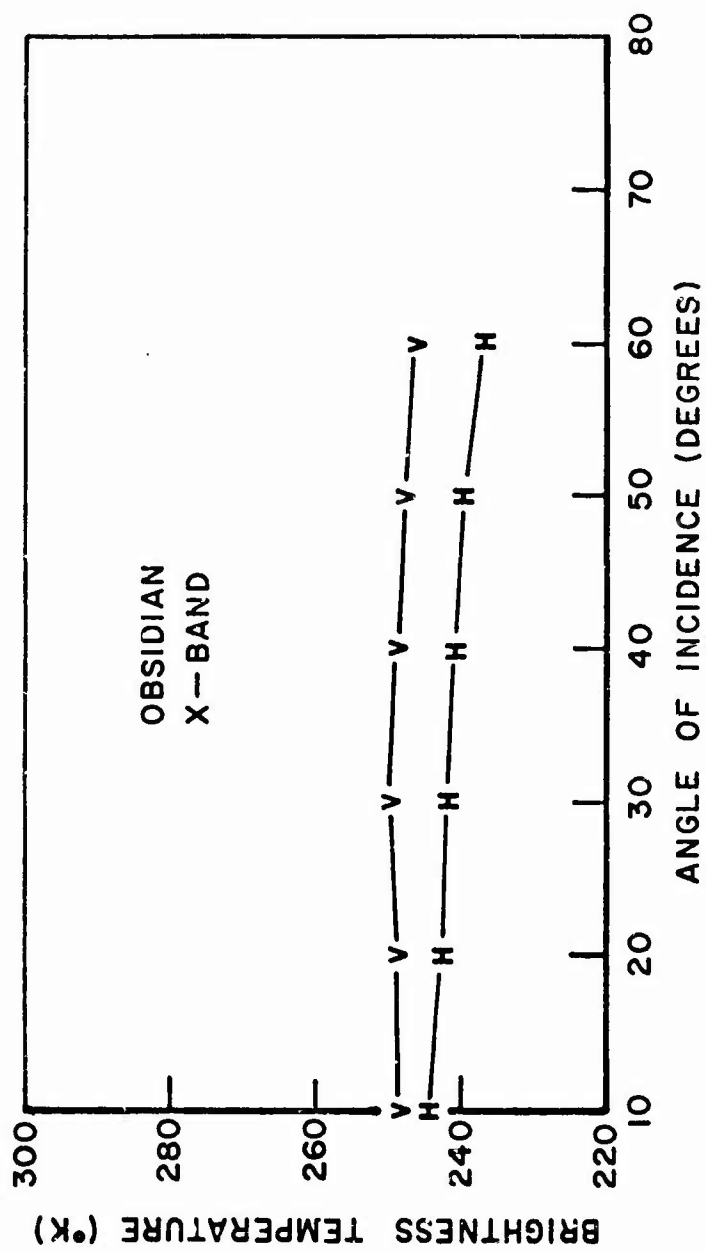


Fig. 153. Brightness temperature for large blocks of obsidian at 10 GHz.

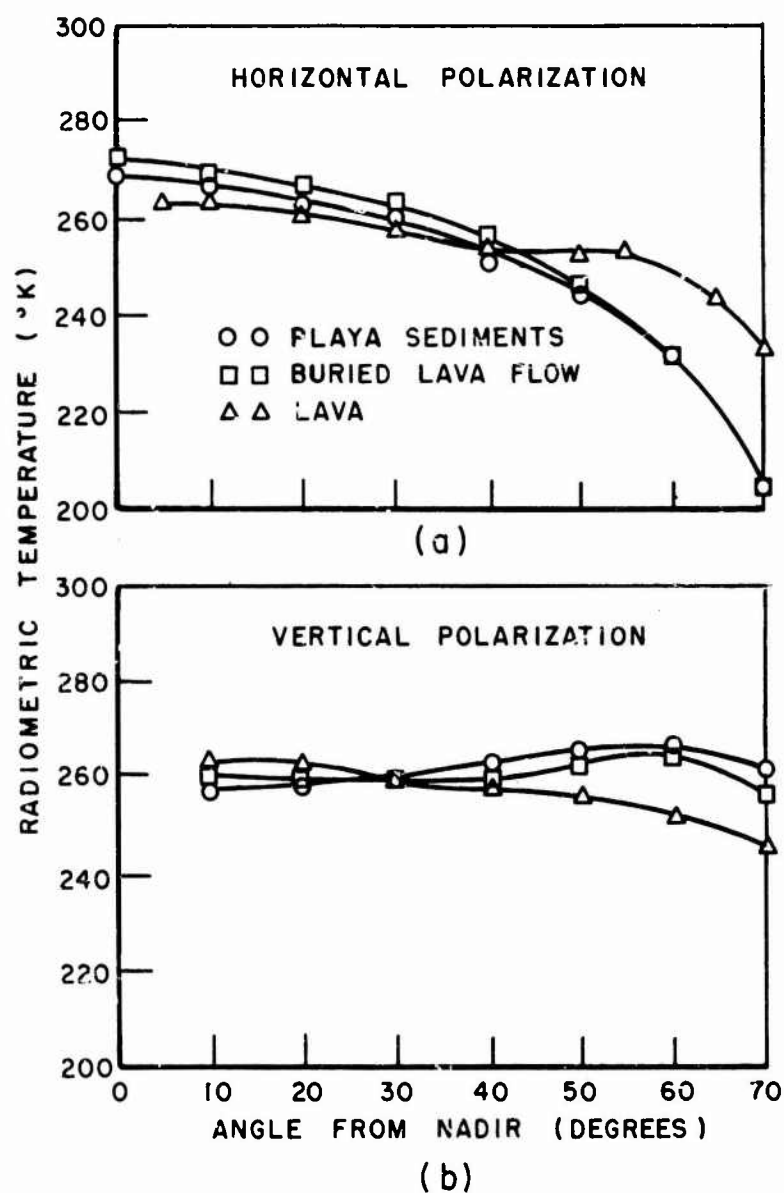


Fig. 154. Radiometric measurements of playa sediments, lava flow, and lava flow beneath playa sediments at 13.5 GHz - Reference 34.

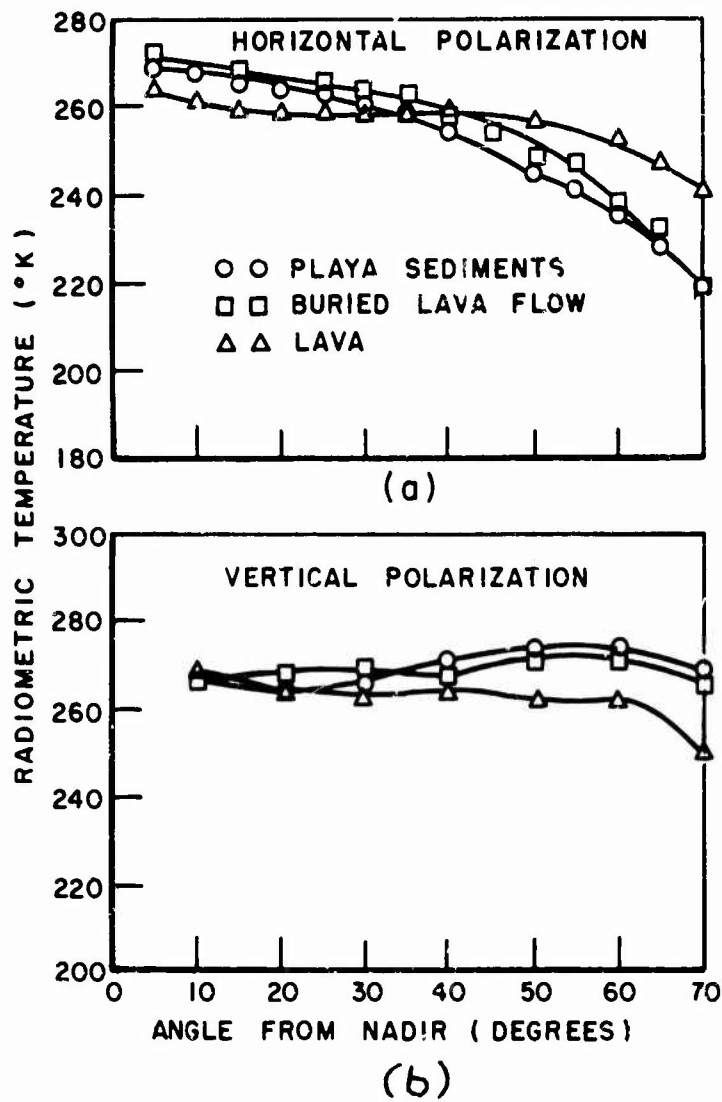


Fig. 155. Radiometric measurements of playa sediments, lava flow, and lava flow beneath playa sediments at 37 GHz - Reference 34.

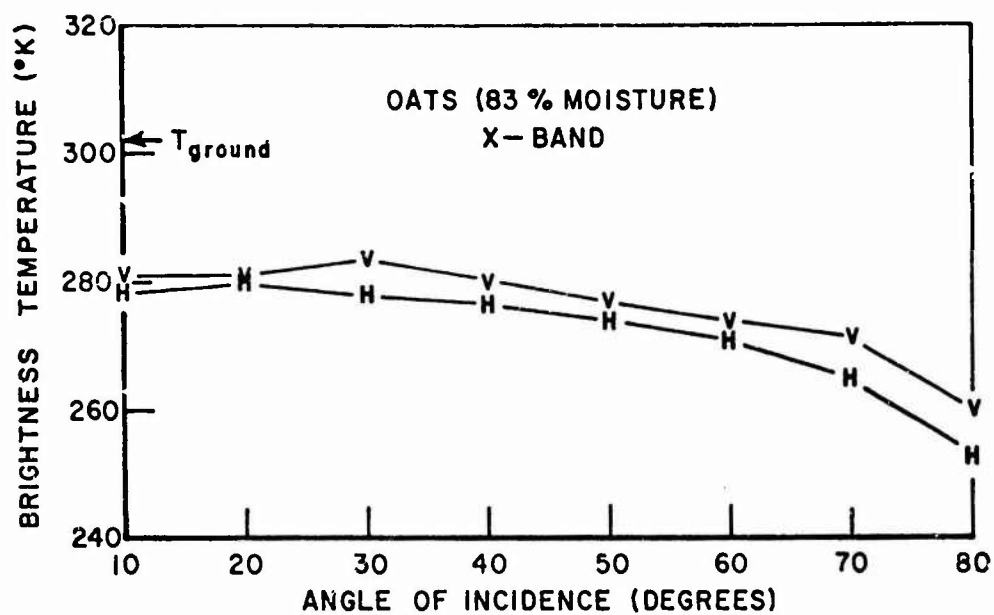


Fig. 156. Brightness temperature of green oats, in head, at 10 GHz.

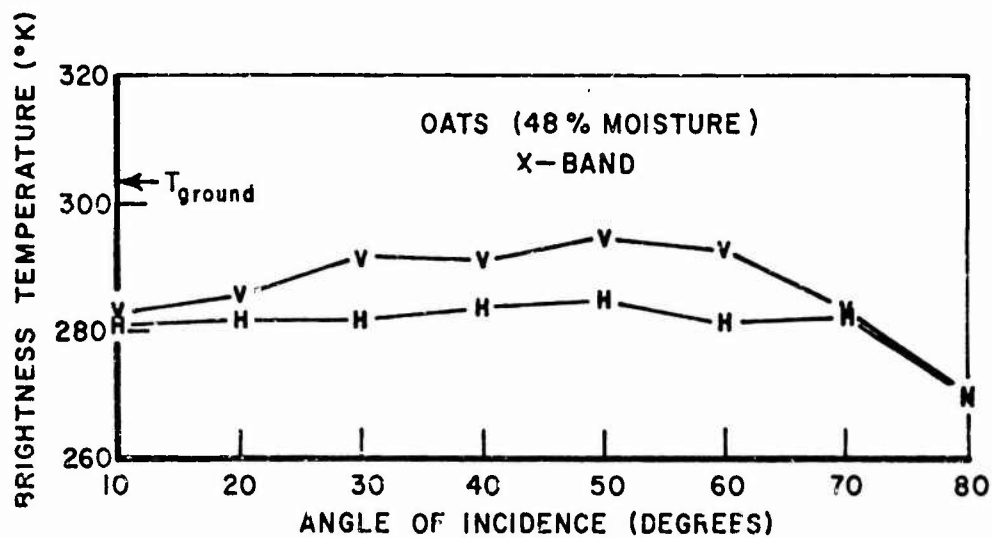


Fig. 157. Brightness temperature of ripe oats at 10 GHz.

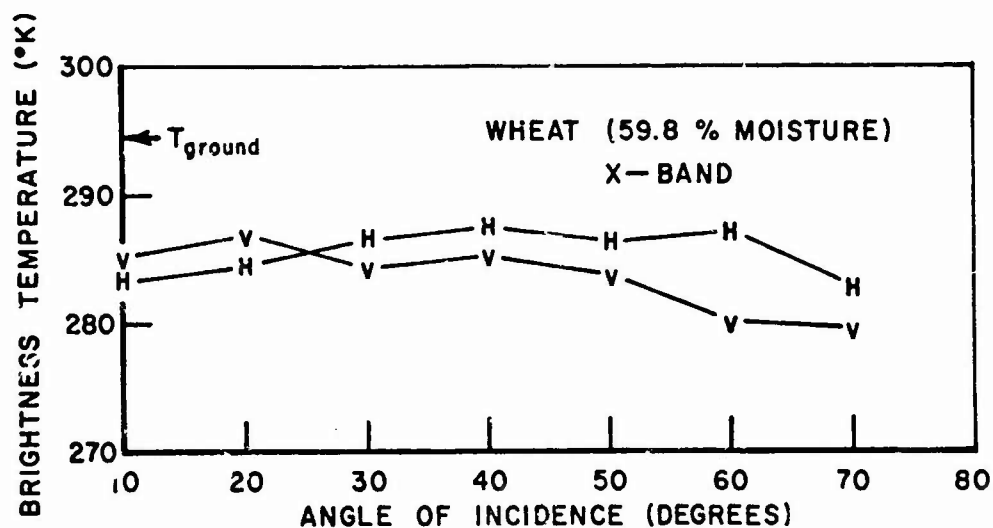


Fig. 158. Brightness temperature of green wheat at 10 GHz.

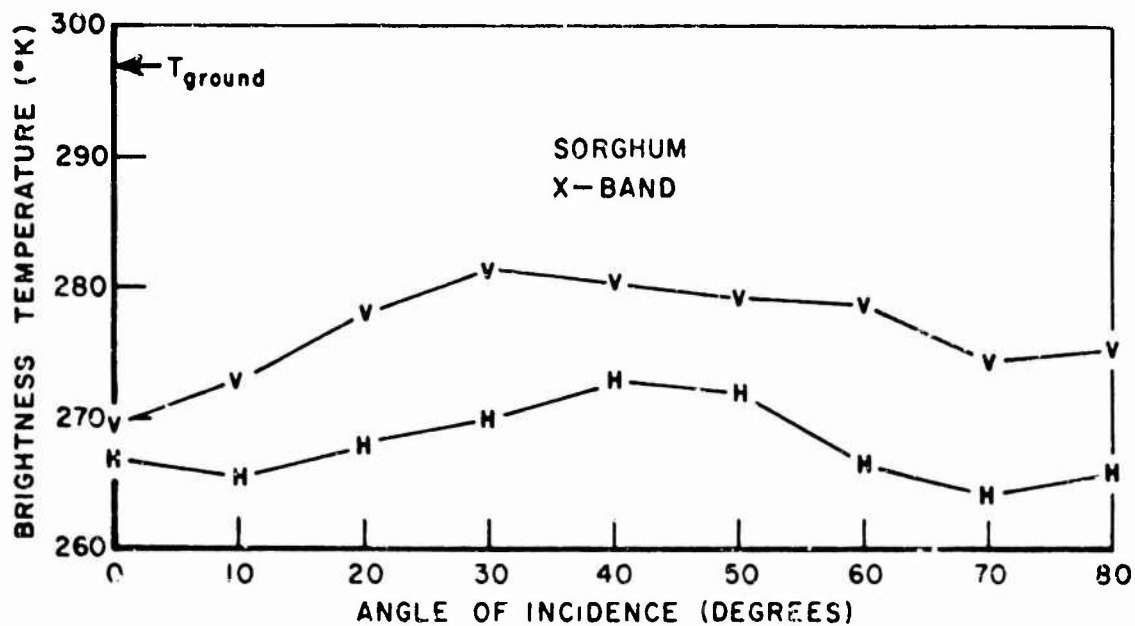


Fig. 159. Brightness temperature of green sorghum, in tassel, at 10 GHz.

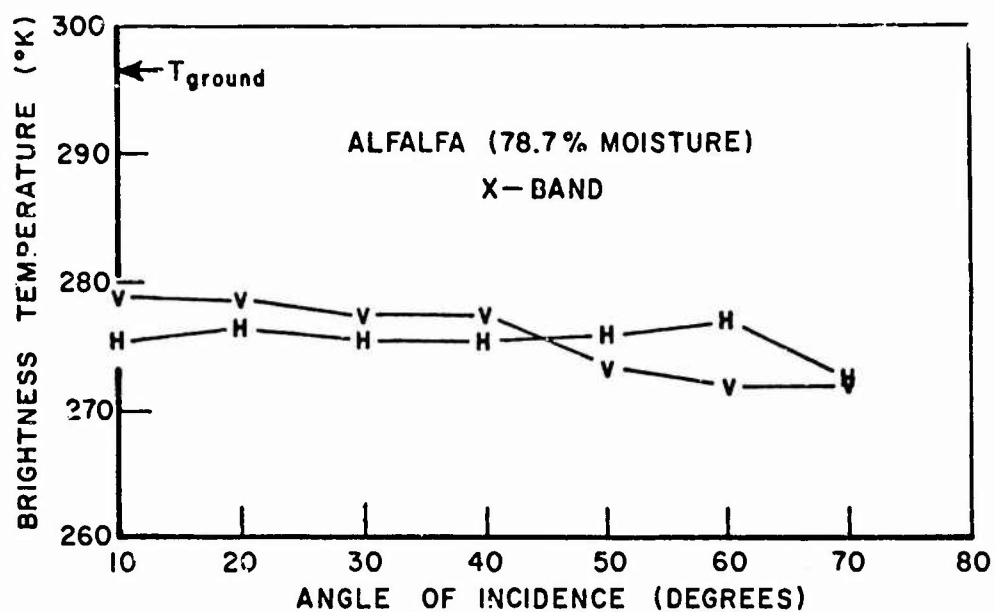


Fig. 160. Brightness temperature of green alfalfa at 10 GHz.

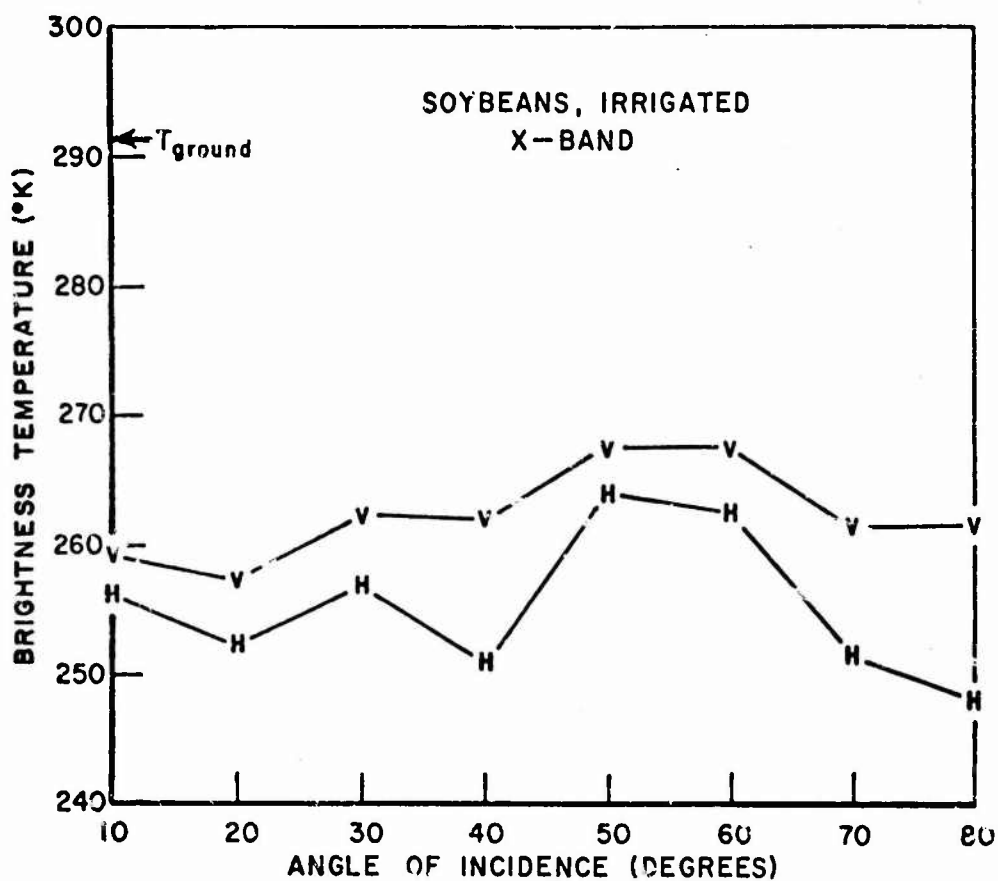


Fig. 161. Brightness temperature of irrigated, green soybeans at 10 GHz. (12 August)

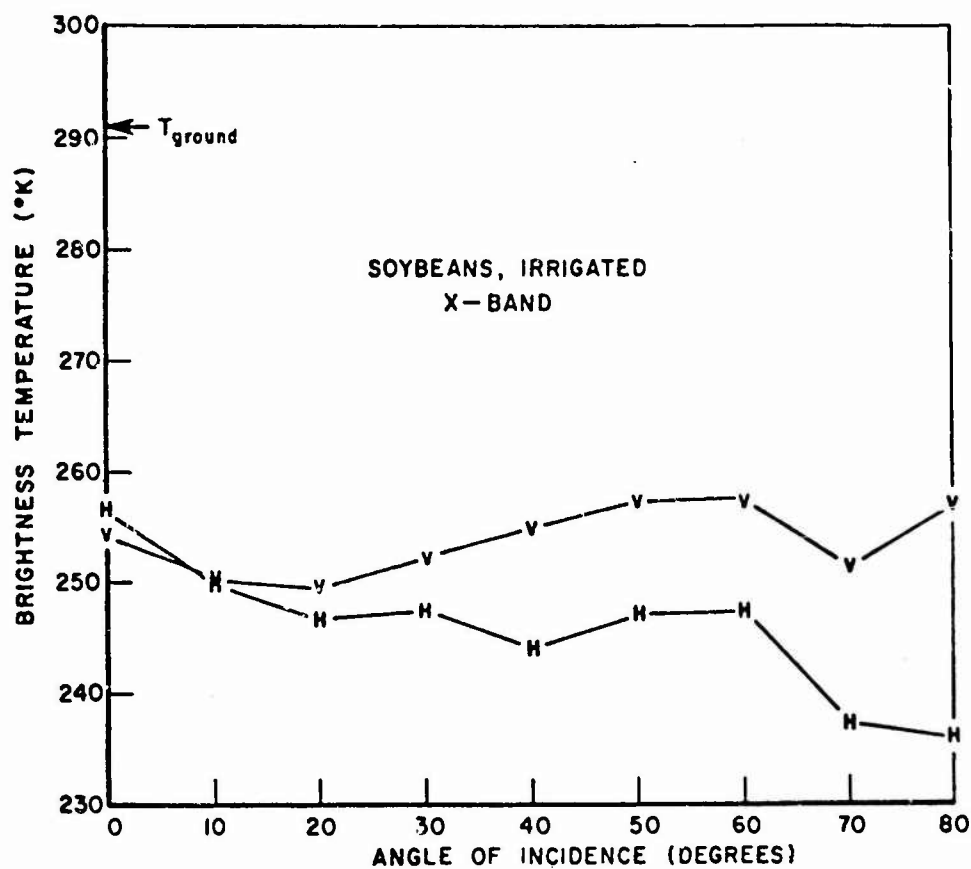


Fig. 162. Brightness temperature of irrigated, green soybeans at 10 GHz. (4 September)

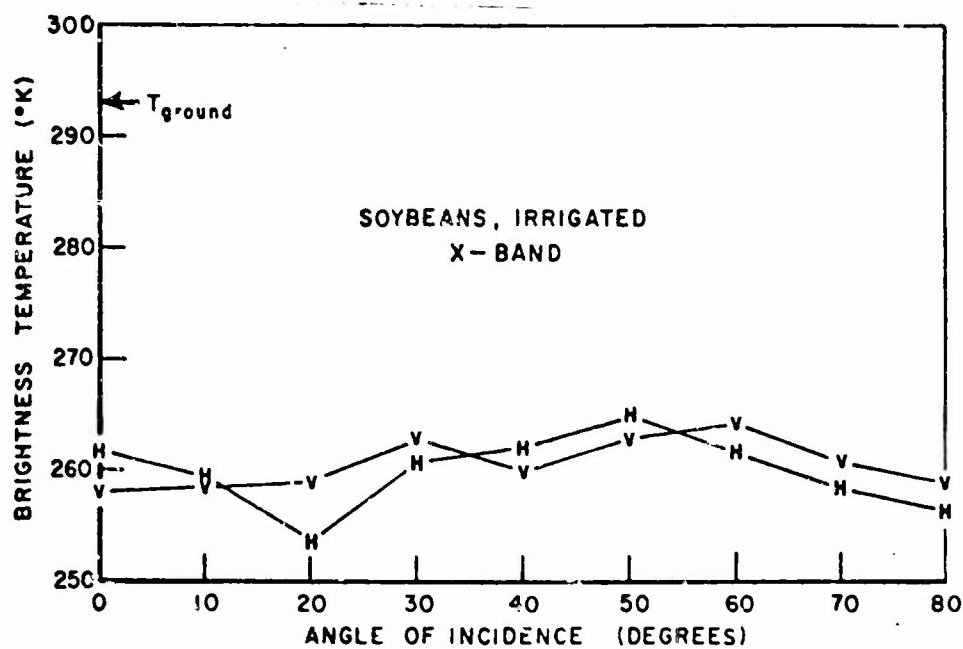


Fig. 163. Brightness temperature of irrigated soybeans at 10 GHz. (13 September)

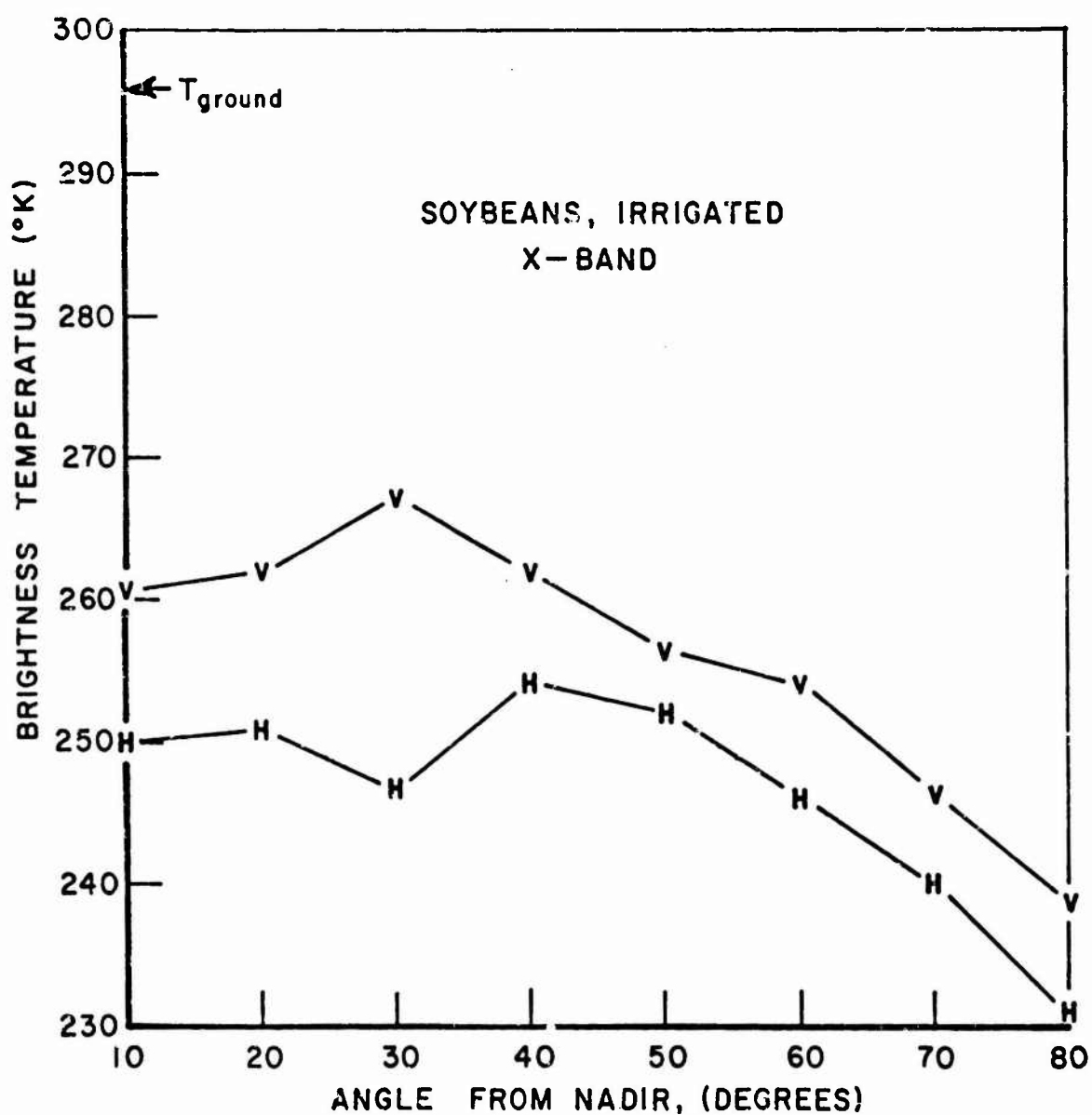


Fig. 164. Brightness temperature of irrigated, ripe soybeans at 10 GHz. (26 September)

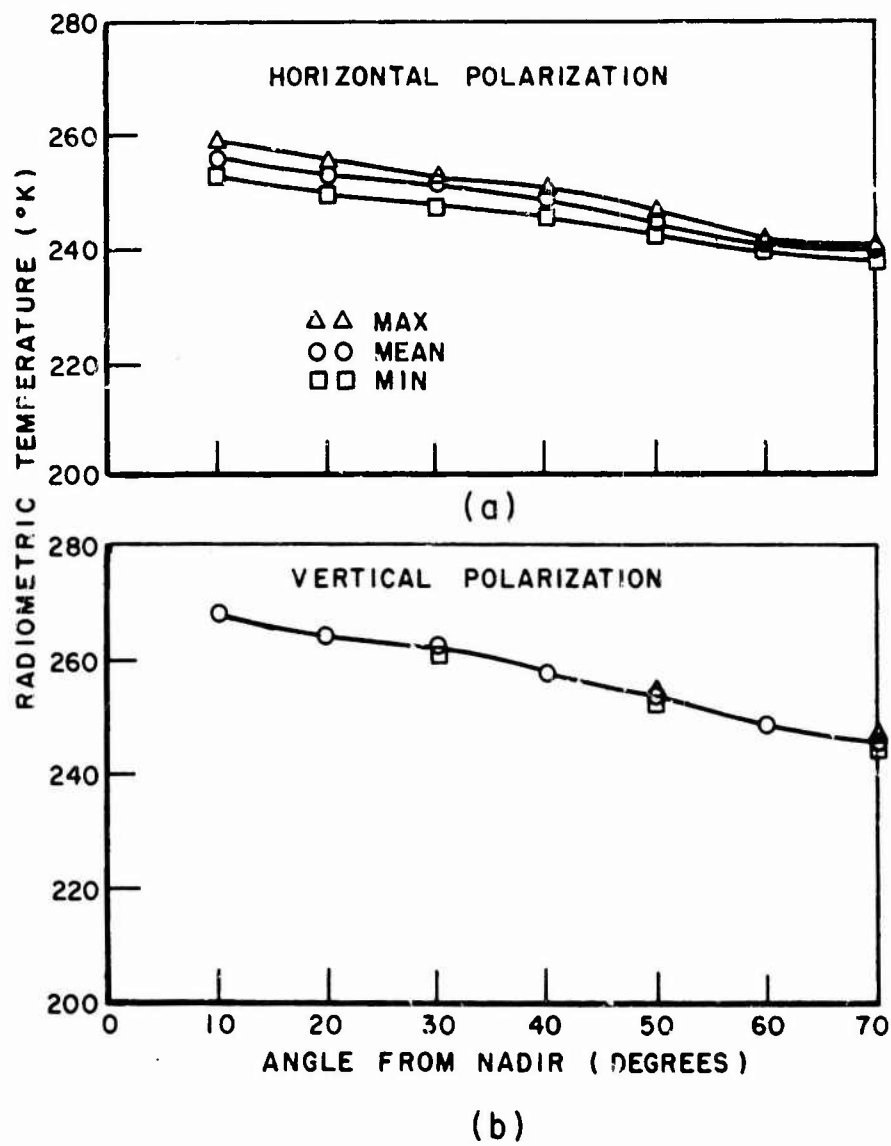


Fig. 165. Deviation envelope and mean value curve for the radiometric temperature of Palo Alto marsh foliage at 13.4 GHz - Reference 34.

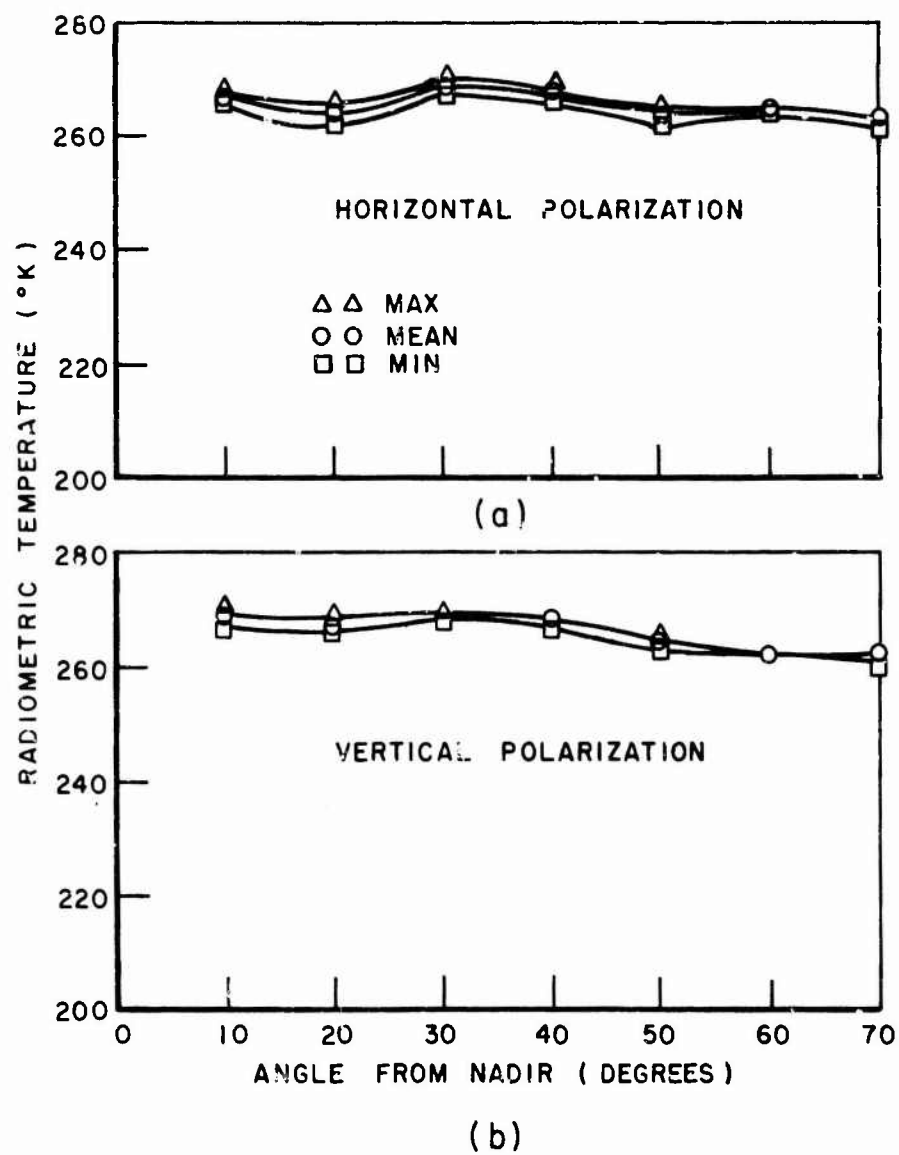


Fig. 166. Deviation envelope and mean value curve for the radiometric temperature of Palo Alto marsh foliage at 37 GHz - Reference 34.

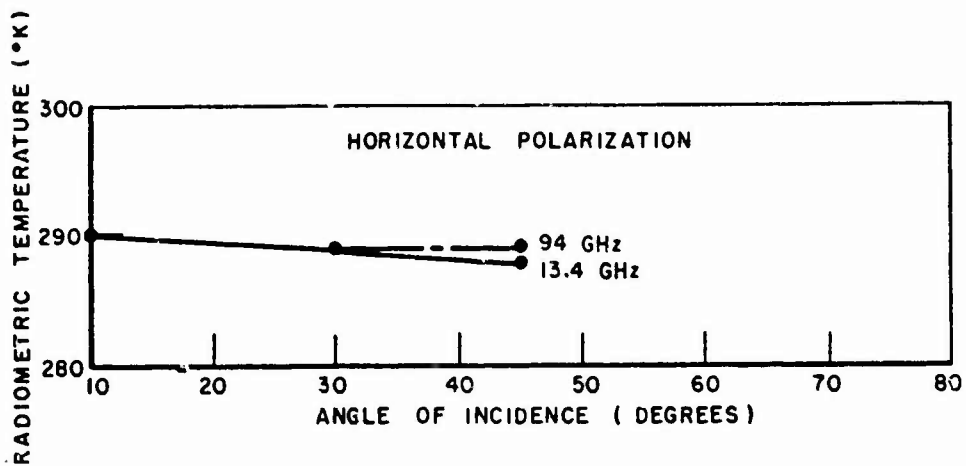


Fig. 167. Radiometric temperature for dense marsh vegetation (Seal Beach Tidal Marsh) at 13.4 and 94 GHz - Reference 35.

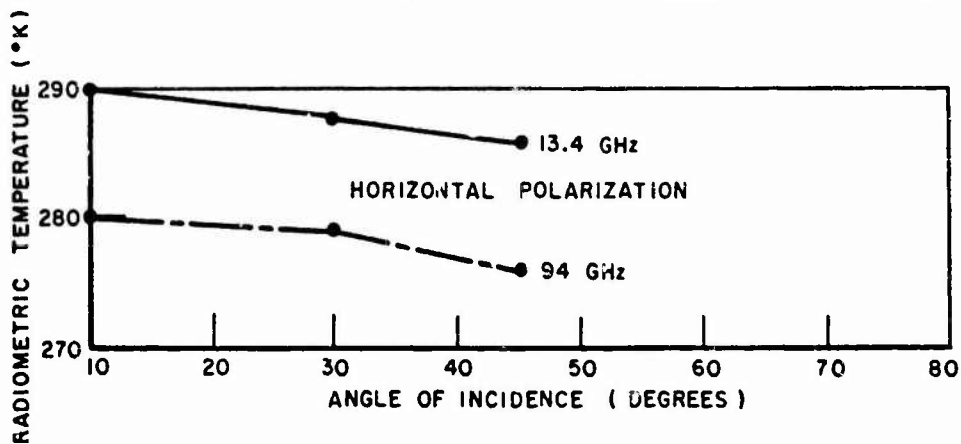


Fig. 168. Radiometric temperature for pasture grass (Thousand Oaks) at 13.4 GHz and 94 GHz - Reference 35.

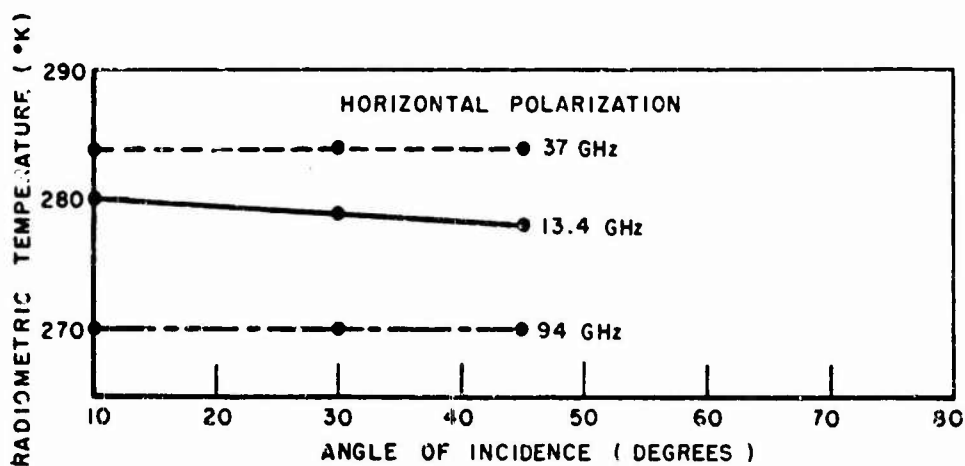


Fig. 169. Radiometric temperature for flower stocks (Oxnard) at 13.4, 37, and 94 GHz - Reference 35.

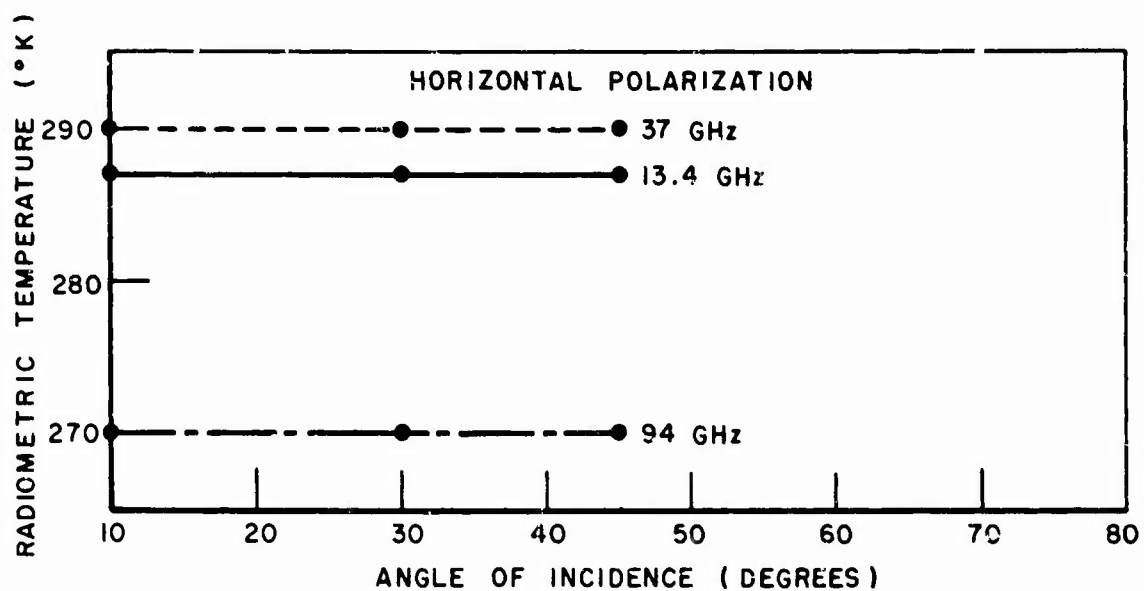


Fig. 170. Radiometric temperature for celery crops (Oxnard) at 13.4, 37, and 94 GHz - Reference 35.

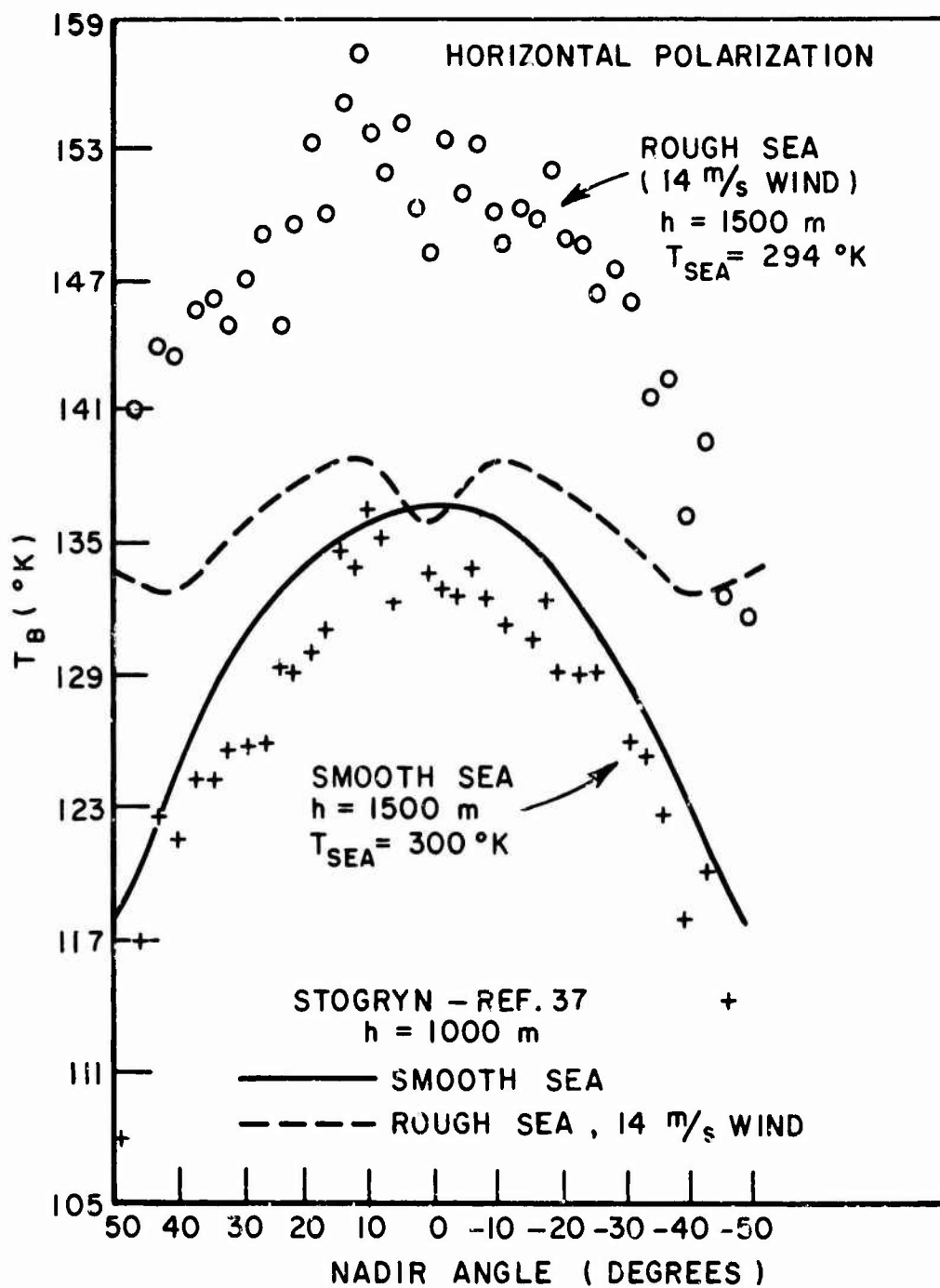


Fig. 171(a). Brightness temperature of the Salton Sea at 1.55 cm - Reference 36.

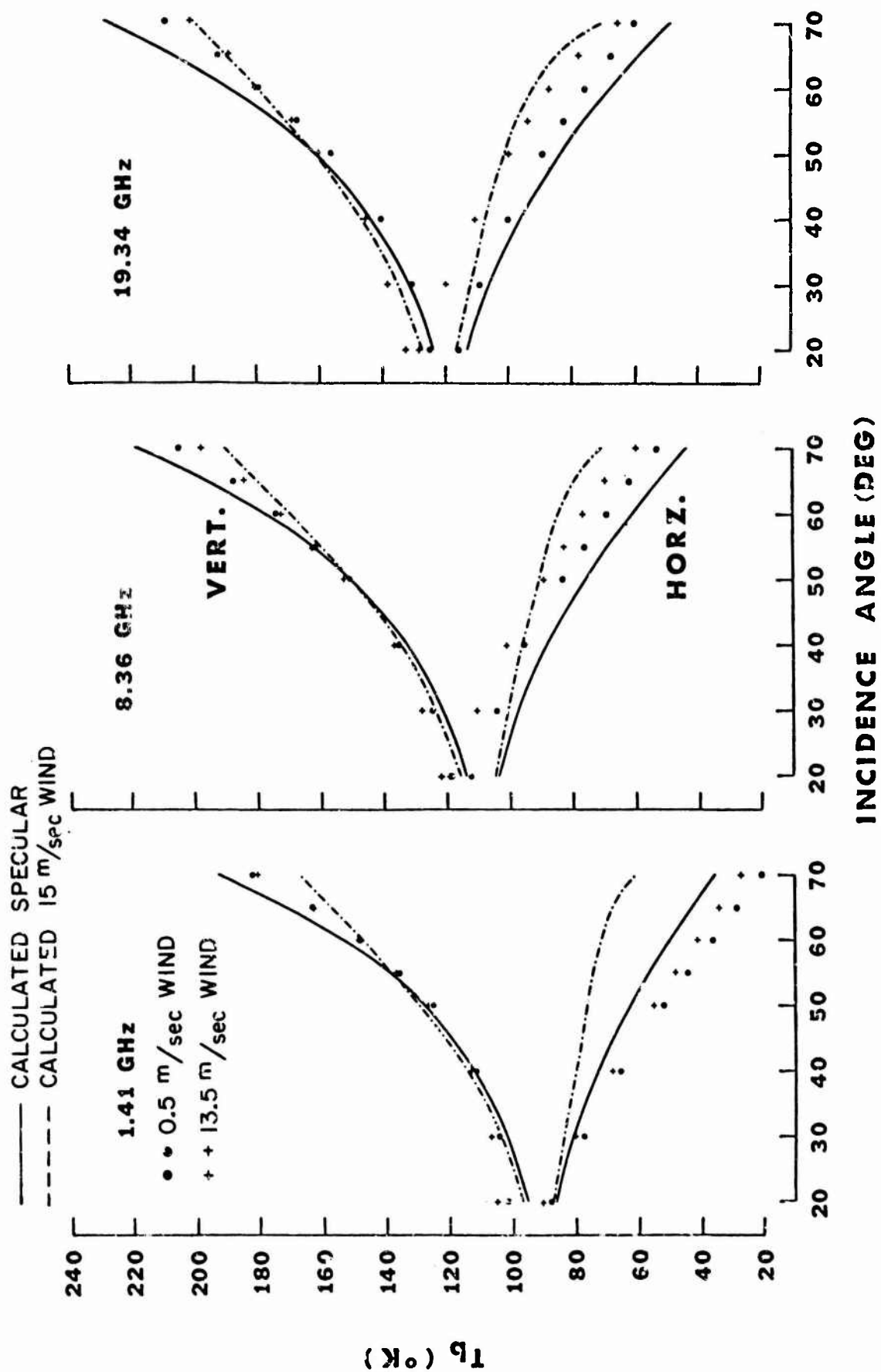


Fig. 171b. Brightness temperature of the ocean for low and moderate wind velocities. (Ref. 39)

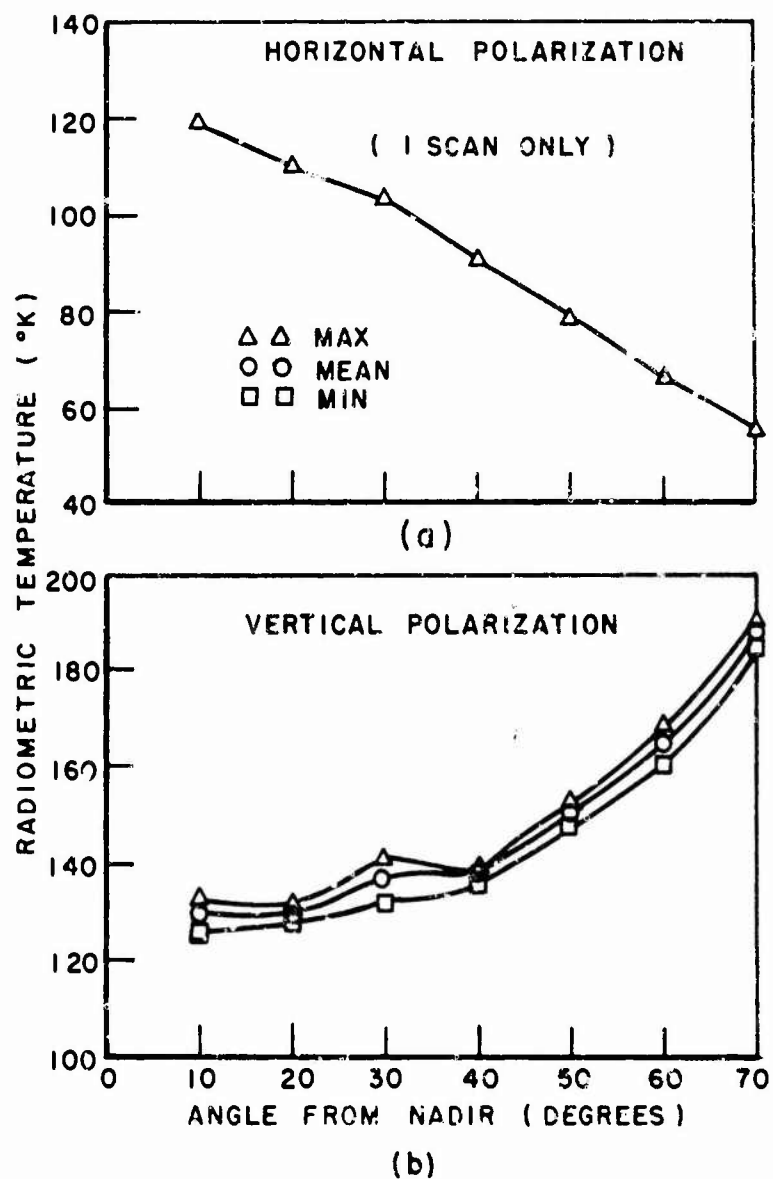


Fig. 172. Deviation envelope and mean value curve for the radiometric temperature of sea water (Palo Alto) at 13.5 GHz-Reference 34.

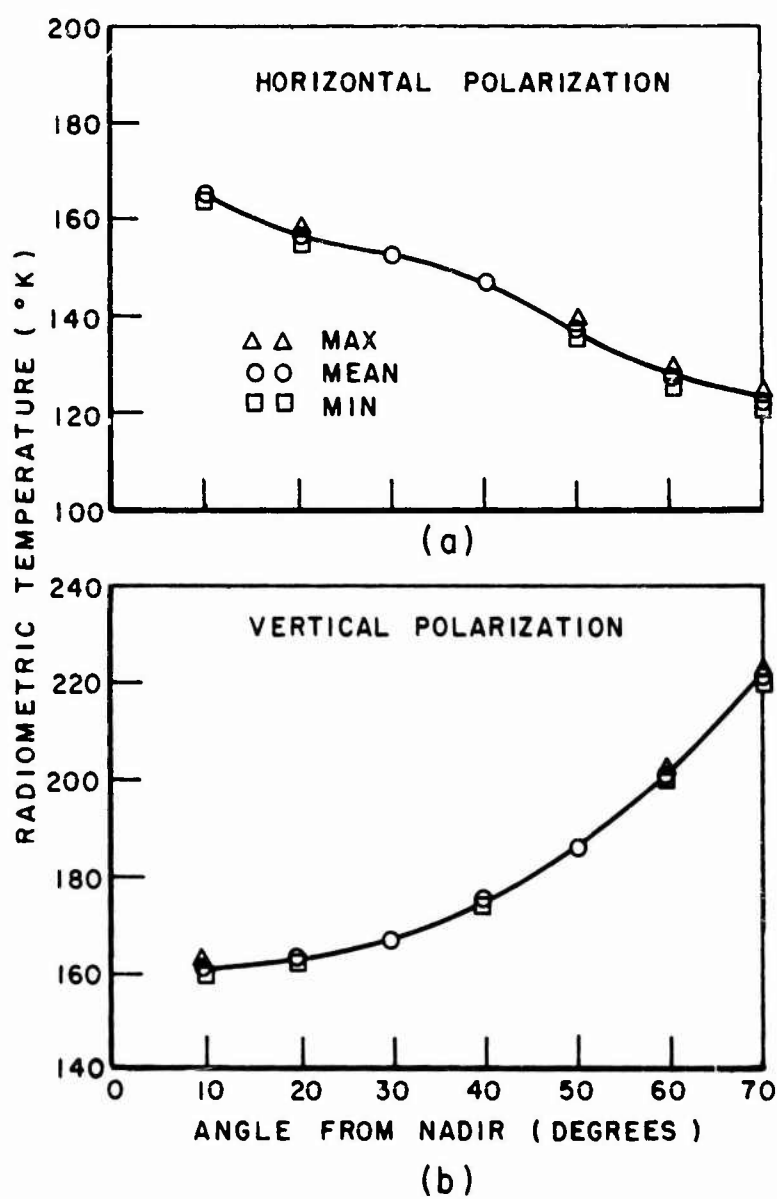
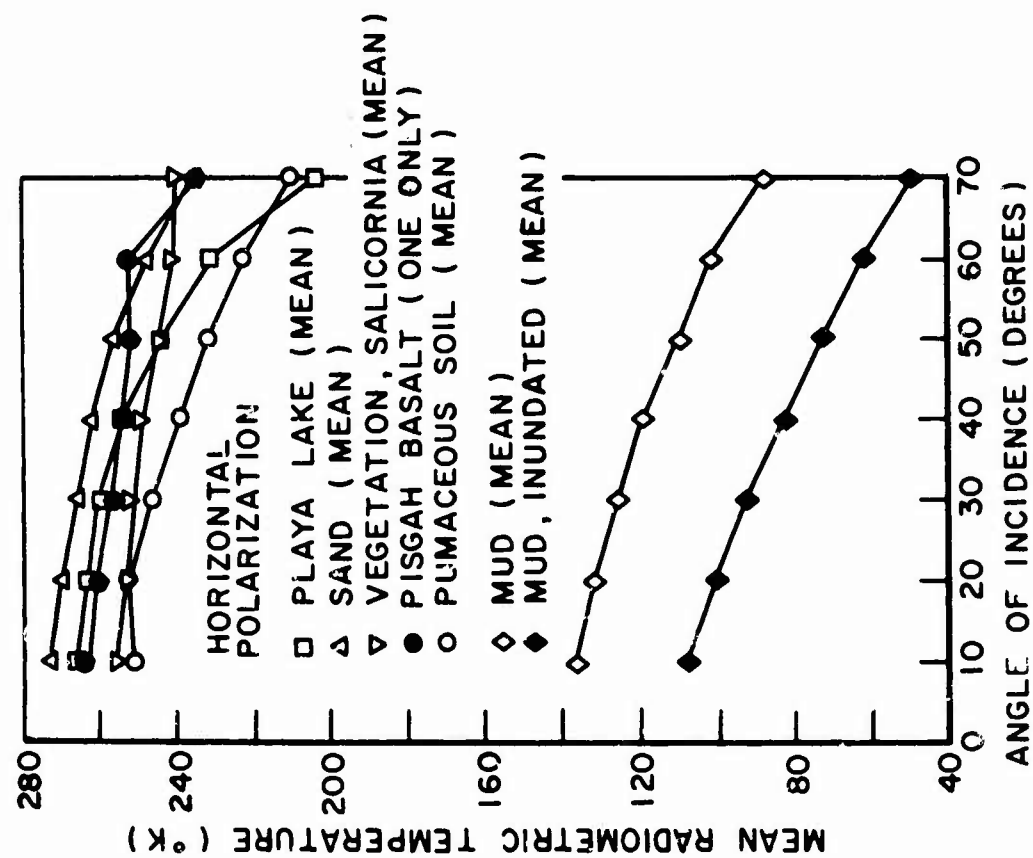
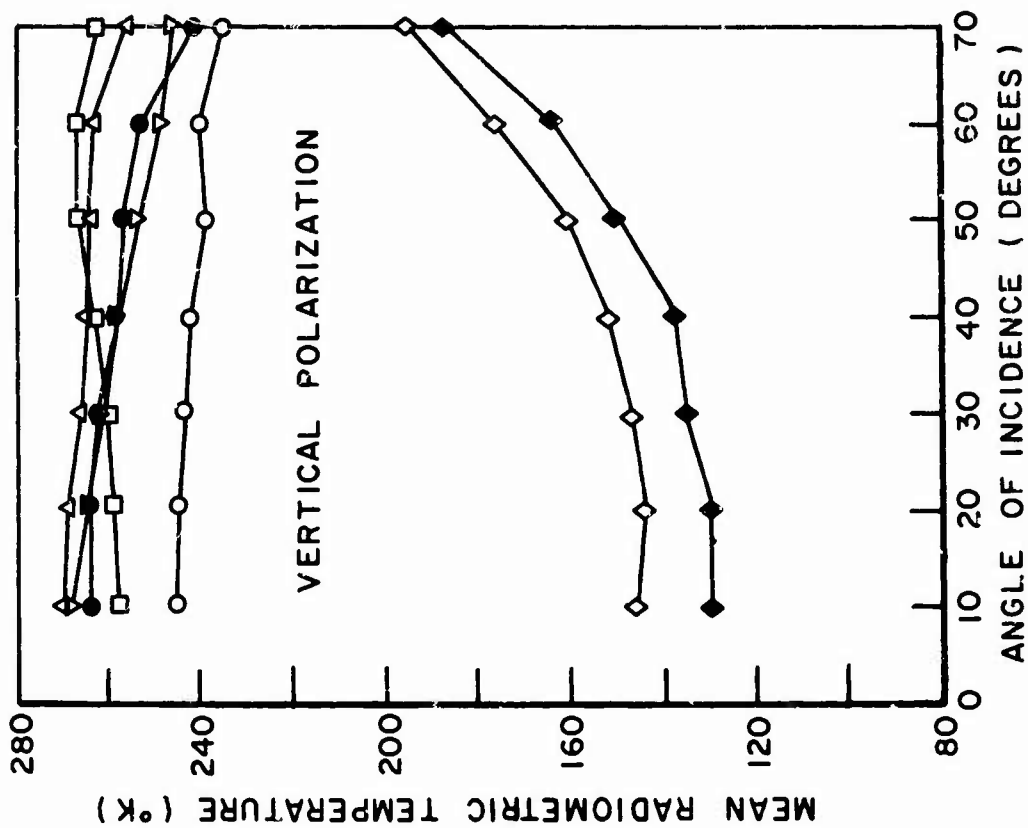


Fig. 173. Deviation envelope and mean value curve for the radiometric temperature of sea water (Palo Alto) at 37 GHz - Reference 34.



(a)



(b)

Fig. 174. Comparison of mean radiometric temperatures at 13.5 GHz - Reference 34.

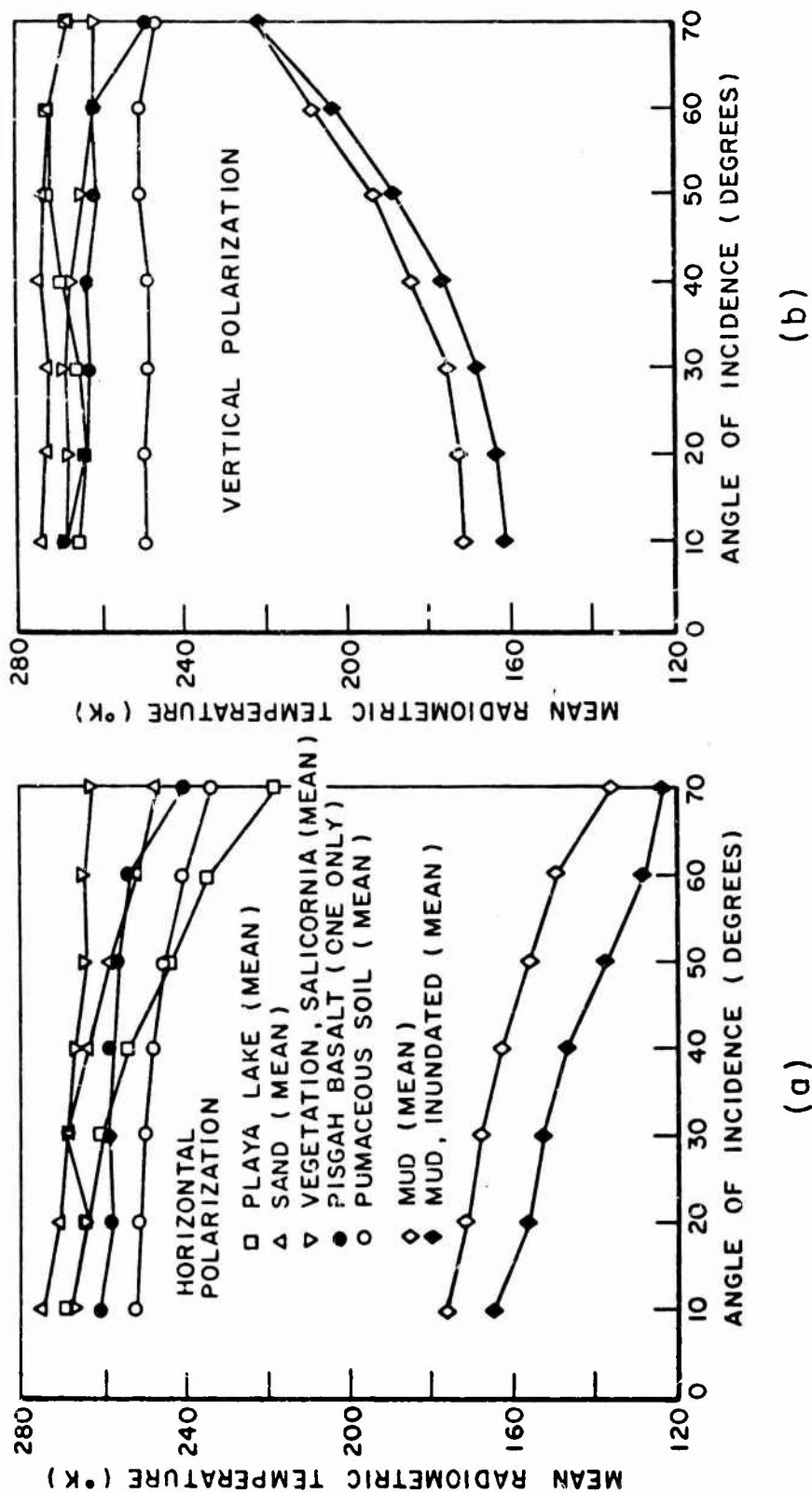
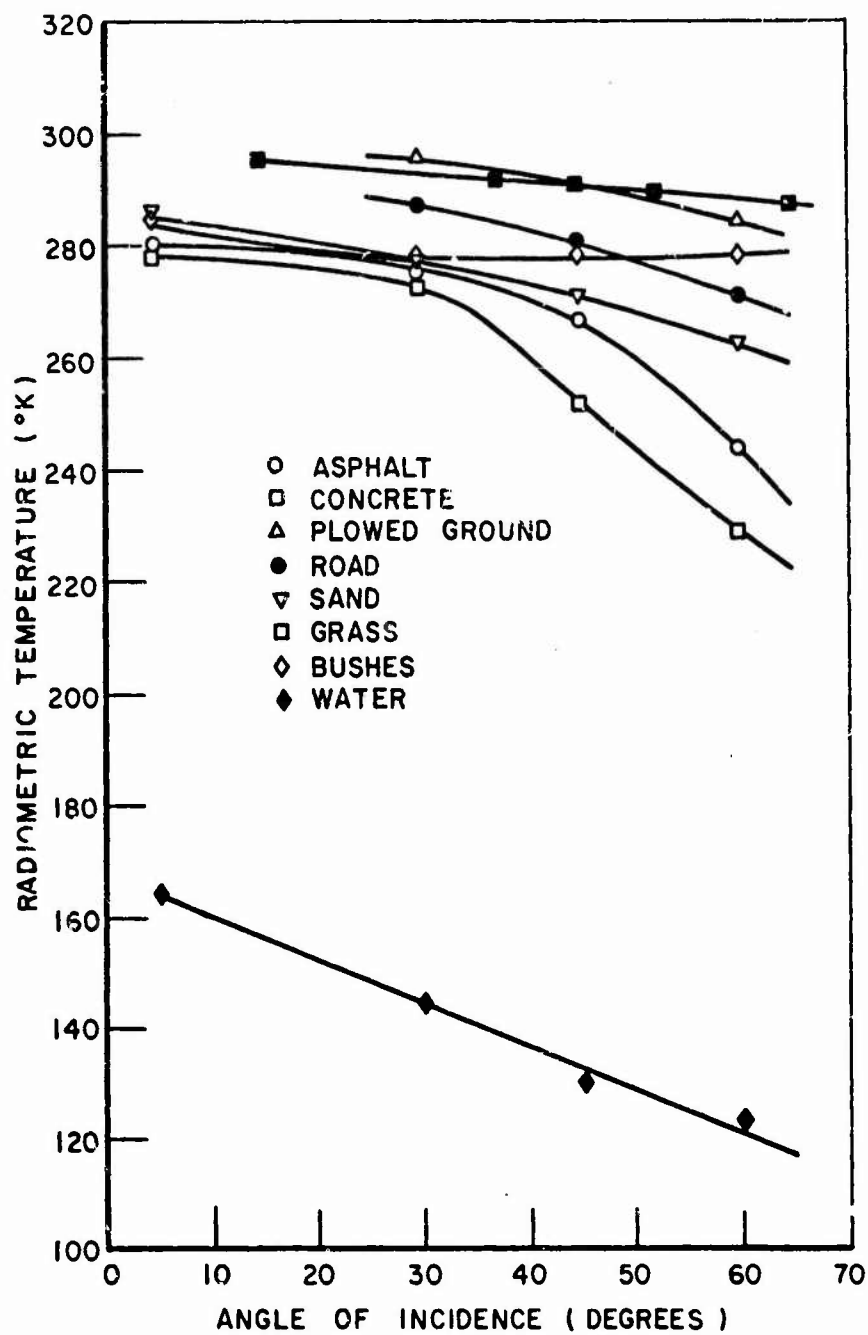
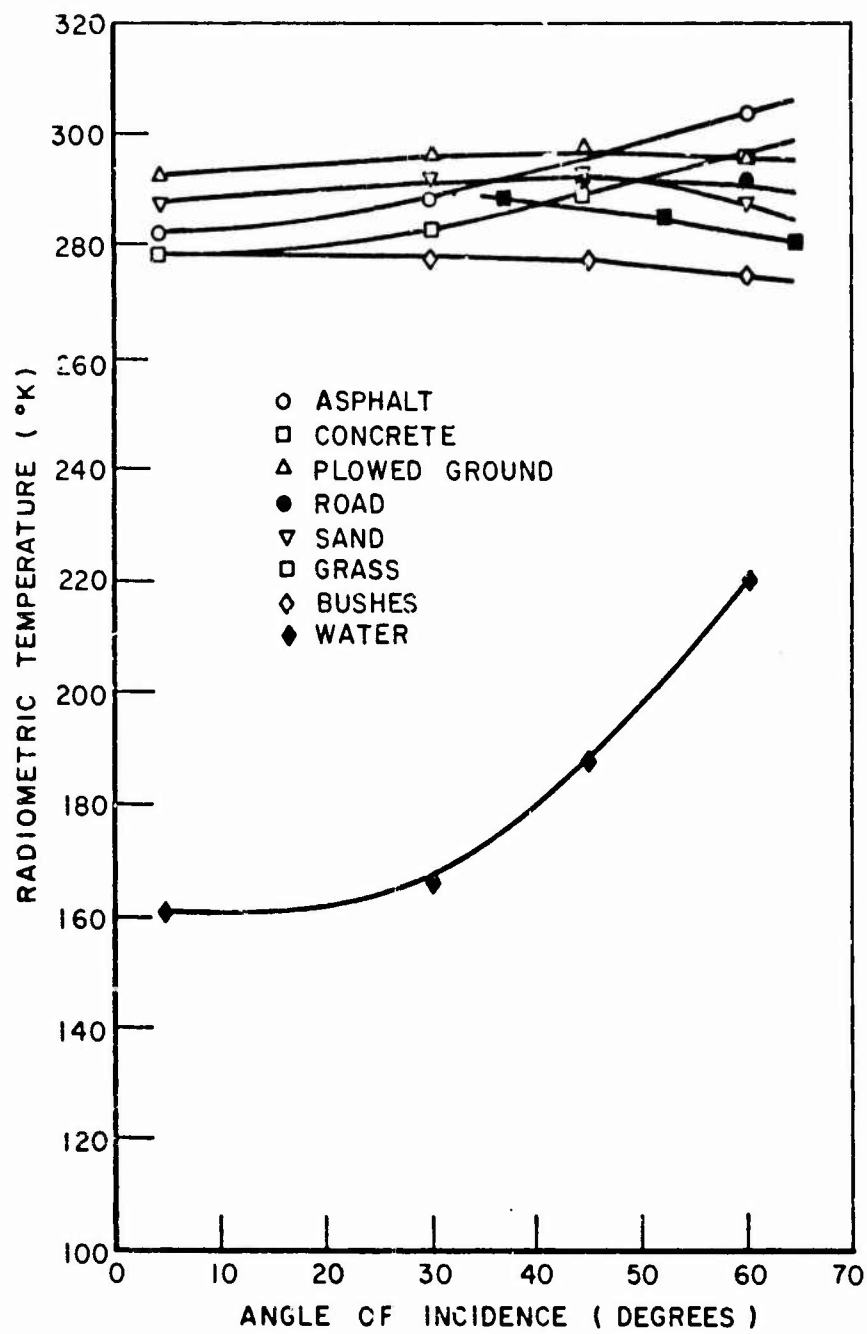


Fig. 175. Comparison of mean radiometric temperatures at 37 GHz - Reference 34.



(a)

Fig. 176. Comparison of measured radiometric temperatures at 35 GHz, horizontal polarization - Reference 38.



(b)

Fig. 176. (Continued)

REFERENCES

1. Cost, S.T., "Measurements of the Bistatic Echo Area of Terrain at X-Band," Report 1822-2, 15 May 1965, ElectroScience Laboratory, Department of Electrical Engineering, The Ohio State University; prepared under Contract No. AF 33(615)-1153 for The University of Michigan, Ann Arbor, Michigan.
2. Peake, W.H. and Cost, S.T., "The Bistatic Echo Area of Terrain at 10 GHz," Wescon Technical Paper 22-2, August 1968.
3. Cosgriff, R.L., Peake, W.H. and Taylor, R.C., "Terrain Scattering Properties for Sensor System Design," (Terrain Handbook II), Engineering Experiment Station Bulletin No. 181, May 1960, The Ohio State University, Columbus, Ohio.
4. Peake, W.H. and Taylor, R.C., "Radar Back-Scattering Measurements from Moon-Like Surfaces," Report 1388-9, 1 May 1963, ElectroScience Laboratory, Department of Electrical Engineering, The Ohio State University; prepared under Grant No. NSG-213-61 for National Aeronautics and Space Administration.
5. Shultz, C.H., Oliver, T.L. and Peake, W.H., "Radar Backscattering Data for Surfaces of Geological Interest," Report 1903-7, 2 December 1969, ElectroScience Laboratory, Department of Electrical Engineering, The Ohio State University; prepared under Contract NSR-36-027 for National Aeronautics and Space Administration.
6. Oliver, T.L. and Peake, W.H., "Radar Backscattering Data from Agricultural Surfaces at Microwave Frequencies," Report 1903-9, 13 February 1969, ElectroScience Laboratory, Department of Electrical Engineering, The Ohio State University; prepared under Contract No. NSR-36-008-027 for National Aeronautics and Space Administration.

7. Riegler, R.L., "Microwave Radiometric Temperatures of Terrain," Report 1903-2, 30 June 1966, ElectroScience Laboratory, Department of Electrical Engineering, The Ohio State University Research Foundation; prepared under Contract NSR-36-008-027 for National Aeronautics and Space Administration.
8. Oliver, T.L. and Peake, W.H., "Microwave Brightness Temperature of Terrain," Report 2440-4, 15 January 1969, ElectroScience Laboratory Department of Electrical Engineering, The Ohio State University Research Foundation; prepared under Contract F 33615-67-C11663 for Air Force Avionics Laboratory, Wright-Patterson Air Force Base.
9. Sherwood, E.M. and Ginzton, E.L., "Reflection Coefficients of Irregular Terrain at 10 cm," Proc. of IRE, 43, pp. 877-878, July 1955.
10. Oliver, T.L., "A Mobile Facility for Measuring the Backscattering and Brightness Temperature of Terrain at Microwave Frequencies," Report 1906-6, 4 October 1968, ElectroScience Laboratory, Department of Electrical Engineering, The Ohio State University Research Foundation; prepared under Contract NSR-36-027 for National Aeronautics and Space Administration.
11. Edgerton, A.T., "Engineering Applications of Microwave Radiometry," 5th Symposium on Remote Sensing of Environment, University of Michigan, April 1968.
12. Peake, W.H., Riegler, R.L. and Schultz, C.H., "The Mutual Interpretation of Active and Passive Microwave Sensor Outputs," Proceedings of the Fourth Symposium on Remote Sensing of Environment (April 1966), Institute of Science and Technology, University of Michigan, Ann Arbor, pp. 771-777.

13. Pidgeon, V.W., "Bistatic Cross Section of the Sea," (Unpublished paper), December 1964, Applied Physics Laboratory, Johns Hopkins University, Silver Spring, Maryland. (See also Proc. IEEE 54, p. 405, 1966)
14. Naval Research Laboratory, 1958 data.
15. Daley, J.C., et.al, "NRL Terrain Clutter Study Phase II," NRL Report 6749, 21 October 1968, Naval Research Laboratory, Washington, D. C.
16. Goodyear Aircraft Corporation, "Final Report: Measurements of Terrain Backscattering Coefficients with an Airborne X-Band Radar," GERA-463, 30 September 1959, AD-229104.
17. Floyd, W.C., et.al, "Scatterometer Data Analysis Program, Final Report," Report No. 57667-2, 21 September 1967, Ryan Aeronautical Company, San Diego, N68-23721.
18. Hagfors, T., "A Study of the Depolarization of Lunar Radar Echos," Radio Science (New Series) 2, 445-465 (1967).
19. Carpenter, R.C., Astron, J., 71, 142.
20. Brown, W.E., Jr., "Radar Studies of the Earth," Proc. of IEEE (Special Issue on Remote Environmental Sensing), Vol. 57, No. 4, pp. 612-620, April 1969.
21. Evans, J.V. and Hagfors, T., "Study of Radio Echoes from the Moon at 23 Centimeters Wavelength," J. Geophysics Res. 71, No. 20, pp. 4871-4889.
22. Massachusetts Institute of Technology, "Radar Studies of the Moon, Final Report," 31 August 1967, N67-40153.

23. Jet Propulsion Laboratory, "Surveyor Project Final Report, Part II, Science Results," Technical Report 32-1265, 15 June 1968.
24. Grant, C.R. and Yaplee, B.S., "Back Scattering from Water and Land at Centimeter and Millimeter Wavelengths," Proc. of IRE, July 1957, p. 976.
25. Lundien, J.R., "Terrain Analysis by Electromagnetic Means: Radar Responses to Laboratory Prepared Soil Samples," Tech. Report No. 3-693, U.S. Army Engineer Waterways Experiment Station, Corps of Engineers, Vicksburg, Mississippi.
26. Westinghouse Defense and Space Center, "Backscatter Flight Test Program," Report No. 1878A, October 1964. AD 608274.
27. Dailey, et.al., "Sea Clutter Measurements on Four Frequencies," NRI Report 6806, 29 November 1968, Naval Research Laboratory, Washington, D.C. (See also Guinard, et.al., Proc. IEEE 58, p. 543, 1970.)
28. Rouse, J.W., Jr., MacDonald, H.C. and Waite, W.P., "Geoscience Applications of Radar Sensors," IEEE Transactions on Geoscience Electronics, Vol. GE-7, No. 1, January 1969.
29. Campbell, J.P., "Back-Scattering Characteristics of Land and Sea at X-Band," Proc. of the National Conference on Aeronautical Electronics, jointly sponsored by the Dayton Section of IRE, the Professional Group on Aeronautical and Navigational Electronics (PGANE-IRE), and the Institute of Aeronautical Sciences, May 1958.
30. Wiltse, J.C., Schlesinger, S.P. and Johnson, C.M., "Back-Scattering Characteristics of the Sea in the Region from 10 to 50 KMC," Proc. of IRE, February 1957.

31. Kranson, H. and Randig, G., "Terrain Backscattering Characteristics at Low Grazing Angles for X- and S-Band," Proc. of IEEE, December 1966, p. 1964.
32. Linell, T., "An Experimental Investigation of the Amplitude Distribution of Radar Terrain Return," sixth Conference of the Swedish National Committee on Scientific Radio, 13 March 1963.
33. Ericson, L.O., "Terrain Return Measurements with an Airborne X-Band Radar Station," Sixth Conference of the Swedish National Committee on Scientific Radio, 13 March 1963.
34. Kennedy, et al., "Passive Microwave Measurements of Snow and Soil - Volume II," 5 November 1966, Space-General Corporation, El Monte, California, AD-647257.
36. Nordberg, W., et al., "Microwave Observations of Sea State from Aircraft," November 1968, NASA Goddard, N69-11537.
37. Stogryn, A., "The Apparent Temperature of the Sea at Microwave Frequencies," IEEE Trans., AP-15, pp. 278-285, 1967.
38. Ring, D.H., "Microwave Research," Final Report No. 24269-K, 30 March 1956, Bell Telephone Laboratories.
39. Hollinger, J., "Passive Microwave Measurements of Sea Surface Roughness, Naval Research Lab. Preprint. (To be published.)